Smart Process-Aware Tolerance Design and Quality Assurance for Additive and Hybrid Manufacturing

BY

AZADEH HAGHIGHI
B.S., Sharif University of Technology, 2011
M.S., KTH Royal Institute of Technology, 2013

THESIS

Submitted as partial fulfillment of the requirements
for the degree of Doctor of Philosophy in Industrial Engineering and Operations Research
in the Graduate College of the
University of Illinois at Chicago, 2020

Chicago, Illinois

Defense Committee:

Dr. Lin Li, Chair and Advisor
Dr. David He, Mechanical and Industrial Engineering
Dr. Houshang Darabi, Mechanical and Industrial Engineering
Dr. Yayue Pan, Mechanical and Industrial Engineering
Dr. Ramille N. Shah, Bioengineering

تقدیم به مادر، پدر و همسر عزیزم

To my loving parents, Hengameh and Saeed, and the love of my life Mojtaba.

ACKNOWLEDGEMENTS

First and foremost, I would like to express my ultimate gratitude to my loving parents, Hengameh and Saeed, my lovely little brother and sister-in-law, Arman and Aysan, and my beloved husband Mojtaba, for their unconditional love and support throughout this journey. Thank you for believing in me and for being there when I needed you. You are a blessing in my life. I love you all.

Next, I would like to thank my Ph.D. advisor, Dr. Lin Li for his support, guidance and advice. Additionally, I would like to thank my Ph.D. committee members, Dr. David He, Dr. Houshang Darabi, Dr. Yayue Pan, and Dr. Ramille N. Shah for their support, constructive feedback, and overwhelming encouragements. I would also like to thank Dr. Yayue Pan for providing me with access to some of the critical experimental equipment to make this research possible.

My next special thanks go to my UIC family; the rest of the faculty and staff members at the Mechanical and Industrial Engineering Department, as well as the UIC research centers including the Electron Microscopy Core (EMC) and Nanotechnology Core Facility (NCF), machine shop, and makerspace specialists for their support and providing me with a thriving environment to grow.

Furthermore, I would like to express my sincere gratitude to Dr. Lihui Wang, my first academic mentor and my previous colleagues and friends at KTH Royal Institute of Technology, Sweden, for helping me grow as a researcher and becoming the person I am today. I will carry the lessons I have learned from you for the rest of my life.

Next special thanks go to my current and previous colleagues and friends at the University of Illinois at Chicago, Morvarid Khazraee, Mahsa Izadmehr, Lisha Wu, Erina Joyee, Haiyang He, Lu

CONTRIBUTION OF AUTHORS

Chapter 1 is an overall introduction of the dissertation including general introduction and background, literature as well as the research motivation, objectives, and contributions.

Chapter 2 represents three of my published papers (<u>Publication A</u>: Haghighi, A., and Li, L. (2018). Study of the relationship between dimensional performance and manufacturing cost in fused deposition modeling. *Rapid Prototyping Journal*, 24(2): 395-408.; <u>Publication B</u>: Haghighi, A., and Li, L. (2020). A hybrid physics-based and data-driven approach for characterizing porosity variation and filament bonding in extrusion-based additive manufacturing. *Additive Manufacturing, 36*, DOI: 10.1016/j.addma.2020.101399.; and <u>Publication C</u>: Li, L., Haghighi, A., and Yang, Y. (2019). Theoretical modelling and prediction of surface roughness for hybrid additive–subtractive manufacturing processes. *IISE Transactions*, 51(2), 124-135.). I have been the major driver of the research and Lin Li (my advisor) contributed to manuscript editing, revision, and general supervision of the research. In (Publication C), the dissertation authors' main contributions include conceptualization and idea generation; methodology; surface profile formulation and surface roughness modeling; programming, software, and data analysis; experimentation; and manuscript writing and revision. Lin Li (my advisor) contributed to the idea generation, writing, revision and general supervision of the research. Co-author Yiran Yang assisted with modeling and data analysis, experimentation, literature review and manuscript drafting and revision.

Chapter 3 represents two of my published papers (<u>Publication C</u>: Li, L., Haghighi, A., and Yang, Y. (2019). Theoretical modelling and prediction of surface roughness for hybrid additive–subtractive manufacturing processes. *IISE Transactions*, 51(2), 124-135.; and <u>Publication D</u>: Li,

L., Haghighi, A., and Yang, Y. (2018). A novel 6-axis hybrid additive-subtractive manufacturing process: Design and case studies. *Journal of Manufacturing Processes*, 33, 150-160.). I have been the major driver of the research. In (Publication D), the dissertation authors' main contributions include methodology; platform design; modeling, design, and fabrication of printing fixtures; coordinate system programming and robot control; process planning; case study generation; experimentation; and manuscript writing and revision. Lin Li (my advisor) contributed to the idea generation, writing, revision, and general supervision of the research. Co-author Yiran Yang assisted with platform design and robot control, experimentation, literature review, and manuscript drafting and revision.

Chapter 4 represents two of my published papers (Publication E: Haghighi, A., and Li, L. (2018). Joint Asymmetric Tolerance Design and Manufacturing Decision-Making for Additive Manufacturing Processes. *IEEE Transactions on Automation Science and Engineering*, 16(3), 1259-1270.; and Publication F: Haghighi, A., Yang, Y., and Li, L. (2017, June). Dimensional performance of as-built assemblies in polyjet additive manufacturing process. In *International Manufacturing Science and Engineering Conference* (Vol. 50732). American Society of Mechanical Engineers.). I have been the major driver of the research. Lin Li (my advisor) contributed to manuscript editing, revision, and general supervision of the research. In (Publication F), co-author Yiran Yang assisted with manuscript editing.

Chapter 5 provides the research conclusions and possible directions for future work.

TABLE OF CONTENTS

LIST OF TABLES

LIST OF TABLES (continued)

LIST OF FIGURES

LIST OF FIGURES (continued)

LIST OF ABBREVIATIONS

AM	Additive Manufacturing
SM	Subtractive Manufacturing
FDM™	Fused Deposition Modeling (trademarked by Stratasys company)
SL	Stereolithography
ABS	Acrylonitrile Butadiene Styrene
PLA	Polylactic Acid
ASTM	American Society for Testing Materials
CIRP	International Institution for Production Engineering Research
UV	Ultraviolet
EBM	Electron Beam Melting
DOE	Design of Experiments
GD&T	Geometric Dimensioning and Tolerancing
CAD	Computer-Aided Design
CAM	Computer-Aided Manufacturing
CAPP	Computer-Aided Process Planning
2/3D	Two/Three Dimensional
IT/ITG	International Tolerance/ International Tolerance Grade
CNC	Computer Numerical Control
ANN	Artificial Neural Network
WC	Worst Case
HASM	Hybrid Additive-Subtractive Manufacturing
SCF	Shrinkage Compensation Factor
SLM	Selective Laser Melting
RSS	Root Sum Square
TAD	Tool Axis Direction
DOF	Degree of Freedom
BF	Barrel Finishing
DFAM	Design for Additive Manufacturing
DFAA	Design for Additive Assembly
PC	Polycarbonate
PPSF	Polyphenylsulfone
STL	Stereolithography/Standard Tessellation Language
ANOVA	Analysis of Variance
NIST	National Institute of Standards and Technology
SS	Sum of Squares
MS/RMSE	Mean Sum of Squares/Root Mean Square Error
MAE	Mean Absolute Error
LCM	Least Common Multiple
ABB	ASEA Brown Boveri
BCa	Bias Corrected and Accelerated
CI	Confidence Interval
GS	Gauss–Seidel
BLP	Binary Linear Programming

SUMMARY

The emergence of Additive Manufacturing (AM) has paved the way for fabrication of highly complex geometries and internal structures, owing to its unique layer-wise manufacturing approach. Moreover, the AM technology holds great potential for improving material efficiency and reducing life cycle environmental impacts and carbon footprint, which helps with promoting a sustainable "green" manufacturing strategy. Recently, the AM trend has shifted from fabrication of prototypes to functional end-use metallic or polymeric products in various critical industries including aerospace, automotive, and healthcare. Consequently, ensuring the final quality of these single-component or multi-component products has become more important than ever. As a result, prediction, control, and enhancing the dimensional, geometric, and mechanical properties of additively manufactured products have attracted significant research interest. Moreover, a promising approach to overcome the limitations of AM in terms of quality is the adoption of hybrid additive-subtractive manufacturing processes. Nonetheless, this approach introduces new challenges for quality assurance and sustainable production planning, as multiple processes with different characteristics are involved.

To date, the majority of the existing literature on quality assurance and tolerance design for AM products is limited to a single component/process. Therefore, quality assurance for multi-component products or those fabricated by hybrid additive-subtractive processes are not fully addressed. This is further aggravated by the fact that the existing geometric dimensioning and tolerancing techniques and standards cannot be directly applied to additive manufactured components as (i) they do not address the unique characteristics of these processes which either do not exist or differ from those in traditional manufacturing processes, (ii) rely on statistical assumptions suitable for mass production scenarios which do not currently apply to AM production

scenarios, i.e., mass customization, and (iii) are generally dealt with separately from the manufacturing-stage decision making, thus not allowing the potential of the process to be fully realized. Moreover, compared to the component's dimensional properties, the geometric and mechanical properties of products are less addressed in the literature, and generally are quantified through empirical approaches. Thus, limited theoretical models for accurate estimation and prediction of these properties are available. Finally, the existing state-of-the-art on the "design-process-property-sustainability" relationship for different additive manufacturing processes (i.e., pre-requisite to any tolerance design problem) is limited and thus offers significant research opportunities. Establishing methodologies and analytical tools for the design and manufacturing of quality-assured single-component and multi-component products using additive and hybrid manufacturing technologies is thus necessary.

The aim of this dissertation is to thus advance the state-of-the-art on quality assurance for additive and hybrid manufacturing at both process and product levels. Analytical models and decision-making tools are established to help designers and manufacturers towards (i) quantifying and improving different quality metrics (i.e., dimensional accuracy, mechanical strength and porosity, and surface roughness) at the micro, meso, and macro scales for different additive and hybrid manufacturing processes while reducing the economic and environmental burdens, and (ii) smart tolerance design and process planning for multi-component products fabricated by the AM technology by considering the manufacturing stage decisions early during the design stage.

A robotic hybrid additive-subtractive platform is developed, and experiments are performed to verify the effectiveness of the established models and decision-making tools for cost-effective quality assurance, tolerance design, and process planning towards smarter additive and hybrid

manufacturing. The outcomes of this research will contribute towards the innovation of smart additive and hybrid manufacturing design software, machines, and equipment.

1. INTRODUCTION

1.1 General Introduction

1.1.1 Additive Manufacturing

Additive manufacturing (AM), also referred to as 3D printing, is defined as "a process of joining materials to make objects from 3D model data (CAD file), usually layer upon layer, as opposed to subtractive manufacturing methodologies" [1]. The general overview of the different stages associated with this manufacturing technology is illustrated in Figure 1.
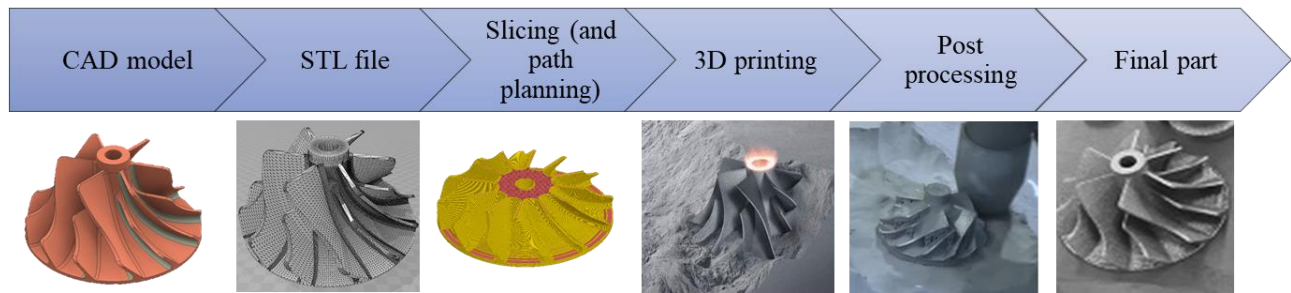
Figure 1. Overview of the different stages in additive manufacturing

Additive manufacturing technologies can be classified based on the type of raw material (e.g., liquid polymer, molten material, discrete particles, or solid sheets) as well as layer building technique [2], [3]. The ASTM F2792 standard [1] categorizes AM technologies into 7 different families of (i) Material Extrusion, (ii) Material Jetting, (iii) Binder Jetting, (iv) Sheet Lamination, (v) Vat Photopolymerization, (vi) Powder Bed Fusion, and (vii) Directed Energy Deposition, as described in Table I.

The advantages of AM technology are fourfold. (1) First, it offers higher capability in producing customized and complex geometries, internal features, heterogeneous compositions, and products with anisotropic properties --- which are costly and sometimes impossible to be

fabricated by traditional manufacturing processes. (2) Second, it significantly reduces the need for jigs, fixtures, and tooling, and offers part-independent build set-up which accelerate the product development and simplify the manufacturing process. (3) Third, it provides the ability to simultaneously produce multiple designs as well as assemblies within a single build cycle [4], [5]. (4) Finally, it holds great potential for improving material efficiency and reducing life cycle impacts and carbon footprint [6], [7].

Table I. AM technology categories[*]

Family	Description	Strength	Typical Material
Material Extrusion	"Material is selectively dispensed through a nozzle or orifice"	- Inexpensive - Color printing	Thermoplastic filaments, liquids, and slurries
Material Jetting	"Droplets of build material are selectively deposited"	- High accuracy - Color printing - Multi-material printing	Photopolymers, polymers, waxes
Binder Jetting	"A liquid bonding agent is selectively deposited to join powder materials"	- Color printing - Wide range of material	Plastic, metal, ceramic and glass powders
Sheet Lamination	"Material sheets are bonded to form an object"	- Relative low cost - Embedded components	Paper, plastic sheets, and metal foils
Vat Photopolymerization	"Liquid photopolymer in a vat is selectively cured by light-activated polymerization"	- High Accuracy - Smooth Surface finish	UV-curable photopolymer resins
Powder Bed Fusion	"Thermal energy selectively fuses regions of a powder bed"	- No need for support - Wide range of material	Plastic, metal and ceramic powders
Directed Energy Deposition	"Focused thermal energy is used to fuse materials by melting as the material is deposited"	- Suitable for repairs - Multi-material printing	Metal wires, powders, and ceramics

* Adopted from [1], [8]

Recently, the AM trend has shifted from the fabrication of prototypes to functional end-use metallic and polymeric products of small to medium volumes [9], [10]. Consequently, AM has attracted significant attention from both academia and industry, and has been adopted in various industries (Figure 2) including automotive and aerospace [11], health care [12]–[14], and electronics [15]. In 2019, the global AM market surpassed $10.6 billion and is expected to increase rapidly over the next few years [16], [17]. Furthermore, it is envisioned that industrial use of AM is likely to reach a level of mainstream adaptation in the near future [18] and further extend from mass customization towards mass production of customized products [19].

However, AM still has several limitations which hinder its application and movement towards becoming the mainstream industrial manufacturing technique. Some of these limitations are listed as follows:

1. The product quality is generally inferior to traditional subtractive processes like computer numerical control (CNC) machines [3], [20]–[22]. As a result, post-processing techniques might be necessary for refining to tighter tolerances.
2. There exists a limited choice and range of material, which further restricts possible new applications.
3. AM has generally longer manufacturing time compared to traditional manufacturing processes [23].
4. The unit cost for large volume production is generally larger compared to injection molding or other traditional processes. Therefore, the application of AM technology for mass production scenarios is not yet economically justified.
5. The maximum size of printable products is usually bounded by the building platform.

6. The current design tools and guidelines are still immature and cannot address the AM characteristics and challenges. Therefore, current research aims to overcome existing limitations and to enhance the capabilities of AM technology.
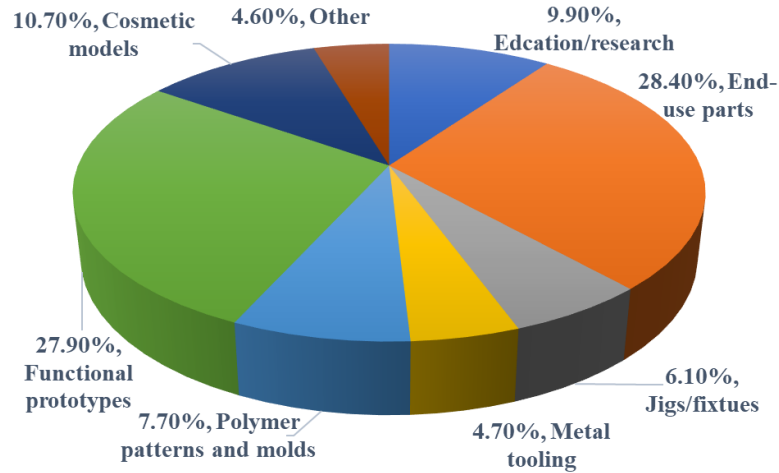
Figure 2. U.S. AM market share in different sectors for the year 2018 [24]

1.1.2 Hybrid Additive-Subtractive Manufacturing

A promising approach to overcome the limitations of AM in terms of quality and production time is the adoption of hybrid additive-subtractive manufacturing processes. According to CIRP [25], a hybrid manufacturing process "combines two or more established manufacturing processes into a new combined set-up whereby the advantages of each discrete process can be exploited synergistically". Accordingly, hybrid additive-subtractive manufacturing processes leverage the advantages of both additive and subtractive manufacturing processes; i.e., achieving complexity of design, dimensional accuracy, and high surface quality simultaneously [26]. Moreover, hybrid additive-subtractive manufacturing processes have shown promising potential in remanufacturing applications [27]. Despite their advantages, hybrid manufacturing processes introduce new challenges regarding the process design, process planning, and quality assurance, which need to

4

be addressed [28]–[32]. Consequently, the characteristics and interaction of all involved processes need to be evaluated and studied

1.1.3 Quality Assurance in Additive Manufacturing

Quality assurance is generally referred to a set of necessary tasks for maintaining the desired quality of a product, as shown in Figure 3.
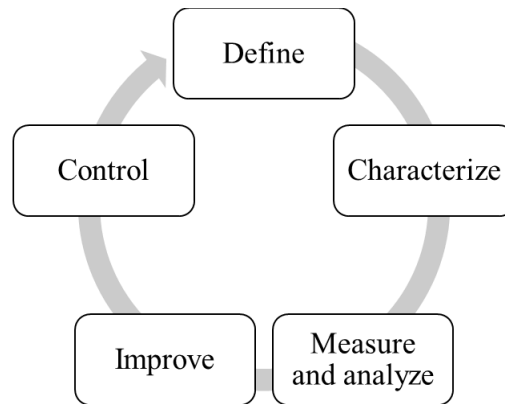
Figure 3. Overview of quality assurance steps

The different tasks of this cycle can be described as follows:

- Define: in this task, tolerances are defined according to the required functionality of the products. The term tolerance is defined as the total amount by which a specific value is permitted to vary and is usually represented by a range (or zone) within which the accepted values can lie. According to the Geometric Dimensioning and Tolerancing (GD&T) standard [33], [34], tolerances can be assigned to dimensional features (i.e., size of components), geometric features such as form, profile, orientation, location, and runout, as well as surface texture attributes including surface roughness. Tolerances are usually specified based on the expected product functionalities at the product design stage, aiming to assure the functionality of the product while reducing the overall cost [35].

5

- Characterize: this step refers to characterizing the final quality characteristics and properties of a product as a function of the design and manufacturing decisions (e.g., process and material selection, process planning, post-processing, etc.). This would require a comprehensive understanding of the AM process and material properties and can be performed using both experimental and theoretical approaches. When established, these predictive models can provide a-priori estimations of the quality characteristics and thus provide guidelines for designers and manufacturers for AM process improvement and selection of achievable tolerances.

- Measure and Analyze: this task refers to accurate measurement and analysis of different quality characteristics of manufactured parts. Different in-situ or off-line monitoring/measurement techniques and metrology systems can be adopted and developed for this purpose [36]–[39].

- Improve: to satisfy the product requirements, off-line improvement of the process and product design can be performed according to the established predictive models in forms of (i) process plan optimization and parameter tuning, (ii) enhancing the slicing algorithm, (iii) machine error compensation, (iv) design adjustments and topology optimization, and (v) secondary/post-processing including the adoption of hybrid additive-subtractive processes.

- Control: this stage refers to controlling the quality of product during the AM process based on the feedback from in-situ or online monitoring systems in real-time. As an example, the observed error from deposited layers can be utilized in real-time to adjust the thickness or deposition strategy of consequent layers to ensure a given dimensional accuracy. Control stage is itself cyclic in nature and refers to constant monitoring and improvement of quality characteristics in real-time.

To further facilitate the reader's understanding, an overview of the different terminologies used in this work to describe the different quality characteristics and performance of the AM process is provided below.

- *Dimensional accuracy* is evaluated by the amount by which the expected value of a set of dimensions is away from the nominal dimension (i.e., target value). The amount of this linear deviation is usually referred to as dimensional deviation or bias and is categorized as a systematic error. The smaller the dimensional deviation or bias is, the higher the dimensional accuracy would be. Generally, the percentage of dimensional deviation relative to the nominal size is used as a measure of dimensional accuracy.

- *Dimensional precision* is evaluated by the variability of a set of dimensions. The variability is normally measured by the standard deviation or in some cases using the range of distribution depending on the type of distribution. In cases where the standard deviation (σ) of the distribution is used, the variation of dimensions is usually represented by the $6\times\sigma$ range [40] The variation among a set of dimensions is usually caused by random errors. The smaller the variation of dimensions, the higher the dimensional precision or repeatability would be.

- *IT Grade or International Tolerance Grade (ITG)* is an indication of the precision of the process considering the nominal size of components. The IT grade is calculated according to the ISO 286-2 standard as:

$$ITG = 5\log(\frac{T}{0.45\times\sqrt[3]{D}+0.001\times D})+16 \tag{1.1}$$

where *T* represents the six-sigma range of the distribution in mm, *D* is the geometric mean dimension in mm, and *ITG* represents the IT grade.

- *Surface roughness* is a measure of surface quality and is generally evaluated by the arithmetic average height parameter, R_a, which is one of the most widely used parameters and provides a good general description of height variations along the length of the specimen's surface [41]. It is theoretically defined as the arithmetic mean of the actual profile's departure from the mean line along the sampling length [42], [43]. The mathematical definition of R_a is as follows:

$$R_a = \frac{1}{l} \int_0^l |y(x)| dx, \qquad (1.2)$$

where $y(x)$ is the surface profile function and l is the evaluation length of the profile. The accuracy of the above model relies heavily on the accuracy of the profile function $y(x)$.

- *Porosity* is a measure of the void/empty spaces inside a fabricated component which directly contributes to its mechanical properties. To quantify the global and local mechanical strength, it is necessary to characterize pore/void size and their variation within the product which requires a deep understanding of the process physics. Generally, the pores/voids in the extrusion-based AM process are structural and depend on the deposition strategy.

- *Bonding degree* or necking radius in the extrusion-based AM process is a measure of the bonding strength between two adjacent deposited filaments and directly contributes to the mechanical strength of the product. As the bonding degree is driven by the thermal energy of deposited filaments, characterizing the temperature profile of filaments through experimental and analytical approaches is critical.

1.1.4 Tolerance Design

As uncertainty and variability are inherent to any manufacturing system, activities towards ensuring the desired product performance regardless of the existing uncertainties are critical to the

survival of manufacturing enterprises. Traditionally, these activities are referred to as "tolerancing", in which the acceptable amount of variation, i.e., the tolerance, for the critical size or form features of components are carefully designed by considering the product functionality as well as the life cycle of the product [44]. Generally, manufacturers prefer a larger tolerance range as it simplifies the production (as larger variability can be accepted) and consequently, the manufacturing cost can be reduced. On the other hand, a narrower tolerance band is generally preferred by the designers as it better assures the functionality of the product. Therefore, tolerance design is the key to cost reduction and quality improvement in manufacturing industries [45].

Despite being a relatively mature field, the emersion of new manufacturing processes (e.g., AM) are creating new avenues of tolerancing research [46]–[48]. More specifically, it is necessary for different activities of tolerance design, namely, tolerance specification, analysis, and allocation, to be further tailored to the emerging manufacturing paradigms, their characteristics, and capabilities [49]. As an example, AM has the ability to make assemblies (either static or mobile) as one integrated unit in a single build [50]. Consequently, assemblies can be reduced to a single component, thus, eliminating the need for assembly, reducing cost, and possibly improving the sustainability performance of the process [51]. Clearance, defined according to the accumulated variation of assembly components [45], is considered as a key factor affecting both the mechanism operation and lifetime of assemblies and needs to be controlled to ensure a desired level of mobility is achieved [52], [53]. However, currently, the capabilities of AM technologies in satisfying the clearance requirements for this type of assemblies are unknown.

An ideal AM tolerance design methodology not only takes into account all the decisions at the manufacturing stage but also provides guidelines for the selection of optimal process plan decisions at the manufacturing stage (e.g., process and material selection, process parameter

9

selection, post-processing, etc.) as shown in Figure 4, thus removing the gap between design and manufacturing stages. To achieve this, a comprehensive understanding of the relationship between (i) product design, (ii) AM process plan decisions, (iii) characteristics of the micro geometries, and anisotropic properties at the macro level, and (iv) the life cycle impact, (i.e., "design-process-property-sustainability" relation) is necessary. As also observed in this figure, in addition to offline predictive models of quality characteristics and life cycle impacts (which guide the tolerance design efforts), the inclusion of online feedback models can also further benefit the system at the manufacturing stage by further improving the products' quality.
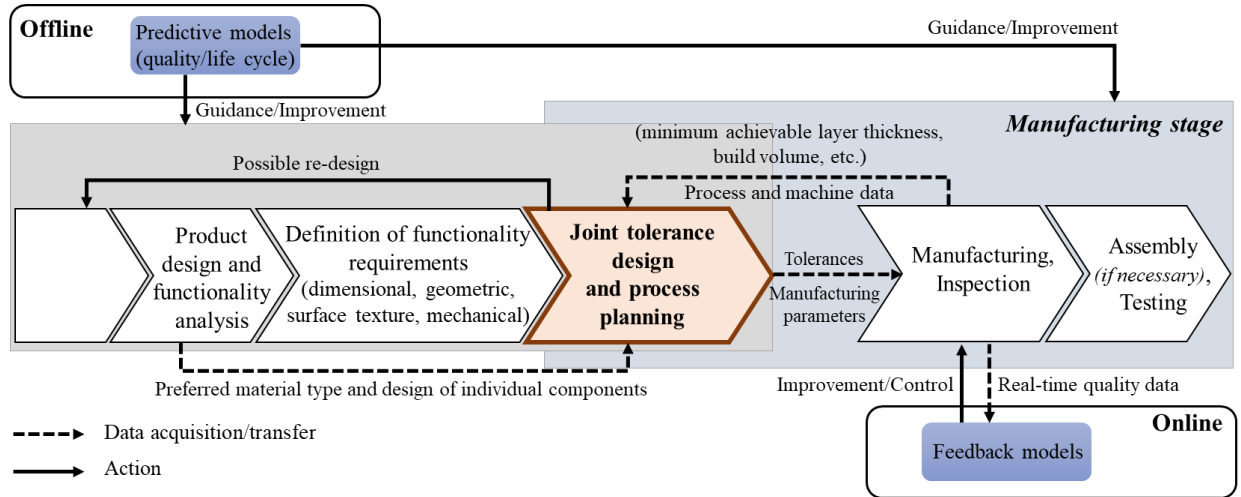
Figure 4. Smart process-aware tolerance design for AM

1.2 Literature Review

The prediction and control of the obtained quality characteristics in different manufacturing processes including additive and hybrid manufacturing processes is a critical requirement for designers and manufacturers [54] that not only allows for checking the compliance with design specifications, but also helps with the determination of manufacturing strategies in the process planning stage [55]. Therefore, several research efforts have been dedicated to the characterization,

enhancement, and control of dimensional, mechanical, geometric, and surface properties in different additive and hybrid manufacturing processes through both empirical and analytical means. In addition, the joint assessment of these quality characteristics together with manufacturing cost and sustainability performance is important, as it allows for the determination of optimal design and manufacturing strategies towards both higher quality and sustainability. Moreover, as AM processes are different in nature from traditional manufacturing processes and have unique capabilities, development of new tolerancing standards, guidelines, and benchmarks are necessary. Finally, the development and evaluation of different hybrid additive-subtractive manufacturing processes has also been another important topic in AM research. As explained earlier, hybrid additive-subtractive processes are adopted to overcome the limitations of AM processes in terms of quality and surface properties. However, the development and control of these processes is challenging and requires significant attention.

To conclude, the existing research on quality assurance and sustainability assessment for AM can be categorized as follows.

(i) Efforts to address the technological barriers (e.g., reduce the minimum achievable layer thickness), and development of more precise machines or smarter material,

(ii) Efforts towards quantifying and benchmarking the capability of different AM processes,

(iii) Efforts towards developing GD&T and design standards considering the characteristics and capabilities of AM processes (e.g., capability to fabricate complex geometries and as-built assemblies, i.e., assemblies as a whole in one build),

(iv) Efforts towards prediction, classification and controlling/reducing the errors through process parameter tuning, machine calibration, design adjustments and compensations [56]–[59], slicing algorithm improvement or modification, and adoption of hybrid additive-subtractive manufacturing processes.

(v) Efforts to bridge the above with the sustainability performance of the process, including energy consumption, emission, material consumption, and manufacturing cost.

In this section, an overview of current literature on some of the mentioned lines of research are presented. For more information on the scope of this literature review, please refer to Section 1.4. Note that the contents of this section are from my previously published works, republished with permission from the publishers. For more information, please refer to the Appendix.

1.2.1 Dimensional Accuracy Analysis and Modeling in Extrusion-based AM Process

Different intrinsic errors of AM processes or machines (e.g. process parameter-related errors, machine errors, and material shrinkage errors) can contribute to the dimensional accuracy of components and their variability. However, as the nature of AM processes and their error sources are not entirely known, empirical studies for process understanding and control form the majority of research efforts. Specifically, regarding the Fused Deposition Modelling (FDM^{TM}) process (trademarked by the company Stratasys), as one of the most common extrusion-based AM techniques [60], several researchers have studied and addressed the dimensional performance of the process using optimization or error compensation techniques.

Sood et al. [61] and Nancharajah et al. [62] applied the Taguchi method to study the effect of process parameters on the dimensional accuracy of parts and found that layer thickness, orientation, and road width have the most significant effect. In addition, it was found that the optimal value of

12

process parameters for achieving the minimum dimensional deviation in length, width, and thickness of parts are different [63]. The design of experiments (DOE) method was used by Galantucci et al. [64] for finding the optimum process parameters and improving the dimensional accuracy of a rectangular test specimen. Among the studied parameters, the tip (nozzle dimension) was observed to have the most significant effect on the length of parts. A methodology for improving the accuracy of the distance between parallel faces was proposed in [65] where a combination of artificial neural networks (ANN) and an optimization algorithm was used. Islam et al. [66] focused on the analysis of the obtained dimensional accuracy of parts in additive manufacturing compared to CNC end milling and wire-cut discharge machining (WEDM). It was shown that the linear dimensional errors are higher in additive manufacturing compared to WEDM and end milling processes. In addition, international tolerance (IT) grades of the three processes were calculated according to the experimental results.

Lieneke et al. [67] compared the dimensional performance of Extrusion-based AM, Laser Sintering (LS), and Laser Melting (LM) using IT grades and dimensional accuracy for different nominal dimensions and spatial alignments. It was shown that both spatial alignment and nominal dimension have a strong influence on the accuracy of parts. The dimensional tolerances (i.e. variability) were studied in [68] by calculating the IT class of a rectangular test part using different nominal dimensions and spatial alignment. In [69], different machine error sources were identified and categorized. Optimal shrinkage compensation factor (SCF) was calculated in [70] for improving the accuracy of parts built by Stratasys.

As is observed, the majority of the literature is based on experimental approaches while few analytical models for characterizing the dimensional accuracy are available [56], [58], [71], [72].

13

1.2.2 Surface Roughness Analysis and Modeling in AM Processes

Surface quality is one of the most important quality measures and is mainly evaluated by the surface roughness parameters defined by the ISO standard [43]. It depends on several factors including material properties and process planning parameters. Despite the numerous advantages of AM technology, the surface quality of printed parts is generally inferior to those fabricated by traditional subtractive processes using Computer Numerical Control (CNC) machines [3], [20]. This relatively lower surface quality is mainly caused by the stair-stepping error due to the AM's layer-by-layer production method and is significantly influenced by process parameters like layer thickness and build orientation [73]–[75]. Furthermore, the support generation and removal that are required in most AM processes can usually cause additional deformation and quality issues, especially if not performed properly. Consequently, extensive research has been dedicated to surface quality improvement through process parameter optimization, which is mainly performed using an empirical approach.

A semi-empirical study was performed by Chryssolouris et al. [76] in which the correlation of process parameters and surface roughness was statistically studied for the Laminated Object Manufacturing (LOM) process. A fractional factorial design of experiments was applied in [73] for studying the effects of layer thickness, build orientation, road width, air gap, and temperature on the surface finish in FDM™. Anitha et al. [77] used the Taguchi technique to evaluate the effects of process parameters on surface roughness in the FDM™ process, where a strong inverse relationship between layer thickness and surface roughness was observed. Campbell et al. [78] developed a methodology and an accompanying software application tool to visualize the surface roughness value in different build orientations, and guide designers to select the optimum build orientation. The different error sources in FDM™ process were identified and quantified in terms

14

of surface roughness, dimensional accuracy, and precision in [69]. An adaptive neuro-fuzzy inference system (ANFIS) was developed in [79] for predicting the surface roughness in the FDM™ process based on critical process parameters, namely, build orientation and layer thickness. The above empirical studies highlight the significant effect of layer thickness and build orientation (also referred to as stratification angle, build angle, or surface angle) on the surface roughness. Furthermore, according to the results of these studies, surface roughness is observed to behave differently for different ranges of stratification angle.

Despite the necessity of empirical approaches for providing preliminary insights on the effect of different process parameters, comprehensive analytical models are generally preferred but less addressed in the literature due to the increased level of complexity. Luis Perez et al. [80] were among the first researchers that addressed this issue and established an analytical model for surface roughness using two different surface profile representation schemes, i.e., sharp edge and round edge. A prediction model for surface roughness in FDM™ process was proposed by Ahn et al. [81] where the inclination of the surface profile was also considered in addition to the layer thickness and stratification angle parameters. Assuming that the surface profile has a slightly platykurtic distribution, Boschetto et al. [82] proposed a periodic arc-based shape to approximate the surface profile. A good agreement of the theoretical model with the experimental data was observed for surface angles between 30° and 150°. The authors in [83] further extended the existing surface roughness models to the Selective Laser Melting (SLM) process. They managed to decrease the prediction error by incorporating the presence of particles on the top surfaces into the model. More recently, a new modeling methodology for AM profile was proposed [84] that categorizes three types of build edge profiles: perimeter, raster, and the combination of both patterns. The authors also proposed a periodic parabolic-based profile scheme to represent the surface profile. Boschetto

and Bottini were among the first researchers to address the surface roughness modeling in hybrid FDM™ and Barrel Finishing (BF) process [85]. The authors incorporated two parameters of layer thickness and deposition angle from the additive process, and material removal from the BF process into their model. However, the developed model cannot be applied to other subtractive processes (e.g., milling or turning) as the cutting tool parameters are not incorporated into the model.

1.2.3 Joint Assessment of Cost, Sustainability and Quality Measures

While the choice of AM process and/or process parameters can affect the part quality as stated by many researchers, it also contributes to the final cost of production [86]. Hopkinson and Dicknes [87] are among the first researchers to study the cost elements of AM processes, namely material extrusion, stereolithography, and laser sintering. They observed that the machine cost (including investment, maintenance, and overhead) has the highest contribution to the total manufacturing cost (59%), followed by material consumption (39%) and labor cost for pre- and post-processing (less than 2%). In general, based on the studied on selective laser melting process, machine cost has shown to be among the most significant cost drivers in AM processes [88]. Build time, influenced by process parameters, is identified as the most important factor affecting energy consumption and machine cost [89]. In fact, the time-dependent energy consumption element (mainly attributed to keeping the heater on) has shown to account for the majority of the total energy consumption in FDM™ [90]. The material and energy consumptions are not only among the cost drivers of AM processes but also are important in terms of process sustainability due to the increasing environmental concerns [91], [92]. It has been highlighted by several researchers that the life cycle performance of AM processes (e.g. energy consumption, material consumption, and manufacturing cost) need to be thoroughly studied and assessed together with other process

attributes (e.g. accuracy and functionality of parts) in order to make the AM technology more sustainable [93], [94]. Therefore, a multi-objective study would be necessary to ensure that the optimal combination of process parameters is selected.

These multi-objective studies have already been addressed for different quality characteristics [74] including surface roughness [95]–[97], staircase error [98], perpendicularity, parallelism, angularity, total runout, circular runout and conicity errors [99], and tensile strength [100], [101] in which at least one of the manufacturing cost elements have been considered in the quality improvement analysis and process parameter selection through empirical studies or theoretical modeling. However, very few efforts have been made for analyzing the combined dimensional performance and sustainability performance measure or manufacturing cost of AM processes in the literature.

1.2.4 As-built Assemblies in Additive Manufacturing

In addition to manufacturing complex geometries, one of the major capabilities of AM is the ability to make assemblies (either static or mobile) as one integrated unit in a single build [50]. Consequently, assemblies can be reduced to a single component, thus, eliminating the need for assembly, reducing cost, and possibly improving the sustainability performance of the process [51]. In the literature, these additive structures have been referred to as "one-piece assemblies" [102], "as-built assemblies" [46], "integrated assemblies" [103], as well as "non-assemblies" [104].

The numerous research directions that have been formed regarding as-built assemblies are the integration of microscale components e.g., electronics and sensors in the assemblies to increase their functionality [105], [106] and improving the functionality and mechanical properties by using multiple materials in the assembly structure [107], [108]. These emerging applications of AM are

17

considered significant and can greatly change the field of product design. Therefore, developing guidelines and standards regarding design for additive manufacturing (DFAM) and assembly (DFAA) needs to be addressed in parallel with these technological advancements [109], [110]. Design for manufacturing and assembly is typically defined as "tailoring the design for eliminating the manufacturing difficulties, and minimizing the manufacturing and assembly costs" [111]. The design phase in AM assemblies is usually much more complicated than the actual manufacturing process, which makes it the current bottleneck for AM to achieve its full potential [112]. Furthermore, the effect of positioning of components in one build cycle (e.g., overlapped, integrated design, etc.) on the distribution of dimensional errors is not addressed in the literature.

One of the main considerations in DFAM is ensuring the functionality of the assembly. Clearance, defined according to the accumulated variation of assembly components [45], is considered as a key factor affecting both the mechanism operation and lifetime of assemblies and needs to be controlled to ensure a desired level of mobility is achieved [52], [53]. On the other hand, the functionality of the mechanism is directly affected by the capability of AM technology to create the desired clearance among components in an as-built assembly scenario. However, the accuracy of current AM technologies is lower than traditional manufacturing processes in general [113] and is limited by a number of technological constraints. For example, the minimum achievable clearance in AM processes is a function of the minimum powder grain size (in powder-based processes) or layer thickness [46]. Therefore, creating clearances smaller than these values is not feasible, which as a result, limits the application of AM technology in producing as-built assemblies. In addition, the successful production of as-built assemblies requires the entire removal of the excess material (support structure) between components. Therefore, in order to produce as-built assembly structures, one might need to redesign the original assembly and

18

components by changing geometries, dimensions, and even the clearance [114], which is usually performed using a trial and error approach.

1.2.5 Hybrid Additive-Subtractive Manufacturing Processes

As explained earlier, additively manufactured parts usually have lower accuracy [21] and strength, unsatisfactory surface quality [22], and longer manufacturing time [23]. Therefore, it is necessary to improve the dimensional and mechanical performance of AM processes while reducing the production time.

Recently, the development of hybrid additive-subtractive manufacturing processes has become a promising solution for improving the current limitations of AM processes and also an effective approach for remanufacturing applications [27]. Many research efforts have been dedicated to proposing suitable hardware and kinematic configurations, control systems, and process planning approaches for hybrid manufacturing systems [29], [115], [116]. The most popular hybrid design in the literature is based on the integration of conventional AM processes and SM processes, such as milling, on a single station. This can be applied by either attaching a SM head to an AM machine/mechanism or vice versa. For instance, Jeng and Lin [117] presented a new method of fabricating and modifying metal rapid prototypes and molds, where selective laser cladding process was used to build up the material layer-by-layer, and milling process was performed to machine the top surface for better accuracy and surface finish. In order to manufacture super alloy integral impellers in aero engines which are vital functional parts with complex freeform surfaces, Xinhong et al. [118] adopted a hybrid process which consists of plasma deposition process and milling process, and managed to improve the insufficient dimensional precision and surface quality. Karunakaran et al. [119] integrated a 3D arc weld deposition process with a commercial CNC machine and found that the hybrid process can save time and cost of production compared to when

19

the parts are fabricated solely by the CNC machine. Choi et al. [120] developed a direct metal fabrication technique which combines CO_2 laser welding and milling processes.

The developed hybrid processes in the literature indicate a promising potential for quality improvement. Nevertheless, they lack fabrication flexibility because of having only three DOF for mobility. To address this limitation, Liou et al. [121] developed a hybrid process for metallic structures including a laser deposition system and CNC milling mechanism in one workstation with five-axis motion modes. It was shown that the five-axis hybrid process could significantly reduce material consumption and production time. In addition, a satisfactory surface quality could be obtained by using the CNC milling process. Lee et al. [122] developed a low-cost hybrid system with an FDM™ extruder and a spindle placed on each end of a rotary axis in a five-axis machine tool. A novel tool changing mechanism was also proposed for switching between extruder and spindle using a 180-degree rotation of the head. A remanufacturing station including three processes of laser cladding, machining, and in-process scanning was developed in [123]. The integrated station was successfully applied to remanufacture turbine blades with lower capital investment costs.

Although the discussed hybrid additive-subtractive processes can have multi-axis motions (mainly caused by the rotatory build platform), the movements of SM and AM heads are usually constrained to three axes of motions (namely X, Y, and Z). Therefore, to incorporate more DOF to the SM and AM heads, employing a robotic arm or mechanism with more than 3-DOF is necessary. According to the literature, the only study on developing a multi-axis robotic hybrid additive-subtractive process is performed by Keating and Oxman [124], where a multi-axis robotic platform named compound fabrication is proposed, which integrates additive, subtractive, and formative processes. This compound fabrication platform is applied for plastic deposition and can

20

achieve a fast printing speed (0.2 m/s) as well as fine surface resolution for large-scale printing. In addition to the advantages obtained by employing a hybrid approach (e.g., reducing material waste, increasing accuracy, and reducing build time), adopting robotic arms for developing hybrid processes can increase the workspace adaptability and flexibility, and thus provides new manufacturing opportunities (e.g., printing on complex 3D surfaces rather than a planar surface or accessing inner surfaces or features). However, despite these numerous advantages compared to the conventional hybrid machines with motion constraints on X, Y, and Z axes, the development and application of robotic structures for hybrid additive-subtractive processes is still limited and not fully addressed in the literature. In addition, most of the research efforts regarding the development of hybrid processes do not consider or focus on the development of an integrated manufacturing platform to support the functionality of different processes.

1.2.6 Porosity and Bonding Characterization in Extrusion-based Additive Manufacturing

Extrusion-based additive manufacturing is a popular AM process in which thermoplastic material is melted and selectively dispensed through a nozzle or orifice to form the geometry in a layer-by-layer approach [125]. An interesting feature of this process is its potential to fabricate structures with locally-controlled properties through adjustment of the material dispensing strategy [126]. To fully exploit this potential, it is important to carefully study and link the (i) material properties, (ii) geometry design, (iii) deposition strategy including process parameters and path planning, (iv) characteristics of the micro geometries, and (v) anisotropic properties at the macro level [127]–[129].

Several studies on linking the deposition strategy in the extrusion-based additive manufacturing process with mechanical properties at the macro level through experimental approaches are found in the literature. For example, the effect of printing speed, layer thickness, raster angle, air gap,

bead/raster width, liquefier temperature, and fill density on different mechanical properties including tensile, yield, flexural, impact, and compressive strengths, modulus of toughness, and elongation at break have been studied [130]–[133]. While these experimental efforts provide valuable insights, they do not provide information on micro geometries/structures and their influence on the mechanical properties at the macro level. Kulkarni and Dutta [134] were among the first to address the important role of microstructures on the mechanical behavior of material in extrusion-based additive manufacturing. Rodriguez et al. [135] and Too et al. [136] highlighted that the extent of bonding between contiguous filament segments and porosity (or void density) directly contribute to the mechanical properties [137]. Li et al. [126] established models for characterizing void density as a function of the air gap parameter in unidirectional specimens. An inverse relationship between mechanical properties and porosity was reported by Kalita et al. [138], Chin Ang et al. [139], and Phuong et al. [140]. To further improve the bonding quality, Ko et al. [141] proposed a material engineering approach in which the viscosity of the polymer is manipulated to increase the tensile strength of specimens.

To fully characterize the extent of bonding between contiguous filaments and porosity of products, however, it is necessary to understand the underlying physical phenomenon of the process. In the extrusion-based AM process or similar path-based processes (e.g., selective laser melting or SLM), the bonding phenomenon and porosity is driven by the thermal energy. Sun et al. [142] investigated the effect of different processing conditions, i.e., the position of layer, liquefier and envelope temperatures, deposition strategy, and building location, on the temperature profile of printed filament segments as well as the bonding quality. Faes et al. [143] applied an experimental approach to study the influence of inter-layer cooling time on the ultimate tensile strength of parts and observed an inverse correlation between these parameters. As real-time

22

monitoring of temperature profile at different points in space and time during the process is extremely challenging, simulation-based or analytical approaches for filaments' thermal history evaluation and characterization have become popular. As an example, a 2-D thermal analysis was performed by Bellehumeur et al. [144] to characterize the thermal profile of a single filament using heat transfer modeling and estimating the degree of bonding between two adjacent filaments [145]. Zhang et al. [146] proposed a finite element model to simulate the temperature variation of a cuboid during and after the extrusion-based AM process with respect to both space and time. D'Amico and Peterson [147] adopted Finite element analysis (FEA) in COMSOL to simulate heat transfer in the extrusion-based AM process. Recently, Costa et al. [148] established a model to evaluate the temperature evolution of filaments with adjusting boundary conditions based on the deposition strategy.

Despite the existing efforts in the literature, there are several challenges and limitations that need to be addressed. First, estimating accurate values of material-related parameters is difficult due to the continuous cooling and heating cycles (e.g., the conduction and convection heat transfer coefficients, rheological properties, etc.) thus, leading to prediction inaccuracies. Second, the domain of validity of existing models on porosity and bonding characterization is limited and has shown to generally lead to prediction inaccuracies [126], [128], [142]. Third, the majority of the existing models do not account for the deformation of micro geometries due to the gravitational force, weight of upper filaments, viscoelasticity stress and creep, and its effect on the bonding degree due to its high modeling complexity [149]. Fourth, based on the existing literature, the spatial variation of bonding extent and porosity cannot be characterized as the majority of models only provide an overall estimation of these parameters [142], [150]–[152]. The ability to characterize these variations is critical towards the production of parts with locally-controlled

properties since different regions of the part might have different dimensional or mechanical properties requirements. Thus, having a priori knowledge on the variation of these factors as a function of the process plan and part geometry allows for optimal control of manufacturing parameters, and verifying or optimizing the design at the early product life cycle stages.

1.2.7 Tolerance Design Research

The importance of tolerance design task for enhancing the cost-effectiveness and quality of products was highlighted in the late 90s [45]. Initially, simple methods like "proportional scaling" and "weight factors" were adopted to distribute the assembly tolerance among different components due to their effectiveness and simplicity. However, they eventually became less popular as they could not address the manufacturing cost [153]. Consequently, more promising approaches using optimization techniques were introduced to minimize the manufacturing cost. Generally, there exist three categories of tolerances: (i) bilateral tolerances, where the tolerances are defined symmetrically around the target, (ii) unilateral tolerances, where the tolerance in one of the positive or negative directions is 0, and (iii) asymmetric or unbalanced tolerances, where the tolerances are either defined on the same direction of the target or are defined on opposite directions but with different lengths. Generally, the first category of tolerance design dominates the literature. Few studies have addressed the asymmetric tolerance design considering asymmetric quality loss functions [154]–[156], but they usually consider the distribution of the quality loss function and its coefficient to be known a-priori. In general, to distribute the assembly tolerance among components, three key elements need to be addressed:

(i) The assembly/design function and the relationship between component tolerances and the final assembly tolerance need to be defined,

(ii) The relationship between component tolerances and cost (referred to as cost-tolerance model), or other penalty functions such as quality loss need to be defined,

(iii) The optimization problem should be constructed and suitable solution approaches (either traditional, heuristic, or hybrid approaches) need to be proposed to tackle the problem.

To establish the relationship between assembly tolerance and components' tolerances, two common models are used in the literature: worst case (WC) and statistical (root sum square, RSS) [35]. These models have been adjusted to also address different dimensionality of assemblies, as shown below:

$$\text{WC:} \qquad \sum_i T_i \leq T_{ASM} \text{ and } \sum_i \left(\left| \frac{\partial f}{\partial x_i} \right| T_i \right) \leq T_{ASM}, \qquad (1.3)$$

$$\text{RSS:} \quad \left[\sum_i T_i^2 \right]^{1/2} \leq T_{ASM} \quad \text{and} \quad \left[\sum_i \left(\frac{\partial f}{\partial x_i} \right)^2 T_i^2 \right]^{1/2} \leq T_{ASM}, \qquad (1.4)$$

in which, T_{ASM} is the given assembly tolerance; T_i is the tolerance of component i; f is the assembly function, and $\left| \frac{\partial f}{\partial x_i} \right|$ and $\left(\frac{\partial f}{\partial x_i} \right)^2$ are the sensitivity of the tolerance stack to each individual tolerance (in two- or three- dimensional assemblies) for the WC and RSS methods, respectively. In addition, the mean shift model [157] for tolerance allocation has been proposed as:

$$\sum_i \left| m_i \frac{\partial f}{\partial x_i} T_i \right| + \left[\sum_i \left((1 - m_i)^2 \frac{\partial f^2}{\partial x_i} T_i^2 \right) \right]^{1/2} \leq T_{ASM}, \qquad (1.5)$$

where m_i is the mean shift factor. However, none of these models can tackle asymmetric or unbalanced tolerances.

Traditionally, cost-tolerance functions are obtained by curve-fitting to empirical data and thus require extensive effort. Alternative techniques such as fuzzy logic, neural networks, and design of experiments are also proposed in the literature to establish the cost-tolerance functions. The application of different traditional solution approaches (e.g., Lagrange multiplier and exhaustive search) and novel heuristic techniques (e.g., genetic algorithm, simulated annealing, or hybrid techniques) to tackle the optimization problem are also investigated in the literature [158].

To conclude, the contributions of tolerance allocation research generally vary in terms of the (i) considered assembly function, its characteristics and complexity, (ii) adopted tolerance accumulation model, (iii) cost-tolerance function formulation, (iv) optimization model formulation and assumptions, (v) incorporated input parameters and objectives, and (vi) proposed solution approach. Some examples of these contributions include tolerance design in multistage manufacturing systems [159], joint optimization of cost with quality loss [160] or maintenance planning [161], and joint design and process/process parameter selection [162], [163].

1.3 Motivation

The increasing application of additive and hybrid manufacturing technologies for fabricating functional polymeric or metallic products has motivated researchers to address the newly introduced challenges in the area of error characterization, quality assurance, tolerance specification, and design. More specifically, the different nature and manufacturing characteristics of the additive manufacturing technologies compared to traditional manufacturing techniques, as well as their currently unknown capabilities in satisfying different tolerances and possible environmental and cost implications, require specific attention from researchers in academia and industry [48]. According to the above literature review, some of the existing limitations in the

26

literature on quality assurance and tolerancing considering this emerging technology can be summarized as follows:

(i)   The majority of the existing literature is focused on quality assurance and tolerancing for single-component/process, thus neglecting multi-component products and hybrid manufacturing processes.

(ii)   Geometric, surface texture, and mechanical properties of components are less addressed compared to dimensional properties.

(iii)   The majority of the existing models are based on experimental approaches, and thus theoretical models for prediction/estimation of different quality characteristics are scarce.

(iv)   Environmental and cost implications of AM technology and lifecycle impacts of products (as the pre-requisite to any tolerance design research) are still not entirely known. Therefore, advancing the state-of-the-art on "design-process-property-sustainability" in different AM processes is necessary.

1.4 Research Scope, Objectives, and Framework

Based on the mentioned motivations and literature review, the following research scope, objective, and framework are proposed.

1.4.1 Research Scope

Among the different quality assurance stages introduced in Figure 3, this thesis would only focus on three stages of "Define", 'Characterize" and "Improve". Therefore, the established predictive models are not necessarily real-time but provide tools for a-priori estimation of quality characteristics towards design and process improvements. In addition, this thesis aims to address methodologies for quality assurance and tolerancing for both single- and multi-component/process.

27

Therefore, some of the quality assurance challenges in multi-components AM products and those fabricated by hybrid additive-subtractive manufacturing process are addressed as well. The application of different analytical, statistical, and data-driven techniques is studied. Among the different quality metrics, this thesis addresses dimensional accuracy, surface roughness, porosity, and bonding strength. Finally, as studying all the different AM processes for the purpose of quality characterization is impossible, this thesis specifically focuses on polymer-based AM processes including Material extrusion AM, Vat photopolymerization AM, and Material jetting AM described in Table I. However, the methodologies established for quality assurance of multi-component AM products are generic and can be adapted to different metal-based or polymer-based AM processes.

1.4.2 Research Objective

Based on the mentioned motivations, literature review, and research scope, the goal of this thesis is to provide designers and manufacturers with a set of decision-making tools for quality assurance and tolerancing of both single-component and multi-component products fabricated by additive and hybrid additive-subtractive manufacturing processes towards design and process improvement, higher sustainability, and smarter manufacturing.

1.4.3 Research Framework

The research framework and scope of this thesis are shown in Figure 5. Evaluating the "design-process-property-sustainability" relation at the process level (i.e., for single components) is a prerequisite to the tolerance design at the product level (i.e., for multiple components). Therefore, the research is performed at two different levels considering the within-component interactions ("design-process-property-sustainability" relation for single components at the process level), and between-component interactions ("design-process-property-sustainability" relation among

multiple components at the product level) for smart selection of tolerances and manufacturing decisions. The process-level quality assurance research is performed for both additive and hybrid manufacturing processes as shown in the figure.
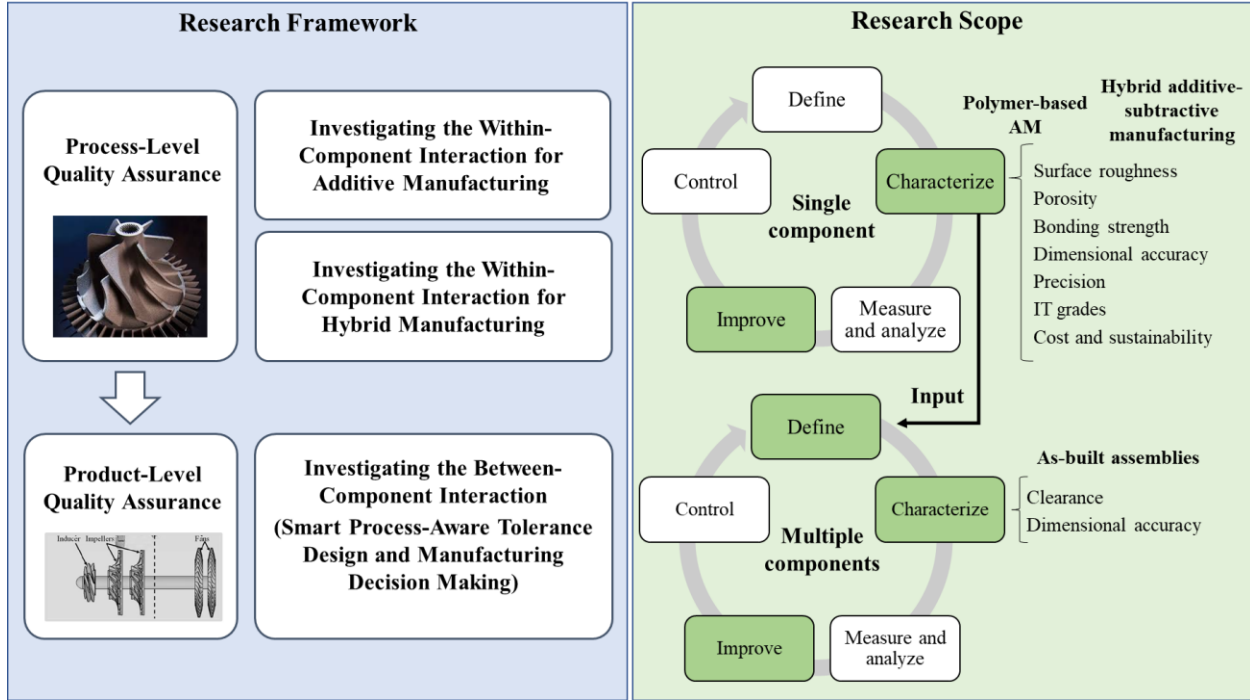
Figure 5. Research framework and scope

At the process-level, several dimensional, mechanical, and surface texture quality characteristics will be addressed. In addition, sustainability measures including cost, energy, and material consumption will be quantified. The established models and outcomes of research from the process-level quality assurance stage will then be incorporated at the product-level quality assurance stage in which multiple components are addressed.

1.5 Contributions and Thesis Outline

The main contributions of this thesis are as follows: First, several quality and sustainability measures of single-component additively-manufactured products including dimensional accuracy,

IT grades, surface roughness, porosity, bonding strength, cost, and energy consumption in polymer-based AM processes are characterized through analytical and experimental approaches. The relation between the process parameters, product design, and these measures are highlighted for process and design enhancement. Second, a novel robotic hybrid additive-subtractive process is developed. Third, the surface roughness of products as a result of this hybrid process is analytically characterized using a geometric modeling approach. Fourth, the dimensional distribution of pre-assembled multi-component products fabricated by AM is characterized. Finally, a comprehensive smart process-aware tolerance design methodology for additively manufactured components is proposed in which the dimensional tolerances and manufacturing decisions are jointly selected and optimized to ensure product quality. The previously established predictive models are used within the proposed methodology.

The rest of this thesis is organized as follows.

In Chapter 2, the within-component interaction for additive manufacturing is studied considering different quality metrics. First, a joint assessment of manufacturing cost and dimensional performance in the extrusion-based AM process is conducted using the design of experiments approach, and the achievable IT-grade for this process is quantified. Second, the surface roughness of components in polymer-based AM processes as a function of layer thickness and orientation is analytically modeled and validated. Third, the porosity, bonding strength, and their variation within a component in the extrusion-based AM process are analytically modeled using a hybrid physics-based and data-driven approach by incorporating heat-transfer modeling, Newtonian sintering model, geometric modeling, and data-driven modeling of filaments' deformation. Experiments are performed to validate the established models. Finally, the conclusions and future works of the chapter are presented.

In Chapter 3, within-component interaction for hybrid manufacturing is studied. First, the development process and capabilities of a robotic hybrid additive-subtractive platform (developed to carry out this research) are discussed and illustrated through several case studies. A process planning methodology for reducing energy consumption and improving quality is proposed. Next, an analytical surface roughness model for hybrid additive-subtractive manufactured surfaces is proposed and validated using the developed platform. Finally, the conclusions and future works of the chapter are discussed.

In Chapter 4, the effect of assembly design on the dimensional distribution of components in the Polyjet process is studied. Next, a joint tolerance design and manufacturing decision-making methodology is proposed and formulated for additive manufactured components and products. The methodology is based on asymmetric distribution of errors and considering assembly requirements, namely specification and confidence level. The bootstrap statistical technique is used to estimate the unknown population's statistics. Due to its suitability, a cyclic optimization approach is adopted to tackle the formulated problem. Finally, the conclusions and possible future works of the chapter are discussed.

Finally, a summary of the main conclusions and possible future works of this thesis are provided in Chapter 5.

2. PROCESS-LEVEL QUALITY ASSURANCE: INVESTIGATING THE WITHIN-COMPONENT INTERACTION FOR ADDITIVE MANUFACTURING

This chapter presents the different studies performed to understand and establish the relation between (1) design, (2) process and process parameters, (3) properties of part: i.e., dimensional accuracy, surface roughness, bonding strength, and porosity, and (4) sustainability measures and economic implications in AM processes using both empirical and analytical approaches. As explained earlier, studying and understanding this relationship allows for selecting tolerances that are both feasible (at the manufacturing process level) considering the capability of the process, and optimal (at the product assembly level) considering product functionality and total manufacturing cost.

In Section 2.1, a joint assessment of cost and dimensional performance in Fused Deposition Modeling (FDM™) process is presented [164], which aims to address the "process-property-sustainability" relation. Cost models are developed and validated considering machine operation

as well as energy and material consumptions. In Section 2.2, the surface roughness as one of the most important quality measures of additive manufactured components is analytically modeled and validated [165]. The model is established by considering the two most important additive manufacturing process parameters; layer thickness and orientation, which exist in all AM processes. In Section 2.3, the porosity and bonding degree variation in the extrusion-based AM process (which contribute to the mechanical strength of components) are modeled based on a hybrid physics-based and data-driven approach [166]. The established models provide a-priori knowledge on the product's surface property and mechanical strength and help designers with assigning feasible surface roughness and stress/strain tolerances and designing products with locally-controlled surface texture and mechanical properties. Finally, the chapter's conclusions are presented in Section 2.4.

2.1 Joint Assessment of Manufacturing Cost and Dimensional Tolerances in Extrusion-based Additive Manufacturing Process

In this Section, a joint assessment of manufacturing cost and distribution of dimensions in the material extrusion process is performed. This study is motivated by the lack of research to analyze the combined dimensional performance and sustainability performance measure or manufacturing cost of this process in the literature for the purpose of tolerance design at the product level. The design of experiments (DOE) methodology is used for evaluating the effect of different process parameters and their interactions on the experiment responses, namely dimensional deviation and variation, as well as energy consumption, material consumption, machine operation cost, and the total manufacturing cost. To provide a cost evaluation tool for designers, mathematical models of the cost elements are also developed and validated using the empirical data. The desirability

function is used to select optimal process parameters for simultaneously improving the dimensional performance and minimizing the total manufacturing cost.

2.1.1 Material Extrusion Process Introduction

As discussed before, Fused Deposition Modeling (FDM^{TM}), is one of the most common extrusion-based AM techniques [60] and is relatively simple to operate and maintain [167]. In this process, a thin filament of thermoplastic material is fed into the machine and is heated over its glass transition temperature to liquify. The liquified material is then pushed and extruded from a small orifice and deposited on the build platform. The relative movements of the extrusion head and the build platform controls the deposition pattern, which is according to the geometry's 2D cross-sections and the programmed G-code. The deposited material is rapidly solidified as its temperature is dropped from the glass transition temperature. Each layer consists of several deposited segments (paths) of material. Once all segments of a layer are deposited, the extrusion head (or the build platform) moves one layer thickness up (or down). This process is repeated until all layers are deposited.

To help support the deposited segments in the air, especially in the case of cavities, support structures are used. The support structures can be of the same type or different from the printing material. The support material needs to be further separated and removed from the printed parts either using manual force or with the help of solvents and solutions. Some of the common materials used in this process are polycarbonate (PC), polylactic acid or polylactide (PLA), acrylonitrile butadiene styrene (ABS), polyphenylsulfone (PPSF), Nylon, etc.

2.1.2 Cost Evaluation and Modeling

The material, energy, and machine operation costs are considered for the cost evaluation and modeling. Since the majority of AM processes do not require specific labor attention during the printing process, the labor cost is usually limited to the machine setup at the pre-processing stage as well as part and support removal at the post-processing stage. In this study, however, the labor cost is not considered as it is expected to be insignificant considering the selected simple product geometry. Therefore, the total manufacturing cost is given as follows [168]:

$$C_{build} = (P_{energy} \times E_{build}) + [P_{material} \times (M_{part} + M_{Support})] + (\dot{C}_{indirect} \times T_{build}), \tag{2.1}$$

where P_{energy}, and $P_{material}$, are the unit costs of energy, and material respectively. $\dot{C}_{indirect}$ is the total indirect cost rate (machine hourly rate) that is estimated according to the machine purchase cost, machine depreciation, production overhead, etc. T_{build} is the total time of build, and E_{build} is the total energy consumption required during the build. Finally, the total material consumption consists of part material consumption (M_{part}) and support material consumption ($M_{support}$).

(1) Energy Consumption Model

Modeling the energy consumption of some AM processes has been addressed in the literature [169], [170]. However, the developed models typically have a general form and do not consider the contribution of different process parameters. Those that address the effect of different process parameters, however, are generally derived using the design of experiments approaches. Therefore, a more detailed energy model is presented. The energy consumption of the FDM™ extrusion-based process can be modeled using the following equation:

$$E_{build} = E_{process} + E_{standby} + E_{heating}. \tag{2.2}$$

Note that $E_{process}$ is the geometry-dependant energy consumption element and can be calculated by summing up the required energy for vertical and horizontal movements of the nozzle for printing the provided geometry, together with the material extrusion energy consumption. $E_{heating}$ is the amount of energy required to initially heat the filament to glass transition temperature and keeping it at a specific temperature range throughout the build duration. $E_{standby}$ is the minimum amount of energy required to keep the machine on during the build process, i.e., the energy consumed by the wires, fan, etc., which is a time-dependant energy consumption element. Assuming that the friction is negligible, the three energy components can be further modeled according to the following set of equations:

$$E_{process} = \frac{e_{xy}}{V^2} \sum_{i=1}^{I} \left(\frac{V_{xy}^2 \sum_{k=1}^{K_i} L_k^i}{D} + \frac{V_{T-xy}^2 \sum_{k=1}^{K_i-1} X_k^i}{D} \right) + (\frac{V_{T-z}}{V})^2 e_z I + P_{Avg-Ext}(T_{build} - T_{initial}) \tag{2.3}$$

$$E_{heating} = P_{H-trans} T_{initial} + P_{H-steady}(T_{build} - T_{initial}) \tag{2.4}$$

$$E_{standby} = P_{M-idle} T_{build} \tag{2.5}$$

where the following symbols are used:

I	Total number of layers
L_k^i	The length of kth continuous path in the ith layer, k=1, …, K_i
X_k^i	The horizontal distance between the endpoint of kth path and beginning of (k+1)th path in the ith layer
V_{xy}	The horizontal printing speed on the xy plane
V_{T-xy}	The transitional horizontal nozzle speed between paths on the xy plane
V_{T-z}	The transitional vertical nozzle speed between layers on the z axis
e_{xy}	The amount of energy required to move the additive head with speed V for the distance of one layer thickness (D) horizontally (on the xy plane)

e_z	The amount of energy required to move the additive head with speed V for the distance of one layer thickness (D) vertically (on the z axis)
$P_{Avg-ext}$	The average power rate required for extruding the filament
T_{build}	Total time of build
$T_{initial}$	Required time for initial heating (which can be found by experiment)
P_{M-idle}	The power rate of the machine at the idle (standby) stage
$P_{H-steady}$	The power rate of the heater at the steady-state stage after the initial heating
$P_{H-trans}$	The power rate of the heater at the transition (initial heating) stage
D	Layer thickness.

In addition to the layer thickness information and number of layers, the values of L_k^i and X_k^i in the geometry-dependant energy consumption element are directly obtained from the G-code generated by the slicing software.

(2) Material Consumption Model

The proposed material consumption model is based on the part's geometry and build parameters. The choice of process parameters affects the length of the printing paths which are then used in the model. Using the average estimated cross-section area of layers, the length of the printing path and the average density of material, the total material consumption for part and support can be calculated using the following models,

$$M_{part} = \frac{\rho\pi}{4} DW \sum_{p=1}^{P} \sum_{k=1}^{K_p} L_k^p$$

$$M_{support} = \frac{\rho\pi}{4} \sum_{s=1}^{S} \sum_{k=1}^{K_s} L_k^s D_k^s W_k^s,$$

(2.6)

where ρ is the average density of material, W is the width of paths, L_k^p is the length of kth continuous path in layer p of part, and L_k^s is the length of kth continuous path in layer s of support. The symbols L_k^s, D_k^s and W_k^s refer to the length, thickness, and width of the kth path in the sth layer

37

of the support structure, respectively. Using different width and thickness values is necessary as they can vary from one layer to another. For the purpose of model validation however, it is assumed that the cross-section area does not change along the printing path (e.g., at the corner points). Moreover, the changes of material density are not considered in the model and the average density of the material is used.

2.1.3 Experiment Design and Methodology

Design of Experiments (DOE) method [171] is used to conduct the experiments. The test part (shown in Figure 6(a)) is first designed in Autodesk Inventor and then converted to STL file format. The studied dimension (aligned toward the Z-axis) is shown in Figure 6(a).
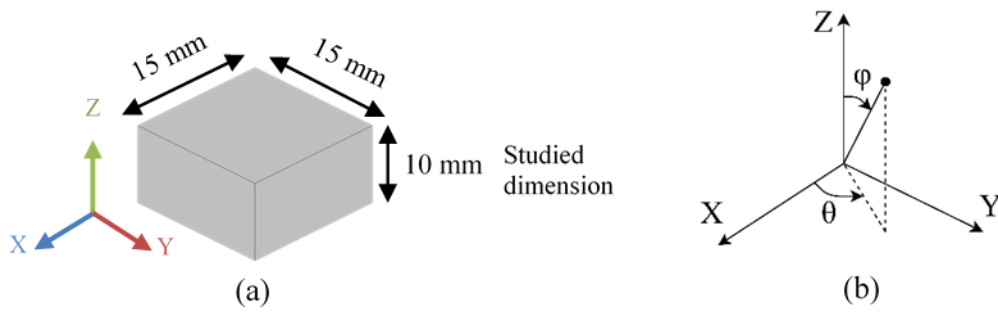
Figure 6. (a) Test part, and (b) orientation representation scheme

The Up-Mini 3D printer is used for fabricating the parts. The initial price of the machine is approximately 600 dollars. The machine operation cost (machine rate per hour) is estimated using the depreciation rate based on 3 hours of print time per day, 100 printing days per year and an amortisation period of 2 years. The machine overhead is assumed to be 25% of the depreciation rate. The hourly machine cost is thus, calculated as 1.3$ per hour. An ABS filament spool with the price of $50 per kg is used for fabricating the parts. The energy consumption cost is also determined using the electricity price of $0.15 per kWh (Table II).

Table II. Machine, material and energy cost parameters and inputs

Machine and Machine Operation Parameters		Material and Energy Parameters	
Machine model	Up-Mini printer	Material type	ABS
Initial cost	$600	Material cost per kg	$50
Hourly cost	$1.3	Electricity cost per kWh	$0.15

A two-level full factorial design is used to establish the experiments including four controllable factors: layer thickness, fill density, inclination, and direction as shown in Table III. In this study, part orientation is represented through two different angles: (1) polar angle (φ), which describes the part relative to the XY plane (build plate) and is represented by the inclination factor, and (2) azimuthal angle (θ), which is the angle between the orthogonal projection of the part in the XY plane and the X-axis and is represented by the direction factor [67]. Therefore, the combinations of the two angles (φ,θ) has been used to represent the part's final orientation as shown in Figure 6(b). The (0,0) orientation is defined as the reference orientation in which the studied dimension is aligned toward the X-axis. Using the reference orientation, the rest of the orientations can be defined using counter-clockwise rotation as shown in Figure 7.

As shown in Table III, layer thickness, inclination, and direction are defined as numerical parameters, and fill density is represented as a categorical parameter. Two levels of high and low are considered for each factor. Three replicate experiments are conducted for each possible combination of the factors at different levels. Six center points are also added to the experiment for studying the process noise or instability as well as checking for the curvature of the response surface. Therefore, a total of 54 experiment runs are conducted. The rest of the process parameters were kept constant and are provided in Table IV.

To have consistency among experiments and reduce the variation factors, the followings were considered. The machine was kept off for a constant duration of time between experiments so that it had enough time to cool down and reach the ambient temperature. All experiments were initialized at the 20-degree Celsius nozzle temperature. The energy consumption rate (power) of the machine was measured for every 5-minute interval using the Yokogawa CW10 power meter, with a maximum AC/DC current of 600A and a maximum AC/DC voltage of 1000V, during the build process. The dimension of part was measured using a digital caliper with the accuracy of 0.01 mm. To account for the shrinkage of parts, each part was measured on the 4th day after the build.

Table III. Control factors

Control Factors	Symbol	Levels		Center Point
		Low (-1)	High (1)	
Layer thickness (mm)	A	0.2	0.3	0.25
Fill density	B	Hollow	Solid	Loose
Inclination φ (degrees)	C	0	90	45
Direction θ (degrees)	D	0	90	45
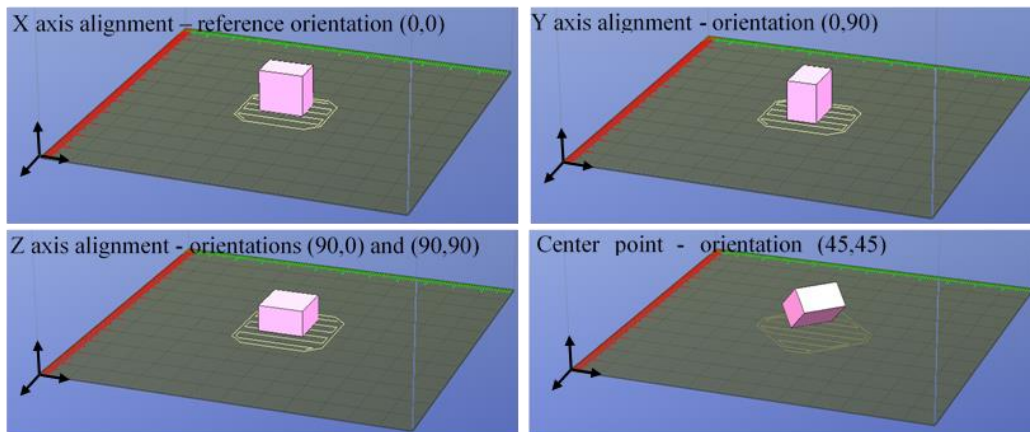
Figure 7. Experiment orientations

Table IV. Constant parameters

Material	ABS
Printing speed	Normal
Number of support layers	7
Number of contours	2
Initial nozzle temperature (˚C)	20

2.1.4 Cost Model Validation

Experimental data are used to validate the models. Two different experimental settings, which are among the settings with best dimensional performance, are selected for validation purposes. The results of the material consumption validation for two of the experimental setting are shown in Table V. The observed error is expected to be mainly due to the approximation of the length of the printing paths and width of layers.

Table V. Material consumption model validation considering two settings

	Material consumption elements (g)	A: 0.3, B: Hollow Alignment: Z	A: 0.2, B: Hollow, Alignment: Z
Model	M_{part}	1.01459	0.84103
	$M_{support}$	0.69782	0.58484
Experiment	M_{part}	1.11767	0.98967
	$M_{support}$	0.83267	0.56767
% Error		12.199%	8.442%

Similarly, the energy consumption model is validated considering the same experimental settings as shown in Table VI. The model shows good accuracy and the error is expected to be mainly due to employing the approximated power consumption rates for different elements of the FDM™ machine instead of the actual power rates, as well as approximating the length of the printing path. Among the different energy elements of the system, the geometry-related energy component ($E_{process}$) has the highest contribution to the increase of total energy when changing the layer thickness from 0.3 to 0.2.

41

Table VI. Energy consumption model validation considering two settings

	Energy elements (J)	A: 0.3, B: Hollow Alignment: Z	A:0.2, B: Hollow Alignment: Z
Model	$E_{process}$	6517	7714
	$E_{heating}$	16650	17950
	$E_{standby}$	10900	11900
	Total	34067	37564
Experiment	Average	37216	38868.3
	standard deviation	515.7	421.466
% Error		8.46%	3.35%

2.1.5 Dimensional Tolerances and Distributions of Components

The experiment results are summarized in Table VII. The experiments are sorted from the smallest observed dimensional deviation to the largest. The linear dimensional deviation is calculated using the observed (D_O) and nominal (D_N) dimensions. The variation is evaluated by calculating the 6×standard deviation range. It is observed that dimensions along the Z-axis (build direction) are usually oversized while the dimensions are generally undersized on the XY plane. In addition, the contribution of machine operation cost to the total cost is approximately 69.8%, followed by the material consumption (29.6%) and energy consumption (0.6%).

The distribution of dimensions in different experiment settings as well as the relative costs are presented in Figure 8. The fundamental deviations for each experiment are calculated according to the GD&T standards. The first experiment has the smallest dimensional deviation and variation compared to all other experiments. In the experiment numbers: 8, 10, 11, and 12, the alignment of the studied dimension is toward the Y-axis and the average variation is smaller compared to the X and Z alignments. However, in the X alignment (experiments 1, 3, 5, and 7) a smaller dimensional deviation compared to the Y alignment is obtained. To conclude, no systematic relation between the fundamental deviation values, IT grades, and relative cost are observed.

Table VII. Experiment results

#	A B C D	D_N (mm)	D_O (mm)	Linear deviation (mm)	Variation $6 \times \sigma$ (mm)	IT grade	Relative cost	% Cost contribution machine/material /energy
1	(-1, -1, -1, -1)	10	9.990	-0.010	0.018	7.32	0.965	76.35/23.1/0.55
2	(-1, -1, 1, 1)	10	10.011	0.011	0.180	12.32	0.855	73.2/26.24/0.56
3	(-1, 1, -1, -1)	10	9.973	-0.027	0.125	11.53	1.146	73.48/26/0.52
4	(-1, -1, 1, -1)	10	10.033	0.033	0.183	12.36	0.858	73/26.45/0.55
5	(1, -1, -1, -1)	10	9.967	-0.033	0.035	8.75	0.880	69.33/30.14/0.52
6	(-1, 1, 1, 1)	10	9.957	-0.043	0.092	10.86	1.030	69.49/30/0.51
7	(1, 1, -1, -1)	10	9.937	-0.063	0.193	12.48	1.067	67.56/31.98/0.46
8	(1, -1, -1, 1)	10	9.933	-0.067	0.092	10.86	0.881	69.26/30.22/0.52
9	(-1, 1, 1, -1)	10	9.907	-0.093	0.125	11.53	1.030	69.48/30.02/0.51
10	(-1, -1, -1, 1)	10	9.897	-0.103	0.035	8.75	0.961	76.62/22.86/0.52
11	(1, 1, -1, 1)	10	9.870	-0.130	0.060	9.95	1.053	67.98/31.56/0.46
12	(-1, 1, -1, 1)	10	9.863	-0.137	0.035	8.75	1.149	73.72/25.77/0.52
13	(0, 0, 0, 0)	10	10.232	0.232	0.116	11.36	1.344	66.14/33.39/0.47
14	(1, -1, 1, 1)	10	10.310	0.310	0.120	11.42	0.862	66.52/32.95/0.53
15	(1, -1, 1, -1)	10	10.353	0.353	0.092	10.83	0.862	66.52/32.96/0.52
16	(1, 1, 1, -1)	10	10.363	0.363	0.330	13.61	1.028	64.51/35.01/0.48
17	(1, 1, 1, 1)	10	10.407	0.407	0.346	13.73	1.029	64.4/35.11/0.49
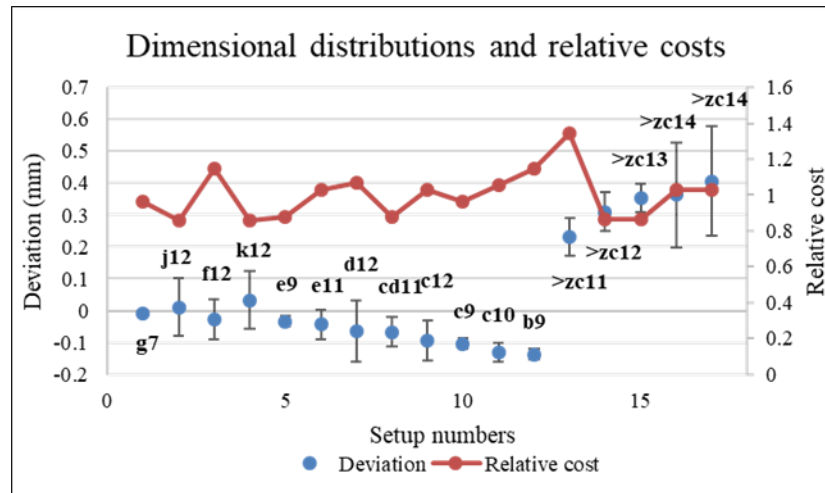
Figure 8. The distribution of dimensions and relative costs for different experiment settings

2.1.6 Factorial Analysis Results

(1) Dimensional Performance

The dimensional performance of the process is evaluated using the percentage change of dimensions from the nominal value as well as the $6 \times \sigma$ range. The analysis of variance (ANOVA)

is performed for both responses (%∆Dimension and 6×σ) to find the significance level of process parameters. It is found that all of the studied factors and their interactions have a significant effect on the variation of dimensions using a 95% confidence level. Regarding dimensional deviation, layer thickness, inclination, and their interactions have shown to play the most important roles.
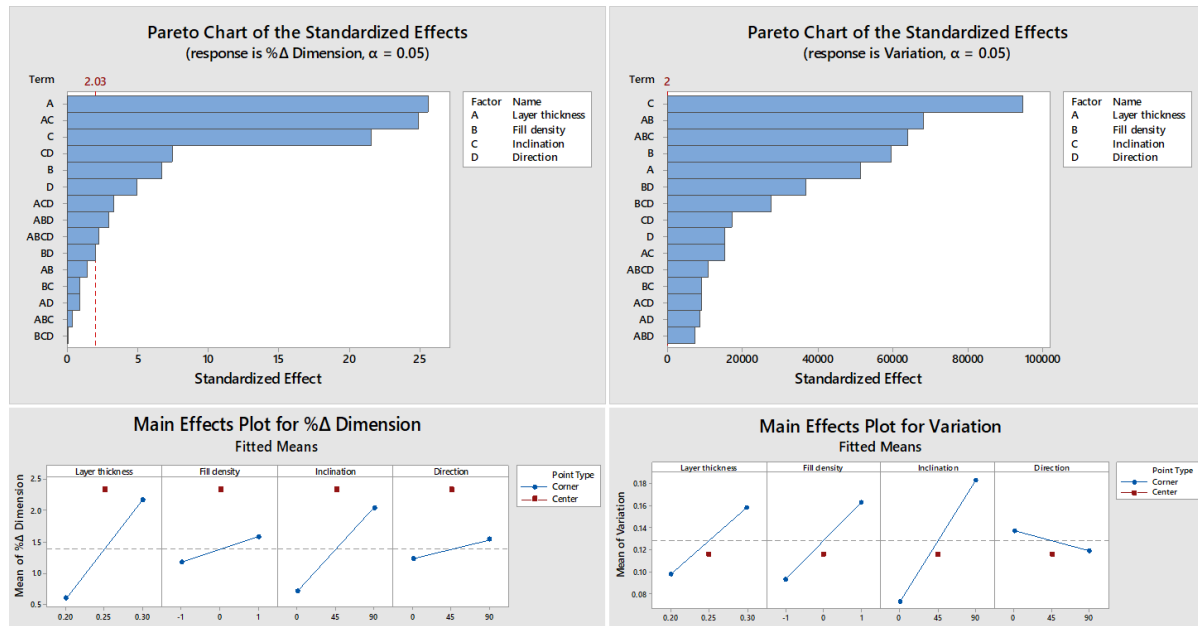
Figure 9. Pareto chart and main effect plot for linear % change of dimensions and variation of dimensions

The Pareto charts and main effect plots of both dimensional performance factors are presented in Figure 9. Although reducing the layer thickness and fill density seem to generally improve the dimensional performance of parts, the interactions between the orientation of part with both layer thickness and fill density makes it almost impossible to propose strategies that guarantee the improvement of dimensional performance at any given orientation. In other words, the orientation plays a key role in identifying the optimum layer thickness or fill density. In addition, the interaction between layer thickness and fill density is different in different orientations (Figure 10).

Therefore, the interaction of parameters in each spatial alignment was further studied. In both X and Y alignments, reducing the layer thickness has shown to result in smaller variability so that a narrower tolerance band can be satisfied. However, reducing the fill density shows contradictory effects on variability for X and Y alignments (reducing X's but increasing Y's). Therefore, no systematic relationship between fill density and variability was observed.
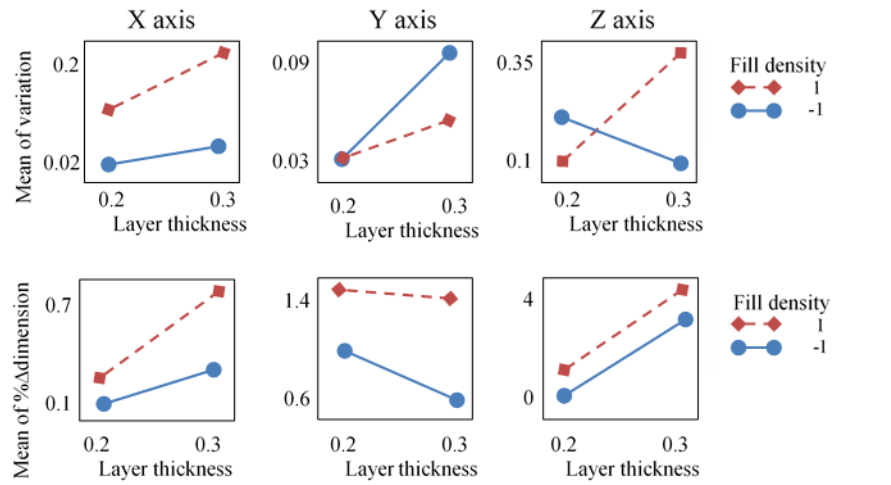
Figure 10. Interaction plot for variation and deviation in different alignments

The dimensional deviation along all three axes shows to be reduced by decreasing the fill density for a given layer thickness value. This is probably due to a smaller shrinkage of material as smaller material volume is deposited in each layer. Note that the amount of deviation for dimensions in the XY plane is also affected by several factors including the geometry of part, machine error, and even the deposition path. Therefore, all of these factors need to be studied in order to identify the best strategy for minimizing the dimensional deviation. For the X and Z axis alignments, it is observed that reducing the layer thickness leads to a reduction in dimensional deviation. However, an opposite behavior is observed in the Y-axis alignment.

(2) Energy Consumption

Smaller energy consumption can generally be obtained by increasing the layer thickness and reducing the fill density (Figure 11) which is predictable as the movements of the additive head and the total build time are decreased. In general, reducing the number of layers, the distance of the printing path within each layer, and the number of vertical nozzle movements for moving from one layer to another can reduce the total energy consumption. As can be seen in Figure 11, the energy consumption and machine operation cost reduction strategies are very similar as the majority of energy consumption cost is attributed to the build time.
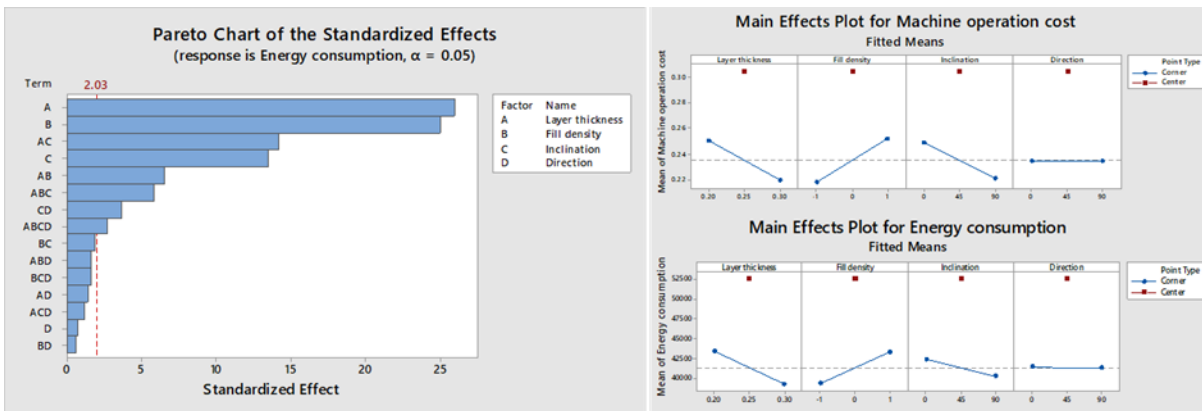
Figure 11. Pareto chart of energy consumption, and main effect plots of machine operation and energy consumption

(3) Material Consumption

It is relatively clear that reducing the fill density can decrease the material consumption. However, the effect of layer thickness has to be further studied. In other words, although reducing the layer thickness will decrease the volume of material in each layer, it also increases the number of layers. The main effect plot and Pareto chart of material consumption are presented in Figure 12. Reducing layer thickness and fill density have shown to generally reduce the material

consumption in a given orientation. The orientation parameter has shown to be mainly responsible for support material consumption.
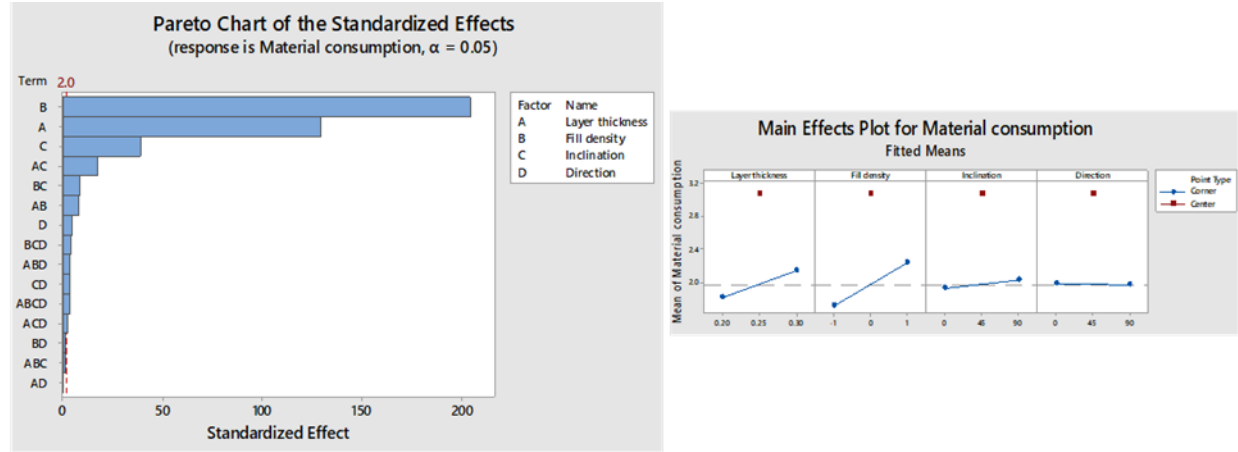
Figure 12. Pareto chart of the standardized effects and Main effect plot for total material consumption

2.1.7 Manufacturing Cost and Dimensional Performance

In this section, the correlation between different responses is studied. To test the significance of the obtained correlation coefficients, t-test is used with $\alpha=0.05$. The null and alternative hypotheses are presented below:

$$
\begin{aligned}
H_0 &: \rho_{xy} = 0 \\
H_1 &: \rho_{xy} \neq 0
\end{aligned}
$$

(2.7)

where ρ_{xy} is the correlation coefficient between variables x and y in the population.

The correlation between x and y in the sample is represented by r_{xy}, and υ-2 is the degree of freedom. The t-statistics and the critical value can be calculated using the followings:

$$\text{t-statistic} = r_{xy}\sqrt{\frac{\upsilon-2}{1-r_{xy}^2}})$$

<div align="right">(2.8)</div>

$$\text{t-critical} = t_{(1-\alpha/2,\upsilon-2)}$$

All correlation coefficients with a t-statistics larger than the critical value are considered significant as they result in the rejection of the null hypothesis. The results of the t-test are presented in Table VIII. As can be observed, the correlation of responses varies as the orientation is changed. Therefore, identifying an appropriate strategy for improving the dimensional performance while reducing the manufacturing cost is a function of the part's orientation. Dimensional deviation shows significant correlation with the dimensional variation in all alignments. Machine operation cost, as the major cost element shows positive relationship with dimensional deviation in Y alignment. However, a negative relationship is observed in both Z and X alignment even though the relationship is not significant.

Although dimensional variation shows to have a significant negative correlation with total manufacturing cost in Y alignment, it shows to have a positive correlation in the X and Z alignments. This observation suggests that reducing the variability of dimensions in the X and Z alignments does not necessarily require a higher investment. This interesting observation is in contrast to the previous cost-variability relationships (also been referred to as cost-tolerance relationship in the literature) in traditional manufacturing. In other words, in the context of traditional processes, it is known that reducing the variability of dimensions is associated with higher manufacturing cost. However, according to the above observation, the orientation has an important role in the definition of the cost-variability function. In other words, there exist orientations in which both dimensional variation and manufacturing cost can vary in the same

direction by changing the process parameters. Therefore, one can easily reduce both dimensional

variation and manufacturing cost by selecting proper process parameters.

Table VIII. T-test analysis of the correlation coefficients

All observation (t-critical=2.007)						
	DD	DV	MO	MC	EC	TC
%Δ Dimension (DD)	-	-	-	-	-	-
6×σ (DV)	4.427	-	-	-	-	-
Machine operation cost (MO)	-0.844	-1.486	-	-	-	-
Material consumption cost (MC)	4.382	2.527	4.899	-	-	-
Energy consumption cost (EC)	-0.011	-0.890	23.930	5.738	-	-
Total cost (TC)	4.504	12.914	2.080	6.906	2.653	-
Z alignment (t-critical=2.074)						
	DD	DV	MO	MC	EC	TC
%Δ Dimension (DD)	-	-	-	-	-	-
6×σ (DV)	2.543	-	-	-	-	-
Machine operation cost (MO)	-1.848	0.735	-	-	-	-
Material consumption cost (MC)	4.260	3.057	2.182	-	-	-
Energy consumption cost (EC)	-1.534	0.799	20.302	2.463	-	-
Total cost (TC)	0.757	2.091	7.736	7.001	8.055	-
X alignment (t-critical=2.228)						
	DD	DV	MO	MC	EC	TC
%Δ Dimension (DD)	-	-	-	-	-	-
6×σ (DV)	2.649	-	-	-	-	-
Machine operation cost (MO)	-0.458	1.353	-	-	-	-
Material consumption cost (MC)	3.279	11.195	0.642	-	-	-
Energy consumption cost (EC)	-0.985	0.561	10.466	0.019	-	-
Total cost (TC)	0.619	3.452	6.787	2.337	4.053	-
Y alignment (t-critical=2.228)						
	DD	DV	MO	MC	EC	TC
%Δ Dimension (DD)	-	-	-	-	-	-
6×σ (DV)	-3.134	-	-	-	-	-
Machine operation cost (MO)	4.622	-6.015	-	-	-	-
Material consumption cost (MC)	1.932	0.546	0.546	-	-	-
Energy consumption cost (EC)	2.924	-3.381	8.499	0.462	-	-
Total cost (TC)	6.971	-2.904	7.129	2.111	5.128	-

Although total cost does not show a significant correlation with the dimensional deviation in

Z and X alignments, it has a positive correlation with dimensional deviation in the Y alignment.

49

However, note that as mentioned earlier, it is easier to compensate for the dimensional deviation by applying error compensation algorithms. Compensating the dimensional variation is, however, usually impossible. Therefore, proper selection of parameters is necessary to reduce the variability. Figure 13 presents the cost-saving potential and accuracy improvement of different experiment settings in each alignment. The percentage cost reduction and the changes of dimensional performance factors in three different alignments of X, Y, and Z are compared to the baseline. The baseline is the setting with the highest manufacturing cost in each alignment (i.e., 0.2 mm layer thickness and solid fill density). A higher % cost reduction is equivalent to a higher amount of savings that can be achieved with respect to the baseline. A higher % dimensional deviation and variation reduction is translated as a better dimensional performance.
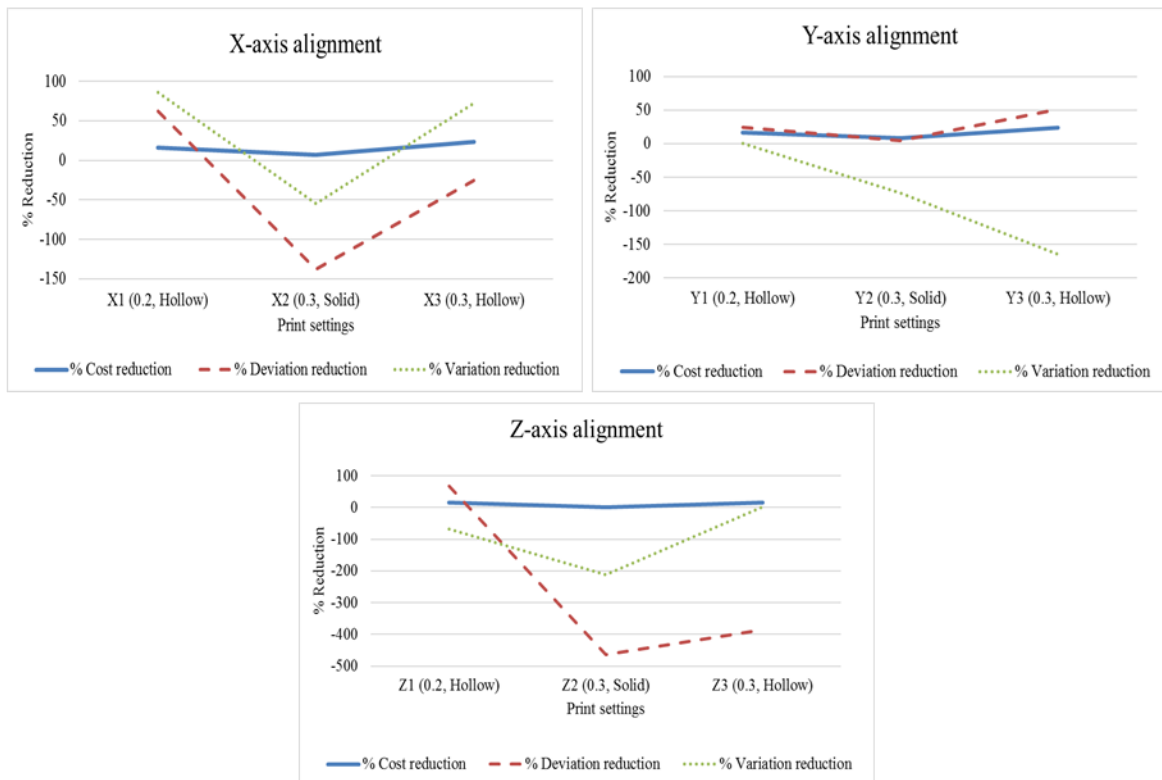
Figure 13. Percentage cost savings, dimensional deviation and variation reduction in each alignment compared to the baseline

As can be seen, the best dimensional performance (more accuracy and smaller variability) is not necessarily associated with the highest cost. In addition, the optimum setting is highly dependent on the orientation of part as different behavior is observed for different orientations. In the X alignment, the best dimensional performance is obtained at X1 while the most cost-effective option (X3) has a worse performance compared to X1. In the Y alignment, the minimum cost is achieved at Y3 which is also associated with the best accuracy but worst variability. In the Z alignment, a similar pattern as the X alignment is observed where Z3 is the most cost-effective setting while it has a worse performance specifically in terms of dimensional deviation compared to Z1.

2.1.8 Multi-Objective Optimization of Cost and Quality

In addition to the important role of orientation in finding the optimum strategies and the interaction of process parameters, the relative importance of responses also plays an important role in determining the optimum strategies. To further illustrate this point, a multi-objective optimization of manufacturing cost and dimensional performance is performed using two different scenarios. In order to determine the optimum process parameters that can simultaneously optimize the set of responses (dimensional performance and manufacturing cost), the desirability function is used. If Y_i is the studied response (i=1,…,n), the desirability function for each of the responses $(d_i(\hat{Y_i}))$ can be calculated depending on what is desired (keep the response at target, minimize or maximize it) [172]. The total desirability function, D, will then be calculated as:

$$D = (\prod_{i=1}^{n} d_i(\hat{Y_i}))^{\frac{1}{n}} \tag{2.9}$$

The algorithm calculates the composite desirability values for different combinations of parameters where a higher desirability shows a more fit solution.

51

- *Scenario 1*: In this scenario, the scale of the part is small and the part is printed only once. Therefore, changes in the total cost are not significant. However, assume that both dimensional variation and deviation are very important and need to be minimized as much as possible. Therefore, a high importance is assigned to the dimensional factors while the cost elements have a much lower relative importance (Table IX). The setting with 0.2 mm layer thickness, hollow fill density, and orientation of (0,0) will be selected as an optimum setting with the composite desirability of 0.9155.

- *Scenario 2*: Assuming that the dimensional deviations are compensated, the role of dimensional variation in the final quality of parts becomes significant. In this case, a high importance factor has to be assigned to dimensional variation while a lower importance can be assigned to dimensional deviation. As a result, the setting with 0.3 mm layer thickness, hollow fill density, and (90,0) orientation (alignment toward Z-axis) is selected as the optimum setting with the composite desirability of 0.8949.

Table IX. Constraints of input parameters and responses

Name	Goal	Lower limit	Upper limit	Weight	Importance Scenario 1	Scenario 2
A: Layer thickness	Limited to 0.2, 0.25, and 0.3	0.2	0.3	1	-	-
B: Fill density	Is in range	-1	1	1	-	-
C: Inclination	Is in range	0	90	1	-	-
D: Direction	Is in range	0	90	1	-	-
Operation cost	Minimize	0.197	0.305	1	1	10
Material cost	Minimize	0.075	0.155	1	1	3
Energy cost	Minimize	0.0015	0.0022	1	1	1
Dimension	Target (10)	9.86	10.41	1	10	1
Variation	Minimize	0.018	0.3464	1	10	10

As can be seen, depending on how one defines the relative importance of responses, different values of process parameters should be selected. Therefore, the geometry of part and machine errors, as well as the relative importance of responses are critical factors for finding the optimum parameter values.

2.1.9 Conclusions

In this Section, a comprehensive analysis of the dimensional performance (dimensional deviation and variation) of the FDM™ extrusion-based process and the manufacturing cost is presented. The total cost of manufacturing is estimated by the summation of material, energy, and machine operation costs. Analytical models are developed for quantifying the material and energy consumptions according to the input process parameters and are validated using the experimental data. The design of experiments is used to initially study the individual responses (dimensional deviation, dimensional variation, machine operation cost, material, and energy consumptions) and identify the optimal process parameters. A statistical correlation study is performed for the manufacturing cost elements and the dimensional performance factors. Finally, a multi-objective optimization, using desirability function, is performed for simultaneously improving the dimensional performance and reducing the manufacturing cost. The main findings of this study can be summarized as follows:

- Identifying the optimal process parameters in terms of dimensional performance and manufacturing cost is highly dependent on both the orientation of part and the relative importance of responses (cost elements versus dimensional performance factors). Furthermore, the interaction of different process parameters and the relationship between experiment responses depends on the selected orientation.

- Dimensional deviation and variation are correlated but the sign of the correlation coefficient is a function of the part's orientation.

- Aligning the dimension in the XY plane has shown to generate a lower IT grade in general compared to the Z-axis. However, it is normally associated with a worse surface roughness.

- The relative importance of responses has a critical effect on the selection of optimum process parameters.

- Finally, it is observed that strategies for obtaining a better dimensional performance (reducing the dimensional deviation and variation) are not necessarily associated with higher manufacturing cost.

Note that, although lowering the fill density has shown to generally have a positive effect on both dimensional performance and manufacturing cost, but it also affects the mechanical properties of parts [100] in a negative way. This trade-off needs to be considered in the optimization process in future works. In addition to orientation and relative importance of responses, the decision on optimal processes relies heavily on the geometry of part, position of the studied dimension in the part's geometry, path planning, and machine error. Therefore, different part geometries and path planning strategies need to be studied to further analyze the relationship between dimensional performance and manufacturing cost. Moreover, this study can be extended to address other types of AM processes.

Finally, it is important to develop analytical models in addition to empirical studies to characterize the dimensional distribution of additive manufactured parts as a function of part's material and geometry, type of AM process, process parameters, and path planning strategies, as well as the machine errors.

2.2 Surface Roughness Modeling and Validation for Additive Manufacturing

To assess the compliance with the design specifications, a priori prediction of surface properties (e.g., surface roughness) in additive manufactured components is necessary. Furthermore, most of the surface roughness modeling studies are based on empirical approaches and usually limited to a certain AM process. Therefore, the objective of this section is to establish a comprehensive mathematical model for the prediction of surface roughness in additive manufactured components. A new surface profile representation scheme for 3D printed surfaces is proposed to increase the prediction accuracy compared to the existing models in the literature.

2.2.1 Additive Surface Profile Representation

Two popular geometrical profile functions to describe the additive profile exist in the literature: (1) triangle function or staircase model [80] and (2) semi-circular function [82], [84], where the latter function is a more realistic representation of the surface profile. In addition, among the existing semi-circular functions in the literature, the parabolic function has shown to lead to an average higher prediction accuracy according to the experimental results [84]. The reason for this better performance lies in the fact that the parabolic function incorporates different error parameters along the layer base and height directions. In reality, the obtained layer thickness usually varies from the designed value due to different errors caused by material, machine, and process properties. Thus, by incorporating these errors into the surface profile function, the accuracy of the surface roughness model is expected to increase.

The proposed surface profile representation scheme is based on the combination of a parabolic curve and a linear line, as shown in Figure 14. The parabolic function is selected to incorporate the errors, and the linear function is added to provide a more accurate representation of the geometrical profile. The proposed surface profile is defined as a function of the stratification angle

(θ) and layer thickness (t). The stratification angle (θ) refers to the angle between the normal vector of the surface of interest and the build direction. The layer thickness (t) represents the designed height of each layer, which is usually altered as a result of different errors during the printing process. To visualize the surface profile more clearly, a 2D (two-dimensional) sketch is shown in Figure 14 for different ranges of the stratification angle. When the stratification angle equals to 90°, a special case occurs in which the surface profile is only represented using the parabolic function. In this work, the build direction is assumed to be vertical at all circumstances which limits our work to 3-axis AM processes.
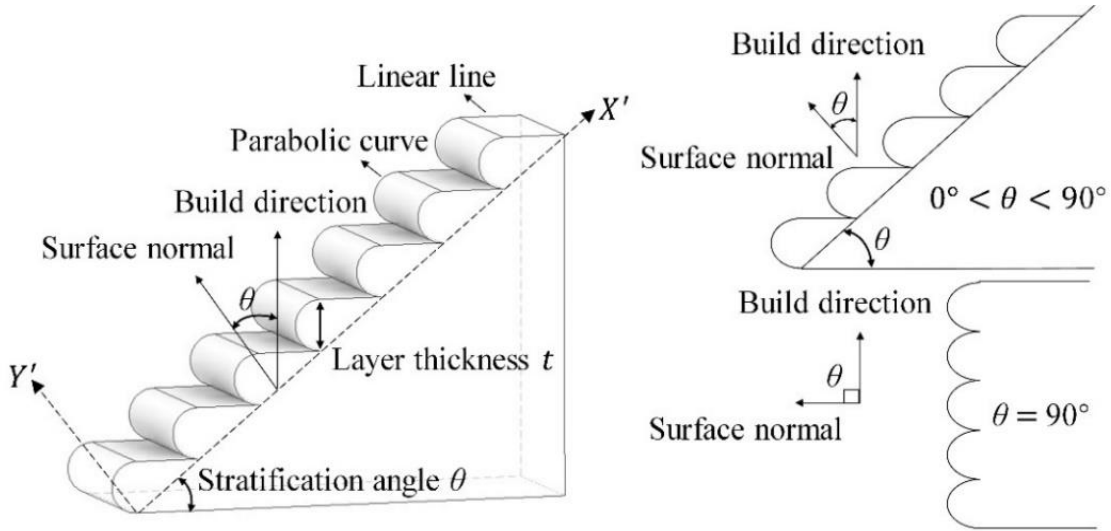
Figure 14. 3D (left) and 2D (right) illustrations of surface profile

2.2.2 Coordinate System Illustration

Two different coordinate systems, XY and $X'Y'$, are considered for the modeling procedure, as shown in Figure 15. The $X'Y'$ coordinate system is established based on the shape of the surface. In $X'Y'$ coordinate system, the surface profiles are periodic combinations of parabolic curve and linear line. This combination forms the unit geometry of surface profile, which is repeated along the length of the surface. A second coordinate system (XY) is established for the unit geometry of

surface profile to further simplify the modeling procedure as the integral function used for surface roughness calculation is not significantly affected by varying the coordinate system from $X'Y'$ to XY (shown in Figure 15). The generated errors as a result of this coordinate system change are considered to be negligible. Another issue that arises by considering the parabolic function in the $X'Y'$ coordinate system is that more than one output might exist for a single x input that contrasts with the mathematical definition of a function, and must be avoided. Note that in this model it is assumed that the mean profile line does not pass through the linear line element of the unit geometry.
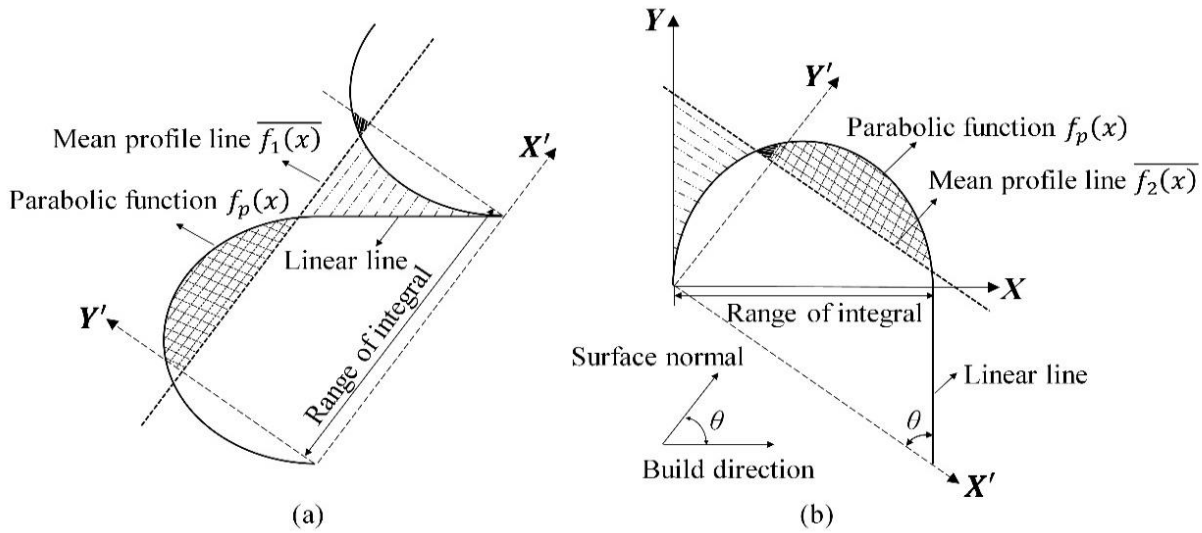
Figure 15. Illustration of unit geometry in (a) X'Y' and (b) XY coordinate systems

2.2.3 Surface Roughness Model

The non-periodic parabolic function of the unit geometry in the XY coordinate system can be formulated based on the values shown in Figure 16(b).

Error coefficients of ε_x and ε_y are defined to represent the deviation of layer thickness along the X and Y directions, respectively. Therefore, the effect of different error sources including

57

geometry, process parameters, machine, and even environment, can be incorporated into the model. Both error coefficients are assumed to follow normal distributions, where $\varepsilon_x \sim N(\mu_{\varepsilon_x}, \sigma^2_{\varepsilon_x})$ and $\varepsilon_y \sim N(\mu_{\varepsilon_y}, \sigma^2_{\varepsilon_y})$, in which their means and standard deviations are obtained by experiment. The non-periodic function of the parabolic curve $f_p(x)$ in the XY coordinate system can thus be represented by:

$$f_p(x) = -2\left[\frac{t - 2\varepsilon_y}{(t - \varepsilon_x)^2}\right]x^2 + 2\left[\frac{t - 2\varepsilon_y}{(t - \varepsilon_x)}\right]x. \tag{2.10}$$
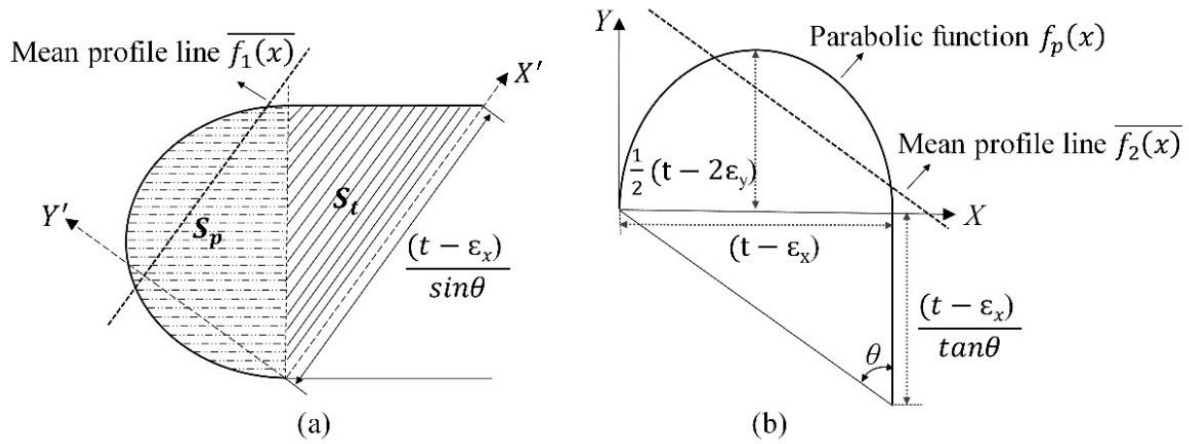
Figure 16. (a) Surface area of the unit geometry and (b) unit geometry parameters in XY coordinate system

To find the mean profile line of the AM profile in XY coordinate system, the mean profile line in $X'Y'$ coordinate system $\overline{f_1(x)}$, as shown in Figure 16(a), is initially calculated using the following equation:

$$\overline{f_1(x)} = \frac{(S_p + S_t)}{(t - \varepsilon_x)}sin\theta, \tag{2.11}$$

where S_p represents the surface area of the parabolic curve and S_t denotes the surface area of the triangle, as shown in Figure 16(a). Parameters S_p and S_t can be obtained from the followings

58

$$S_p = \frac{(t - \varepsilon_x)(t - 2\varepsilon_y)}{3}, \tag{2.12}$$

$$S_t = \frac{(t - \varepsilon_x)^2 \cot\theta}{2}. \tag{2.13}$$

Using equations (2.11)-(2.13), the mean profile line in $X'Y'$ coordinate system $\overline{f_1(x)}$ can be calculated as:

$$\overline{f_1(x)} = \frac{1}{6}\left[2\sin\theta(t - 2\varepsilon_y) + 3\cos\theta(t - \varepsilon_x)\right]. \tag{2.14}$$

The function $\overline{f_1(x)}$ is then reformulated by converting the coordinate system to $X'Y'$, and is referred to as $\overline{f_2(x)}$ which is presented below.

$$\overline{f_2(x)} = -(\cot\theta)x + \frac{1}{3}(t - 2\varepsilon_y) + \frac{1}{2}(t - \varepsilon_x)\cot\theta. \tag{2.15}$$

Therefore, the surface roughness of additive manufactured surfaces can be calculated as:

$$R_a = \frac{\sin\theta}{(t - \varepsilon_x)}\int_0^{(t-\varepsilon_x)}\left|f_p(x) - \overline{f_2(x)}\right|dx. \tag{2.16}$$

2.2.4 Experimental Plan and Apparatus

To validate the proposed model, a geometry containing a diverse range of stratification angles: 20°, 30°, 40°, 50°, 60°, 70°, and 90°, is designed as shown in Figure 17(a) and fabricated using FDM™ process. Polylactide (PLA) material is used for printing the test parts in a 3-axis configuration (i.e., constant build direction) and with maximum fill density. As frequently adopted in the literature, a layer thickness of 0.25 mm is selected to allow for the comparison of results.

Several replicated test parts are fabricated, and multiple surface roughness measurements are obtained for each surface (associated with each stratification angle) using the Bruker-Nano Contour GT-K Optical Profilometer. The surface height variation data are also obtained from the optical profilometer, which are then used for fitting the surface profile and comparison with the profile image. In addition, to evaluate the layer error coefficients and obtain a high-resolution image of the actual surface profiles, the Micro-Vu Precision Measurement System with a 1.0 µm scale resolution is used. Furthermore, statistical analysis was conducted to ensure no outlier exists among the measurements.
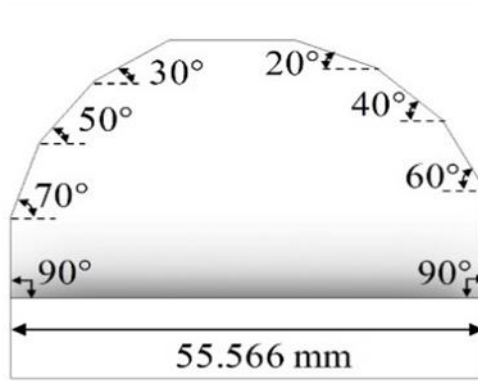
Figure 17. Designed geometry

2.2.5 Surface Profile Analysis

To verify the proposed surface profile representation scheme, the two error coefficients (ε_x and ε_y) are first measured by the Micro-Vu System. The distributions of the error coefficients are obtained based on 10 different measurements for each surface profile and are presented in Table X. The mean and standard deviation of each error element with respect to different stratification angles are then calculated based on the obtained measurements.

Table X. Distributions of the error coefficients

$\varepsilon_x \sim N\left(\mu_{\varepsilon_x}, \sigma_{\varepsilon_x}^2\right)$ $\varepsilon_y \sim N\left(\mu_{\varepsilon_y}, \sigma_{\varepsilon_y}^2\right)$	Stratification angle θ (deg)						
	20°	30°	40°	50°	60°	70°	90°
μ_{ε_x}(mm)	0.0178	0.0102	0.0144	0.0114	0.0190	0.0421	0.0165
σ_{ε_x} (mm)	0.0144	0.0144	0.0205	0.0127	0.0173	0.0112	0.0149
μ_{ε_y}(mm)	0.0357	0.0483	0.0417	0.0541	0.0454	0.0817	0.0558
σ_{ε_y} (mm)	0.0162	0.0038	0.0063	0.0035	0.0043	0.0052	0.0073

Figure 18(a) shows the top view of the raw profile (obtained by the Bruker-Nano Contour GT-K Optical Profilometer) where each area between two parallel lines represents a path of extruded material. Figure 18(b) illustrates the surface profile along the horizontal X-axis according to the selected cross-sections. The surface variation data are then further filtered using the smoothing spline function and used for fitting a quadratic function to each individual period/layer. The profile variations ("raw data" shown in Figure 19(a)) are obtained using the Bruker-Nano Contour GT-K Optical Profilometer as shown in Figure 18.

The average fitted profile is illustrated in Figure 19(a) and is referred to as the "fitted profile". In addition, the actual surface profile image is obtained from the Micro-Vu System for comparison with the fitted profile and is presented in Figure 19(b). According to Figure 19(a) and (b), the periodic parabolic trend is observed in both fitted profiles based on the raw data and the surface profile image, which verifies the adopted surface profile representation scheme used in the proposed surface roughness models.
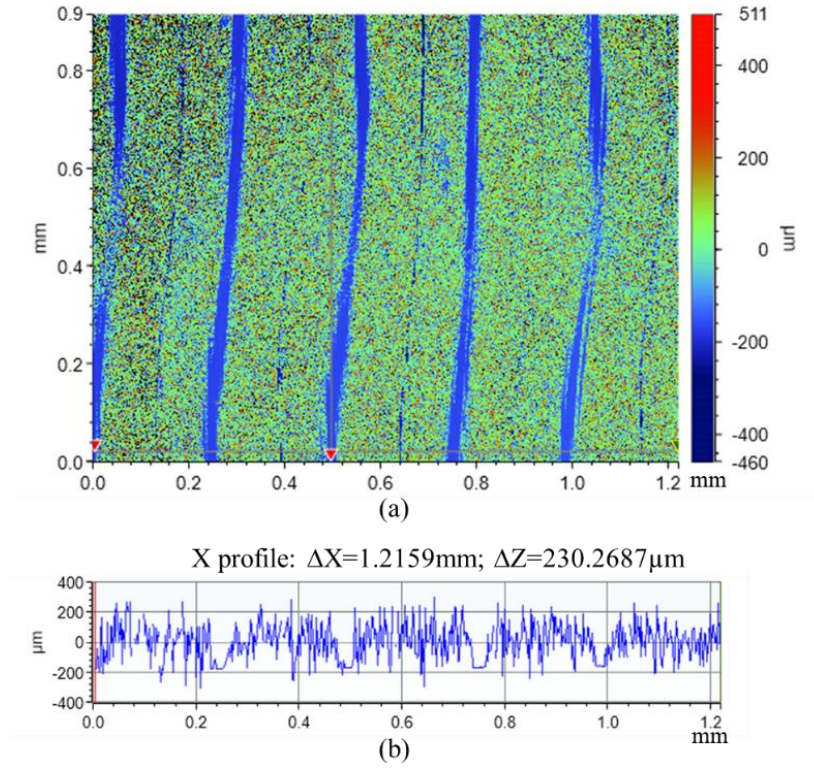
Figure 18. The raw profile data obtained from optical profilometer: (a) the top view of the raw

profile, and (b) the X-axis profile
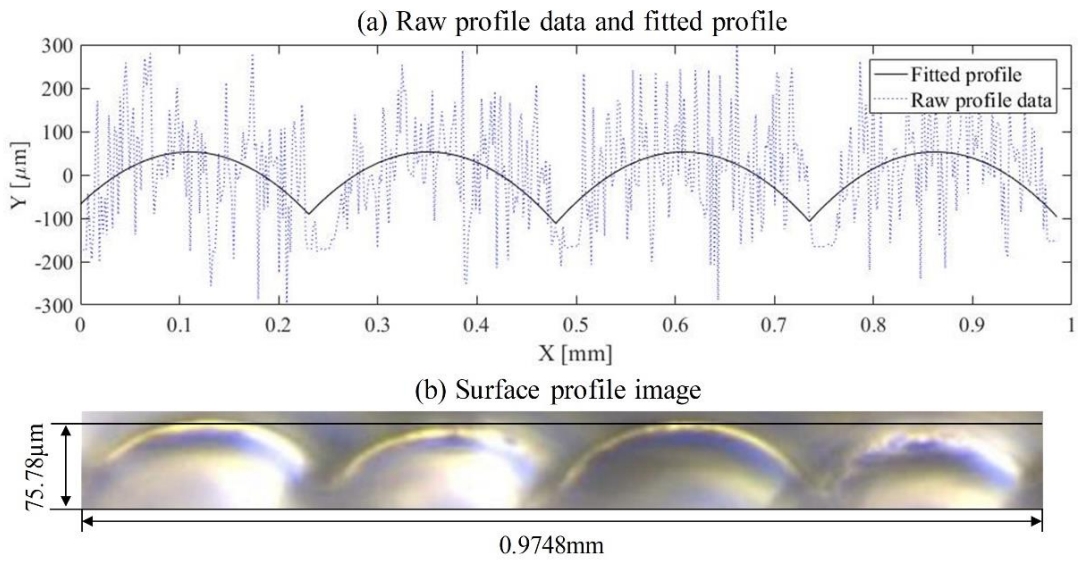
Figure 19. Comparison of (a) raw profile data and fitted profile, and (b) surface profile image

2.2.6 Surface Roughness Model Validation

    Table XI presents the results of the experiments to evaluate the effectiveness and validity of

the proposed surface roughness model. The main input parameters of the additive profile include

the layer thickness (t), stratification angle (θ), and layer error coefficients (ε_x and ε_y).

Table XI. Validation of the proposed model

θ (deg)	Observed Ra (μm)	Predicted Ra (μm)	Percentage error (%)
20°	54.069	55.023	1.764
30°	56.021	52.683	5.958
40°	50.651	46.789	7.625
50°	40.006	40.294	0.720
60°	30.808	32.560	5.689
70°	18.868	19.904	5.491
90°	17.332	17.762	2.484
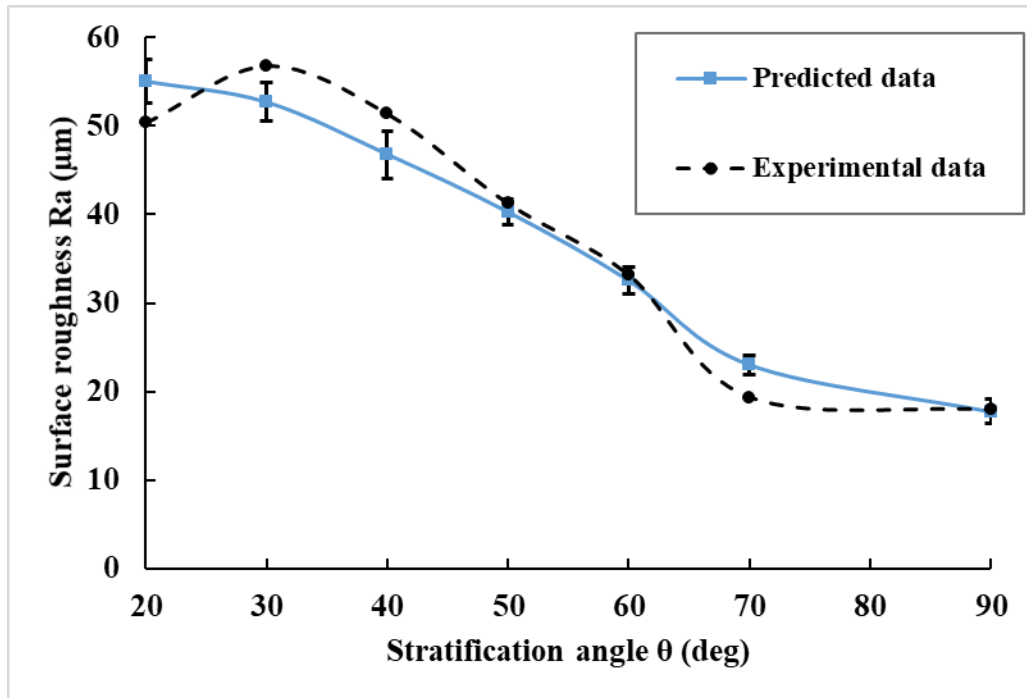
Figure 20. Comparison of predicted and experimental surface roughness values for AM

The average prediction error is found to be less than 5%. In Figure 20, the performance of the model is demonstrated for different stratification angles. Confidence intervals are generated for the predicted roughness values based on the distribution of the error coefficients in Table X. According to the figure, the confidence intervals are generally larger for smaller stratification angles. In Table XII, the accuracy of the proposed surface roughness model for AM case is compared with the existing models in the literature. According to this comparison, the proposed model has superior performance compared to the existing models in most cases. The proposed representation scheme of the surface profile can be one of the reasons for this superior performance.

Table XII. Comparison of the proposed AM surface roughness model with the literature

Angle θ (deg)	Experiment (μm)	(Pandey et al. 2003)		(Boschetto and Bottini 2015)		(Taufik and Jain 2016)		Proposed model	
		Prediction (μm)	Error (%)	Prediction (μm)	Error (%)	Prediction (μm)	Error (%)	Prediction (μm)	Error (%)
0°	NA	28.150	NA	NA	NA	29.518	NA	NA	NA
20°	54.069	51.678	4.422	46.913	13.235	28.433	47.413	55.023	1.764
30°	56.021	35.377	36.850	32.090	42.717	33.465	40.263	52.683	5.958
40°	50.651	27.530	45.648	24.961	50.720	27.809	45.097	46.789	7.625
50°	40.006	23.105	42.246	20.943	47.650	23.334	41.674	40.294	0.720
60°	30.808	20.441	33.649	18.524	39.872	20.639	33.007	32.560	5.689
70°	18.868	18.840	0.148	17.071	9.524	19.019	0.800	19.904	5.491
90°	17.332	17.705	2.155	16.038	7.463	17.868	3.096	17.762	2.484

2.2.7 Conclusions

In this section, surface roughness in the AM process is mathematically modeled and analyzed. The model is a function of two important process parameters: layer thickness and stratification

angle. In addition, it takes into account the layer to layer variation using the layer's error coefficients. A new surface profile representation scheme compared to the literature is proposed to increase the prediction accuracy. Experiments are performed to verify the surface profile representation scheme and validate the developed models. According to the experimental results, the proposed model performs generally well with an average of 4.25% error.

2.3 Characterizing Porosity Variation and Filament Bonding in Extrusion-based Additive Manufacturing

In addition to dimensional and geometric properties studied above, it is necessary to account for the mechanical properties of products fabricated by AM technology. To quantify the global and local mechanical strength, it is necessary to characterize the microstructures and their variation within the product. The extent of bonding between adjacent filaments, both within and between layers, as well as porosity are two of the most important parameters that directly contribute to the mechanical strength of parts in extrusion-based additive manufacturing. However, most of the existing analytical models in the literature either significantly underestimate these parameters or fail to quantify or address their variation along the deposition path and build direction. Therefore, the objective of this section is to establish methodologies for accurate estimation of these parameters by integrating the process physics and machine learning techniques.

2.3.1 Methodology

An overview of the adopted methodology can be described as follows. First, the geometry of interest is decomposed into anisotropic voxels (i.e., voxels with unidentical width, length, and height) based on the selected layer width and thickness values as well as the user-defined computational step size. Next, the temperature history at the center of each voxel is estimated using an analytical heat transfer modeling approach. Assuming that necking (i.e., formation of bond

among contiguous filaments during the sintering process) occurs during the first few seconds of deposition, the inter-layer and intra-layer bonding values are characterized based on the interface temperature of the neighboring voxels using the Newtonian sintering model. Next, to account for the deformation of micro geometries and their effect on the bonding degree, a machine learning-based model is established, in which, first the deformation values are obtained from the specimen's cross-sectional images through image processing, and then fed into a neural network model. Finally, the calculated inter-layer and intra-layer bonding values, as well as the void boundaries are updated based on the obtained filament deformation values and the law of conservation of mass through a geometric-based modeling approach. The flowchart of this work's methodology is presented in Figure 21, and the details are provided in the following sub-sections.
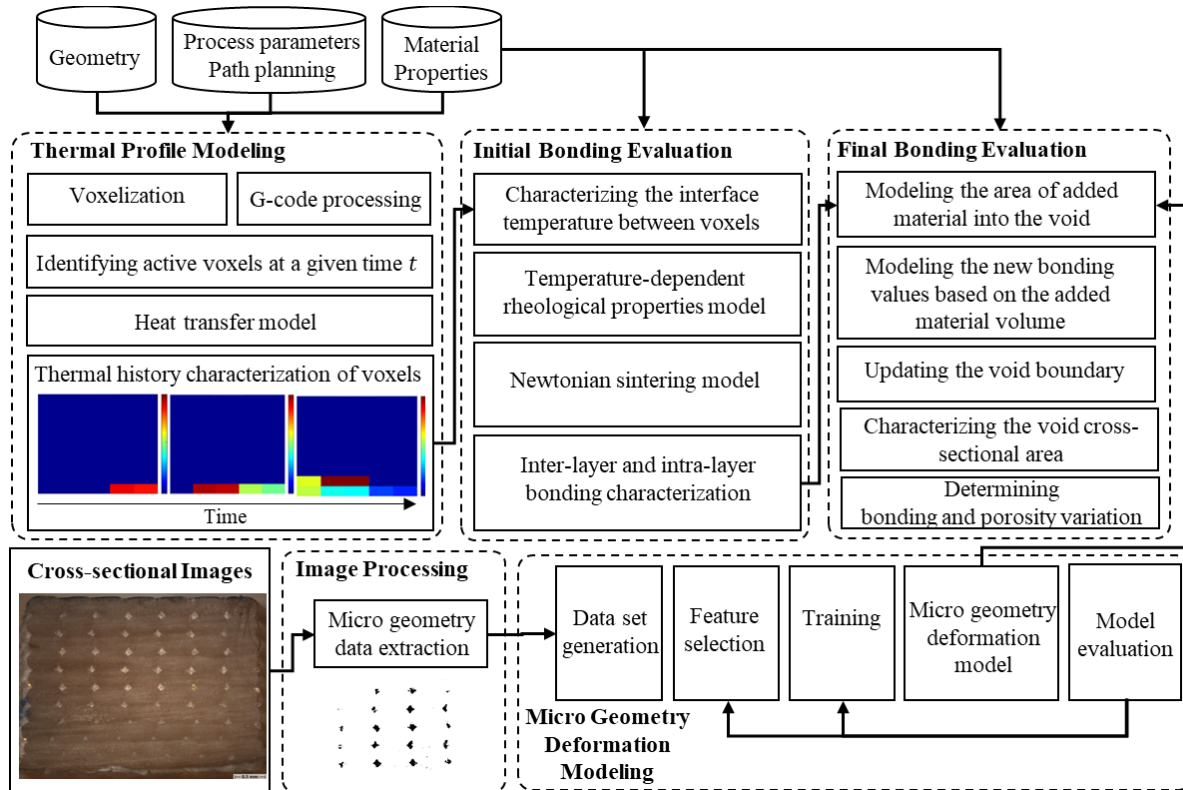
Figure 21. Flowchart of the proposed methodology.

2.3.2 Nomenclature

d	Selected layer thickness
w	Selected layer width
i	Index of the layer number, $i \in \{1, \dots I\}$
d_i	Thickness of ith layer
w_i	Width of ith layer
P	Perimeter of filament's cross-section (m)
λ_k	Fraction of perimeter P
A	Area of filament's cross-section (m^2)
x	The location of voxel of interest along X axis (assumed to be colinear with the filaments)
y	The location of voxel of interest along Y axis
$T(x, y, i, t)$	Temperature (°C) of voxel (x, y, i) at time t
T_E	Temperature of environment (°C)
T_D	Temperature of filament at time of deposition (°C)
$t(x, y, i)$	Activation time of voxel (x, y, i)
h_{Conv}	Convective heat transfer coefficient $(W/m^2\,°C)$
h_{Cond}	Conductive heat transfer coefficient $(W/m^2\,°C)$
δ	Necking radius
$\delta_Y^{y,y'}(x, i)$	Intra-layer necking radius between distinct neighboring filament sections represented by voxels (x, y, i) and (x, y', i) without considering the filament's deformation, $|y - y'| = 1$
$\delta_Z^{i,i'}(x, y)$	Inter-layer necking radius between distinct neighboring filament sections represented by voxels (x, y, i) and (x, y, i') without considering the filament's deformation, $|i - i'| = 1$
$\delta_{YF}^{y,y'}(x, i)$	Intra-layer necking radius between distinct neighboring filament sections represented by voxels (x, y, i) and (x, y', i) after accounting for the filament's deformation, $|y - y'| = 1$

$\delta_{ZF}^{i,i'}(x,y)$	Inter-layer necking radius between distinct neighboring filament sections represented by voxels (x,y,i) and (x,y,i') after accounting for the filament's deformation, $|i-i'|=1$
β	The angle representing the necking radius between fused filaments
ρ	Density (kg/m^3)
C	Specific heat capacity $(J/kg\,°C)$
$\gamma(T)$	Surface tension (N/m) at temperature T
$\mu(T)$	Viscosity (m^2/s) at temperature T
μ^*	Fitting parameter for viscosity model
b	Fitting parameter for viscosity model
M	Molar mass (kg/mol)
P_s	Parachor number
α	Coefficient of thermal expansion $(°C^{-1})$
$VA_{y,y'}^{i,i'}(x)$	Void cross-sectional area encompassed by four voxels (x,y,i), (x,y',i), (x,y,i'), and (x,y',i')
$\alpha_1, \alpha_2, \alpha_3, \alpha_4$	Angles of quadrilateral edges representing the void boundary
P_r	rth corner of the initial void boundary, r=1,2,3,4
P_r'	rth corner of the final void boundary, r=1,2,3,4
$\boldsymbol{P}$	Matrix of initial void boundary coordinates
$\boldsymbol{P'}$	Matrix of updated void boundary coordinates
X_r	Euclidian distance between corner points P_r and P_r' on initial and final void boundaries
D	Linear distance between the centers of two horizontally neighboring filament segments
$\Delta_z^{i,i'}$	Vertical shrinkage distance between two vertically neighboring filament segments of layers i and i'
$\bar{T}_{y,y'}(x,i,t)$	Temperature at the interface of two horizontally neighboring voxels (x,y,i) and (x,y',i) at time t

$\bar{T}_{i,i'}(x,y,t)$	Temperature at the interface of two vertically neighboring voxels (x,y,i) and (x,y,i') at time t
$A(\theta_0,\theta_1)$	Area of the elliptical arc bounded by two points on an ellipse
θ_0,θ_1	polar angles representing the intersection points of two ellipses

2.3.3 Thermal Profile Modeling

The evolution of temperature is a factor of heating and cooling rates of filaments upon arrival and leaving of the extrusion head, axial conduction, conduction with adjacent filaments (either from the main printing material or support material) as well as convection with air. These rates depend on many factors including the: (1) material properties (e.g., glass transition temperature, thermal conductivity, density, surface tension, and viscosity), (2) process parameters and strategy of build (e.g., liquefier temperature, layer thickness, extrusion width, feed rate, and sequence and direction of filaments to be printed), (3) part geometry, and (4) environment (e.g., envelope/ platform properties and temperature).

To characterize the temperature profile, the part is initially decomposed into anisotropic voxels where the X-axis direction is aligned with the deposition direction on the build platform. The Y and Z axes represent the filament segments and layer numbers, respectively. The voxel size is defined as (s,w,d) where s represents a user-defined computational step size (generally a small value) along the deposition direction $s=dx$, w is the selected layer width, and d is the selected layer thickness. Both w and d values can be obtained from the printing stage. The raster gap between filament segments is assumed to be zero and the deposition strategy is assumed to be unidirectional. Next, a temperature tensor is defined to represent the temperature of each voxel. The temperature distribution within each voxel is assumed to be uniform. Provided that no material is deposited into a voxel, its temperature is assumed to be similar to the environment. As material

is deposited into the voxels, the values of the temperature tensor are updated according to the closed-form solution proposed in [148].

A voxel is called "active" if it contains material. Activation time of a voxel is defined as $t(x, y, i)$ which represents the time that material is deposited into voxel (x, y, i). Note that for a given layer thickness and width value, activation time $t(x, y, i)$ would depend on velocity, path planning strategy, and the geometry of interest. As suggested by the literature, it is assumed that axial conduction along X direction is not significant [148], [173] and thus, is neglected in this work. Consequently, by neglecting those neighboring voxels along the X direction, and based on the assumption of unidirectional path planning strategy, each voxel (x, y, i) can have at most two active neighbors at $t(x, y, i)$, and at most 4 active neighbors at time $t > t(x, y, i)$. The sequence in which material is deposited into the voxels, information on active neighbors, and deposition velocity are directly obtained from the G-code based on the selected deposition strategy.

An illustrative example of the number of active neighbors at time of deposition for a 3 layered structure and with 3 filaments within each layer is provided in Figure 22. The total 9 stages of printing, from (1) to (9), at a given transverse section based on a unidirectional deposition strategy are presented. In stage (1) the bottom right voxel (here represented in 2D) is activated as material is deposited into it. The number inside this voxel represents the number of active neighbors of this newly deposited voxel. As can be seen, no active neighboring voxel exists for the newly deposited voxel in this stage, thus the value is zero. Moving to stage (2), the second voxel is activated. As the voxel to its right is already active, the number of active neighbors is 1. Similarly, in stage (5), the newly deposited voxel has two already active neighbors (to its left and its bottom). Note that the diagonal voxels are not considered neighbors as they do not share any boundary with the voxel of interest.
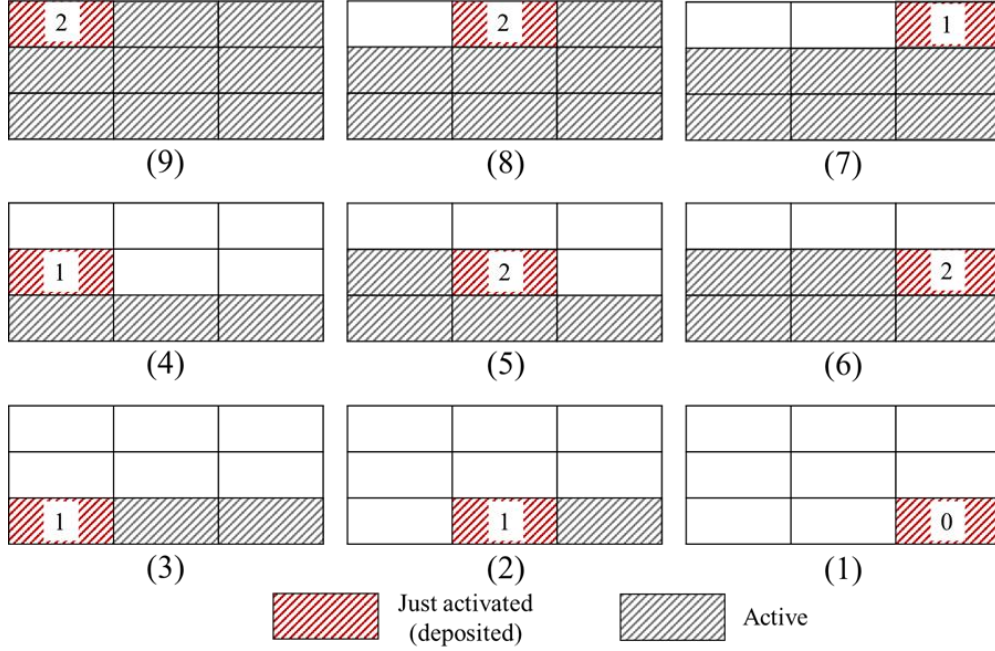
Figure 22. An illustrative example of the number of active neighbors at time of deposition for a 3 layered structure and with 3 filaments within each layer.

The temperature at voxel (x, y, i) at production time t can be approximated as follows [148]:

$$
\begin{aligned}
T(x, y, i, t) = C_1 \exp & \left[\frac{-Pf(n^1_{(x,y,i,t)}, \dots, n^K_{(x,y,i,t)})}{\rho C A} (t - t(x, y, i)) \right] \\
& + g(n^1_{(x,y,i,t)}, \dots, n^K_{(x,y,i,t)})
\end{aligned}
\tag{2.17}
$$

Where,

$$
C_1 = T_D - g(n^1_{(x,y,i,t)}, \dots, n^K_{(x,y,i,t)})
\tag{2.18}
$$

$$
f(n^1_{(x,y,i,t)}, \dots, n^K_{(x,y,i,t)}) = h_{conv} \left(1 - \sum_{k=1}^{K} n^k_{(x,y,i,t)} \lambda_k \right) + \sum_{k=1}^{K} n^k_{(x,y,i,t)} \lambda_k \, h_{cond}
\tag{2.19}
$$

$$
\begin{aligned}
& g(n^1_{(x,y,i,t)}, \dots, n^K_{(x,y,i,t)}) \\
& = \frac{h_{conv} \left(1 - \sum_{k=1}^{K} n^k_{(x,y,i,t)} \lambda_k \right) T_E + \sum_{k=1}^{K} n^k_{(x,y,i,t)} \lambda_k \, h_{cond} T^k_{(x,y,i,t)}}{f(n^1_{(x,y,i,t)}, \dots, n^K_{(x,y,i,t)})}
\end{aligned}
\tag{2.20}
$$

$$n^k_{(x,y,i,t)} = \begin{cases} 1, & \text{if } k\text{th neighbor of voxel } (x,y,i) \text{ is active at time t,} \quad k = 1, \ldots, K \\ 0, & \text{else} \end{cases} \quad (2.21)$$

The filament's elliptical cross-sectional area (A) and perimeter (P) are calculated as:

$$A = \frac{\pi}{4} dw \tag{2.22}$$

$$P = \frac{\pi}{2}(d + w)\left(1 + \frac{3h}{10 + \sqrt{4 - 3h}}\right), \quad h = \frac{(w - d)^2}{(w + d)^2} \tag{2.23}$$

2.3.4 Initial Filament Bonding Model

The initial bonding occurs during the first few seconds of deposition as the temperature of interface is generally above the critical sintering temperature. In this work, the temperature of interface between two neighboring active voxels is estimated by averaging the temperature of the individual voxels. The Newtonian sintering model [145] (a modification of the Frenkel's model in 1945 [174]) is adopted.

$$\frac{d\beta}{dt} = \frac{\gamma(T)}{a_0 \mu(T)} \frac{2^{-5/3} \cos\beta \sin\beta \, (2 - \cos\beta)^{1/3}}{(1 - \cos\beta)(1 + \cos\beta)^{1/3}} \tag{2.24}$$

where $\beta = \sin^{-1} \delta/a$, and β, δ, a_0, and a are the dimensionless necking radius, necking value, initial and final particle radiuses, as shown in Figure 23.
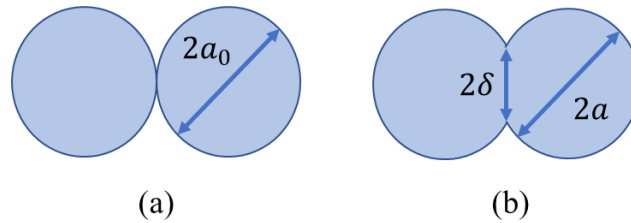
Figure 23. Bond formation: (a) surface contacting, and (b) neck growth.

Note that as the printed filaments are generally elliptical, the following definition for a_0 is adopted.

72

$$a_0 = \begin{cases} d/2 & \text{if } \delta = \delta_Y^{y,y'}(x,i) \text{ or } \delta_Y^{y,y'}(x,i') \\ w/2 & \text{if } \delta = \delta_Z^{i,i'}(x,y) \text{ or } \delta_Z^{i,i'}(x,y') \end{cases} \tag{2.25}$$

The interface temperature T is calculated by averaging the temperatures of neighboring voxels, calculated from Equation (2.17), at the time of deposition.

T

$$= \begin{cases} \bar{T}_{y,y'}\left(x,i,t(x,y',i)\right) = \dfrac{\left(T\left(x,y,i,t(x,y',i)\right) + T\left(x,y',i,t(x,y',i)\right)\right)}{2} & \text{if } \delta = \delta_Y^{y,y'}(x,i) \\[2ex] \bar{T}_{y,y'}\left(x,i',t(x,y',i')\right) = \dfrac{\left(T\left(x,y,i',t(x,y',i')\right) + T\left(x,y',i',t(x,y',i')\right)\right)}{2} & \text{if } \delta = \delta_Y^{y,y'}(x,i') \\[2ex] \bar{T}_{i,i'}\left(x,y,t(x,y,i')\right) = \dfrac{\left(T\left(x,y,i,t(x,y,i')\right) + T\left(x,y,i',t(x,y,i')\right)\right)}{2} & \text{if } \delta = \delta_Z^{i,i'}(x,y) \\[2ex] \bar{T}_{i,i'}\left(x,y',t(x,y',i')\right) = \dfrac{\left(T\left(x,y',i,t(x,y',i')\right) + T\left(x,y',i',t(x,y',i')\right)\right)}{2} & \text{if } \delta = \delta_Z^{i,i'}(x,y') \end{cases} \tag{2.26}$$

The surface tension $\gamma(T)$ and viscosity $\mu(T)$ parameters play an important role in estimating the necking value. Nonetheless, these rheological properties are functions of temperature. To account for this dependency, the viscosity parameter is assumed to obey the Reynolds viscosity model:

$$\mu(T) = \mu^* \exp(-bT) \tag{2.27}$$

where μ^* and b are fitting parameters based on experimental data.

Characterizing the temperature dependency of surface tension for thermoplastics (especially in their melted state) is generally not straightforward. Therefore, the Parachor model is adopted Additional information on this approach are provided in [175] and [176].

$$\gamma = \left(\frac{\rho P_s}{M}\right)^4 \tag{2.28}$$

where P_s is the Parachor number. To account for the effect of temperature, the above equation is re-written as follows.

$$\gamma(T) = \left(\frac{\rho P_s}{M[1 + \alpha(T - T_E)]^3}\right)^4 \qquad (2.29)$$

where α is the thermal expansion coefficient. The thermal expansion is assumed to be isotropic.

Finally, the intra-layer and inter-layer necking radius, i.e., $\delta_Y^{y,y'}(x,i)$ and $\delta_Z^{i,i'}(x,y)$ are calculated by solving the differential equation provided in (2.24) and based on the derived temperature profiles from Equation (2.17).

2.3.5 Final Filament Bonding after Accounting for the Filament's Deformation

Modeling of the filament deformation due to built-in stresses, gravity, weight of filaments, and constant pressure of nozzle during the printing process is extremely complex. In addition, if raster gap between filaments is small, the dynamics of bonding further affect the filament's deformation. To account for the complex effect of these factors on the deformation of filaments, a machine learning approach is adopted in this work. The predicted deformation factors (i.e. bead size changes along width and thickness) are then used to update the inter-layer and intra-layer bonding values from 2.3.4 (and thus the void boundaries) based on the law of conservation of mass and a proposed geometric modeling approach. The detailed steps of this process are provided as follows.

Step 1. Characterizing the micro-geometries deformation using artificial neural network

Artificial neural network (ANN) is a popular machine learning algorithm capable of nonlinear mapping between several input and output parameters. In this work, a backpropagation neural network structure is adopted to characterize the filament deformation [177]. The inputs of this

model include extrusion width, total number of neighbors, printing speed, layer index, and location along the deposition path, and the output is the filament deformation (along the build direction). The general structure of the adopted neural network model is as follows. The output of each neuron is calculated as some function (i.e. activation function) of the weighted sum of its inputs, as shown below

$$y_i = f\left(\sum_j w_{ij}x_j + w_{0j}\right) \tag{2.30}$$

where w_{ij} refers to the weight from unit j to unit i, and w_{0j} is the bias term. In this work, the log-sigmoid function is used as the activation function. Therefore, the output is calculated as:

$$y_i = \frac{1}{1 + e^{-(\sum_j w_{ij}x_j + w_{0j})}} \tag{2.31}$$

In the backward learning, the loss function (usually defined as the sum of square of errors based on the Euclidian distance between target and estimated values) is evaluated and then used to update the w_{ij}'s, so that the network converges eventually. The Levenberg-Marquardt algorithm is used in this work for training the data which uses Jacobian matrix, i.e. $J^T J$, to approximate the Hessian matrix H. Therefore, the weights w_{ij} are updated as

$$w_{ij}^{k+1} = w_{ij}^k - [J^T J + \mu I]^{-1} J^T E \tag{2.32}$$

where μ is a scalar, I is the identity matrix and E is the error function.

Step 2. Updating the void boundary based on the new micro-geometry characteristics

Once the deformation of filaments (beads) for a given layer i is predicted, it is used to update the void boundary and the intra-layer and inter-layer bonding values as shown in Figure 24(a) and

Figure 24(b). In other words, as the layers are compressed and according to the law of conservation of mass, the material would have no option but to pour into the existing void boundaries (see Figure 24(c)).
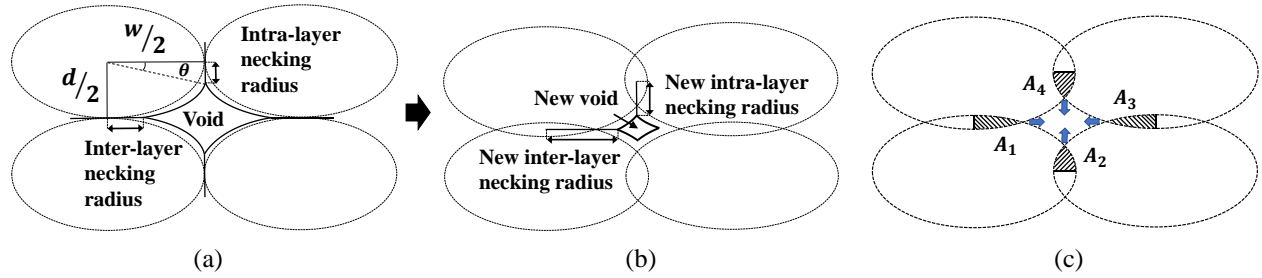
Figure 24. The representation of (a) initial filament bonding and void, (b) final filament bonding and void, and (c) the intersection areas A_1, A_2, A_3, and A_4 pouring into the void.

Let $A_{y,y'}^{i,i'}(x)$ be the area representing the amount of material that will pour into a given void boundary due to the deformation of two consecutive layers i and i'. This area is obtained by the summation of the four areas A_1, A_2, A_3, and A_4 as shown in Figure 24(c). It is assumed that $A_1 = A_3$ as the vertical shrinkage distance is similar. However, as $d_i \neq d_{i'}$, the areas A_2 and A_4 would be different.

The intersection areas A_1, A_2, A_3, A_4 can be estimated as follows [178]:

$$\frac{1}{2}\left[2A(\theta_0,\theta_1) - |x_1 y_0 - x_0 y_1|\right] \tag{2.33}$$

where $A(\theta_0,\theta_1)$ is the area of the elliptical sector between angles θ_0 and θ_1, and (x_0, y_0) and (x_1, y_1) are the coordinates of the intersection points between two ellipses. The area $A(\theta_0,\theta_1)$ can be calculated as,

$$A(\theta_0, \theta_1) = \int_{\theta_0}^{\theta_1} \frac{1}{2} r^2 d\theta \tag{2.34}$$

where r is the radius of the polar coordinate system which represents the elliptical function with semi-major and semi-minor axis length of $\frac{w_i}{2}$ and $\frac{d_i}{2}$, respectively. The w_i value is estimated as $\frac{dw}{d_i}$ based on the law of conservation of mass. As a result, r can be calculated as,

$$r^2 = \frac{w_i^2 d_i^2}{4(d_i^2 \cos\theta + w_i^2 \sin\theta)} \tag{2.35}$$

Now by substituting (2.35) in (2.34), $A(\theta_0, \theta_1)$ can be calculated as,

$$A(\theta_0, \theta_1) = F(\theta_1) - F(\theta_0) \tag{2.36}$$

where $F(\theta)$ is the antiderivative of the integrand as described below,

$$F(\theta) = \frac{w_i d_i}{8}\left[\theta - tan^{-1}\left(\frac{(d_i - w_i)sin2\theta}{(w_i + d_i) + (d_i - w_i)cos2\theta}\right)\right] \tag{2.37}$$

For areas A_2 and A_4, the intersection points (x_0, y_0) and (x_1, y_1) are calculated as,

$$\left(\frac{D}{2}, \pm\frac{d_i}{2w_i}\sqrt{w_i^2 - D^2}\right) \tag{2.38}$$

where D is the initial distance between the center of filaments segment, i.e. $D = w$ in this work. Therefore, the angles corresponding to these points are calculated as follows.

$$\theta_0 = 2\pi - tan^{-1}\left(\frac{d_i\sqrt{w_i^2 - D^2}}{Dw_i}\right) \tag{2.39}$$

$$\theta_1 = tan^{-1}\left(\frac{d_i\sqrt{w_i^2 - D^2}}{Dw_i}\right) \tag{2.40}$$

For areas A_1 and A_3, the intersection points (x_0, y_0) and (x_1, y_1) are calculated as follows.

$$\left(\pm \frac{w}{2d} \sqrt{2d\Delta_z^{i,i'} - {\Delta_z^{i,i'}}^2}, \frac{\left(d - \Delta_z^{i,i'}\right)}{2} \right) \tag{2.41}$$

where $\Delta_z^{i,i'} = 2d - (d_i + d_{i'})$ is the vertical shrinkage distance between the center of filament segments, and d_i and $d_{i'}$ are obtained from Step 1. In addition, the angles corresponding to these points can be formulated as follows.

$$\theta_0 = tan^{-1} \left(\frac{d - \Delta_z^{i,i'}}{2} \middle/ \frac{w}{2d} \sqrt{2d\Delta_z^{i,i'} - {\Delta_z^{i,i'}}^2} \right) \tag{2.42}$$

$$\theta_1 = \pi - tan^{-1} \left(\frac{d - \Delta_z^{i,i'}}{2} \middle/ \frac{w}{2d} \sqrt{2d\Delta_z^{i,i'} - {\Delta_z^{i,i'}}^2} \right) \tag{2.43}$$

We assume that the new void boundary is convex, quadrilateral, and its edges possess the same slope as the initial void edges. The cross-section of the void between four voxels (x, y, i), (x, y', i), (x, y, i'), and (x, y', i'), and the initial and final void boundaries are presented in Figure 25. According to this figure, P_1, P_2, P_3 and P_4 are the corner points of the quadrilateral representing the initial void boundary, P_1', P_2', P_3' and P_4' are the corner points of the quadrilateral representing the new void boundary. Assuming that the origin of the coordinate system is at the virtual intersection of the filament boundaries, the matrices P and P' can be defined as follows.

$$P = \begin{bmatrix} \delta_Z^{i,i'}(x,y') - \dfrac{w}{2} & 0 \\ 0 & \delta_Y^{y,y'}(x,i) - \dfrac{d}{2} \\ \dfrac{w}{2} - \delta_Z^{i,i'}(x,y) & 0 \\ 0 & \dfrac{d}{2} - \delta_Y^{y,y'}(x,i') \end{bmatrix} \tag{2.44}$$

$$P' = \begin{bmatrix} \delta_Z^{i,i'}(x,y') + X_1 - \dfrac{w}{2} & 0 \\ 0 & \delta_Y^{y,y'}(x,i) + X_2 - \dfrac{d}{2} \\ \dfrac{w}{2} - X_3 - \delta_Z^{i,i'}(x,y) & 0 \\ 0 & \dfrac{d}{2} - X_4 - \delta_Y^{y,y'}(x,i') \end{bmatrix} \tag{2.45}$$
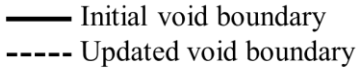
Figure 25. Initial and updated void boundary representation for four voxels (x,y,i), (x,y',i), (x,y,i'), and (x,y',i').

It is observed that

$$\begin{aligned} \frac{A_1}{2} + \frac{A_3}{2} + A_2 \\ = \frac{\|P_1'P_2'\| + \|P_1P_2\|}{2}(\|P_2'P_2\|\cos\alpha_2) \\ + \frac{\|P_2'P_3'\| + \|P_2P_3\|}{2}(\|P_2'P_2\|\cos\alpha_1) \end{aligned} \tag{2.46}$$

and

$$\frac{A_1}{2} + \frac{A_3}{2} + A_4$$

$$= \frac{\|P_1'P_4'\| + \|P_1P_4\|}{2} (\|P_4'P_4\| \cos \alpha_4) \qquad (2.47)$$

$$+ \frac{\|P_3'P_4'\| + \|P_3P_4\|}{2} (\|P_4'P_4\| \cos \alpha_3)$$

where $\|\ \|$ denotes the Euclidian distance. Furthermore, angles α_1 to α_4 are calculated as,

$$\alpha_1 = \tan^{-1} \left(\frac{d - 2\delta_Y^{y,y'}(x,i)}{w - 2\delta_Z^{i,i'}(x,y)} \right) \qquad (2.48)$$

$$\alpha_2 = \tan^{-1} \left(\frac{d - 2\delta_Y^{y,y'}(x,i)}{w - 2\delta_Z^{i,i'}(x,y')} \right) \qquad (2.49)$$

$$\alpha_3 = \tan^{-1} \left(\frac{d - 2\delta_Y^{y,y'}(x,i')}{w - 2\delta_Z^{i,i'}(x,y)} \right) \qquad (2.50)$$

$$\alpha_4 = \tan^{-1} \left(\frac{d - 2\delta_Y^{y,y'}(x,i')}{w - 2\delta_Z^{i,i'}(x,y')} \right) \qquad (2.51)$$

where $\delta_Y^{y,y'}(x,i)$, $\delta_Y^{y,y'}(x,i')$, $\delta_Z^{i,i'}(x,y)$, and $\delta_Z^{i,i'}(x,y')$ are previously calculated. Now based on the previous assumption that the slope of a distinct edge from the quadrilateral representing the initial void boundary is the same as the slope of the equivalent edge from the quadrilateral representing the final void boundary, the following set of equations are formulated.

$$\|P_3'P_3\| \left(2\delta_Y^{y,y'}(x,i) - d \right) = \|P_2'P_2\|(2\delta_Z^{i,i'}(x,y) - w) \qquad (2.52)$$

$$\|P_1'P_1\| \left(2\delta_Y^{y,y'}(x,i) - d \right) = \|P_2'P_2\|(2\delta_Z^{i,i'}(x,y') - w) \qquad (2.53)$$

Now by solving the set of equations in (2.46), (2.47), (2.52) and (2.53), the coordinates of corner points P_1', P_2', P_3' and P_4' of the final void boundary can be calculated.

Step 3. Updating the necking radius values and estimating the void cross-sectional area

Once the new corner points are obtained from Step 2, the new necking radius values can be calculated as follows.

$$\delta_{ZF}^{i,i'}(x,y) = \delta_Z^{i,i'}(x,y) + \|P_3'P_3\|\tag{2.54}$$

$$\delta_{YF}^{y,y'}(x,i) = \delta_Y^{y,y'}(x,i) + \|P_2'P_2\|\tag{2.55}$$

$$\delta_{ZF}^{i,i'}(x,y') = \delta_Z^{i,i'}(x,y') + \|P_1'P_1\|\tag{2.56}$$

$$\delta_{YF}^{y,y'}(x,i') = \delta_Y^{y,y'}(x,i') + \|P_4'P_4\|\tag{2.57}$$

Finally, the void cross-sectional area encompassed by the four voxels (x,y,i), (x,y',i), (x,y,i'), and (x,y',i') at a given location x can be estimated as

$$VA_{y,y'}^{i,i'}(x) = \frac{\|P_2'P_4'\| \times \|P_1'P_3'\|}{2}\tag{2.58}$$

Similarly, the bonding values and void cross-sectional areas of all sets of neighboring four voxels in the geometry of interest can be calculated.

2.3.6 Experimental Procedure and Material Properties

The selected test part is a 100(L)×5(W)×3(H) mm cuboid, presented in Figure 26(b). Two critical process parameters of speed (feed rate) and extrusion width are selected and varied, from 1800 to 2700mm/min and 0.45 to 0.6 mm, respectively, to generate specimens with different cooling rates, as shown in Table XIII.

Multiple replicas for each specimen have been manufactured to reduce the variability of the experiment results. A unidirectional deposition strategy is adopted, i.e. the raster angle is set to zero. Once a layer is deposited, the deposition path is reversed as illustrated in Figure 26(a), and

the printing is continued. To simplify the image processing step, the layer thickness of 0.3 mm is selected and kept constant among all specimens. The rest of the fixed parameters are presented in Table XIV.
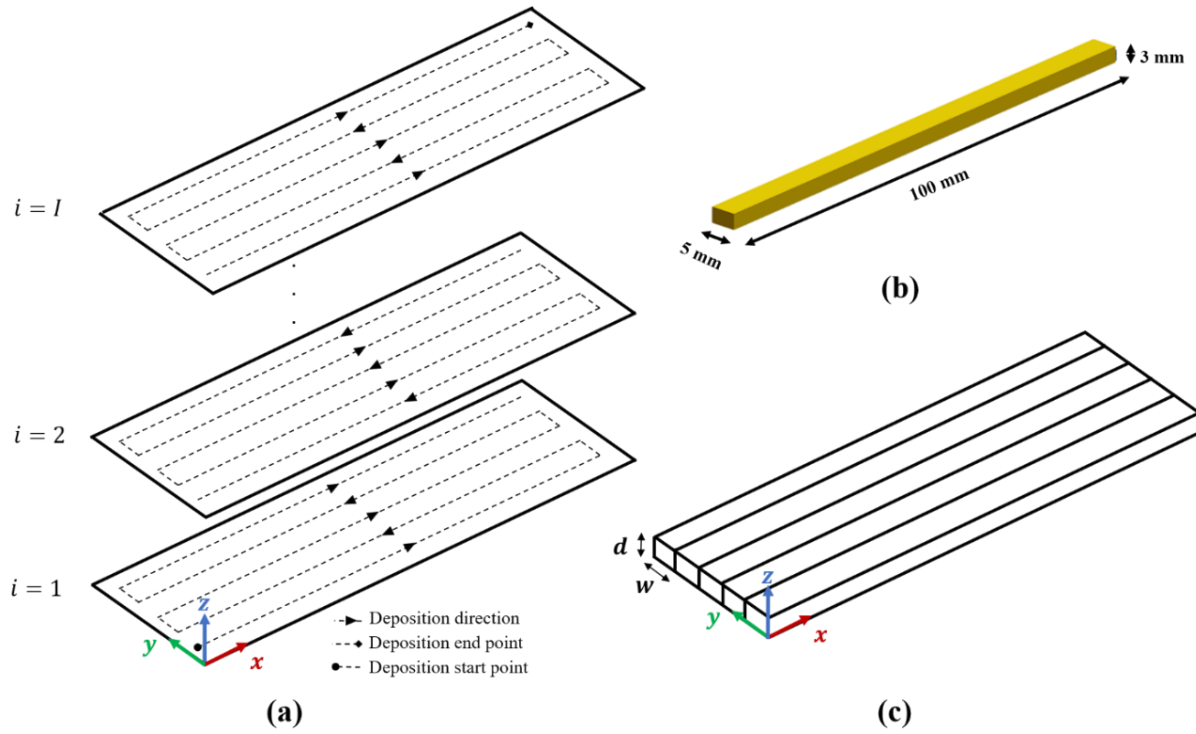
Figure 26. (a) Deposition pattern of each layer, (b) test part geometry, and (c) filament segments within each layer.

The specimens were then transversely cut at different locations along the deposition path with different distances ranging from 15 to 95 mm from the deposition start point using a 650 minitom from South Bay Technology Inc. with a 0.012-inch diamond wheel. The cross-sections were then polished and cleaned with alcohol to remove any dust or particles. The Micro-Vu SOL precision measurement system with 1-micron resolution was used to take high-resolution pictures of the cross-sections. The figures were then analyzed using image processing software for evaluating and measuring the dimensional characteristics of the printed beads as well as the void area.

Table XIII. Experiment design and specimen details

Specimen	Feed rate (mm/min)	Layer width (mm)
A1	2700	0.6
A2	2250	0.6
A3	1800	0.6
B1	2700	0.53
B2	2250	0.53
B3	1800	0.53
C1	2700	0.45
C2	2250	0.45
C3	1800	0.45

Table XIV. Fixed experimental parameters

Layer thickness	0.3 mm
Liquefier temperature	220 ℃
Heated bed temperature	70 ℃
Fan setting	off
Build location on platform	Center

The material used in this work is Polylactid acid also known as PLA with a chemical composition of $(C_3H_4O_2)_n$ [179]. While abundant data is available on ABS (Acrylonitrile butadiene styrene) material and its properties, rheological and thermal characteristics of PLA is less studied in the literature. Based on a comprehensive review of the PLA material and experimental data literature, the data provided in Table XV are adopted in this work. The molecular Parachor is calculated based on the approach used in [180] using the contribution of each atom/group/linkage according to the PLA chemical composition. The viscosity model coefficients are estimated based on the data obtained from the literature. Figure 27 demonstrates the fitted and experiment data for the viscosity of PLA at different temperatures.

Table XV. PLA material properties

| Properties	Value	Reference/Source
Density (g.cm^{-3})	1.25	[129], [181]
Glass transition (°C)	60±5	[129]
Complete melting (°C)	165±5	[129]
Molecular Parachor	148.1	Calculated based on the approach proposed in [180] using the atom/group/linkage contribution
Molecular weight (g.mol^{-1})	72	[182]
Thermal expansion coefficient (°C^{-1})	436×10^{-6}	[183]
Viscosity model coefficient μ^* (Pa.s)	1379×10^4	Fitted based on data provided in [129], [175]
Viscosity model coefficient b	0.0499	Fitted based on data provided in [129], [175]
Specific heat capacity (J/kg°C)	2175.69	Calculated from data provided in [184]
Surface tension N.m-1 (at 160°C)	0.022	[175]
Thermal conductivity (W/m°C)	0.19 - 1.47	[179], [185]–[187]
Critical sintering temperature	150-155	[175], [188]
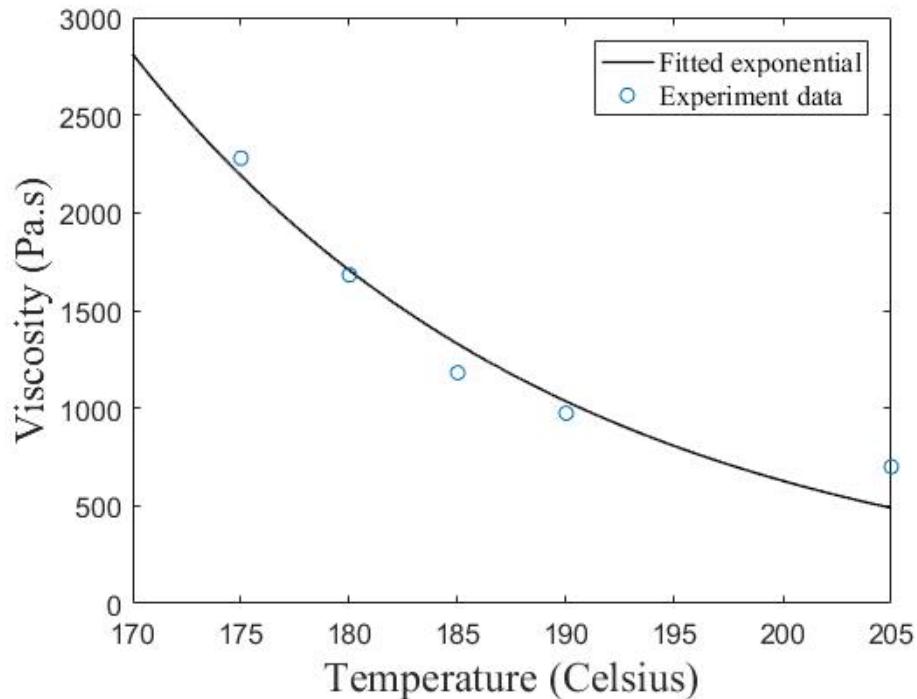
Figure 27. Comparison of the fitted PLA viscosity model and experimental data in the literature.

2.3.7 Temperature Model Results

A MATLAB code was generated based on the approach presented in 2.3.3 to characterize and analyze the temperature history. The part geometry characteristics, process parameters, and material properties described in 2.3.6 are incorporated in the code. Note that as the scale of the part is small (specially along the build direction), the surrounding environmental temperature is assumed to be close to the heated bed temperature. The step size along the X-axis is defined as 1 mm, $dx = 1$. Note that a smaller step size can possibly increase the accuracy of the model but on the other hand will lead to a higher computation time. The processing of the temperature code for the specified test part in Figure 26(b) takes around 5 minutes using a desktop with Intel Xeon E5-2620 2.40-GHz processor and 16-GB RAM.

Figure 28(a) illustrates the cross-sectional view of temperature distribution for A1 specimen at location x=90 along the deposition path and time 61.468 seconds of the build. Based on the adopted unidirectional path planning strategy, the activation sequence of these voxels is as follows: (10,1,1), (10,2,1), (10,3,1), (10,4,1), (10,5,1), (10,5,2), (10,4,2), (10,3,2), (10,2,2), (10,1,2), (10,1,3), (10,2,3), and so on.

Figure 28(b) demonstrates the temperature profile of voxels (10,1,1) to (10,1,2) from the above sequence during the first 61 seconds of the built. As can be observed, all temperature profiles are slowly converging to the environment temperature. Furthermore, the activation of neighboring voxels leads to an increase in the temperatures of adjacent filaments. For example, voxel (10,1,1) has two main neighbors: (10,2,1) and (10,1,2). According to the activation sequence, neighboring voxel (10,2,1) is the first to be activated at about 4.312 seconds from the activation of (10,1,1) voxel. This leads to a peak in the temperature profile of the (10,1,1) voxel.
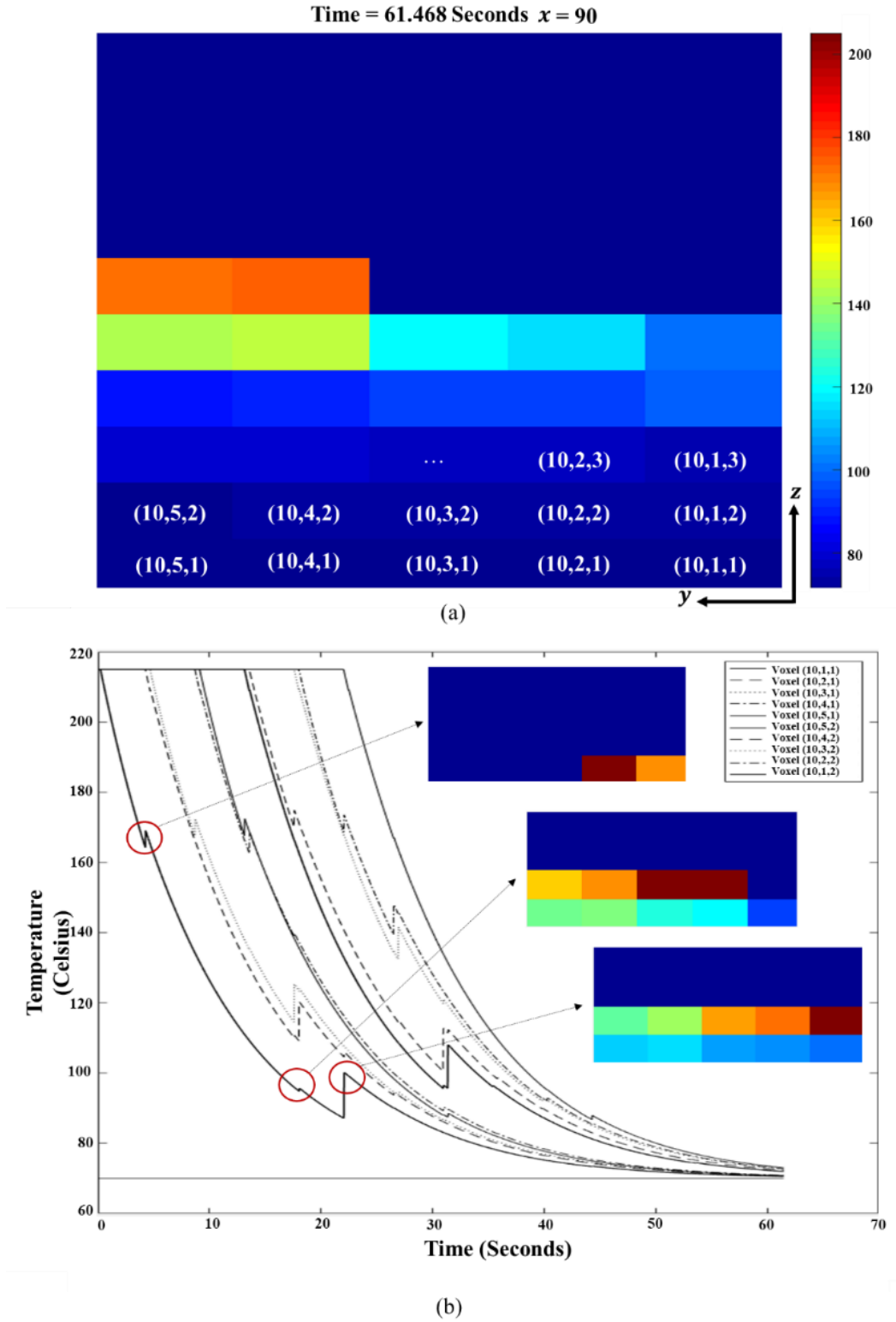
85

Figure 28. (a) Cross-sectional view of temperature distribution for A1 specimen at location x=90, and (b) Temperature profile of filament segments for the first two layers.

The next observable peak occurs at time 18.304 seconds when (10,2,2) is activated. Note that although (10,2,2) is not a direct neighbor of (10,1,1) but is in contact with the neighbors of (10,1,1), i.e., (10,2,1), thus, can cause a slight increase in their temperature and consequently the temperature of their neighbors. Finally, the last and the largest peak occurs at time 22.176 seconds when voxel (10,1,2) is activated. Due to a larger contact area between (10,1,2) and (10,1,1), the observed temperature peak is larger than the previous peaks. The obtained patterns of temperature profiles due to interlayer and intralayer reheating are consistent with those reported in the literature [146], [148], [152].

2.3.8 Filament Deformation Modeling and Results

To analyze the filament deformation, a dataset with 270 entries is generated in which the deformation factor, i.e. distribution of layer thickness for different specimens, is measured. The final data set is $\{(x_{rs}, y_{rs})\}_1^{270}$, where $x_{rs} \in \mathbb{R}^5$ is a vector of the 5 input parameters with respect to the rth filament segment of sth specimen (i.e., extrusion width, total number of neighbors at a given cutting location, printing speed, layer index, cutting location along the deposition path), and y_{rs} is the new value of layer thickness due to deformation. From this data set, 20 data points are randomly put aside as the test set. The remaining data are used for training and validation purposes. For every x_{rs} in this data set, each of the k parameters are mapped to the closed interval [0,1]. This scaling ensures that during training, each of the k parameters is equally important. A 10-fold cross-validation is used on the resulting normalized data set $\{(x'_{rs}, y_{rs})\}_1^{270}$, where $x'_{rs} \in [0,1]^k$. The dataset is randomly divided into 10 subsets, and the performance of the generated model based on the remaining 9 subsets was checked on the selected subset. This process was repeated over all subsets and then an average score was generated. The correlation analysis is used to reduce the dimensionality of the input parameters and increase the accuracy of prediction. Furthermore, the

parameters of the neural network model were optimized during the training process using a greedy algorithm. Finally, the performance of the trained ANN model for characterizing the layer thickness values along different layers was tested on the test data set.

The accuracy metrics of root mean square error (RMSE), mean absolute error (MAE), and coefficient of determination (R-squared) are presented in Table XVI. The R-squared parameter for the training, validation, and test data sets is found to be 92%, 90.6%, and 90.3%, respectively. Figure 29 demonstrates the performance of the fitted model and the distribution of prediction error along the build direction. According to this figure, it appears that the model overestimates the smaller layer thickness values (generally from the initial transition layers). Furthermore, the prediction error has a decreasing trend as the index of layer number is increased.

Table XVI. Performance of the fitted artificial neural network model

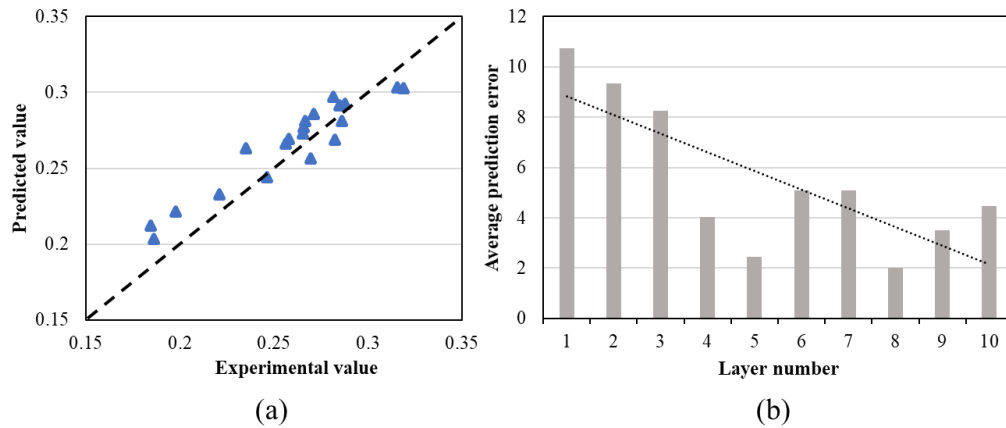|	Training	Validation	Test
RMSE	0.009±0.003	0.011±0.004	0.015±0.000
MAE	0.007±0.002	0.009±0.003	0.013±0.007
R-squared (%)	92±1.5	90.6±4.1	90.3

(a)   (b)

Figure 29. (a) Comparison of predicted and experimental layer thickness values for the test data set, and (b) distribution of average prediction error among different layers.

2.3.9 Bonding Degree/Necking Radius Estimation

To evaluate the performance of the proposed approach in estimating the bonding degree/necking radius, two different scenarios are considered. In Scenario 1, the inter-layer and intra-layer necking radius values are estimated using the Newtonian sintering model in Equation (2.24) together with the temperature profile data obtained from Equation (2.17) without considering the filament deformation factor. In Scenario 2, the inter-layer and intra-layer necking radius values are estimated by incorporating the filament deformation data based on the newly established models in this work.

A total of 38 different inter-layer and intra-layer bonding values, from different locations along the deposition path and build direction of specimens are selected to ensure that the proposed approach can address the variation of these parameters within the part.

Figure 30 presents the performance of the proposed model (Scenario 2) in comparison to the experiment data and Scenario 1. 95% confidence intervals for the experimental data are constructed. According to this figure, the proposed models for inter-layer and intra-layer bonding have an average accuracy of 95% and 94%, respectively, which are significantly better compared to Scenario 1. More specifically, in Scenario 1, both inter-layer and intra-layer necking radiuses are underestimated. However, a significantly better accuracy in predicting the intra-layer necking radius values, Figure 30(b), compared to the inter-layer necking radius values, Figure 30(a) is observed in Scenario 1. The possible explanation for this observation would be the assumption of circular filaments in the Newtonian sintering model as well as the higher contribution of filament deformation effect on inter-layer necking radius compared to the intra-layer necking radius.
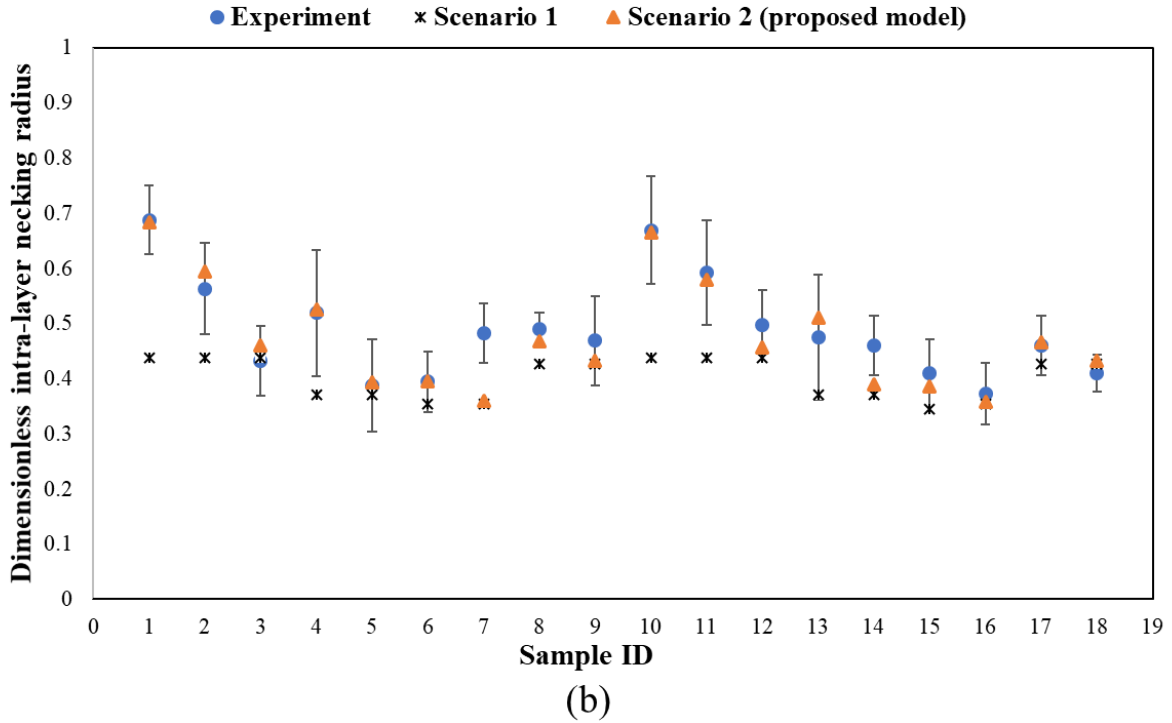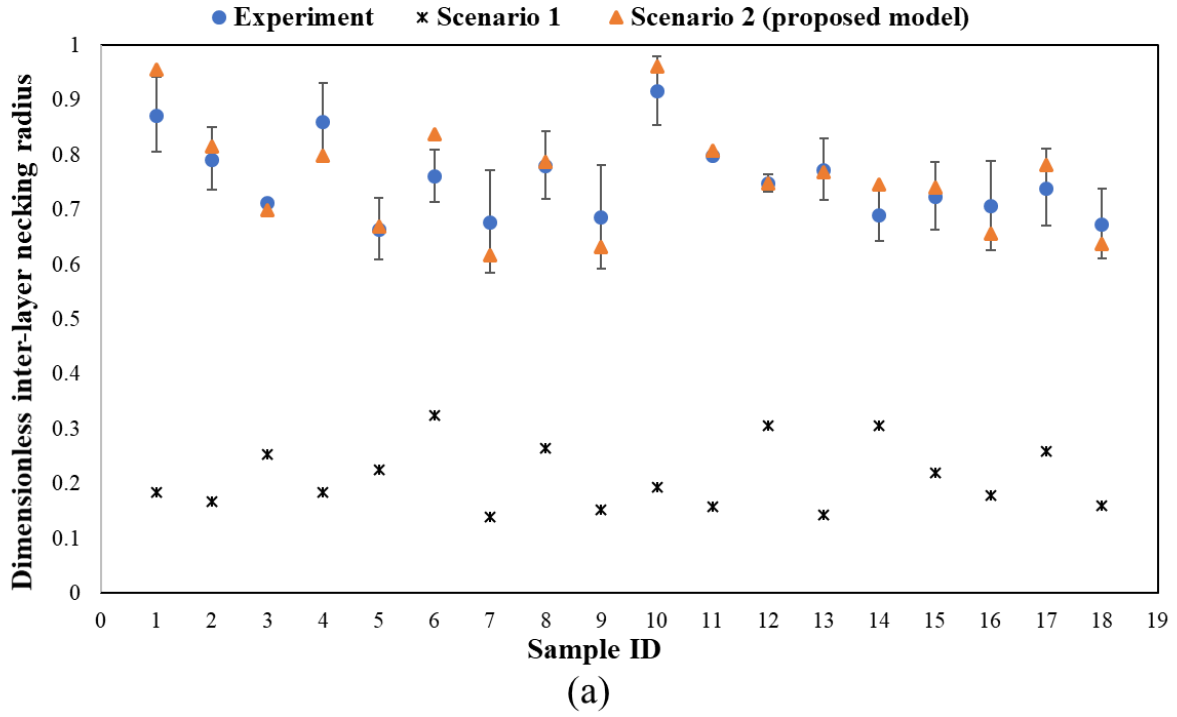
Figure 30. Performance of the proposed model for estimating the dimensionless (a) inter-layer necking radius, and (b) intra-layer necking radius.

The intra-layer necking radius prediction error in Scenario 1 is largest for samples 1, 2, 10, and 11. Interestingly, these samples are obtained from the first transitional layers of specimens which have significant levels of deformation. Therefore, it appears that in Scenario 1, the intra-layer necking radiuses from the bottom layers are significantly underestimated but a higher accuracy for predicting the intra-layer necking radius of top layers is observed. This observation is further illustrated in Table XVII. According to this table, our proposed model (Scenario 2) outperforms Scenario 1 in estimating the necking radiuses for both the bottom and top layers.

Table XVII. Comparison of the model performances for bottom and top layers of A1 specimen

	Experiment data		Prediction based on Scenario 1		Prediction based on Scenario 2 (proposed model)	
	Top layers	Bottom layers	Top layers	Bottom layers	Top layers	Bottom layers
Dimensionless Intra-layer neck radius	0.465	0.678	0.404	0.437	0.432	0.687
Standard deviation (μm)	46.3	12.6	-	-	-	-

2.3.10 Porosity Estimation

To evaluate the porosity model performance, two specimens of A1 and B3 and two locations of x=15 and x=90 along the deposition path are selected, and 18 random void samples from these cross-sections are chosen along the build direction. Figure 31 demonstrates the selected specimens and void samples for the purpose of porosity model validation.

The performance of the proposed model for quantifying the variation of porosity within a part is illustrated in Figure 32. According to this figure, despite the small scale of the cross-sectional void areas (generally less than 0.02 mm^2), the proposed model can provide good estimates of their variation within the part and follows the trend obtained by the experimental data. However, the

average prediction accuracy for the void samples at the bottom layers (specifically in B3 specimen) is lower compared to the top layers of the specimens. This is consistent with the trend of thickness prediction error for the bottom (average 6.9 %) and top layers (average 4 %) shown in Figure 29(b). Therefore, it is suspected that the main factor contributing to the observed error is the prediction error from the filament deformation modeling stage.
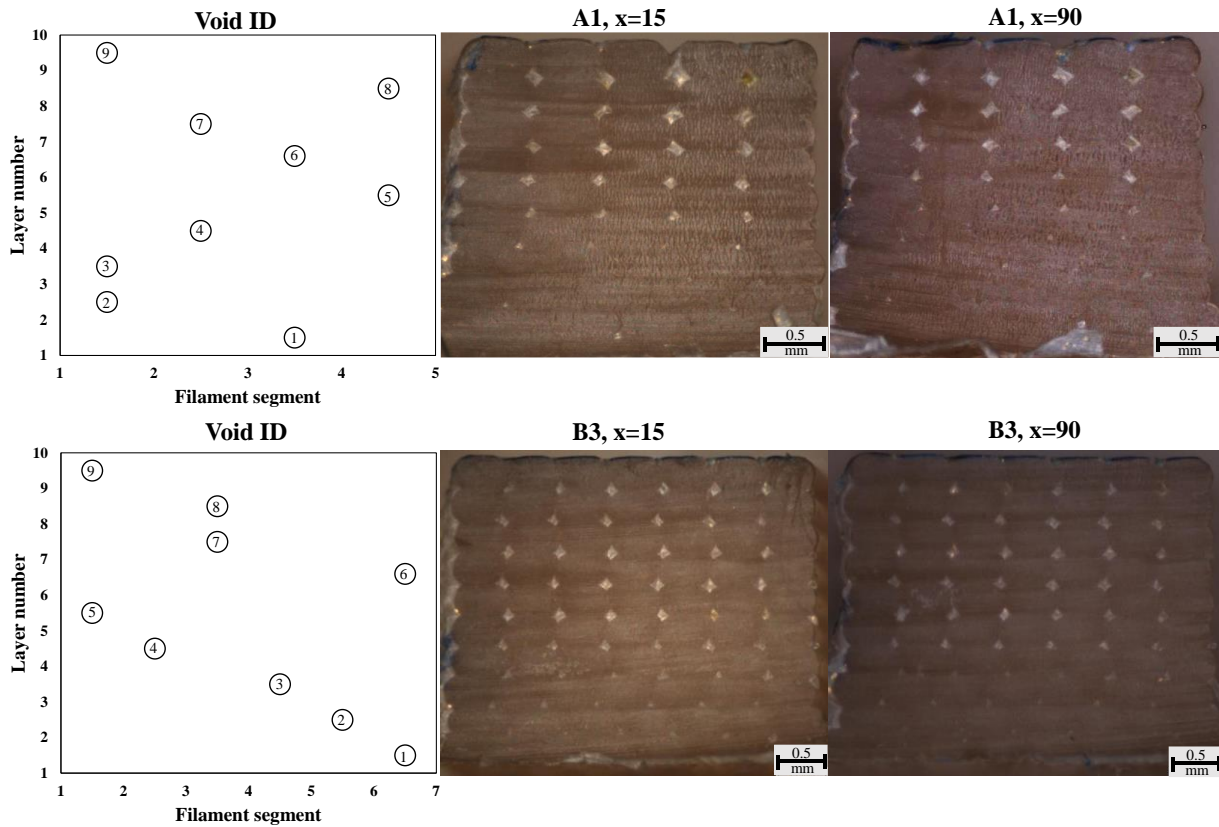

Figure 31. Selected specimens and void samples for the purpose of model validation.

Furthermore, it is observed that the model performance is much better for A1 specimen (with larger extrusion width) compared to the B3 specimen, specially regarding the bottom layers. One possible explanation for this observation is the slight shift of the B3 specimen filaments at the first few transitional layers to both right and left directions as shown in Figure 31 which leads to a

different morphology/shape of the voids (triangle) versus the assumption in this work (quadrilateral). As this observation has not been incorporated into the proposed model, it can lead to prediction inaccuracies. Note that this slight shift also exists in the A1 specimen, however, due to the larger extrusion width of the A1 specimen, the void cross-sectional areas are almost zero or generally smaller than those in the B3 specimen. Therefore, the model prediction errors will be smaller.
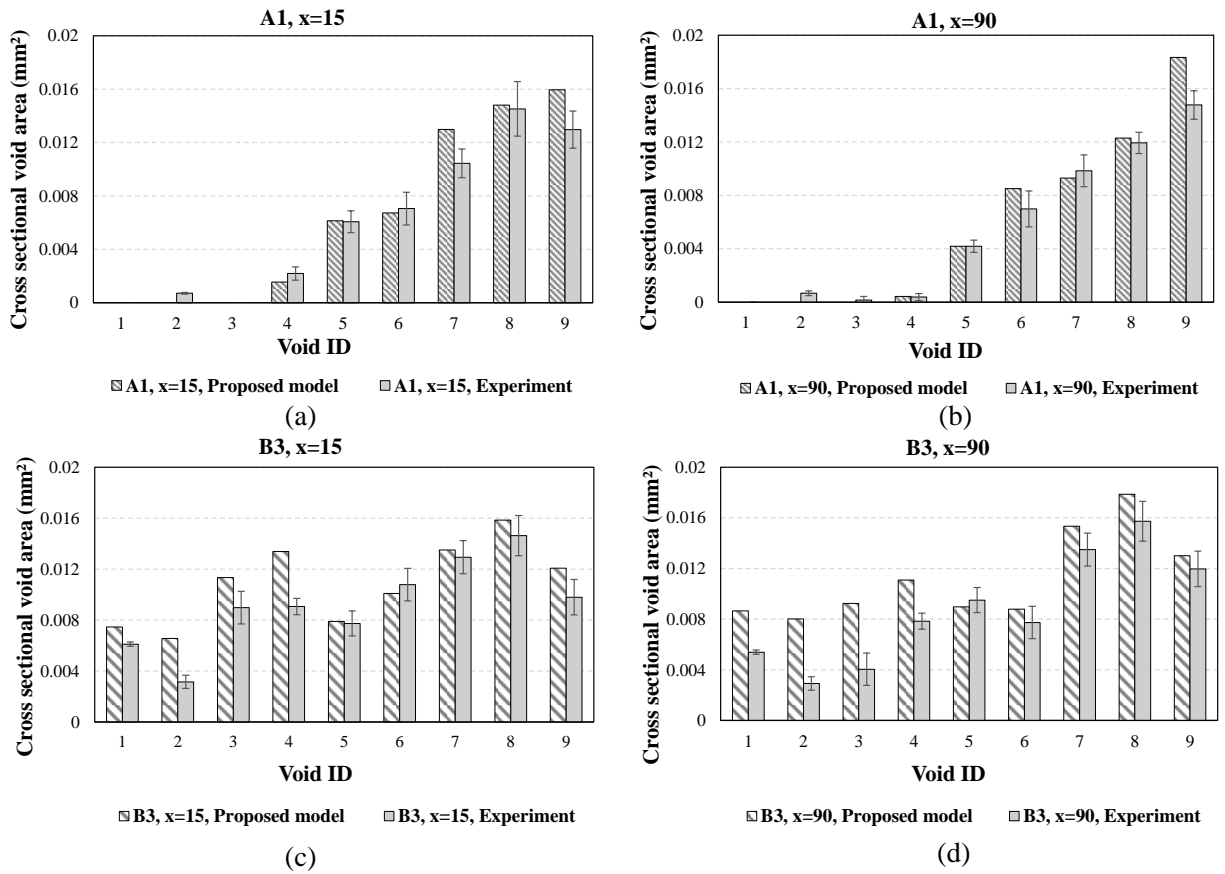

Figure 32. Performance of the proposed model for estimating porosity and its variation within the (a) A1 specimen at location x=15, (b) A1 specimen at location x=90, (c) B3 specimen at location x=15, and (d) B3 specimen at location x=90.

As is observed in Figure 31 and Figure 32, similar void samples of each specimen have significantly different cross-sectional areas along the deposition path due to their different cooling and heating rates which can clearly be captured by the proposed model. Furthermore, it is observed that the cross-sectional void area has an increasing trend by moving from the bottom layers to the top layers.

<u>2.3.11 Conclusions</u>

Mathematical models are established to characterize and quantify the inter-layer and intra-layer bonding, porosity, and their distributions within a geometry of interest, based on the extrusion-based additive manufacturing process and a unidirectional deposition strategy. These models are among the first in the literature that can quantify the distribution of these parameters within manufactured parts. The established models can be used to quantify the global and local mechanical strength of parts in the extrusion-based additive manufacturing process. The effect of filament deformation on bonding and porosity, generally neglected in the literature, is incorporated into the models using machine learning approaches. The established models for inter-layer and intra-layer bonding have an average accuracy of 95% and 94%, respectively. In addition, it is found that the porosity variation model performs better for top layers compared to bottom layers with an average of 51% higher accuracy.

2.4 Concluding Remarks

In this chapter, efforts to address the process-level quality assurance problems in additive manufacturing are presented using both empirical and analytical approaches. Dimensional tolerance and distribution of components are experimentally studied in the extrusion-based AM process, and their correlation with sustainability and economic impacts are analyzed. A multi-objective optimization using desirability function is performed for simultaneously reducing the

dimensional errors as well as manufacturing cost, by tuning the process parameters. Mathematical models are established to evaluate the sustainability measures (e.g., energy and material consumption), manufacturing cost, as well as the surface properties, i.e., surface roughness and mechanical properties; i.e., porosity and bonding degree, of components to provide guidelines during the tolerance design task at the product level. Several experiments are conducted to validate the proposed models. A geometric-based modeling approach is adopted for evaluating the surface roughness of components, i.e., the mathematical function of the geometry representing the surface profile is formulated. The porosity, bonding degree, and their variation within a component are characterized using a hybrid physics-based and data-driven approach by addressing the temperature profile and deformation of deposited paths.

3. PROCESS-LEVEL QUALITY ASSURANCE: INVESTIGATING THE WITHIN-COMPONENT INTERACTION FOR HYBRID MANUFACTURING

[Parts of this chapter were previously published as "Li, L., Haghighi, A., and Yang, Y. (2019). Theoretical modelling and prediction of surface roughness for hybrid additive–subtractive manufacturing processes. *IISE Transactions*, 51(2), 124-135.; and Li, L., Haghighi, A., and Yang, Y. (2018). A novel 6-axis hybrid additive-subtractive manufacturing process: Design and case studies. *Journal of Manufacturing Processes*, 33, 150-160.).", reprinted, with permission, from the publishers. For more information, please refer to the Appendix (Copyright Statement).]

This chapter presents the different studies performed to understand and establish the relation between (1) design, (2) process and process parameters, (3) properties of part: i.e., dimensional accuracy, variation and surface roughness, and (4) sustainability measures and economic implications in hybrid additive-subtractive processes. As explained earlier, studying and understanding this relationship allows for selecting tolerances that are both feasible (at the manufacturing process level) considering the capability of the process, and optimal (at the product assembly level) considering product functionality and total manufacturing cost.

In Section 3.1, the development process and capabilities of a robotic hybrid additive-subtractive platform are discussed and illustrated [189]. The surface roughness of components that are processed by the hybrid additive-subtractive process is then analytically modeled and validated in Section 3.2 [165]. The model is mainly tailored to the milling process and considers both additive and subtractive manufacturing process parameters. The developed hybrid platform in Section 3.1 is used for conducting the experiments in Section 3.2. Finally, in Section 3.3 the chapter's conclusions and future work are discussed.

3.1 Hybrid Additive-Subtractive Process Development

To perform research on hybrid manufacturing processes, it is important to first establish the necessary platform. Therefore, a hybrid additive-subtractive manufacturing (HASM) process is designed and developed in this section. Finally, several case studies are performed to illustrate the capabilities of the developed hybrid platform.

3.1.1 System Design

The hardware configuration design for the HASM process is shown in Figure 33. The hardware mainly consists of four components: a six degree of freedom (6-DOF) industrial robot arm, two changeable heads for both AM and SM processes, and an integrated manufacturing platform equipped with necessary features to support both AM and SM processes. The industrial robot arm adopted in the HASM process weights 25 kg and has a 3 kg payload with a reach of 580 mm. The changeable heads, currently developed for FDM™ and milling processes, are both screwed to a self-designed fixture which is connected to the end-point of the industrial robot arm. A unique self-designed fixture is also printed using the PolyJet AM technology for fixing the AM stepper motor and extruder to the robot end-point fixture. A direct connection of hot end and extruder is adopted for the AM head for a more precise guidance of the plastic filament into the extruder.

The maximum payload of the robot arm is considered during the design and development of the two heads. In addition to the additive and subtractive heads, an integrated manufacturing platform equipped with a heated bed for the additive process and a T-slot structure and clamping set for fixturing the parts during the subtractive process is also designed. The developed hardware layout is shown in Figure 34.
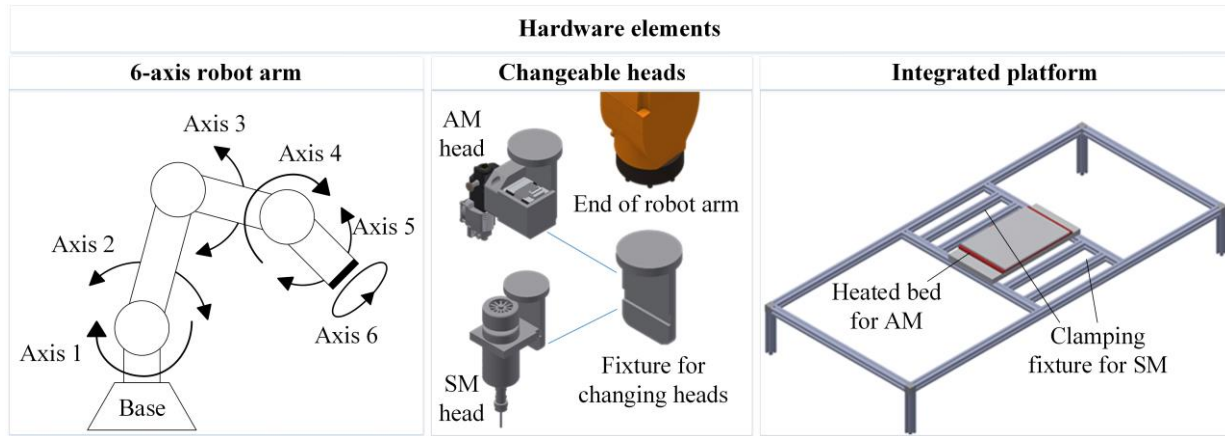
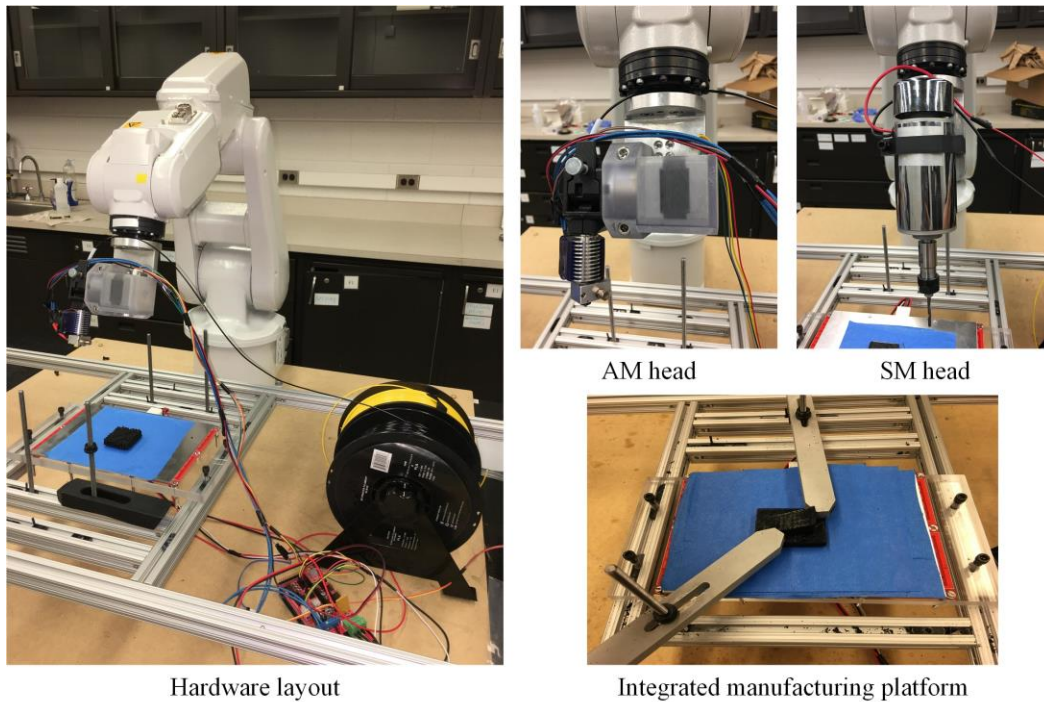Figure 33. Hardware design and configuration for HASM process

Figure 34. Illustration of hardware layout of HASM process

3.1.2 System Software and Control

The HASM process requires new software to be developed to deal with different tasks, namely (i) process planning, (ii) controlling the elements of additive and subtractive heads (e.g., extrusion, heated bed, fan, spindle speed), (iii) controlling the printing path through the robot arm controller, and (iv) communicating between the robot arm controller and both additive and subtractive heads.

It is important that the robot arm controller and the additive/subtractive head controllers can synchronize and communicate for providing robust and high-quality prints. Process planning refers to all the necessary steps (tasks) for transforming a design into a manufactured part. Considering the traditional manufacturing processes, process planning consists of several tasks including fixture design, setup, and tool path planning as shown in Figure 35. Computer technologies mainly CAD (computer-aided design) and CAM (computer-aided manufacturing) have contributed significantly to the process planning research.
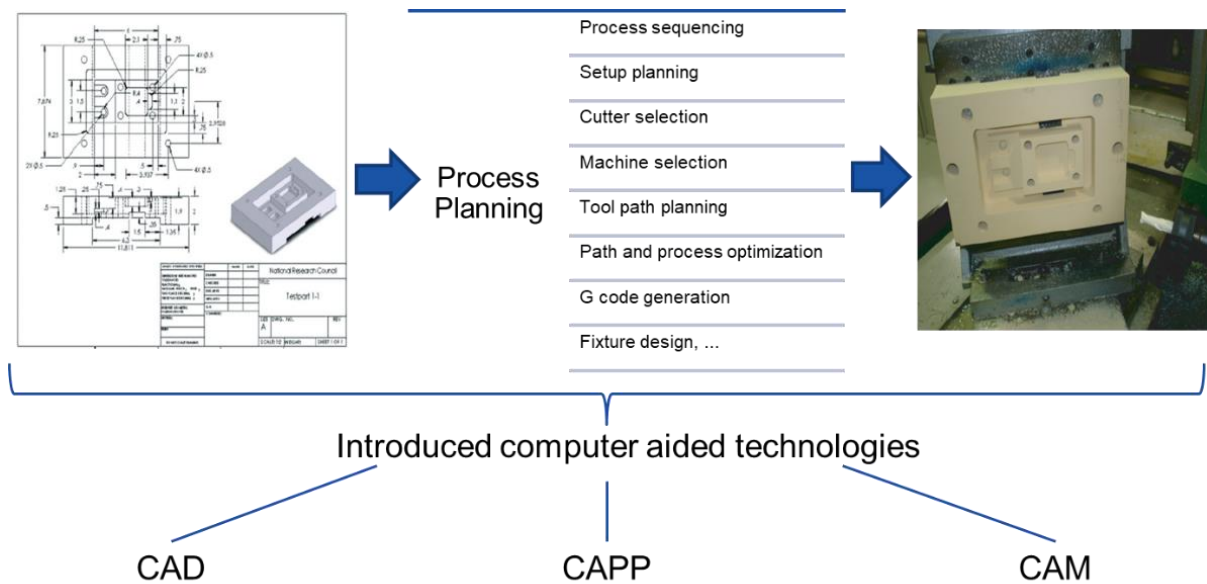

Figure 35. Process planning in traditional manufacturing processes

However, to address the characteristics of hybrid additive-subtractive processes, necessary adjustment to the traditional process planning tasks should be performed. In the HASM process, the necessary process planning steps are as follows.

(1)   *3D model generation and input*: Initially, a 3D model is generated through CAD software or 3D scanning equipment. In this thesis, the Autodesk Inventor software is used for generating the necessary CAD files.

(2)   *Feature recognition*: Feature recognition refers to the decomposition of a geometry into additive (AM) and subtractive (SM) features. Traditionally, subtractive features (also known as machining features) are defined as "those shapes, such as step, slot, pocket and hole, which can be easily achieved by the available resources and defined machining technologies" [190]. AM features, however, can be extremely complex with no standard form. Current literature defines AM feature as "a geometrical shape and associated technological attributes for which at least an AM process is known; this AM process is also independent from processes of all other features" [191]. Different algorithms for machining feature recognition are available in the literature [192]. However, the research area of feature recognition in hybrid additive-subtractive processes is new. Currently, a knowledge-based approach by evaluating the complexity of components is used for feature recognition in the developed platform. The higher the complexity level of geometries, the more AM is suitable for their fabrication. As an example, sharp inner cuts and undercuts are difficult to be fabricated by subtractive processes. The combination of several different parameters can be considered for evaluating the level of geometry complexity including bounding box volume, ratio of solid (filled) volume to the blank (empty) volume inside the bounding box, connectivity of the blank volumes, location of the blank volumes in the bounding box, the ratio of surface area to the part volume, ratio of triangle number (in the STL file) to the surface area, relative angle of normal vectors for neighboring triangles, etc.

(3)   *Setup planning:* Setup planning refers to the positioning the workpiece on the build platform. Traditionally, the largest surface areas are selected for positioning of the workpiece as they provide more stability. However, in the AM process, the setup planning step is equivalent to the build direction selection. For hybrid additive-subtractive processes, especially with a large number of degrees of freedom, this decision becomes complex as it can directly affect the

feasibility of the process and quality of components. Currently, a knowledge-based approach is used for setup planning in the HASM process which considers both the quality aspects and geometrical constraints.

(4)   *Feature sequencing:* This task refers to the sequencing of recognized features (obtained from step (2)). A greedy algorithm is adopted to perform feature sequencing to minimize the energy consumption of the system. First, precedence matrix (or graph) is generated (Equation (3.1)) for the recognized features considering both hard and soft precedence constraints including geometrical constraints, critical datum/tolerances, and the non-critical tolerances [193]:

$$
\mathbf{M}_p = \begin{array}{c} \\ 1 \\ . \\ . \\ . \\ n \end{array}
\begin{array}{c} 1 \quad . \quad . \quad . \quad n \\
\begin{bmatrix}
x_{11} & . & . & . & x_{1n} \\
. & . & . & & . \\
. & & x_{ij} & & . \\
. & & & . & . \\
x_{n1} & . & . & . & x_{nn}
\end{bmatrix}
\end{array}
\tag{3.1}
$$

where $n = I + J$ refers to the total number of features (I SM features, and J AM features), and x_{ij} is a binary variable. Therefore, the precedence of F_i to F_j is represented by $x_{ij} = 1$.

The energy consumption of the system is characterized into three categories of (i) SM feature processing, (ii) AM feature processing, and (iii) tool travel and tool/process change. SM feature processing refers to the energy consumption used for fabricating the SM feature and includes the energy consumption for material removal, feeding, and spindle rotation. The specific energy consumption (J/cm^3) and volume of the SM feature i in cm^3 (which is removed), will be used for calculating the energy consumption for each SM feature as shown below.

$$
E_{SMF}^i = SEC_i \times V_i
\tag{3.2}
$$

where V_i can be calculated from the MRR_i (material removal rate) for the milling and drilling processes.

The energy consumption for AM feature j is calculated according to equations in Section 2.1. Finally, the energy consumption for tool travel and tool/process change is calculated as follows.

$$E_k^{k+1} = \begin{cases} E_{k^e}^{(k+1)^s} & P_{ij} = 1 \text{ and } T_{ij} = 1 \\ E_{k^e}^{\text{home}} + E_{tool\ change} + E_{\text{home}}^{(k+1)^s} & P_{ij} = 1 \text{ and } T_{ij} = 0 \\ E_{k^e}^{\text{home}} + E_{process\ change} + E_{\text{home}}^{(k+1)^s} & P_{ij} = 0 \end{cases} \tag{3.3}$$

where k is the index of the feature in the sequenced order, k^e is the coordinates of the endpoint of the kth feature, $(k+1)^s$ is the coordinates of the start point of (k+1)th feature, *home* represents the coordinates of the home position, and P_{ij} and T_{ij} are given as:

$$P_{ij} = \begin{cases} 1 & \text{Features i and j have same process} \\ 0 & \text{else} \end{cases} \tag{3.4}$$

$$T_{ij} \big| (P_{ij} = 1) = \begin{cases} 1 & \text{Features i and j have same tool} \\ 0 & \text{else} \end{cases} \tag{3.5}$$

Signal Analyzer module from the RobotStudio software [194] is used to evaluate the E_k^{k+1}, which represents the total robot energy consumption (as well as the energy consumption of individual joints) for moving from one configuration/coordinate to a second configuration/coordinate, as shown in Figure 36. The sequencing is then performed according to Figure 37 and using the above information [195].
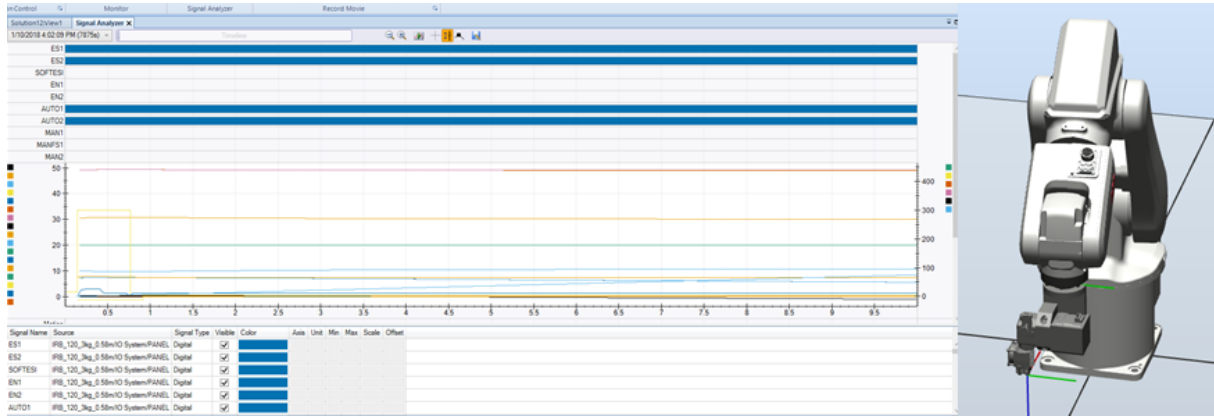
Figure 36. The signal analyzer module in the Robotstudio Software (Left) and the virtual HASM
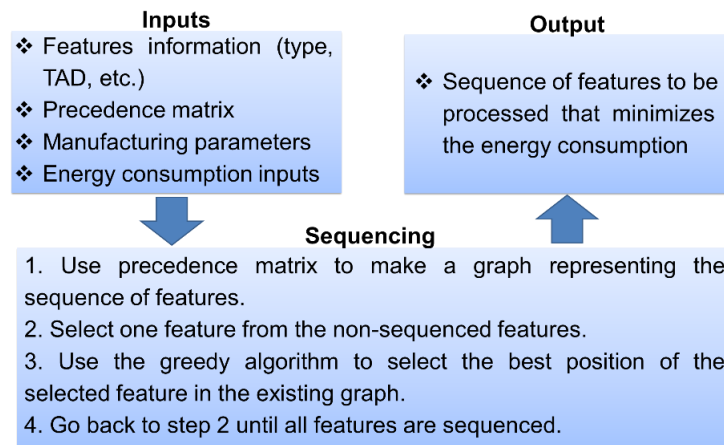
platform (right)

Figure 37. Feature sequencing using greedy algorithm

(5)   *Slicing and support generation:* For AM features, slicing algorithm is applied to slice the

component into layers. The tool axis direction (TAD) strategy is considered during this step. In

other words, due to the high flexibility of the 6-DOF mechanism, a single feature can be fabricated

with different TAD strategies, namely, use of (1) constant TAD: fabricating a feature using only

one TAD, (2) multiple TADs: fabricating a feature using multiple TAD, and (3) dynamic TADs:

fabricating a feature by continuously adjusting the TAD to match the surface normal. To utilize

this added flexibility, new slicing algorithms to support multiple TADs (e.g., in multi-plane tool paths [196]) or dynamic TADs (e.g., in freeform tool paths [197]) are required.

(6)   *Path planning, merging, and feasibility check:* Path planning and merging is performed for the AM and SM features based on the slicing outputs and considering the mechanical/geometrical requirements and constraints using a knowledge-based approach. To perform the path planning, coordinate transformation (from the slicing software to the integrated build platform) is necessary. A MATLAB code is thus, developed and used for the transformation and processing of the path data. The virtual robot arm platform is used for checking the feasibility of the path plans.

(7)   *Code dispatch and calibration:* Finally, required codes are generated and dispatched to the HASM process controllers (robot arm and additive-subtractive head controllers). An ethernet connection is used for transferring the code to the robot arm controller. The code for the additive/subtractive heads is, on the other hand, transferred through a USB port. Although tool selection and fixture design are important elements of process planning, they have not been considered in this work. Therefore, only one type of milling tool and fixture design are used for the case study section. The platform calibration is initially performed in the robot software and by using an exact replica of the hybrid platform. Therefore, the robot arm will automatically calculate the coordinate of targets relative to the world, base, and tool coordinate systems. However, due to the errors caused by the platform fabrication process, a trial and error approach for finding the optimum minimum Z value is performed.

The generated code which is dispatched to the robot arm controller contains the path-related data: (1) the coordinates of targets, (2) the sequence of targets, (3) the configuration and orientation of the robot arm at each target, (4) the coordinate systems of the robot and SM/AM heads, (5) tool's weight, center of gravity, and center point, and (6) robot movement instructions (e.g. joint

or linear movement, speed, termination form of a target). The dispatched code to the additive-subtractive head controllers, however, has a G-code format which includes the following data: (1) the coordinates of targets, (2) the sequence of targets, (3) robot movement speed, (4) the extrusion rate/spindle speed, and (5) additional information (fan on/off control, hot end, and heated bed temperature control, etc.).
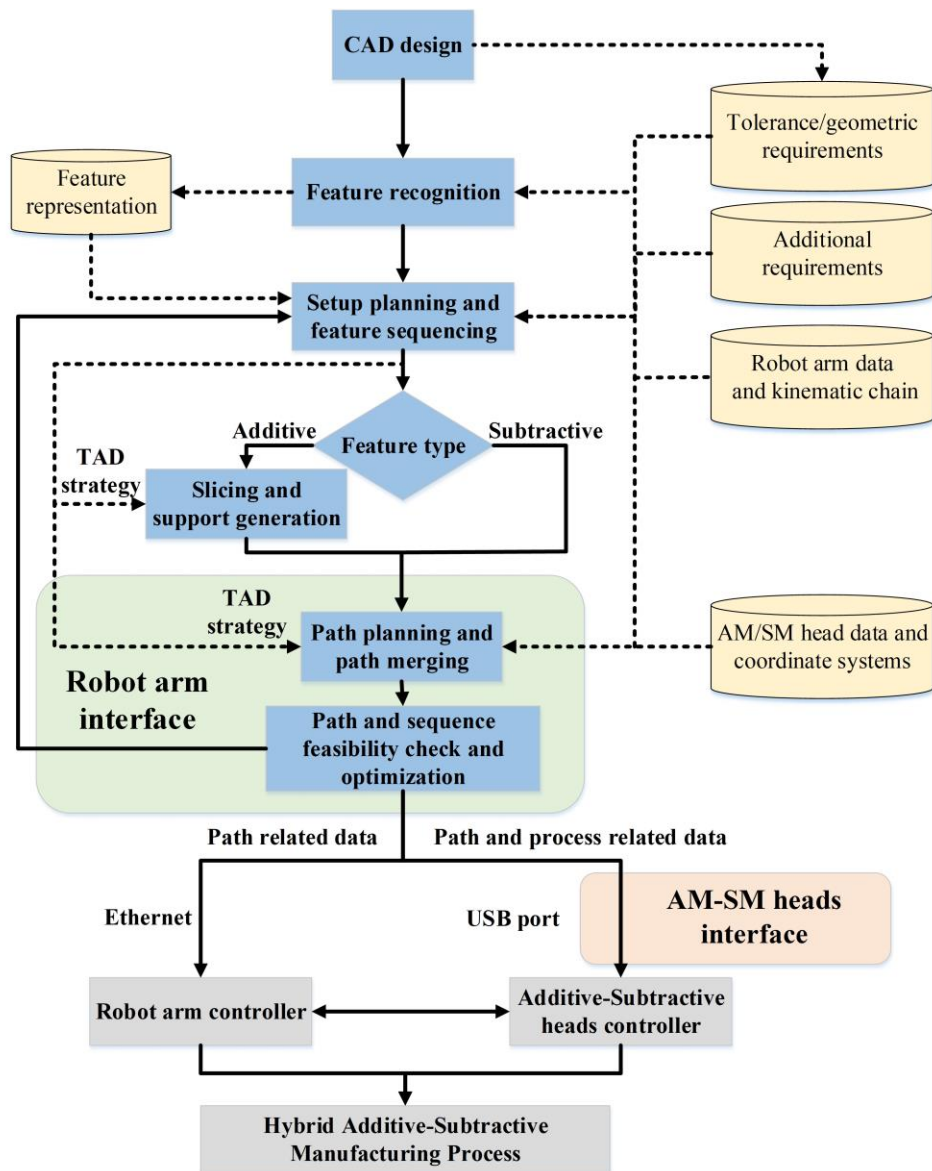

Figure 38. Schematic view of the software and control flow for the HASM process

The Arduino mega board is used for integrated control of the additive head, heated bed, and fan. The subtractive head is controlled using a control board for adjusting the spindle speed. The movements of the additive or subtractive heads, on the other hand, is controlled by the robot arm controller. Currently, a trial and error approach has been adopted for synchronizing the controllers by calculating and compensating for the time delay between controllers. In the future, a DeviceNet network can be established which allows for a more robust communication between controllers. The schematic view of the developed HASM process is shown in Figure 38.

3.1.3 Coordinate Systems

The different coordinate systems of the HASM process are shown in Figure 39. Coordinate transformation is necessary to move the generated coordinates from the slicing software on the manufacturing platform. The coordinates of the integrated build platform should be considered to ensure that all points are translated to coordinates above and within the build platform range. Therefore, the slicing software coordinates (XYZ) should be changed into ($X'Y'Z'$) coordinates in the world/base coordinate system while bringing all targets on the build platform through both rotatory and translational linear transformations. Since the scaling factor for the transformation is 1, the homogenous transformation matrix (H) can be represented in the following form:

$$
H = \begin{bmatrix} r_{11} & r_{12} & r_{13} & t_x \\ r_{21} & r_{22} & r_{23} & t_y \\ r_{31} & r_{32} & r_{33} & t_z \\ 0 & 0 & 0 & 1 \end{bmatrix} \tag{3.6}
$$

where r_{ij} are the elements of the rotation matrix $R_{3 \times 3}$ given the yaw, pitch, and roll rotation angles, and t_x, t_y, and t_z are the linear translations of center point along the X, Y and Z axes.

A 90-degree rotation along the Z axis is performed (φ=90) in a clockwise direction. The translations of δx, δy, $\delta' z$ and $\delta' x$ are also performed to move the targets to the center, and then forward to a higher altitude on the build platform. The transformation is represented below:

$$
\begin{bmatrix} X' \\ Y' \\ Z' \\ 1 \end{bmatrix} = \begin{bmatrix} 1 & 0 & 0 & \delta'x \\ 0 & 1 & 0 & 0 \\ 0 & 0 & 1 & \delta'z \\ 0 & 0 & 0 & 1 \end{bmatrix} \begin{bmatrix} \cos\varphi & -\sin\varphi & 0 & 0 \\ \sin\varphi & \cos\varphi & 0 & 0 \\ 0 & 0 & 1 & 0 \\ 0 & 0 & 0 & 1 \end{bmatrix} \begin{bmatrix} 1 & 0 & 0 & -\delta x \\ 0 & 1 & 0 & -\delta y \\ 0 & 0 & 1 & 0 \\ 0 & 0 & 0 & 1 \end{bmatrix} \begin{bmatrix} X \\ Y \\ Z \\ 1 \end{bmatrix} \quad (3.7)
$$

where XYZ is the initial coordinate in the slicing software coordinate system and $X'Y'Z'$ is the final transformed coordinates in the world/robot base coordinate system. The slicing software coordinate system and world coordinate systems have been overlapped for this transformation.
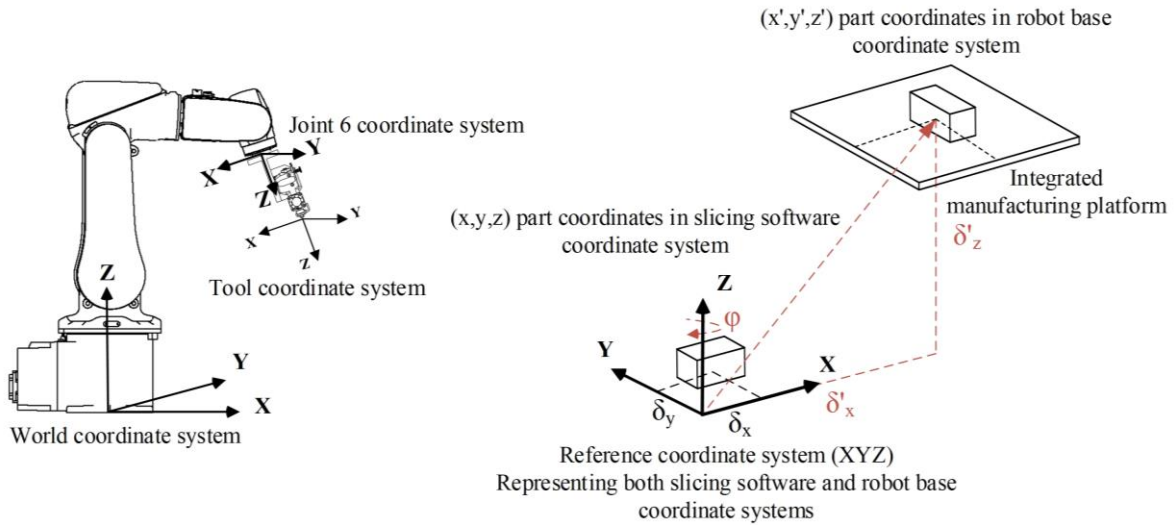

Figure 39. HASM process coordinate systems illustration and transformation

(Robot arm drawing is adopted from http://new.abb.com/products/robotics/industrial-robots/irb-120/irb-120-cad)

3.1.4 Hybrid Platform Capabilities

(1) Dynamic TAD adjustment

The 6-DOF flexibility of the HASM process provides new manufacturing opportunities and can lead to higher efficiency and better quality of parts. One of the opportunities is the capability of defining trajectory movements that are not necessarily linear. In other words, the TAD can be adapted according to the geometrical and manufacturing requirements. For example, a dynamic TAD strategy can be used where the TAD adjusts to the surface normal vector while moving along the path. This capability can help towards improving the surface quality of parts. In addition, it can allow for accessing inner features or surfaces by adjusting the active kinematic chain to match the geometrical constraints of the part.

To demonstrate the dynamic TAD adjustment capability of the developed HASM process, a freeform surface with a sine function was designed. Both additive and subtractive heads could successfully move along the path while adjusting the coordinate system of the tool to match the normal vector of the freeform surface during the printing or milling process, as shown in Figure 40(left). The unique integrated platform of the HASM process allowed the test part to be clamped during the milling process once the printing process was finished. The rectangular base of the freeform geometry was used for clamping the part, as shown in Figure 40(right). Since the part was not re-located after the printing process (its coordinate system was not changed), it was possible to automatically derive the path coordinates for the milling process. However, the tool coordinate system was updated as the manufacturing head was changed. A 100% fill density and 0.2 mm layer thickness parameters were selected for the print to minimize the porosity and improve the surface quality during the milling process.
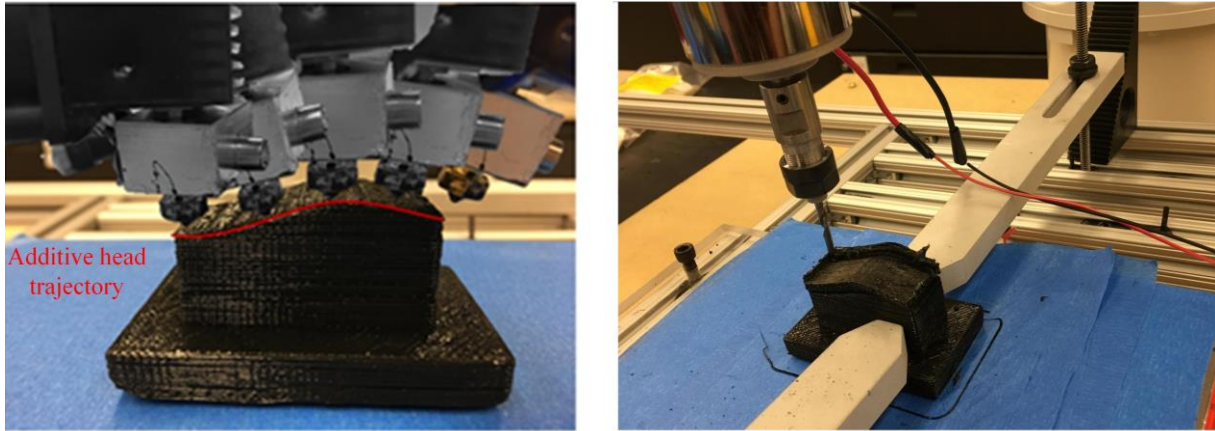
Figure 40. Freeform surface printing and milling: (left) freeform printing, and (right) freeform

milling

(2) Improved surface quality as a result of the hybrid process

The HASM process can improve the surface quality by using the SM head to perform the surface finishing process on additive manufactured parts. This capability is however expected and has already been well explored in the literature [118].

In Figure 41, the surface profiles of the test part in Figure 40 as a result of our HASM process, shown in Figure 41(b), is compared with the surface profiles of the same part fabricated using only the AM technique, in Figure 41(a), as well as the surface of extruded plastic bars which can be bought from supplier companies, Figure 41(c). Even without quantifying the surface roughness, it is clearly observed that the surface profile from the HASM process has a better quality compared to when the part is solely manufactured by the AM process (in our case, the FDM™ process). However, the surface quality is still not as good as the extruded plastic bars from supplier companies.
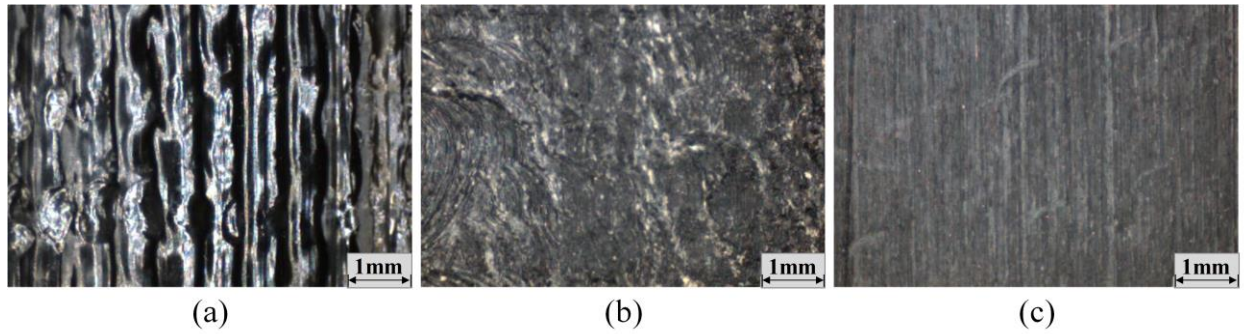
(a)　　　　　　　　　(b)　　　　　　　　　(c)

Figure 41. Surface profile of (a) printed surface, (b) machined surface of a printed part, and (c) surface of extruded plastic bars

(3) Improved surface quality as a result of 6-DOF capability

In addition to adopting the SM process for surface finishing, the surface quality can be improved by adjusting the orientation of the AM head during the printing process to reduce the staircase error. Therefore, the adoption of SM head for surface finishing might not be necessary. Staircase error is one of the most common quality issues in 3-DOF AM processes, which directly affects the surface quality of printed parts [198], and is significantly affected by the angle between the surface's normal vector and build orientation as well as the adopted layer thickness. The 6-DOF HASM process, is however, not constrained to the 3 axes of X, Y and Z, and can adapt the build direction to match the surface normal. Therefore, the staircase error can be reduced or eliminated. To illustrate this capability, a case study was performed where a right triangular prism was printed using two different scenarios of: (a) constant TAD, and (b) multiple TADs. In the constant TAD scenario, the configuration of the additive head was fixed during the entire process so that the Z axis of the tool (Figure 39) was aligned with the build direction along the Z axis of the platform. However, in the multiple TADs scenarios, the component was first printed using a constant TAD configuration similar to the first scenario. Finally, an additional layer was printed

on the angled surface of the component to reduce the effect of staircase error using a different TAD from the initial TAD.
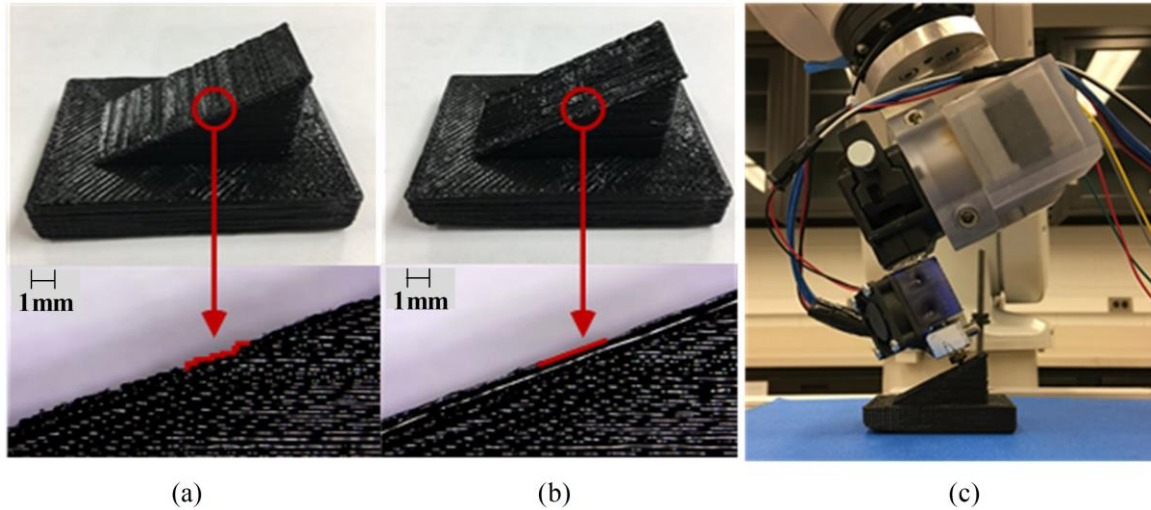

Figure 42. Comparison of surface quality (a) using 3-DOF printing (constant TAD), (b) using HASM process (multiple TAD), and (c) configuration of AM head during deposition of the final layer

As can be seen in Figure 42, a smoother surface is obtained using the HASM process, and the staircase error is significantly reduced. Figure 42(c) shows the robot arm configuration when using multiple TADs scenario to print the final layer for improving the surface quality.

(4) Multi-plane processing

One of the main capabilities of the HASM process is multi-plane processing (i.e., printing/milling) using either the AM or SM head. This multi-plane processing is achieved by changing the printing/milling plane using the 6-DOF configuration. In addition, due to the hybrid capabilities of the process in one integrated station, a part with both subtractive and additive features can be manufactured without re-location or setup change. To demonstrate the mentioned

capability, a part with both additive and subtractive features was designed as shown in Figure 43(a). An extruded block of PLA material is used as the raw workpiece. The fabrication of this part starts with machining the slot feature on the PLA block by using the SM head, as shown in Figure 43(b). Next, the center piece (main body) is printed using 3-DOF AM process (Figure 43(c)), during which the layers are printed on a horizontal plane (vertical TAD). The TAD is then changed to horizontal by using the 6-DOF capability to fabricate the hanging feature on the center piece, where the printing is continued on a vertical plane. No support material is required as a result of this change of TAD. In addition to the multi-plane printing capability, HASM process is also capable of multi-plane milling. It is important to note that in most hybrid additive-subtractive manufacturing processes in the literature, the application of the subtractive process is usually limited to surface finishing. Therefore, the potentials of the subtractive process are not used to their fullest. However, this case study has demonstrated that the subtractive manufacturing can also be used to fabricate different machining features not necessarily for the purpose of surface finishing (e.g., the slot feature shown in Figure 43(b)).
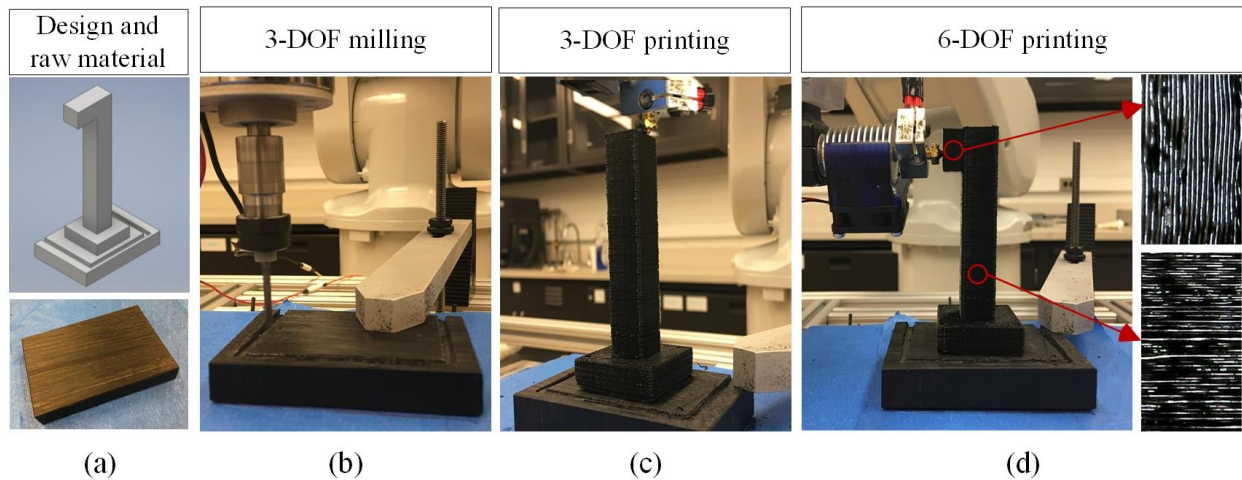

Figure 43. Hybrid manufacturing through multi-plane processing

(5) Higher collision avoidance capability

The additional degree of freedom provided by the 6th rotational axis in the developed 6-DOF hybrid process provides a higher collision avoidance capability compared to 5-DOF hybrid additive-subtractive processes. To demonstrate this capability, the test part in Figure 43 is slightly altered and used as shown in Figure 44. In the new test part, two overhang features exist and therefore the vertical printing (i.e., printing on a vertical plane) should be performed on both sides. Considering the tool coordinate system and to perform the vertical printing on the left side, the tool configuration can be easily adjusted without involving the 6th rotational axis. However, to reach a suitable configuration for vertical printing on the right side, all of the 6 axes need to get involved to avoid collision between the additive head and the printing platform (as illustrated in Figure 45, Figure 46, and Figure 47).
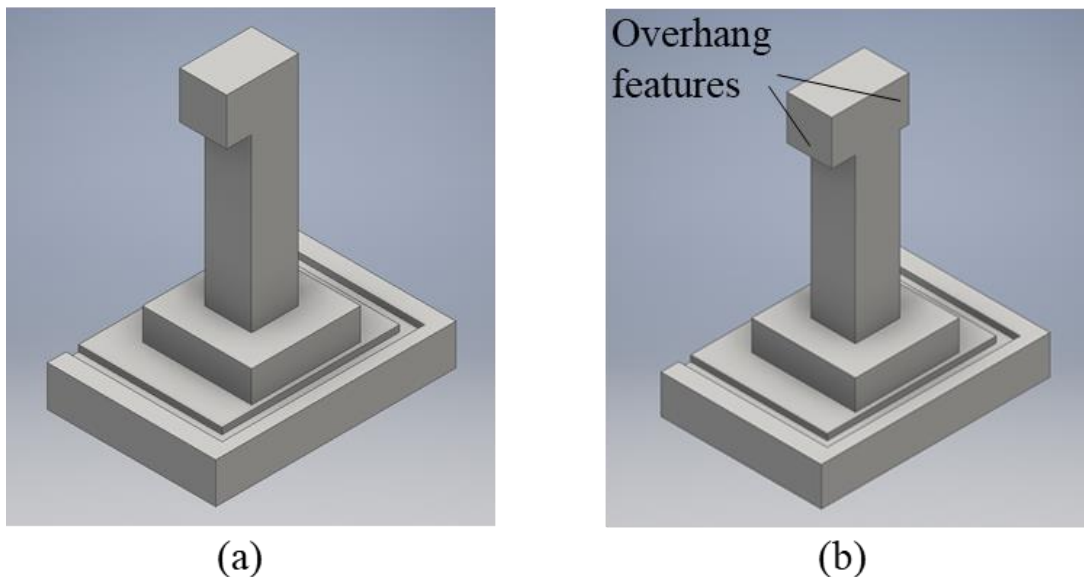

Figure 44. (a) the previous test part in Figure 43 and (b) the new test part to demonstrate the capability of the sixth axis
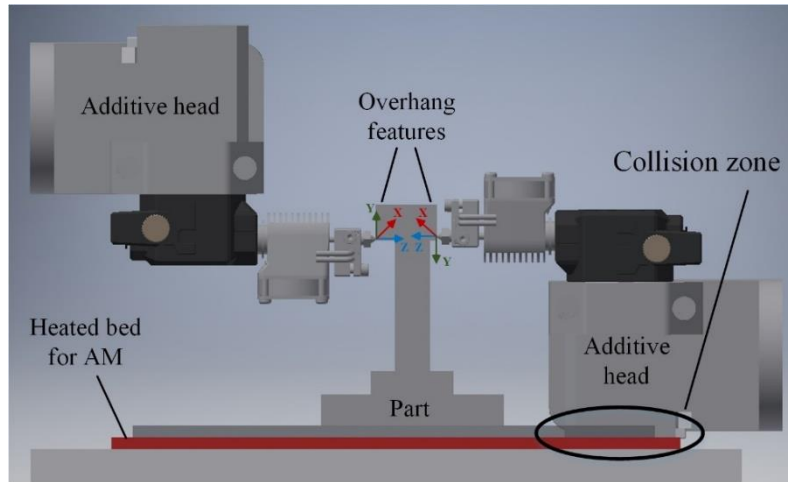
Figure 45. The only feasible configuration of additive head using the 5-DOF capability which
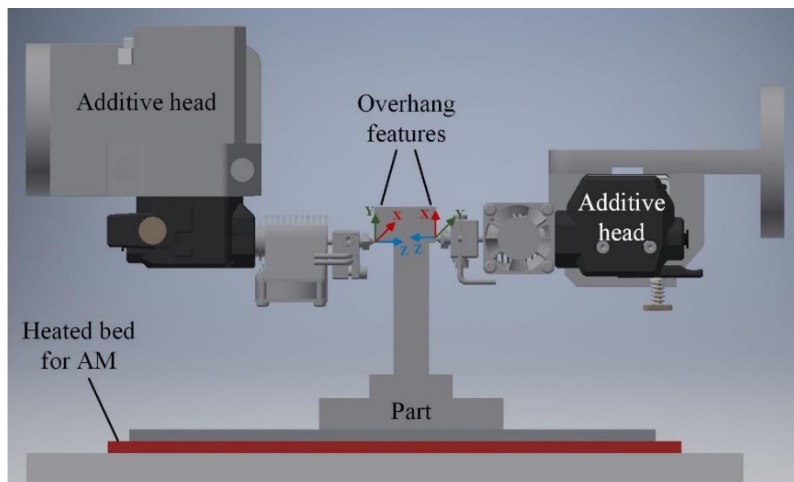
leads to collision

Figure 46. The configuration of additive head using the sixth rotational axis to avoid collision

Without the additional degree of freedom provided by the 6th axis, the only possible approach to fabricate the part is to change the setup by re-locating the part which can lead to additional production time. In addition, the inevitable loss of datum during the re-location can negatively affect the accuracy of part. Since the FDM™ process is currently adopted as the additive process, the feasibility of configurations not only needs to be evaluated considering the robot arm limitations but also considering the limitations introduced by the attached filament and wires to

the additive head. For example, continuous rotational movement of the head will not be feasible considering the current setup. However, integrating other additive processes through a more flexible and innovative design might increase the freedom of movement and help with fully utilizing the capability of the 6th axis.
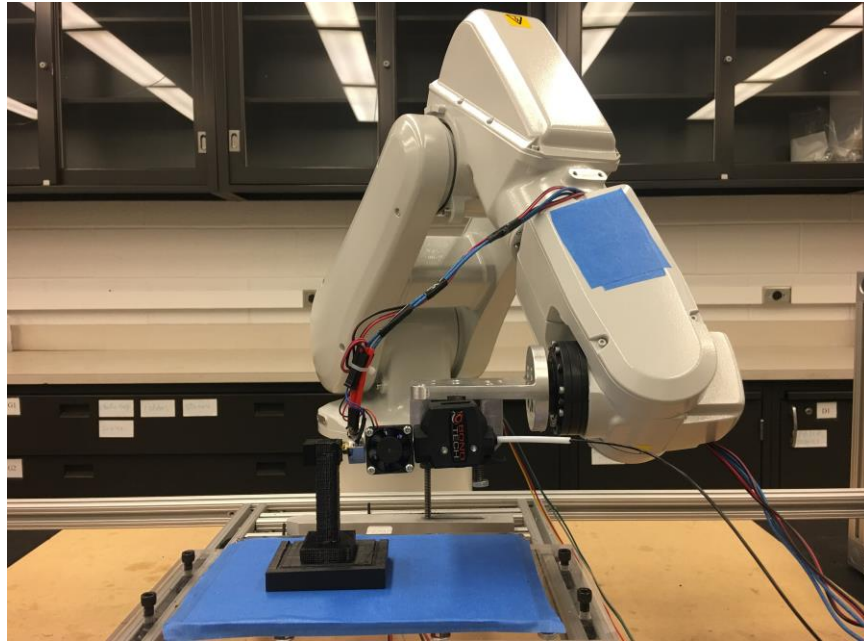

Figure 47. The robot arm configuration using the sixth rotational axis to avoid collision

(6) Reduced material waste and production time

As explained in the previous case studies, the flexibility of movement and processing provided by the 6-DOF HASM process not only can improve the quality but also can reduce the number of setups, production time, and material waste. To better demonstrate the production time and material waste reduction capability, the following case study is designed. Three different manufacturing scenarios for the test part shown in Figure 44(a) are considered and the obtained material wastes and required production times are compared.

Case I is the scenario studied in Figure 43. The final part is fabricated by the developed hybrid system (HASM process) using 3-DOF milling (for the slot feature), 3-DOF printing (for the main body), and 6-DOF printing (for the overhang feature). In Case II, the same part is manufactured by the HASM process but only using 3-DOF capability for printing (printing both main body and overhang feature) and 3-DOF for milling (for the slot feature). Note that in both Case I and Case II, the PLA block shown in Figure 43(a) is used as the raw workpiece. Finally, in Case III, the part is entirely built by 3-DOF printing (including the 3D print of the block, main body and overhang feature). Note that when using 3-DOF printing for fabricating the overhang feature, the support structure is required as illustrated in Figure 48.
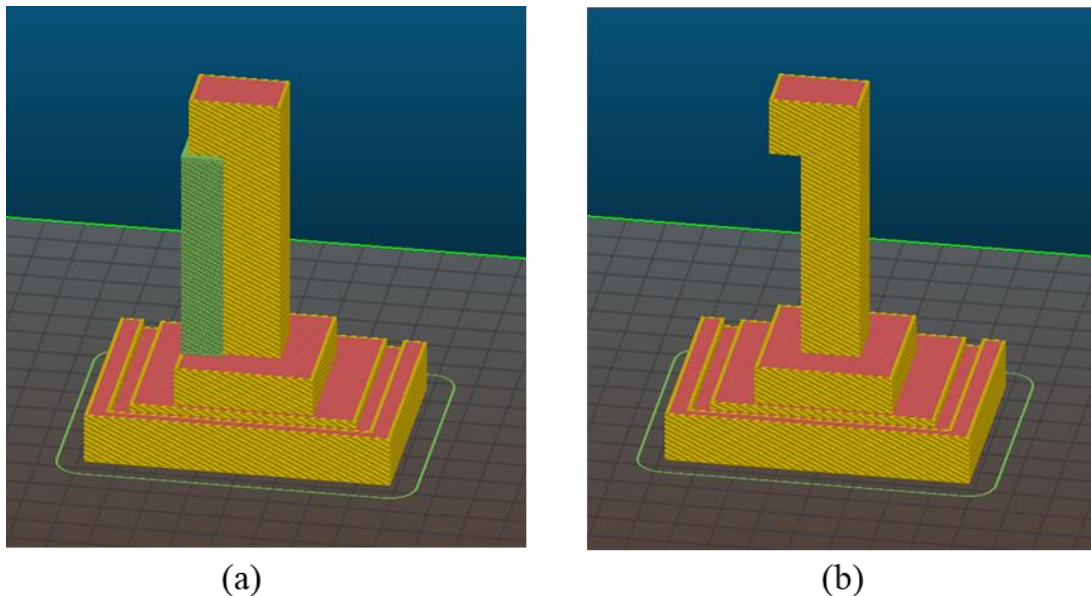

Figure 48. The designed test part (a) with, and (b) without support structure

The comparison of material waste and production time for three different manufacturing scenarios is shown in Table XVIII. It can be observed that adopting the developed HASM process for fabricating the part (Case I) can reduce the material waste percentage by 63.39% and 43.45%, compared to Cases II and III, respectively. In Case I, the material waste is mainly generated as a

result of the milling process for fabricating the slot feature. In Case II, in addition to the above machining waste, the support structure that is required due to the use of 3-DOF AM process for fabricating the overhang feature accounts for around 62% of the total material waste. In Case III, however, the material waste comes from the support structure, as the part is entirely fabricated using the AM process. Furthermore, the hybrid manufacturing scenario in Case I can save the production time by 6.72% and 59.59% compared to the production times of Case II and Case III, respectively. The total production time in Case I consists of the time for milling process (SM), tool changeover (from SM head to AM head), 3-DOF printing of the main body (AM), TAD adjustment (i.e., changing the configuration from printing on a horizontal plane to a vertical plane) and 6-DOF printing of the overhang feature (AM). In Case II, the 3-DOF printing time is longer than that of Case I as the support structure for the overhang feature needs to be printed as well. On the other hand, the required time for TAD adjustment and 6-DOF printing are saved. Consequently, the total production time is slightly larger than Case I. In Case III, the entire workpiece (including the PLA block) is fabricated by 3-DOF printing, which therefore requires a substantially longer period compared to former cases. The detailed production time breakdown is illustrated in Table XIX and Figure 49.

Table XVIII. Comparison of material waste

	Case I: Hybrid manufacturing (6-DOF capability)	Case II: Hybrid manufacturing (3-DOF capability)	Case III: Additive manufacturing (3-DOF capability)
PLA filament used (g)	32.08	34.60	91.33
PLA block used (g)	59.33	59.33	0
Material waste (g)	1.46	4.10	2.54
Waste percentage	1.60%	4.37%	2.78%

Table XIX. Contribution of different factors in the production time for the studied cases

	Case I: Hybrid manufacturing (6-DOF capability)	Case II: Hybrid manufacturing (3-DOF capability)	Case III: Additive manufacturing (3-DOF capability)
3-DOF printing	79.24%	94.07%	100%
Milling	5.08%	4.74%	N/A
6-DOF printing	13.98%	N/A	N/A
Tool changeover	1.27%	1.19%	N/A
TAD adjustment	0.42%	N/A	N/A

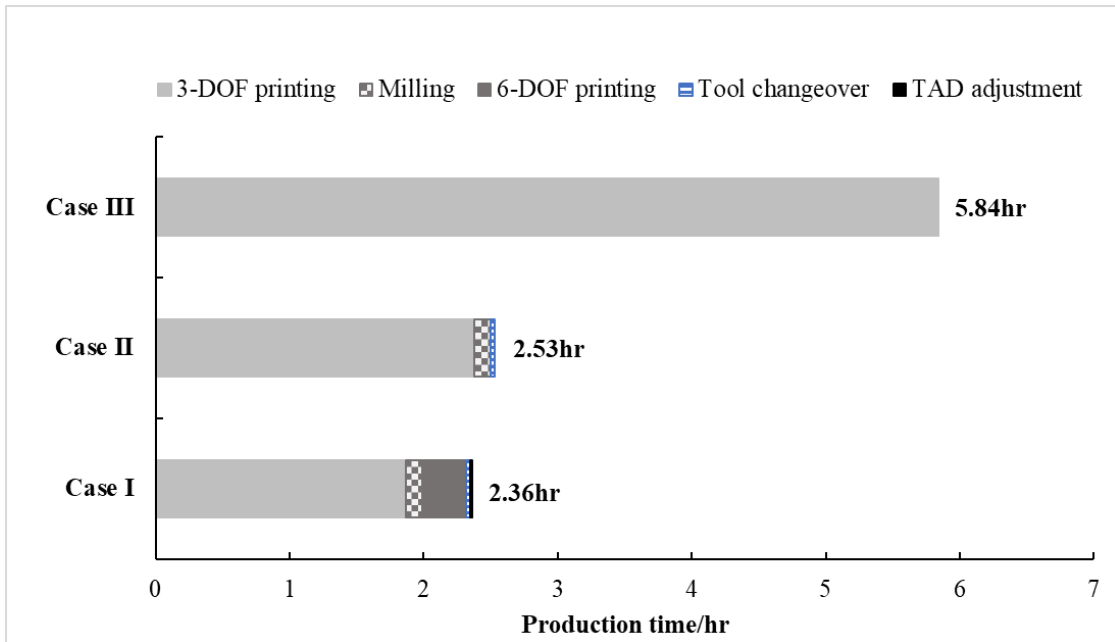Figure 49. The production time breakdown for the studied cases

3.1.5 Conclusions

In this section, the development of the 6-DOF hybrid additive-subtractive manufacturing (HASM) process is presented. The described hybrid platform is mainly developed for conducting

118

research on tolerance design challenges of hybrid manufactured components. The different elements of the hardware, software, and control system of HASM are explained and discussed. Two additive and subtractive heads and an integrated manufacturing platform to support the functionality of each process are developed. The proposed 6-DOF HASM process is capable of non-linear trajectory movements by adjusting the tool axis direction to match the surface normal vector. The capability of this HASM process is demonstrated through five different case studies. It has been shown that HASM process can reduce material waste, production time, and improve the surface quality of parts.

3.2 Surface Roughness Modeling and Validation for Hybrid Additive-Subtractive Manufacturing

In this section, analytical models for predicting the surface roughness of hybrid additive-subtractive manufactured components are proposed and validated. As the existing surface roughness models in the literature do not address the effect of secondary processes, the proposed model provides a critical tool for designers to evaluate the surface quality and check the feasibility of designed tolerances. The subtractive process is considered for surface finishing, which aims to improve the surface roughness of 3D printed parts. To simplify the modeling process, the following terminologies are adopted. The term "additive profile" is used to refer to the obtained surface profile from the AM process; "milling profile" is used to refer to the obtained surface profile from flat end milling process on a non-3D printed surface; and "intersected profile" is used to refer to the obtained surface profile from flat end milling process on a 3D printed surface.

3.2.1 Surface Profile Representation

To understand and model the intersected profile, different parameters such as cutting parameters, milling tool geometry, and characteristics of the existing additive profile need to be

considered. In this work, a sawtooth function is selected to represent the smallest unit of the milling profile in an ideal condition [199], as shown in Figure 50.
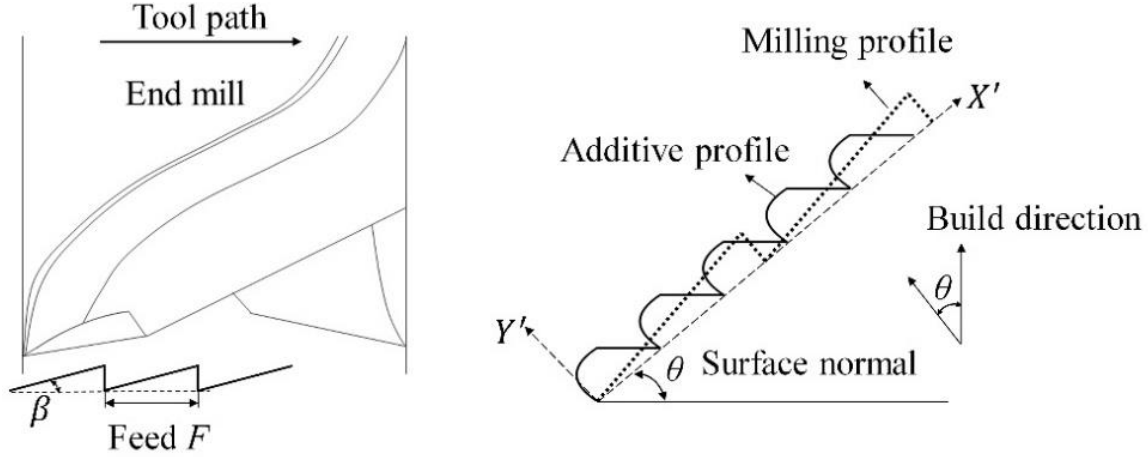

Figure 50. Representation of the milling profile

Two parameters of feed (F) and working minor cutting edge angle (β) are incorporated into the sawtooth function to reflect the tool geometry and cutting parameters. The amplitude of the sawtooth function is defined as AP_s, where $A = \tan(\beta)$ is the slope of the sawtooth function and $P_s = F$ is the periodicity of the sawtooth function. Note that all the other parameters as well as the machine errors during the milling process are neglected in this work.

3.2.2 Model Assumptions

The following assumptions are adopted for the surface roughness modeling: (1) the starting coordinates of additive and milling profiles are similar; (2) the sawtooth function intersects with each parabolic curve at exactly two points; (3) the building direction is vertical at all circumstances; (4) the periodicity of sawtooth function (P_s) is always greater than the periodicity of parabolic function (P_p); and (5) both P_s and P_p are rational numbers. To further analyze the intersected profile and surface roughness, two cases are considered based on the stratification angle: (I) $\theta =$

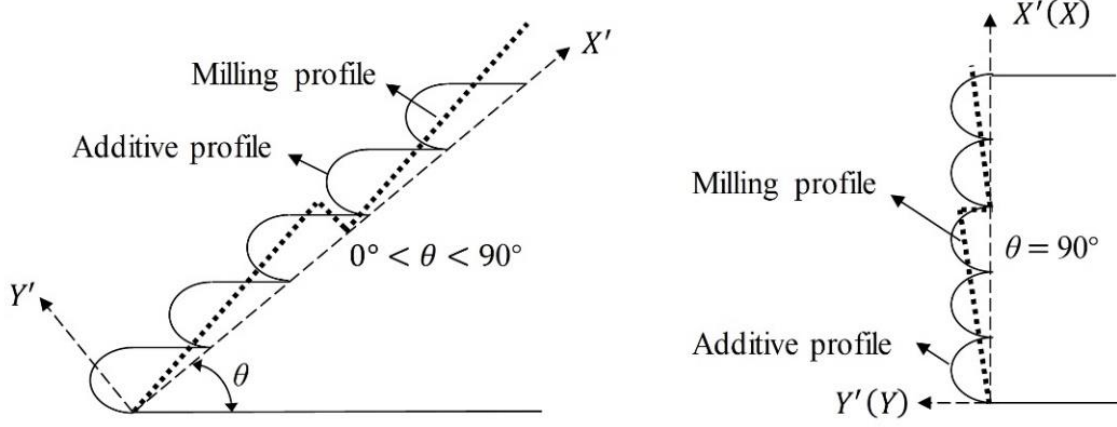90° and (II) $0° < \theta < 90°$ as shown in Figure 51. Note that the special case $\theta = 0°$ is not considered.

Figure 51. Representation of the intersected profile for different stratification angles

3.2.3 Surface Roughness Model for $\theta = 90°$

To study the obtained intersected profile, the periodic functions of both additive and milling profiles are derived using the Fourier's theorem.

Fourier's theorem: It is known, that the general representation of Fourier trigonometric series for function $f(x)$ with a periodicity of L ($0 \leq x \leq L$) is:

$$f(x) = a_0 + \sum_{n=1}^{\infty} \left[a_n \cos\left(\frac{2\pi nx}{L}\right) + b_n \sin\left(\frac{2\pi nx}{L}\right) \right], \tag{3.8}$$

where coefficients a_0, a_n and b_n can be obtained from the following equations:

$$a_0 = \frac{1}{L} \int_0^L f(x)dx, \tag{3.9}$$

$$a_n = \frac{2}{L} \int_0^L f(x) \cos\left(\frac{2\pi nx}{L}\right) dx, \tag{3.10}$$

$$b_n = \frac{2}{L} \int_0^L f(x) \sin\left(\frac{2\pi n x}{L}\right) dx. \tag{3.11}$$

Using Fourier's theorem, the Fourier series representing the sawtooth function $f_s'(x)$ and periodic parabolic function $f_p'(x)$ can be derived as:

$$f_s'(x) = \frac{AP_s}{2} + \sum_{n=1}^{\infty} \left[-\frac{AP_s}{\pi n} \sin\left(\frac{2\pi n x}{P_s}\right) \right], \tag{3.12}$$

$$f_p'(x) = \frac{1}{3}(t - 2\varepsilon_y) + \sum_{n=1}^{\infty} \left[-\frac{2(t - 2\varepsilon_y)}{\pi^2 n^2} \cos\left(\frac{2\pi n x}{P_p}\right) \right], \tag{3.13}$$

where P_p denotes the periodicity of parabolic function and can be calculated as $P_p = (t - \varepsilon_x)$. The intersected profile $f_{p-s}'(x)$ can be calculated by subtracting the milling profile from the additive profile (shown in Figure 52), and can be represented using the following equation:

$$f_{p-s}'(x) = \min\{f_s'(x), f_p'(x)\}, \forall x \tag{3.14}$$

The periodicity of the intersected profile can be calculated as $\psi = \text{LCM}(P_p, P_s)$, where LCM represents the least common multiple. Note that the periodicity of the intersected profile ψ always exists according to the model assumptions and *lemma 1*:

Lemma 1: if $x, y \in \mathbb{Q}$, then $LCM(x, y) \neq \emptyset$.

Therefore, we have:

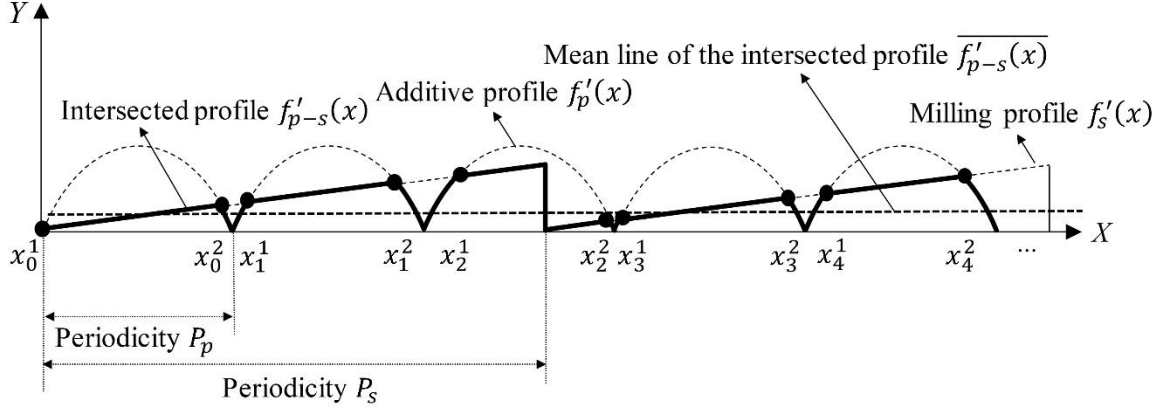$$f_{p-s}(x) = \min\{f_s'(x), f_p'(x)\}, \forall x \in [0, \psi] \tag{3.15}$$

Figure 52. Illustration of the intersected profile and the intersection points

The mean of the intersected profile is shown in Figure 52 and can be calculated according to the following

$$\overline{f'_{p-s}(x)} = \frac{W}{\psi},\tag{3.16}$$

where W denotes the surface area of the intersected profile, and can be obtained by the following equation:

$$W = \frac{\int_0^\psi f'_p(x)dx + \int_0^\psi f'_s(x)dx - \int_0^\psi |f'_p(x) - f'_s(x)|dx}{2},\tag{3.17}$$

and $\int_0^\psi f'_p(x)dx$, $\int_0^\psi f'_s(x)dx$, and $\int_0^\psi |f'_p(x) - f'_s(x)|dx$ can be calculated as follows.

$$\int_0^\psi f'_p(x)dx = \frac{\psi}{3}(t - 2\varepsilon_y) + \sum_{n=1}^\infty \left[-\frac{(t - 2\varepsilon_y)(t - \varepsilon_x)}{\pi^3 n^3} \sin\left(\frac{2\pi n\psi}{t - \varepsilon_x}\right) \right],\tag{3.18}$$

$$\int_0^\psi f'_s(x)dx = \frac{\tan(\beta)F\psi}{2} + \sum_{n=1}^\infty \left[\frac{\tan(\beta)F^2}{2\pi^2 n^2}\cos\left(\frac{2\pi n\psi}{F}\right) - \frac{\tan(\beta)F^2}{2\pi^2 n^2} \right],\tag{3.19}$$

123

$$\int_0^\Psi \left| f_p'(x) - f_s'(x) \right| dx$$

(3.20)

$$= \int_0^\Psi \left| \left(\frac{2(t - 2\varepsilon_y) - 3\tan(\beta)\,F}{6} \right) \right.$$

$$+ \sum_{n=1}^{\infty} \left[-\frac{2(t - 2\varepsilon_y)}{\pi^2 n^2} \cos\left(\frac{2\pi n x}{t - \varepsilon_x} \right) \right.$$

$$\left. + \frac{\tan(\beta) F}{\pi n} \sin\left(\frac{2\pi n x}{F} \right) \right] \left| dx. \right.$$

Finally, the surface roughness of the intersected profile can be calculated as:

$$R_a = \frac{1}{\Psi} \int_0^\Psi \left| f_{p-s}(x) - \overline{f_{p-s}(x)} \right| dx,$$

(3.21)

where $\overline{f_{p-s}(x)} = \overline{f'_{p-s}(x)}$. Note that to solve the above integral, the $f_{p-s}(x)$ function should be re-written, so that the value of the function is known for any given input, x. To do so, the intersection points between the parabolic and sawtooth functions for one period of Ψ need to be determined. The $f_{p-s}(x)$ function can thus be re-written as:

$$f_{p-s}(x) = \begin{cases} f_s(x) & x_m^1 \le x < x_m^2 \\ f_p(x) & x_m^2 \le x < x_{m+1}^1 \end{cases} \quad m = 0, \dots, M - 1.$$

(3.22)

where $x_m^{1,2}$ are the intersection points between the additive and milling profiles as shown in Figure 52 and can be calculated using the proposed algorithm in Section 3.2.5. Finally, the surface roughness can be calculated as follows:

124

$$R_a = \frac{1}{\Psi} \sum_{m=0}^{M-1} \left[\int_{x_m^1}^{x_m^2} |f_s(x) - \overline{f_{p-s}(x)}| \, dx + \int_{x_m^2}^{x_{m+1}^1} |f_p(x) - \overline{f_{p-s}(x)}| \, dx \right]. \qquad (3.23)$$

3.2.4 Surface Roughness Model for $0° < \theta < 90°$

For cases where the stratification angle θ is within the range of $(0°, 90°)$, the surface profile is simplified to a linear function as shown in Figure 53. The reason for such approximation is the unnecessarily long computation time for surface roughness calculation which might not necessarily lead to a significant improvement of the prediction accuracy. Furthermore, since the amplitude of the sawtooth function is very small, and its periodicity is much larger than the additive profile, a linear function can provide a good approximation. Therefore, for $0° < \theta < 90°$, the milling profile is represented using a linear function $f_c(x)$, which is parallel to the reference line 1 as shown in Figure 53.
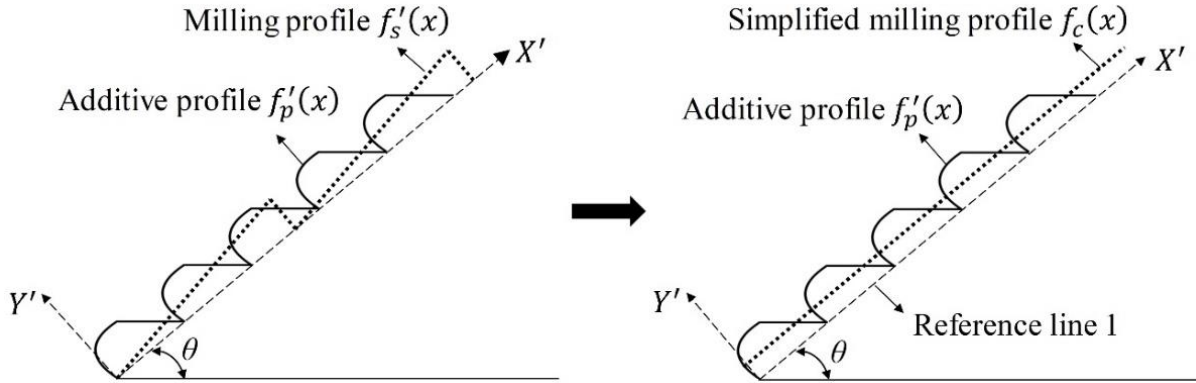

Figure 53. Illustration of the milling profile for $0° < \theta < 90°$

Clearly, the axial depth of cut will highly affect the obtained profile since the additive profile is represented using the combination of two different functions. As can be seen in Figure 54, any milling profile above the reference line 2, will only cut through the parabolic function. However, both the parabolic and the linear functions will be involved in the intersected profile if the milling profile is lower than reference line 2.

Therefore, two separate cases are considered. The distance between the reference lines 1 and 2 is $(t - K_b) \cos \theta$, and the distance between the milling profile position and reference line 1 is represented by D, as shown in Figure 54. Note that, in practical applications, the optimum axial depth of cut should be decided based on both the surface roughness and dimensional accuracy requirements. In addition, due to the existence of voids inside the printed part, increasing the depth of cut might not necessarily be beneficial.
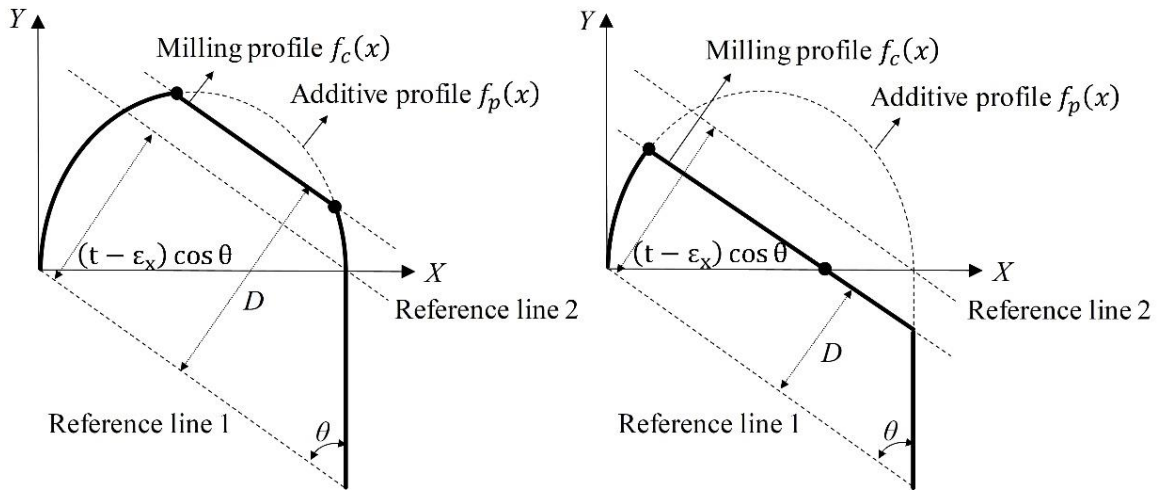

Figure 54. Different milling profile scenarios: case 1 (left) and case 2 (right)

Case 1: The milling profile is above or on reference line 2 ($D \geq (t - \varepsilon_x) \cos \theta$)

The mean line of the intersected profile $\overline{f_{p-s}(x)}$ in $X'Y'$ coordinate system can be calculated as

$$
\overline{f_{p-s}(x)} = \frac{\sin\theta}{t - \varepsilon_x} \left[\frac{(t - \varepsilon_x)^2}{2\tan\theta} + \frac{(t - \varepsilon_x)(t - 2\varepsilon_y)}{3} \right.
$$
$$
\left. - \int_{x_0}^{x_1} \left(f_p(x) - f_c(x) \right) dx \right],
$$

(3.24)

where the linear function $f_c(x)$ representing the milling profile can be formulated as

126

$$f_c(x) = -\cot\theta \left(x - \frac{D}{\cos\theta} \right),$$ (3.25)

and $f_p(x)$ is calculated in Chapter 2. Finally, the surface roughness can be calculated as

$$R_a = \frac{\sin\theta}{t - \varepsilon_x} \left[\int_0^{x_0} \left| f_p(x) - f_{p-s}^*(x) \right| dx + \int_{x_0}^{x_1} \left(f_c(x) - f_{p-s}^*(x) \right) dx \right.$$
$$\left. + \int_{x_1}^{t-\varepsilon_x} \left(f_p(x) - f_{p-s}^*(x) \right) dx + \int_{x_1}^{t-\varepsilon_x} \left| -f_{p-s}^*(x) \right| dx \right],$$ (3.26)

where x_0 and x_1 are the intersection points of $f_p(x)$ and $f_c(x)$. Also, $f_{p-s}^*(x)$, the mean line in XY coordinate system can be obtained as shown below.

$$f_{p-s}^*(x) = -\cot\theta \left(x - \frac{\overline{f_{p-s}(x)}}{\cos\theta} \right).$$ (3.27)

<u>Case 2: The milling profile is below reference line 2 ($D < (t - \varepsilon_x)\cos\theta$)</u>

In this case, both additive and milling profiles are involved in forming the intersected profile $f_{p-s}(x)$. Similarly, the mean of the intersected profile can be calculated as

$$\overline{f_{p-s}(x)} = \frac{\sin\theta}{t - \varepsilon_x} \left[\frac{(t - \varepsilon_x)^2}{2\tan\theta} + \frac{(t - \varepsilon_x)(t - 2\varepsilon_y)}{3} - \frac{\left((t - \varepsilon_x)\cos\theta - D \right)^2}{\sin2\theta} \right.$$
$$\left. - \int_{x_0}^{x_1} \left(f_p(x) - f_c(x) \right) dx - \int_{x_1}^{t-\varepsilon_x} f_p(x) dx \right],$$ (3.28)

where x_0 is the intersection point of $f_p(x)$ and $f_c(x)$, and x_1 is the intersection point of $f_c(x)$ with the function $f(x) = 0$ in the XY coordinate system. Finally, using the mean line in XY coordinate system, the surface roughness can be calculated as

$$R_a = \frac{\sin\theta}{t - \varepsilon_x}\left[\int_0^{x_0} \left|f_p(x) - f_{p-s}^*(x)\right| dx + \int_{x_0}^{t-\varepsilon_x} \left(f_c(x) - f_{p-s}^*(x)\right) dx\right]. \tag{3.29}$$

3.2.5 Solution Algorithm

The following algorithm is developed for determining the intersection points which are necessary for calculating the surface roughness when $\theta = 90°$. In general, to calculate the intersection points of two periodic functions $f'(x)$ and $g'(x)$ with the maximum order of 2, the following is enforced:

$$f'(x) = g'(x). \tag{3.30}$$

However, if the periodic functions are represented with Fourier series, calculating the intersection points can become very complex. The following lemmas are thus used to simplify the calculation.

Lemma 2: if $f'(x)$ is a periodic function:

$$f'(x) = f'(x - \delta P_1), \qquad \forall \delta \in \mathbb{Z}$$

where P_1 is the periodicity of function $f'(x)$.

Lemma 3: if $f'(x)$ is a periodic function:

$$f'(x) = f(x - \delta_1 P_1), \qquad \exists \delta_1 \colon x - \delta_1 P_1 \in [0, P_1] \text{ or } \delta_1 = \left\lfloor \frac{x}{P_1} \right\rfloor.$$

where $f(x)$ is the equivalent non-periodic function of $f'(x)$ for one period of P_1 and $\lfloor \rfloor$ is the floor function.

Using the above lemmas, we have:

128

$$f(x - \delta_1 P_1) = g(x - \delta_2 P_2), \quad \forall x \in I \tag{3.31}$$

where P_1 and P_2 are the periodicities of functions $f'(x)$ and $g'(x)$ respectively, δ_1 and δ_2 can be calculated based on lemma 3, and I is the set of all intersection points.

Assuming that the periodicity of the intersected profile exists and is $P^* = LCM(P_1, P_2)$, it is known that:

$$\delta_1 \in \mathbb{Z} \cap \left\{ 0, \dots, \frac{P^*}{P_1} - 1 \right\}, \tag{3.32}$$

$$\delta_2 \in \mathbb{Z} \cap \left\{ 0, \dots, \frac{P^*}{P_2} - 1 \right\}. \tag{3.33}$$

Using all the feasible combinations of (δ_1, δ_2) from the above sets, where equation (94) stands, the intersection points of the two functions can be calculated. However, before that, all the feasible combinations of (δ_1, δ_2) need to be determined. For $\forall x \in I$ we can write:

$$\delta_1 P_1 + \alpha_1 = \delta_2 P_2 + \alpha_2, \tag{3.34}$$

where $0 \leq \alpha_1 < P_1$ and $0 \leq \alpha_2 < P_2$. Therefore, we have:

$$\delta_2 = \frac{\delta_1 P_1 + \alpha_1 - \alpha_2}{P_2}. \tag{3.35}$$

For any given $\delta_1 \in \mathbb{Z} \cap \left\{ 0, \dots, \frac{P^*}{P_1} - 1 \right\}$, we can thus write δ_2 as a function of the unknown value $(\alpha_1 - \alpha_2)$. However, the maximum and minimum values of $(\alpha_1 - \alpha_2)$ is known. Therefore, we have:

$$\delta_2 \in \mathbb{Z} \cap \left[\delta_1 \left(\frac{P_1}{P_2} \right) - 1 \ , \ \delta_1 \left(\frac{P_1}{P_2} \right) + \frac{P_1}{P_2} \right]. \tag{3.36}$$

Assuming that $P_1 < P_2$, we can derive that:

$$\delta_2 = \left\lfloor \left(\frac{P_1}{P_2} \right) (\delta_1 + 1) \right\rfloor. \tag{3.37}$$

Therefore, using the above equations, all the feasible sets of (δ_1, δ_2) can be obtained, which are then used to calculate the intersection points. As we have assumed that the functions are of maximum order of two, we can get a maximum of two roots by solving the $f(x - \delta_1 P_1) = g(x - \delta_2 P_2)$ equation. Assuming that exactly two intersection points exist per each period P_1, the proposed algorithm can be summarized as follows:

Step1. Set $\delta_1 = 0$ and $m = 0$.

Step2. Set $\delta_2 = \left\lfloor \left(\frac{P_1}{P_2} \right) (\delta_1 + 1) \right\rfloor$.

Step3. If the $f(x - \delta_1 P_1) = g(x - \delta_2 P_2)$ has any solution, go to **Step 4**.

Else set $\delta_1 = \delta_1 + 1$, and go to **Step 2**.

Step 4. Set $x_m^1 = x_{min}$ (the smallest root) and set $x_m^2 = x_{max}$ (the largest root).

Step 5. If $\delta_1 < \frac{P^*}{P_1}$, set $\delta_1 = \delta_1 + 1$ and $m = m + 1$, and go to **Step 2**.

Else, go to **Step 6**.

Step 6. End.

The set of all intersection points, I, can thus be written as:

$$I = \{x_0^1, x_0^2, x_1^1, x_1^2, x_2^1, x_2^2, \dots, x_M^1\} \text{ or } I = \{x_m^{1,2}, x_M^1\} \quad m = 0, \dots, (M-1). \qquad (3.38)$$

where $x_M^1 = P^*$. Also, note that the above set I is sequenced in a monotonically increasing order.

3.2.6 Experiment Design

To validate the proposed model, the geometry in Figure 17 is adopted. To perform the case studies, the developed hybrid additive-subtractive process, described in Section 3.1 is used. Polylactide (PLA) material is used for printing the test parts in a 3-axis configuration (i.e., constant build direction). As frequently adopted in the literature, a layer thickness of 0.25 mm is selected. A four-flute end-mill tool with the diameter of 1/8 inch and nose radius of zero is then applied for further processing of the surfaces using a 6-axis configuration (i.e., six degrees of freedom) which helps with reducing the setup time significantly. Several replicated test parts are fabricated, and multiple surface roughness measurements are obtained for each surface using the Bruker-Nano Contour GT-K Optical Profilometer. The layer error coefficient distributions presented in Table X from Chapter 2 are used.

3.2.7 Model Validation

Table XX presents the results of the experiments to evaluate the effectiveness and validity of the proposed surface roughness models. A MATLAB code was developed and implemented for calculating the surface roughness values for the hybrid case based on the proposed mathematical models and the developed algorithm in which the experimental error coefficient values in Table X were considered. The milling profile parameters (including the working minor cutting edge angle (β) and feed (F)) are obtained based on the milling tool geometry and the selected machining parameters including the robot movement speed, and the estimated spindle speed. In addition, the parameter n is a main input parameter for the 90° case.

Table XX. Validation of the proposed surface roughness model

| θ (deg) | Surface roughness results | | | % Ra reduction due to the secondary process | |
	Observed Ra (μm)	Predicted Ra (μm)	Percentage error (%)	Observed (%)	Predicted (%)
20°	24.511	25.562	4.288	54.667	53.543
30°	23.457	22.886	2.432	58.129	56.559
40°	15.340	17.159	11.862	69.715	63.327
50°	12.064	13.549	12.314	69.846	66.375
60°	8.065	7.768	3.683	73.821	76.143
70°	4.870	4.931	1.253	74.189	75.226
90°	11.445	13.889	21.354	33.966	21.805

It is observed that the surface roughness generally tends to get smaller as the stratification angle increases, except for the 90° hybrid case. The average prediction errors for the AM and hybrid cases are found to be less than 5% and 9% respectively. About 21.35% error is observed for the 90° stratification angle in the hybrid case which is higher than the errors obtained for other values of θ as a different model is used. In addition, the computation time and the accuracy of the sawtooth and periodic parabola functions, used in the 90° hybrid model, depend on the value of n. As n gets closer to infinity, the sine and cosine waves will be further dampened so that a more accurate approximation of the profile functions can be obtained. Note that however, there is a difference between the accuracy of the proposed profile functions and the accuracy of the surface roughness prediction. Although ideally expected, a more accurate profile representation is not necessarily associated with a more accurate prediction of surface roughness. Therefore, it is necessary to study the behavior of the model and the computation time to determine the optimum value of n. Therefore, the prediction accuracy was evaluated based on different values of n (2, 5, 50, and 100). Finally, $n = 2$ was selected as the best prediction accuracy was obtained. In addition

to optimizing the model parameters, increasing the number of samples and measurements is expected to further reduce the obtained errors.

In Figure 55, the performance of the surface roughness model is presented for different stratification angles. For better understanding, the performance of the model for the hybrid case is illustrated together with the performance of the model for additive case (Figure 20 in Chapter 2). Confidence intervals are generated for the predicted roughness values based on the distribution of the error coefficients in Table X. According to the figure, the confidence intervals are generally larger for smaller stratification angles. It should be noted that the confidence intervals for 70° and 90° are too narrow to be visible in the figure. The confidence intervals for 70° and 90° angle are [4.484, 5.379] and [13.770, 14.007], respectively.
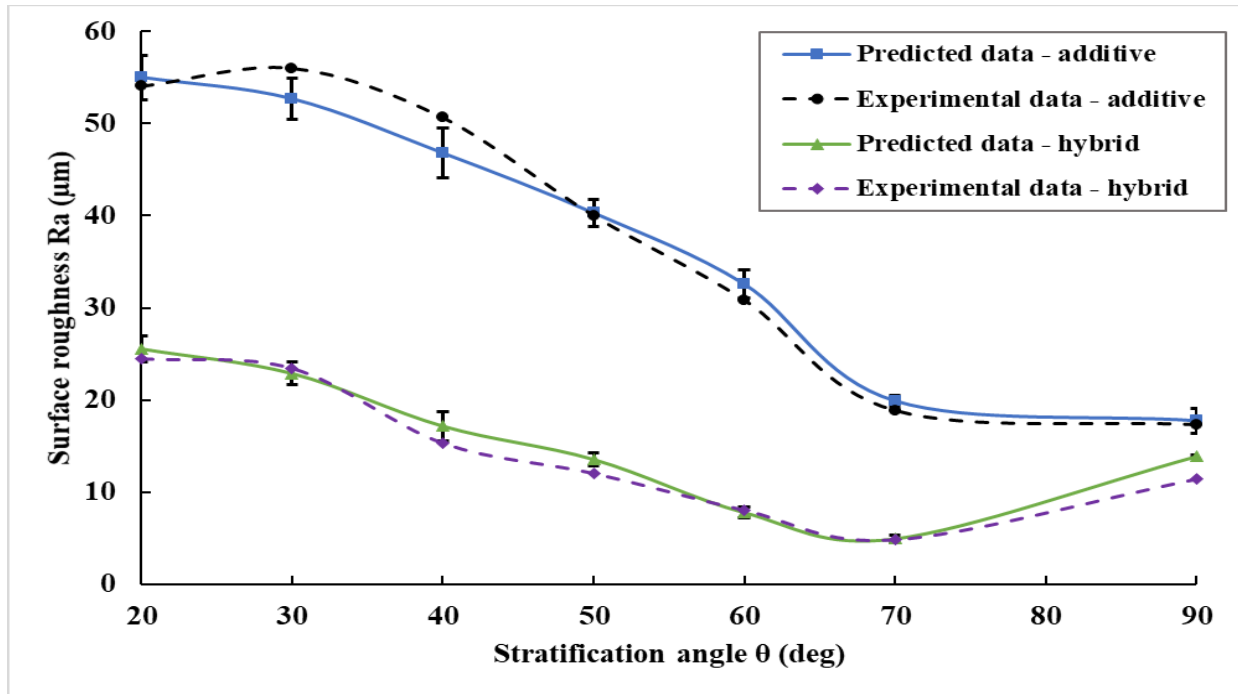
Figure 55. Comparison of predicted and experimental surface roughness values for both additive and hybrid cases

3.2.8 Conclusions

In this section, mathematical models for surface roughness of hybrid additive-subtractive manufactured surfaces are established. Layer thickness, stratification angle, layer's error coefficients, and cutting tool's parameters are incorporated into the developed models. Experiments are performed to validate the developed models. An average of 91.83% accuracy is obtained which is significant specifically considering that no other similar models exist in the literature. Extending the current model to the $\theta = 0°$ or $180°$ scenario, considering other subtractive processes or profile models, and incorporating other parameters into the model are among the possible future works.

3.3 Concluding Remarks

In this chapter, efforts to address the process-level quality assurance problems in hybrid additive-subtractive manufacturing are presented using both empirical and analytical approaches. First, a hybrid additive-subtractive manufacturing platform is developed and described. The developed platform uses a robot arm with 6 degrees of freedom which provides additional manufacturing capabilities compared to the 3-5 axis commercial hybrid additive-subtractive platforms. The development process, including the designed software, control, and hardware are presented and explained. The capabilities of the developed platform are illustrated through several case studies.

Second, as the process planning decisions have experimentally shown to affect the energy consumption in the developed hybrid platform [200], an approach for optimum sequencing of the additive and subtractive manufacturing features during the process planning of the hybrid process was developed. The proposed approach aims to minimize the energy consumption of the hybrid platform using a greedy algorithm and based on the characterized energy consumption elements,

by proposing the best sequence among features. The proposed model uses the Signal Analyzer module in ABB RobotStudio Software to derive the robot arm energy consumption during movement or at different configurations. Note that mathematical approaches to study the robot arm energy consumption exist in the literature [200], [201], and can be used to be further integrated into the proposed feature sequencing approach.

Finally, analytical models for prediction of surface roughness of additive manufactured surfaces which are further processed by the subtractive process (in our model, milling process) are proposed. The proposed models are based on the proposed AM surface profile representation scheme in Section 2.2.1. The sawtooth function is adopted to represent the SM surface profile. Both additive and milling parameters, namely layer thickness, layer error coefficients, stratification angle, working minor cutting edge angle of the milling tool, feed, and cutting depth are considered. Several experiments are performed to validate the proposed models. According to the experiment results, the accuracy of the proposed models was found to be 91.83% in average. The proposed models provide guidelines for designers in the tolerance design stage for assigning feasible and optimal tolerances.

4. PRODUCT-LEVEL QUALITY ASSURANCE: INVESTIGATING THE BETWEEN-COMPONENT INTERACTION FOR ADDITIVE MANUFACTURING

This chapter presents the different studies performed to understand and address product-level quality assurance challenges considering multi-component additively manufactured products. In Section 4.1, the clearance of assemblies using the PolyJet AM process is empirically studied as a function of different assembly design and manufacturing decision parameters [202]. In Section 4.2, a methodology for integrated optimum tolerance design and parameter tuning in the additive manufacturing process is proposed and illustrated [203]. The main idea is to take advantage of the frequent systematic shifts in AM during the manufacturing process by tuning the process parameters of each individual component in such a way that the errors cancel each other out. Therefore, the need for AM error compensation, which is generally complex and requires a lot of

effort, can be eliminated, or minimized. Finally, the conclusions and futures work of this chapter are summarized in Section 4.3.

4.1 Dimensional Distribution of As-Built Assemblies in PolyJet Additive Manufacturing Process

4.1.1 PolyJet Additive Manufacturing Process Introduction

One of the most promising AM processes for printing as-built assemblies is the PolyJet technology (Figure 56) because of its high precision and accuracy. PolyJet is a 3D printing process similar to the Inkjet process which jets thin layers of curable liquid photopolymer resins onto the building tray and cures them using UV energy [3].

In this process, the head moves in the X and Y directions while jetting out arrays of photopolymers in shapes of droplets which are then cured by the ultraviolet lamps after each layer is finished. PolyJet technology has shown to have a very good dimensional performance compared to other AM processes [204], [205].
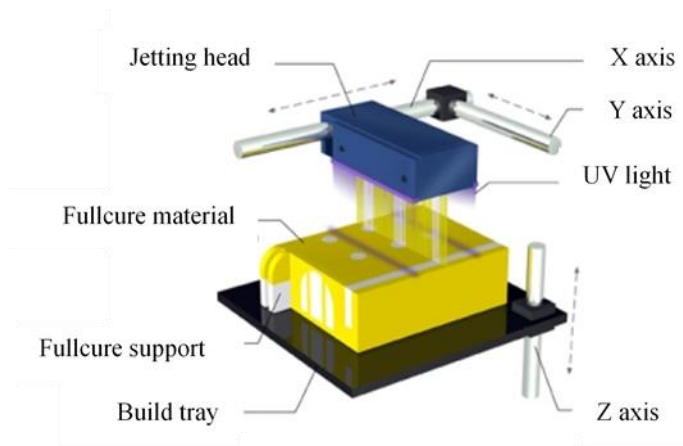

Figure 56. Schematic view of PolyJet technology (adopted from

http://www.3daddfab.com/technology/)

A two-component prismatic assembly structure (shown in Figure 57) is used for the experiments which consists of a prismatic base component (shaft) and a top component with an inner prismatic hole.

The reason for selecting a prismatic design for components instead of the more common cylindrical shaft and hole design is to reduce the contribution of tessellation error. Tessellation is referred to as rendering a 3D object and using triangle meshes to represent its surface. However, representing a curved surface using triangles will always introduce some dimensional errors which can be minimized by reducing the size of triangles. Two marks on both of the components are designed which are solely used as a guide in order to assemble the parts in a uniform direction. This way, we can make sure that the measurements at different height levels of components are comparable. The assembly has a rectangular shape and thus, requires two different clearance values to be assigned for each of the width (clearance W) and length (clearance L) directions (Figure 58).

Currently, a trial and error approach (through experiments and simulation) is usually applied for finding the optimal design clearance, dimensions, and support structure when as-built assemblies are printed [104], [110]. The clearance of 0.2 mm is selected for the assembly according to the empirical data [206] to ensure that components do not fuse together during the printing process. In other words, if the clearance value is small enough, distinguishing and separation of different assembly components would not be possible. Additional experiments are also performed to verify the suitability of the selected clearance values.
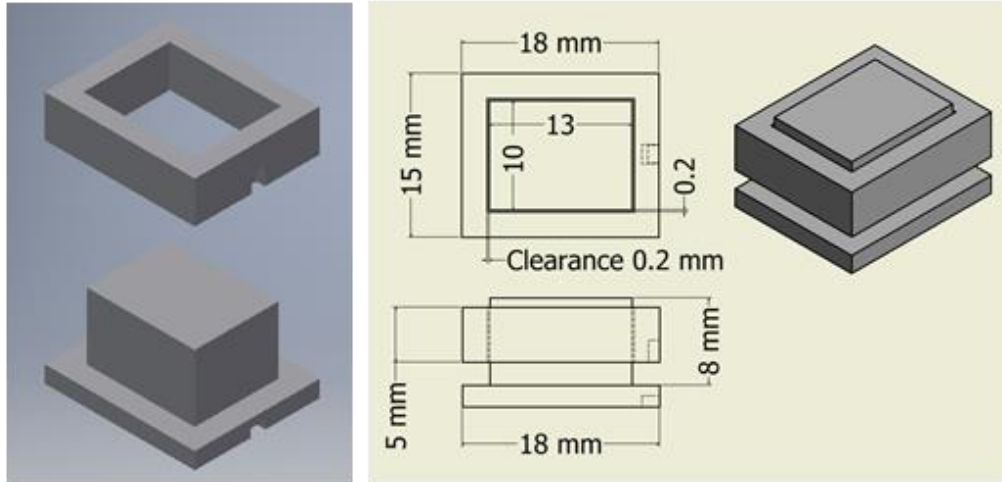
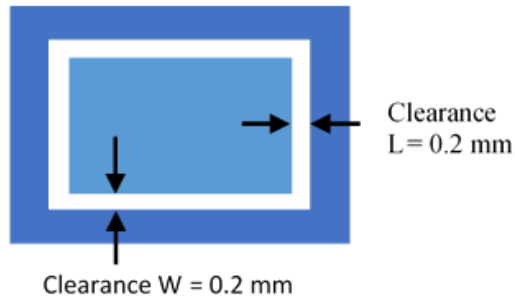Figure 57. Dimensions of the two-component assembly

Figure 58. Width (W) and length (L) clearances

The DOE approach is used for analyzing the effects of two different decision factors (assembly type and orientation) on the two clearance values (clearance W and clearance L) of the assembly. Assembly type is a categorical parameter that refers to the alternative design/manufacturing option. Two possible types of assembly are considered: (1) as-built assembly (i.e., printing the assembly as a whole with overlapped geometries) and (2) individual assembly (i.e., printing the components individually with no overlapped geometries). The second studied factor is the orientation of components. Two different orientations of vertical and horizontal are considered. The vertical and horizontal orientations are presented in Figure 59, where Z-axis shows the build direction. Therefore, a 2^2 full factorial design is applied to study the effects of decision parameters on the

139

clearance values. Finally, the best setting for obtaining more accurate assemblies is identified by

using the desirability function. Two replicas are built for each experiment scenario. Therefore, a

total of 8 assemblies are printed. The control factors of the study are shown in Table XXI. Table

XXII presents the parameters that are kept constant during all experiments.

Table XXI. Control factors

Factors	Symbol	Levels	
		-1	1
Assembly type	A	Individual	As-built
Orientation	B	Vertical	Horizontal

Table XXII. Constant parameters

Material	VeroClear-RGD810
Layer thickness	28 µm
Fill density	100%
Print mode	High Speed (HS)

The Objet30 Prime 3D desktop printer from Stratasys based on PolyJet technology is used for

fabricating the parts. The Objet30 Prime machine, is capable of achieving a layer thickness of 28

µm for Tango materials and 16 µm for other materials, and has a resolution of 6000 dpi on X-axis,

6000 dpi on Y-axis, and 1600 dpi on Z-axis [207]. The VeroClear-RGD810 translucent material

is used for fabricating the parts which has been proved to have a good dimensional stability and

surface smoothness. The objet30 prime machine uses a gel-like nontoxic support material which

can be easily removed with a waterjet after the part is printed [207]. As a result of this capability

and the high resolution of the machine, small clearances in as-built assemblies can be easily

realized. A digital caliper with an accuracy of 0.01 mm is used for measuring the dimensions of components and the obtained clearance.
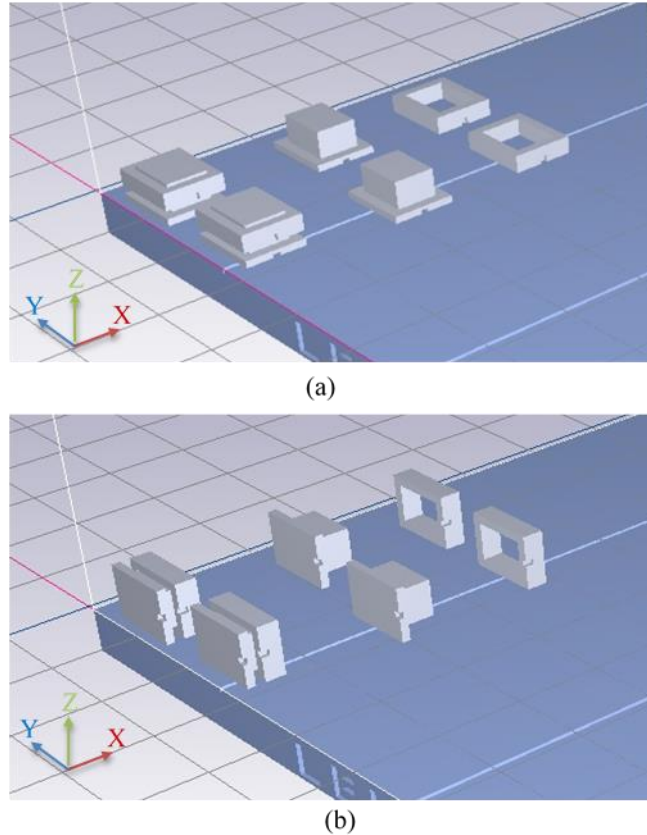

(a)

(b)

Figure 59. (a) Vertical and (b) Horizontal orientations

4.1.3 Factorial Analysis Results

The fabricated components before and after the support removal are presented in Figure 60 and Figure 61. The support material has been removed using a waterjet to ensure the dimensional values remain intact. The remaining support structure is further cleaned before the measuring process. To measure the obtained clearance along the length of assembly (clearance L) in each scenario, the lengths of the shaft and hole were measured at two different height positions (top and bottom) due to the inconsistency of the dimensional profile along the height of components. The measurements were repeated 10 times. The average of the repeated measurements for the top and

bottom positions of each component were used to calculate the estimated length of components. The final clearance values were calculated by finding the difference between the base component's length and the length of the hole. A similar approach is applied for calculating the clearance value along the width of assembly (clearance W). The results of the measurements for each scenario are presented in Table XXIII. All obtained clearances are smaller (within a range of 19%-92%) than the initial 0.2 mm designed clearance due to the shrinkage/expansion of components.
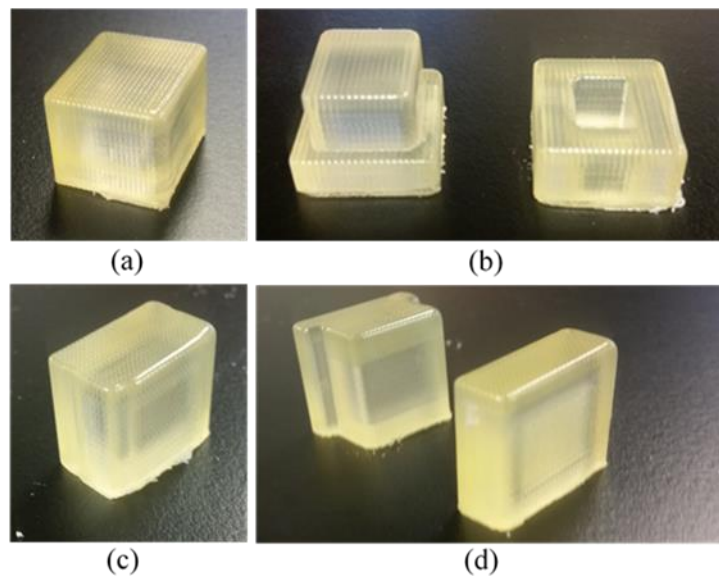
Figure 60. Support Structure; (a) As-built, vertical, (b) Individual, vertical, (c) As-built, horizontal, and (d) Individual, horizontal

Figure 61. Fabricated components

It is observed that in all horizontal orientations, clearances are larger than the corresponding vertical orientations. In addition, clearance L is larger in the individual scenario compared to the

as-built assembly scenario. This observation, however, does not apply to clearance W; in the horizontal orientation, the as-built scenario is slightly better than the individual scenario. Also, note that clearance L is aligned toward the Y-axis of the machine in the vertical orientation. As the orientation is changed to horizontal, the alignment of clearance L does not change. However, the alignment of clearance W in the machine coordinate system changes as the orientation is changed. Initially, at the vertical orientation, clearance W is aligned toward the X-axis of the machine. By changing the orientation to horizontal, the alignment of clearance W will be changed toward the Z-axis (build direction). These different alignments can also contribute to the observed different errors of vertical/horizontal settings and also between clearance L and clearance W.

Table XXIII. Obtained clearance values

#	Assembly type	Orientation	Clearance L (mm)	Clearance W (mm)	Nominal (L, W)
1	As-built	Vertical	0.02275	0.02325	0.2
2	As-built	Vertical	0.02275	0.01525	0.2
3	As-built	Horizontal	0.08685	0.16025	0.2
4	As-built	Horizontal	0.10325	0.15	0.2
5	Individual	Vertical	0.08175	0.04125	0.2
6	Individual	Vertical	0.0655	0.0555	0.2
7	Individual	Horizontal	0.15775	0.1475	0.2
8	Individual	Horizontal	0.1665	0.146	0.2

The analysis of variance for both clearance W and L are presented in Table XXIV. It is observed that with a 95% confidence interval, the effect of assembly type on the clearance W is not statistically significant (p-value of 0.09). However, the p-values of both orientation factor and the interaction between orientation and assembly type are less than the significance level of 0.05. Therefore, they both have a significant relationship with the final value of clearance W. In contrast

to the findings for clearance W, the assembly type has shown to have a statistically significant relationship with clearance L using a 95% confidence interval (p-value of 0.001). In addition, orientation has also shown to play a significant role in the final value of clearance L. However, the interaction between orientation and assembly type does not show a statistically significant relationship with clearance L (with a p-value of 0.26). The main effect plots for both clearance L and clearance W (shown in Figure 62 and Figure 63) again highlight that orientation plays a significant role in the final clearance of components. As mentioned earlier, the final clearance is always larger in the horizontal orientation compared to the vertical orientation. In addition, using as-built assemblies can significantly reduce the clearance L compared to the individual scenario. However, a significant reduction of clearance W is not observed when changing the assembly type from individual to as-built.

Considering that all clearances have shrunk compared to the initial design clearance, the best setting is the setting in which the obtained clearance values are larger (closer to the design clearance). Considering clearance L, the best setting would be the "Individual, Horizontal" setting as selecting these two levels will increase the final clearance. The horizontal orientation also will generate larger clearances for clearance W. However, according to Table XXIII, the as-built assembly type will lead to a better clearance compared to the individual assembly type for clearance W. Since both clearance L and clearance W need to be kept close to their target value of 0.2 mm, and assuming they have similar importance and weight factors, a desirability function can be used to select the best experiment setting while optimizing both clearances. The "Individual, Horizontal" setting shows to have the highest desirability of 0.745 and thus, is selected as the optimum setting in terms of dimensional accuracy.

Table XXIV. Analysis of variance for clearance L and W

ANOVA for Clearance L (α = 0.05)				
Source	Degree of freedom	Sum of squares (SS)	Mean sum of squares (MS)	P-value
A	1	0.006956	0.006956	0.001
B	1	0.012928	0.012928	0.000
A*B	1	0.000131	0.000131	0.260
Error	4	0.000305	0.000076	-
Total	7	0.020320	-	-

ANOVA for Clearance W (α = 0.05)				
Source	Degree of freedom	Sum of squares (SS)	Mean sum of squares (MS)	P-value
A	1	0.000215	0.000215	0.099
B	1	0.027437	0.027437	0.000
A*B	1	0.000703	0.000703	0.018
Error	4	0.000187	0.000047	-
Total	7	0.028542	-	-
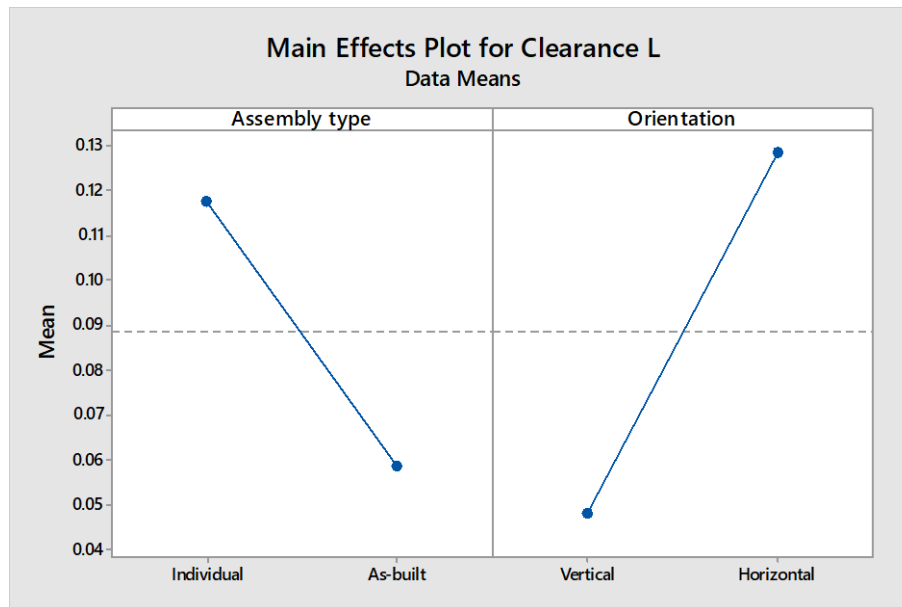
Figure 62. Main effect plot of clearance L

145
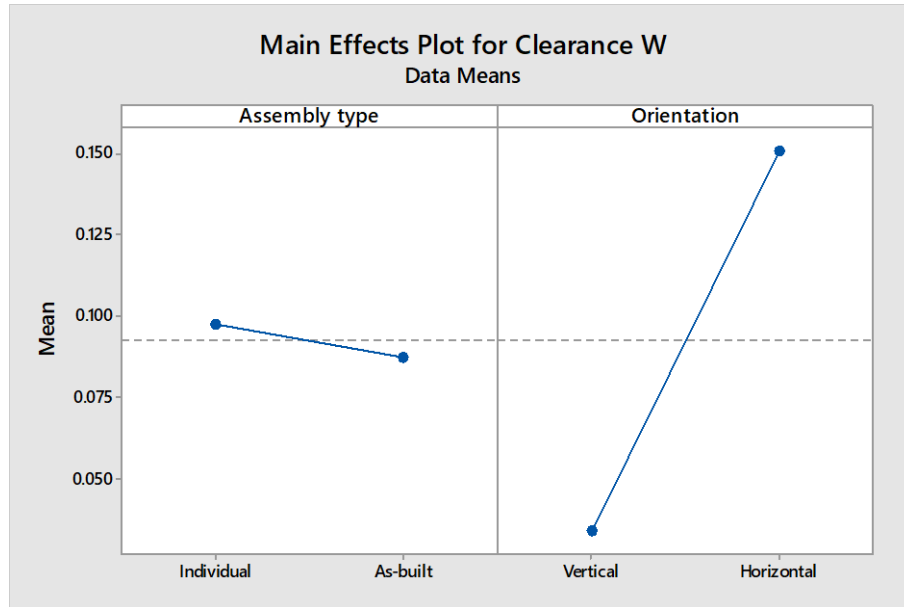
Figure 63. Main effect plot of clearance W

4.1.4 Dimensional Profiles and Distributions

Another interesting observation from the experiments is the difference of dimensional profile of assembly components in different experimental settings. Table XXV shows the measured dimensions at the top and bottom positions of each component for different experiment settings: (1) vertical, as-built, (2) vertical, individual, (3) horizontal, as-built, and (4) horizontal, individual. The bottom position is the position on the profile of component that is the closest to the embedded mark in the design. In the vertical orientation, the bottom position is closest to the building platform and the top position is the closest to the printing head. It is observed that in all individual scenarios, the base component (shaft) has a higher expansion rate at the bottom position compared to the top position. In other words, the deviation on the bottom position is higher compared to the top position. Similar behavior is observed for the top and bottom dimensions of the hole component along the width dimension in the individual scenarios. However, the difference of dimensions is not as significant as in the shaft component. In addition, it is observed that the dimensional changes of top and bottom positions in the as-built scenario are more uniform compared to the individual

146

scenario. To better visualize this different behavior, the dimensional profile of as-built and ordinary assemblies in the vertical orientation and along the length of components is shown in Figure 64.

Table XXV. Dimensional profile of components

Component	Direction/Position	1	2	3	4
1-Shaft	Length/Top	13.237	13.074	13.170	13.006
1-Shaft	Length/Bottom	13.217	13.240	13.152	13.119
2-Hole	Length/Top	13.281	13.303	13.355	13.356
2-Hole	Length/Bottom	13.265	13.306	13.347	13.418
1-Shaft	Width/Top	10.324	10.199	10.034	10.013
1-Shaft	Width/Bottom	10.312	10.437	10.086	10.095
2-Hole	Width/Top	10.364	10.399	10.365	10.338
2-Hole	Width/Bottom	10.349	10.431	10.375	10.357

Table XXVI shows the mean, standard deviation, and range of measured dimensions at the top and bottom positions. It is observed that (i) the shaft dimensions are oversized while the hole dimensions tend to be undersized, and (ii) the standard deviations of the measured dimensions at the top and bottom positions of as-built assemblies (mainly for the shaft component) are smaller compared to the corresponding individual assemblies.

Different reasons could contribute to this uniform behavior of dimensional change for as-built assemblies. One of the possible explanations for this different behavior could be the different geometrical interaction in as-built assemblies compared to the individual scenario. These geometrical interactions could refer to both interactions between the assembly components, and between the components and the support structure. The different interaction can also affect the freedom of expansion/shrinkage of material and thus, lead to different dimensional behavior. In other words, due to the connection of components to each other and to the added support structures,

the capability of the layers to expand/shrink freely could become limited compared to the individual scenario. The support structure/material properties can also affect this different behavior and need to be studied.

The different support structures in our experiments are presented in Figure 60. As can be seen, there exists a difference between support structure in as-built and individual cases which could have contributed to the observed dimensional difference. In addition to the support structure and different geometrical interactions, the curing process of droplets needs to be studied to see if UV light can contribute to this different behavior. Therefore, the different behavior in as-built assemblies and individual assemblies and the contributing factors need to be further studied and modeled for better prediction of the final assembly clearances.
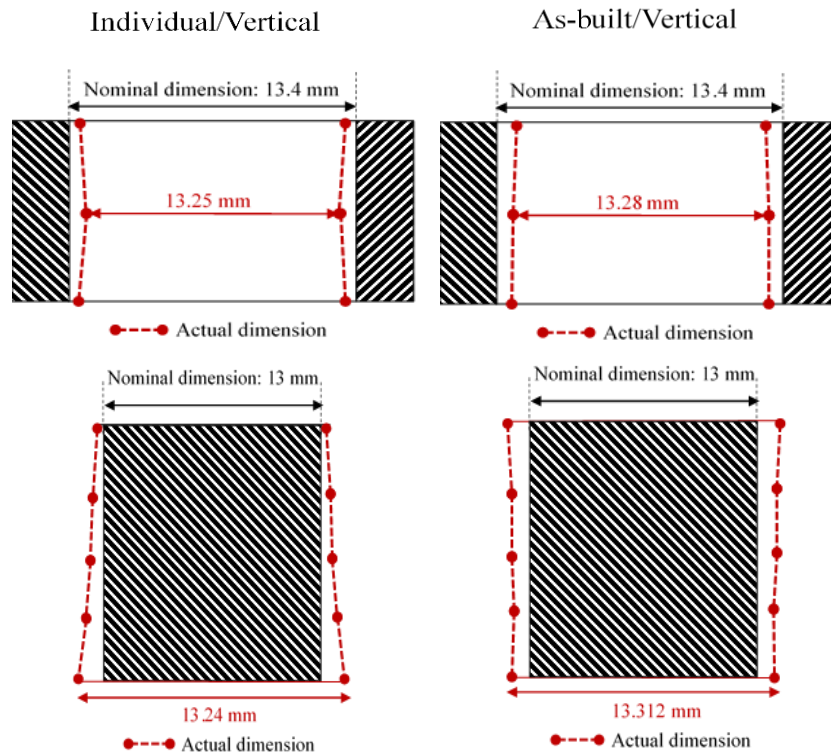
Figure 64. Dimensional profile of assemblies in the vertical orientation and along the length

Table XXVI. Dimensional distribution of components

| Component | Direction | Vertical | | | | | | Nominal |
| | | As-built | | | Individual | | | |
		μ	σ	Range	μ	σ	Range	
1- Shaft	Length	13.2270	0.0141	0.02	13.1568	0.1170	0.1655	13
2-Hole	Length	13.2725	0.0113	0.016	13.3040	0.0021	0.003	13.4
1-Shaft	Width	10.3178	0.0088	0.012	10.3178	0.1679	0.2375	10
2-Hole	Width	10.3563	0.0103	0.014	10.4145	0.0226	0.032	10.4

| Component | Direction | Horizontal | | | | | | Nominal |
| | | As-built | | | Individual | | | |
		μ	σ	Range	μ	σ	Range	
1- Shaft	Length	13.1607	0.0125	0.018	13.0625	0.0799	0.113	13
2-Hole	Length	13.3508	0.0060	0.009	13.3868	0.0442	0.0625	13.4
1-Shaft	Width	10.0598	0.0364	0.052	10.0540	0.0580	0.082	10
2-Hole	Width	10.3700	0.0071	0.01	10.3475	0.0134	0.019	10.4

4.1.5 Conclusions

In this section, the dimensional performance of as-built assembly structures compared to ordinary assemblies (in which parts are printed individually and assembled together) in the PolyJet AM process is studied. The DOE has been used to study the effect of the assembly type and orientation in the final clearance of assemblies. A full factorial design with a total of 8 experiments are conducted where two clearance values (along the width and length of components) are analyzed as the experiment responses. In addition, the dimensional profiles of components are studied in different scenarios. The "Individual, Horizontal" setting has been found to be the optimum experiment setting in terms of dimensional accuracy. The main finding of this study is that the assembly design strategy (fabricating components in an overlapped/integrated scenario versus non-overlapped scenario) significantly impacts the dimensional profile of components and assembly clearance, and thus, should be considered for the purpose of tolerance design. The rest of the experimental findings are summarized below:

- The dimensions of the shaft (either along the width or length) are generally oversized while the hole dimensions are generally undersized using the PolyJet process.

- All obtained clearance values are reduced within a range of 19% to 92% compared to the original design clearance.

- Orientation has shown to have a significant effect on the final clearance of assemblies. In our experiments, all horizontal orientations led to a larger clearance (closer to the design clearance).

- The assembly type has a significant contribution to clearance L in contrast to clearance W. The interaction of assembly type and orientation factors also contributes to the clearance W.

- The decision on how to print assemblies (as-built vs. ordinary) is critical as it can affect the clearance values even if all of the process parameters are kept constant. Therefore, if the assembly is designed in a way that we have a freedom to alter between as-built and ordinary assemblies (e.g., it is possible to remove the support between moving components), assembly type has to be also considered as an important factor beside process parameters when optimizing the dimensional accuracy of components.

- The obtained clearance in different directions and alignments is also different when using similar printing parameters. In our case, clearance L and W show different behaviors which could be as a result of their different alignments in the machine coordinate system.

- The dimensional deviation of assembly components (mainly shaft) is more uniform along their profile in as-built assemblies compared to the individual scenario.

- The measured dimension at the bottom position of shaft is always larger than the top position in the individual assembly scenario. This applies to both width and length measurements.

- As a result of the above, it can be concluded that a different dimensional behavior exists in as-built assemblies (overlapped or integrated geometries) compared to ordinary assemblies (non-

overlapped geometries). This different behavior can probably be caused by the different geometrical interactions and different movement limitations (either among components or among components and support structure).

The different dimensional behavior of as-built assemblies and ordinary assemblies is one of the main findings. The implications of this different behavior are that the current dimensional accuracy improvement techniques, error compensation values, and optimal process parameters for individual AM components might not necessarily be applicable/optimal for the as-built assembly structures and need to be further studied as a future work. However, note that the findings of this paper are only specific to the PolyJet process. Therefore, similar studies have to be performed for other additive manufacturing processes, different material and geometries to indicate if similar behavior is observed or not.

4.2 Joint Tolerance Design and Parameter Tuning in Additive Manufacturing Processes

In this section, a methodology for optimum tolerance design and parameter tuning in additive manufacturing process is proposed and illustrated. The main idea is to take advantage of the frequent systematic shifts in AM during the manufacturing process by tuning the process parameters of each individual component in such a way that the errors cancel each other out. Therefore, the need for AM error compensation, which is generally complex and requires a lot of effort, can be eliminated or minimized. In other words, error compensation will adjust the process mean to the nominal mean, thus increasing the accuracy of parts. However, for the aim of tolerance design, it is not necessary for all the components to have high accuracy, as long as the assembly specifications are met. By considering the manufacturing decisions at the tolerance design stage, an optimal tolerance design can be proposed. More specifically, build direction is one of the most important parameters which should be considered during the tolerance design stage as it

151

significantly affects the distribution of dimensions. As a result, the design and manufacturing stages become hugely interrelated.

Moreover, the normal distribution which is generally considered in the traditional tolerance design problems, might not be suitable for AM process due to its different application domain, i.e., mass customization. In other words, due to the generally slower production speed of AM processes compared to traditional processes, as well as the small number of unique components, it is generally not required nor cost-effective to print large enough number of parts to justify the adoption of normal distribution assumption or derive the moments of the distribution. Therefore, the assumption of normal distribution might lead to calculation inaccuracies if the distributions are in fact not normal. Some researchers have highlighted the non-normal and generally skewed behavior of observed dimensions specifying that the application of standard deviation can be inappropriate in AM processes [68]. Therefore, in this section, the above issue is addressed by adopting the bootstrap technique to generate the distribution parameters.

4.2.1 Preliminaries and Problem Description

Consider a one-dimensional (1-D) assembly chain consisting of N individual components, each with a fixed nominal size of D_n $(n = 1, ... N)$ defined by the designer. The assembly specification is defined as: $D_A \pm T_A$, where D_A is the nominal size of the assembly and T_A denotes the assembly tolerance (defined symmetrically around D_A). In addition, it is required that the assemblies lie within the provided specification with a confidence level P_A. It is assumed that the components are fabricated with different AM processes or materials due to the design requirements. Therefore, no two components of the assembly can be built together in a single setup. To fabricate the components, a set of process parameters should be selected from the J feasible or preferred

152

combinations of process parameters. The feasible candidate sets of the process parameters are assumed to be given based on manufacturer's experience as well as the process/machine constraints, and generally are assumed to include statistically significant parameters like layer thickness and build direction [63], [74], [75].

Let C_{nj} be the cost of manufacturing component n using the jth set of process parameters. Therefore, the $N \times J$ cost matrix, $\boldsymbol{C} = \{C_{nj}\}$ can be defined. Note that the cost can be evaluated from many AM cost formulations available in the literature (e.g., see [208]–[210] and the references therein). Let $f(D_n, \boldsymbol{pr_j})$ denote the pdf of dimensions given the nominal dimension D_n and using the jth set of process parameters. In most cases, the above pdf of data is unknown. One technique would be to use the central limit theorem and assume normality of data. However, this approach requires large number of samples for each individual component to be obtained which is not very practical considering the generally longer production time of AM technology compared to the traditional manufacturing processes, and the assumption of independent setups made earlier. Finally, a confidence interval $I_{nj}^{p_n} = \left[\alpha_{nj}^{p_n}, \beta_{nj}^{p_n}\right]$ for the area in which the data are more likely to lie can be constructed for a given nominal dimension D_n, process parameter set $\boldsymbol{pr_j}$, and confidence level p_n using the Bootstrap statistical technique described in Section 4.2.2.

Given the above information, the goal is to assign the optimum set of process parameters and components' tolerances (maximum confidence level vector $\boldsymbol{p}$) so that the total manufacturing cost is minimized, while the assembly tolerance requirements (both specification and confidence level) are satisfied. Since the optimum confidence level vector defines the area in which the component's dimensions should lie to satisfy the assembly tolerance requirements, it can be further translated

as the optimum tolerance range for individual components. In the next subsection, the Bootstrap statistical technique and the approach for constructing the confidence intervals are presented.

4.2.2 Construction of Confidence Intervals

Bootstrapping (a special case of Monte-Carlo simulation) is the key technique used for constructing the confidence intervals in this paper. The term Bootstrap was coined and popularized by Efron [211]. The key idea of nonparametric Bootstrap method is to use the available sample data as a "surrogate population" for estimating the sampling distribution of a statistic [212]. The bootstrap samples are generated through resampling with replacement from the original sample data. Finally, the distribution of different population statistics is computed from the bootstrap samples based on the law of large numbers.

Consider $(x_1, \dots, x_m)$ are m sample points drawn from an unknown probability distribution F. A bootstrap sample is a resample of the above data point (usually) with the same size of m. Suppose θ is the population parameter of interest to be studied and $\hat{\theta}$ is the sample statistic obtained from the data points $x_1, \dots, x_m$. Bootstrap technique allows us to approximate the distribution of $\hat{\theta} - \theta$ using the bootstrap distribution of $\hat{\theta}_b - \hat{\theta}$, where $\hat{\theta}_b$ is the statistic computed from the resamples (R), as R becomes large. Although the underlying logic is easy to grasp, the execution of this technique is less straightforward. The implementation of this method is relatively inexpensive as it can operate with a limited number of samples, but relies heavily on the modern computational power.

One of the main applications of Bootstrap technique is constructing confidence intervals for different statistics [213]. The "first-order" interval formed from the quantiles of the bootstrap distribution has a major limitation as it does not adjust for the skewness of data. The bias corrected

154

and accelerated (BCa) percentile method (also referred to as the "second-order" accurate bootstrap method) was thus proposed to address this issue [214]. Accordingly, the skewed behavior of data and long production time in AM make the Bootstrap technique a suitable statistical approach for evaluating the distribution of components' dimensions.

Let vector $\boldsymbol{p} = (p_1, p_2, \ldots, p_n, \ldots, p_N)$ represent the set of selected confidence levels for components. To construct the confidence interval for each component given the value of p_n (i.e., generate a point estimate of lower and upper percentiles; $\alpha_{nj}^{p_n}$ and $\beta_{nj}^{p_n}$), the following approach is applied. Two confidence intervals around the $(1 - p_n)/2$ th percentile and $(1 + p_n)/2$ th percentile of the data is initially established using the "second-order" Bootstrap statistical technique with sample number R. These confidence intervals can be referred to as: $[l_{\frac{1-p_n}{2}j}, u_{\frac{1-p_n}{2}j}]$ and $[l_{\frac{1+p_n}{2}j}, u_{\frac{1+p_n}{2}j}]$. Both confidence intervals are re-constructed based on T different simulation instances for a specific set of dimensions (D_n), confidence level (p_n), and process parameter set (j).

By re-simulating the confidence intervals, the effect of nonlinear error can be addressed for generating the point estimates of percentiles, and thus can increase the accuracy of point estimates. As a result, $2T$ values representing the confidence interval points for each percentile is obtained. The point estimate for each of the lower and higher percentiles, is thus calculated as the weighted arithmetic mean of the $2T$ data points as follows.

$$\hat{\alpha}_{nj}^{p_n, T} = (2T)^{-1} \left(\sum_{q=1}^{Q} \omega_q y_q \right), \tag{4.1}$$

$$\hat{\beta}_{nj}^{p_n,T} = (2T)^{-1}\left(\sum_{q'=1}^{Q'} \omega'_{q'}\, y'_{q'}\right),\qquad (4.2)$$

where $\hat{\alpha}_{nj}^{p_n,T}$ and $\hat{\beta}_{nj}^{p_n,T}$ are the point estimates of lower and higher percentile for the given T simulation instances of the confidence interval respectively. In addition, Q and Q' represent the total number of sets with unique values y_q and $y'_{q'}$ from the observed $2T$ data points. Furthermore, ω_q and $\omega'_{q'}$ denote the assigned weight which are equal to the number of data points in each set. Observe that we have:

$$\sum_{q=1}^{Q} \omega_q = \sum_{q'=1}^{Q'} \omega'_{q'} = 2T,\qquad \forall T. \qquad (4.3)$$

The flowchart of the described method for generating point estimates of the percentiles is illustrated in Figure 65.

Remark: Note that implementing the bootstrap technique to construct confidence intervals for the extreme points of the pdf can be a little problematic especially if the true extreme points of the pdf are not within the sampled data. In other words, in such a case, the extreme points can never be generated by merely resampling the existing data.

As a result, the bootstrap intervals might not be close to the correct asymptotic values. Consequently, the application of this method for extreme points should be performed with caution. In such cases, one suggested remedy is to use a small fraction of the initial sample size as the size of the bootstrap samples.
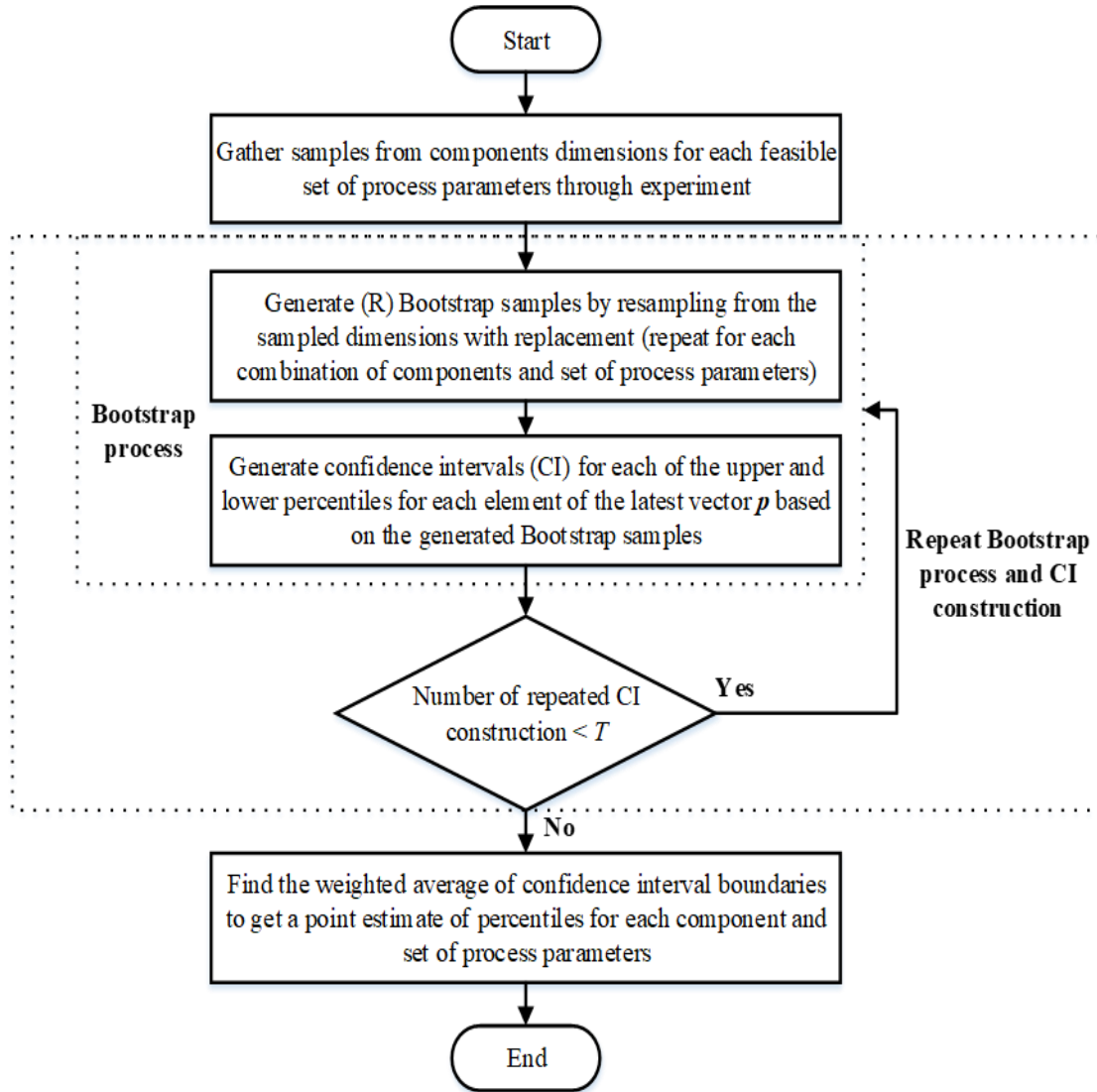
Figure 65. Percentile point estimation based on Bootstrap statistical process

4.2.3 Dimensional Tolerance Definition

Once the optimal values of p_n's are known, the component's tolerances can be defined. Depending on the position of the percentile point estimates with respect to the nominal value, the dimensional tolerances can be defined in three different ways as follows:

$$
\begin{cases}
Case\ 1: D_n \dfrac{+\left(\hat{\beta}_{nk}^{p_n,T} - D_n\right)}{+\left(\hat{\alpha}_{nk}^{p_n,T} - D_n\right)}, & D_n < \hat{\beta}_{nk}^{p_n,T}, D_n \leq \hat{\alpha}_{nk}^{p_n,T} \\[3mm]
Case\ 2: D_n \dfrac{+\left(\hat{\beta}_{nk}^{p_n,T} - D_n\right)}{-\left(D_n - \hat{\alpha}_{nk}^{p_n,T}\right)}, & D_n < \hat{\beta}_{nk}^{p_n,T}, \hat{\alpha}_{nk}^{p_n,T} < D_n \\[3mm]
Case\ 3: D_n \dfrac{-\left(D_n - \hat{\beta}_{nk}^{p_n,T}\right)}{-\left(D_n - \hat{\alpha}_{nk}^{p_n,T}\right)}, & \hat{\beta}_{nk}^{p_n,T} \leq D_n, \hat{\alpha}_{nk}^{p_n,T} < D_n
\end{cases}
\tag{4.4}
$$

where k represents the optimum selected process parameter set for component n based on the optimization model in Section 4.2.5 and the proposed solution approach in Section 4.2.7. These three cases are further illustrated in Figure 66.
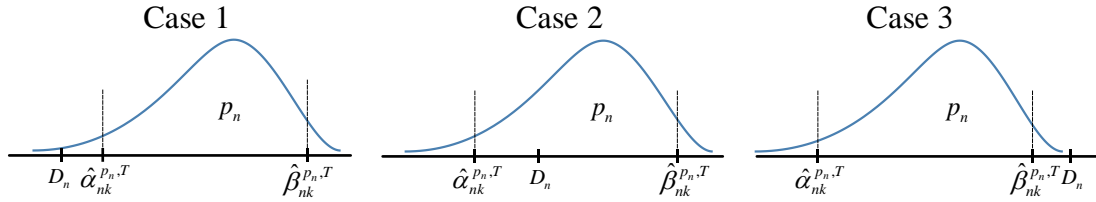
Figure 66. Illustration of different forms of asymmetric tolerances

Due to the skewed behavior of dimensions, the dimensional tolerances are not necessarily symmetric around the nominal. The main reason for using the asymmetric tolerance format is to reduce the number of nonconforming products and increase the efficiency of the tolerance band given the assumption of fixed nominal value. In other words, by adopting a symmetric form, some portions of the tolerance band will never be visited by the dimension's pdf and can be considered as wasted bounds. In this work, it is assumed that given the known D_n's and set of p_n's, there exists at least one set of process parameters with which the assembly tolerance specification is satisfied with the given confidence level P_A. Therefore, at least one feasible solution exists with the given nominal values and no error compensation would be necessary. However, if no feasible solution is found, one should either consider additional sets of process parameters or perform an

additional analysis on the D_n's where the nominal dimensions are adjusted/altered so that a feasible search space is generated. This second analysis can be referred to as "dimension allocation" which compensates systematic errors of some or all of the components by alternating the nominal values and needs to be performed together with the tolerance allocation task.

4.2.4 Tolerance Scaling

Once the tolerances are defined according to Section 4.2.3, an additional step is performed to evaluate the efficiency of the consumed assembly tolerance band based on the assigned tolerances. In other words, any unused portion of the assembly tolerance band, if exists, will be distributed within all or some of the tolerance bands of components, in either one or both directions. Although not necessary, this additional step provides an opportunity to possibly further reduce the number of nonconforming parts from the maximum tolerable level. Note that however, the percentage reduction in the number of nonconforming parts depends on the adopted scaling approach. Ideally, one might want to employ a scaling approach that can minimize the possible maximum number of nonconforming parts.

In this work, we employ a weighted approach which does not necessarily consider the number of nonconforming parts but instead considers the weight coefficient of each component (decided by the designer/manufacturer) for scaling the tolerances. The weight coefficient can depend on many factors including the used AM process, the derived width of the tolerance band, component's material, etc. For example, if the recycling process of a material is expensive in case of waste, a higher weight coefficient can be assigned to that component so that less non-conforming parts are generated. As another example, if the determined tolerance band for a component is too narrow, the designer might also want to increase it to further reduce the number of possible defects.

159

The proposed weighted approach is as follows. Let $\boldsymbol{W_{N\times 2}}$ denote the given component's weight matrix with its first and second columns given as $\boldsymbol{w^-} = (w_1^-, \dots, w_N^-)^T$ and $\boldsymbol{w^+} = (w_1^+, \dots, w_N^+)^T$, $\sum_{n=1}^{N} w_n^- = 1$, $\sum_{n=1}^{N} w_n^+ = 1$, $0 \leq w_n^-, w_n^+ < 1$, where $\boldsymbol{w^-}$ and $\boldsymbol{w^+}$ represent the components' weight vectors along positive and negative directions, and subscript T denotes matrix transpose. Also, let T_R^- and T_R^+ represent the remaining tolerance bands on negative and positive directions after determining the component tolerances. The additional distributed allowance to each component along negative and positive directions is simply calculated by:

$$\boldsymbol{T_D} = \operatorname{diag}(T_R^-, T_R^+)\boldsymbol{W^T}. \tag{4.5}$$

4.2.5 Optimization Model

Let matrix $\boldsymbol{X} = \{X_{nj}\}$ be the decision matrix with each element X_{nj} representing the binary decision variable to denote the process plan. Therefore, X_{nj} takes the value of one if component n is fabricated by the jth set of process parameters ($\boldsymbol{pr_j}$), and zero otherwise. The above joint tolerance allocation and manufacturing decision-making problem can be formulated with the objective function (4.6) and constraints (4.7-4.11) as follow:

$$\min_{\boldsymbol{X,p}} \sum_{n=1}^{N} \sum_{j=1}^{J} C_{nj} X_{nj} - \lambda \sum_{n=1}^{N} \tilde{p}_n \tag{4.6}$$

$$s.t. \quad p_A \leq \prod_{n=1}^{N} p_n, \tag{4.7}$$

$$\sum_{n=1}^{N} \beta_{nk}^{p_n} \leq D_A + T_A, \quad \left(k = j \ \ iff \ X_{nj} = 1\right), \tag{4.8}$$

$$\sum_{n=1}^{N} \alpha_{nk}^{p_n} \geq D_A - T_A, \quad (k = j \;\; iff \;\; X_{nj} = 1), \tag{4.9}$$

$$\sum_{j=1}^{J} X_{nj} = 1, \quad \forall n, n = 1, \dots, N \tag{4.10}$$

$$X_{nj} \in \{0,1\}, \quad 0 < p_n \leq 1, \quad p_n \in \mathbb{R}^+. \tag{4.11}$$

In (4.6), the cost minimization objective is formulated with the decision variables of matrix $\boldsymbol{X}$ and vector $\boldsymbol{p}$ where $\tilde{p}_n$ represents the natural logarithm of the confidence level p_n, and λ is a small number. Using λ allows us to formulate the objective of maximizing $\boldsymbol{p}$ together with the cost minimization objective.

As stated in (4.6), the objective is to minimize the total cost of manufacturing by determining the optimal decision matrix $\boldsymbol{X}$ (Boolean matrix with entries from the Boolean domain $\{0, 1\}$) and component confidence levels (equivalently the value of individual tolerances).

Constraint (4.7) is established to address the relationship between the assembly confidence level and components' confidence levels, and is based on the following theorem:

Theorem 1: if d_{nk} is a randomly obtained dimension from an unknown pdf: $f(D_n, \boldsymbol{pr}_k)$, where k represents the optimum selected process parameter set for component n, and assuming that the component's dimensions are independence (this is true based on our initial assumption as no two components are printed in one setup), the probability that the final assembly lies within the assembly specification is:

$$P\left(\left(\sum_{n=1}^{N} d_{nk}\right) \subseteq [D_A - T_A, D_A + T_A]\right)$$

(4.12)

$$\geq \quad P\left(\bigcap_{n=1}^{N}(d_{nk} \subseteq I_{nk}^{p_n})\right) = \prod_{n=1}^{N} p_n,$$

which according to the problem formulation should be at least P_A. Therefore, to satisfy this requirement, constraint (4.7) is needed.

Corollary 1.1: If all p_n's are selected as equal, for a given assembly confidence level P_A, the p_n's should be at least $\sqrt[N]{P_A}$.

Note that constraint (4.7) has a quadratic form which can increase the complexity of the solution approach. To transform this constraint into a linear format, we take the natural logarithm of both sides of the inequality. Therefore, this constraint can be re-written as:

$$\tilde{p}_A \leq \sum_{n=1}^{N} \tilde{p}_n,$$

(4.13)

where superscript ~ denotes the natural logarithm.

Constraints (4.8) and (4.9) are formulated to address the acceptable total error based on the assembly specifications. An alternative formulation of these constraints is represented below:

$$\sum_{n=1}^{N} \sum_{j=1}^{J} \boldsymbol{B}_{nj}^{p} X_{nj} \leq D_A + T_A,$$

(4.14)

$$\sum_{n=1}^{N} \sum_{j=1}^{J} A_{nj}^{p} X_{nj} \geq D_A - T_A, \tag{4.15}$$

where $\mathbf{A}$ and $\mathbf{B}$ are the matrices of the $\hat{\alpha}_{nj}^{p_n,T}$ and $\hat{\beta}_{nj}^{p_n,T}$ for $\mathbf{p}$.

Remark: Note that characterizing the total assembly error by summing up the lower bounds $\alpha_{nj}^{p_n}$'s together (and doing the same thing with $\beta_{nj}^{p_n}$'s), as stated in constraints (4.8) and (4.9) might not be very accurate specifically when the confidence levels are not large, and can lead to some inaccuracies in the evaluation of the final error. In that case, the correct approach for characterizing the assembly error is the convolution of individual pdfs of individual components. However, for cases where the pdfs do not exist or the likelihood functions are not completely known, one can use a similar approach as stated in [215], [216]. As an example, Barlow suggested the following likelihood function to address the asymmetric error ($\pm_{\sigma^-}^{\sigma^+}$) for 68% confidence level:

$$\ln L(\vartheta) = -\frac{1}{2} \left(\frac{\ln \left(1 + \frac{\vartheta}{\gamma} \right)}{\ln \omega} \right) \tag{4.16}$$

Where $L(\vartheta)$ is the likelihood function, $\omega = \frac{\sigma^+}{\sigma^-}$, and $\gamma = \frac{\sigma^+ \sigma^-}{\sigma^+ - \sigma^-}$.

In constraint (4.10), the number of assigned process parameters set for each component is limited to 1. Finally, in (4.11), the decision variables X_{nj} are defined as binary, and p_n's are limited to the continuous range from zero to one.

4.2.6 Input Parameters and Decision Variables

In general, the input parameters in this work can be divided into four different categories: (i) Design-related parameters, (ii) Process-related parameters, (iii) Bootstrap-related parameters, and

(iv) Optimization-related parameters. The parameters of the first two categories are mainly decided by the designer and with the inputs from the manufacturer regarding the feasible process parameter sets, or cost of manufacturing. The last two categories are related to the optimization model and the implemented bootstrap method. The notation and description of the input parameters in this work are provided in Table XXVII.

The decision variables of the optimization problem comprise of decision matrix X and confidence level vector p, and are presented in Table XXVIII. Once the optimum decision variables are obtained, the components' tolerances will be calculated based on the intermediate parameters of $\hat{\alpha}_{nk}^{p_n,T}$ and $\hat{\beta}_{nk}^{p_n,T}$ (for all n). These two parameters are the point estimates of lower and upper percentiles of the distribution for nth component printed with the optimum set of process parameters (k), respectively, and are a function of optimum p_n.

Table XXVII. Input parameters

Category	Notation	Description
(i)	N	Number of components
	D_n	Nominal dimension of the nth component
	D_A	Nominal dimension of the final assembly
	T_A	Dimensional tolerance of the assembly
	P_A	Confidence level of the assembly
	w^-	Weight vector (negative direction)
	w^+	Weight vector (positive direction)
(ii)	J	Number of process parameter sets
	pr_j	The jth set of process parameters
	$C = \{C_{nj}\}$	Cost matrix
(iii)	R	Number of Bootstrap samples
	T	Number of repeated simulation runs for constructing the confidence intervals
(iv)	λ	Objective function coefficient
	Ω	Initial manufacturing cost
	ξ	Cost cut-off value

Table XXVIII. Decision variables

$\boldsymbol{p} = (p_n)$	Confidence level of components
$\boldsymbol{X} = \{X_{nj}\}$	Manufacturing decision matrix

4.2.7 Solution Approach

We have adopted a cyclic (or alternating) optimization approach, for finding the optimum values of the decision variables X_{nj}'s and p_n's. This method has also been referred to as block relaxation, block-nonlinear Gauss–Seidel (GS), or cyclic coordinate descent method in the literature. Cyclic optimization is a well-known optimization approach for solving multivariate optimization problems and similar complex problems that arise in machine learning and data analysis, particularly in "big data" settings [217]. In addition, it has shown to work well in many problems with good convergence properties, and thus is very popular with practitioners [218]. The key idea is to convert the optimization problem to a univariate optimization problem (usually much simpler to handle) by optimizing the function along one direction at a time through cyclic iterations. The main reason for adopting the cyclic optimization in this work was that it could simplify the optimization process due to the unique structure of our formulation.

Consider the function $g: \mathcal{R}^m \to \mathcal{R}$ and the vector variable $\boldsymbol{y} = (Y_1, \ldots, Y_m)^T \in \mathcal{R}^m$, where subscript T denotes matrix transpose. It is assumed that the scalar variables in $\boldsymbol{y}$ can be partitioned into s sub-vectors as $(\boldsymbol{y_1}, \ldots, \boldsymbol{y_s})^T$, $\boldsymbol{y_i} \in \mathcal{R}^{t_i}$ $(i = 1, \ldots, s)$, where $\sum_{i=1}^{s} t_i = m$. Using the cyclic optimization approach, one can minimize the function $g(\boldsymbol{y_1}, \ldots, \boldsymbol{y_s})$ over $\boldsymbol{y_1}, \ldots, \boldsymbol{y_s}$, by first generating an initial point $\boldsymbol{y^0} = \left(\boldsymbol{y_1^0}, \ldots, \boldsymbol{y_s^0}\right)^T$ that preferably belongs to the set of feasible solutions, denoted by Ψ. The solution is then obtained using the following iterative approach until either no significant change is obtained in two consecutive iterations or a maximum tolerable number of iterations is reached [219], [220]:

$$y_i^{r+1} = \arg \min_{y_i \in \Psi_i} g(\cancel{y_1^{r+1}}, \dots, \cancel{y_{i-1}^{r+1}}, y_i, \cancel{y_{i+1}^r}, \dots, \cancel{y_s^r}), \qquad i = 1, \dots, s, \qquad (4.17)$$

where Ψ_i is the set of feasible y_i's, r denotes the iteration number, and the strikethrough notation indicates a vector that is considered to be fixed.

The algorithm starts by generating a random vector p which satisfies constraint (4.13). The optimization problem is then solved with respect to X using Binary Linear Programming (BLP) in which constraint (4.13) is relaxed. Next, the optimization problem is solved with respect to p and by fixing the optimum matrix X obtained from the previous step. The reduction in the total manufacturing cost caused by the changes to the values of vector p and matrix X is evaluated at each cycle and is compared with a user-defined threshold ξ. The algorithm stops when the cost reduction becomes insignificant and the latest values of p and X will be reported as the final solution. Note that for each optimization cycle, the model coefficient matrices B_{nj}^p and A_{nj}^p are evaluated based on the Bootstrap algorithm presented in Figure 65. The detailed steps of the proposed cyclic optimization algorithm are presented below.

Step 1. Set $i = 0$ and $f_{TC}(p^{-1}, X^{-1}) = \Omega$, where Ω is a large number.

Step 2. Generate a vector p where for the given value P_A, constraint (4.13) is satisfied, and denote it as p^i.

Step 3. Fix the vector $p = p^i$ and solve the optimization problem (objective function (4.6) and constraints (4.8-4.11), where constraint (4.7) is relaxed) with respect to matrix X^i: $X^i = \arg\min f_{TC}(p, X^i)$.

Step 4. Evaluate the cost reduction: $\delta TC_i = f_{TC}(p^i, X^i) - f_{TC}(p^{i-1}, X^{i-1})$. If the total cost reduction is significant; $|\delta TC_i| > \xi$, go to **Step 5**, else go to **Step 8.**

Step 5. Increase i by one.

Step 6. Fix the matrix $X = X^{i-1}$ obtained from **Step 3** and solve the optimization problem (objective function (4.6) and constraints (4.7-4.11)) with respect to vector p^i: $p^i = \arg\min f_{TC}(p^i, X)$.

Step 7. Go to **Step 3**.

Step 8. End.

The flowchart of the algorithm is illustrated in Figure 67. The general illustration of the proposed cyclic optimization approach is shown in Figure 68. As is shown, the total cost will eventually converge as each optimization cycle is performed. The total cost is guaranteed to converge based on the monotone convergence theorem.
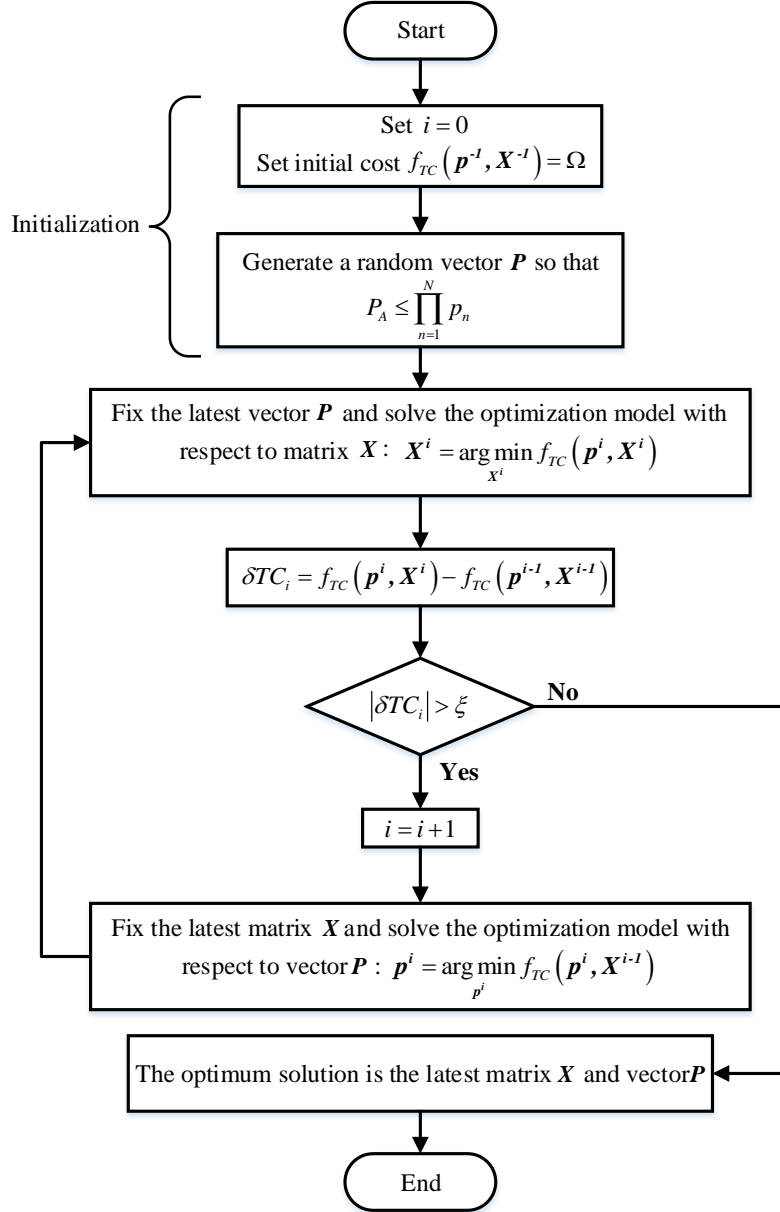
Figure 67. Flowchart of the proposed cyclic optimization algorithm

Theorem 2: If sequence $\{q_k\}$ is lower bounded and monotonically decreasing, then $\{q_k\}$ is convergent.

If the reduced cost at cycle i of the optimization is denoted as $\delta TC_i = f_{TC}(\boldsymbol{p}^i, \boldsymbol{X}^i) - f_{TC}(\boldsymbol{p}^{i-1}, \boldsymbol{X}^{i-1})$, where $f_{TC}(\boldsymbol{p}^i, \boldsymbol{X}^i)$ denotes the value of the objective function at cycle i, the sequence $\{\delta TC_i\}$ would be a monotonically decreasing sequence. Furthermore, it is clearly observed that the objective function in (4.6) is lower bounded at zero. Therefore, the above theorem guarantees the convergence of the total cost but does not necessarily guarantee to find the global optimum. In other words, this theorem will ensure a locally optimum solution for vector $\boldsymbol{p}$ and matrix $\boldsymbol{X}$ which determine the assigned tolerances and the selected process parameters for each component respectively.

$$f_{TC}\left(\boldsymbol{P^0}, \boldsymbol{X^0}\right) > f_{TC}\left(\boldsymbol{P^1}, \boldsymbol{X^0}\right) > f_{TC}\left(\boldsymbol{P^1}, \boldsymbol{X^1}\right) > f_{TC}\left(\boldsymbol{P^2}, \boldsymbol{X^1}\right) > \dots$$
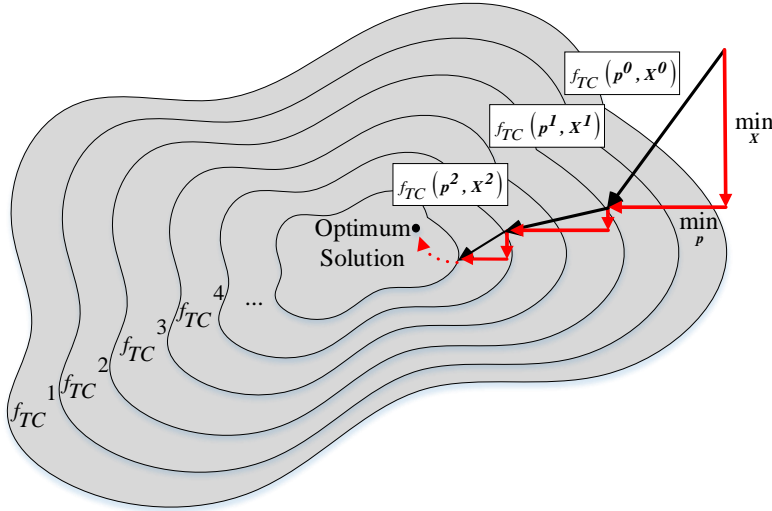
Figure 68. General illustration of cyclic optimization approach

4.2.8 Numerical Example

To demonstrate the effectiveness of the proposed method for joint determination of component tolerances and process parameters in AM processes, a case study is designed and implemented.

The proposed method is then adopted to determine component tolerances as well as the optimum set of process parameters to be used for fabricating each component. Finally, sensitivity analysis is performed to investigate the effect of different input parameters on the obtained solutions.

A one-dimensional five-component assembly chain is considered. It is assumed that the assembly is required to satisfy the 85±0.15 mm design specification with an 80% confidence level. Note that 80% confidence level is a minimum requirement, however, any additional improvement is preferred as it can further decrease the number of non-conforming parts. The nominal dimensions of the components are given as 10, 15, 18, 20, and 22 mm and are assumed to be fixed. Note that earlier we highlighted that if our proposed method does not find any solution, it might be necessary to re-assign the nominal dimensions or consider additional process parameter sets. However, in this case study the existence of feasible solutions has been previously investigated. Therefore, altering the nominal dimensions would not be necessary. Four possible sets of process parameters are considered for printing each component. For each combination of components and process parameter sets, six independent samples are considered. Therefore, a total of 120 samples are used. The 95% confidence interval for the three first moments of the distribution: mean ($\hat{\alpha}_1$), standard deviation ($\hat{\alpha}_2$), and skewness ($\hat{\alpha}_3$), are also calculated for each component and combination of process parameters using the bootstrap technique. The adjusted Fisher-Pearson coefficient of skewness is used to evaluate the skewness of the component's distributions:

$$\hat{\alpha}_3 = \frac{\sqrt{N_d(N_d - 1)} \sum_{i=1}^{N_d}(Y_i - \bar{Y})^3}{N_d(N_d - 2)s_d^3} \tag{4.18}$$

where N_d is the number of data points, $\bar{Y}$ is the mean and s_d is the standard deviation.

As is observed in Table XXIX, some of the distributions tend to be skewed which thus affects the optimum tolerances to be assigned for a given assembly confidence level. The cost for fabricating each component using each set of process parameters is also known and is given in Table XXX. The rest of the input parameters are presented in Table XXXI. the proposed methodology is then applied to determine the component tolerances as well as the process parameters. The methodology and optimization is implemented in MATLAB. The overall flowchart of the implemented methodology in MATLAB is presented in Figure 69.

Table XXIX. Confidence intervals of distribution statistics for input data

Statistic	pr_1	pr_2	pr_3	pr_4
$\hat{\alpha}_1$	[10.16,10.21]	[9.99,10.03]	[9.88,9.97]	[9.89,9.97]
$\hat{\alpha}_2$	[0.02,0.05]	[0.02,0.04]	[0.02,0.08]	[0.03,0.08]
$\hat{\alpha}_3$	[-1.79,0.71]	[-1.13,1.48]	[-0.23,1.75]	[-0.23,1.75]
$\hat{\alpha}_1$	[14.96,15.03]	[14.99,15]	[15.01,5.09]	[14.9,15.01]
$\hat{\alpha}_2$	[0.03,0.06]	[0.01,0.02]	[0.03,0.08]	[0.008,0.011]
$\hat{\alpha}_3$	[-1.71,0.52]	[-1.79,1.05]	[-1.74,0.37]	[-1.79,1.12]
$\hat{\alpha}_1$	[17.98,18.04]	[17.99,18.02]	[17.78,17.8]	[18.12,18.18]
$\hat{\alpha}_2$	[0.03,0.05]	[0.01,0.02]	[0.01,0.02]	[0.03,0.05]
$\hat{\alpha}_3$	[-1.51,1.16]	[-1.57,1.13]	[-1.79,1.34]	[-0.53,1.74]
$\hat{\alpha}_1$	[20.10,20.15]	[19.99,20.05]	[19.97,20.02]	[19.88,19.91]
$\hat{\alpha}_2$	[0.02,0.05]	[0.03,0.04]	[0.02,0.04]	[0.01,0.02]
$\hat{\alpha}_3$	[-0.99,1.30]	[-1.74,1.34]	[-0.82,1.79]	[-0.71,1.79]
$\hat{\alpha}_1$	[22.2,22.26]	[21.92,21.99]	[22.83,22.13]	[21.89,21.93]
$\hat{\alpha}_2$	[0.02,0.05]	[0.04,0.07]	[0.02,0.04]	[0.02,0.04]
$\hat{\alpha}_3$	[-0.56,1.79]	[-1.64,1.08]	[-1.69,0.59]	[-0.71,1.79]

Table XXX. Cost matrix

pr_1	pr_2	pr_3	pr_4
3	3	2.5	4
4.75	5	4	5
8.75	8.5	8.5	9
1.5	2	1.75	1.25
5.5	6.5	5	6

Table XXXI. Parameter values

N	5	D_2	15	D_5	22	P_A	0.8	Ω	0.001
J	4	D_3	18	D_A	85	λ	0.001	R	2000
D_1	10	D_4	20	T_A	0.15	ξ	500	T	20
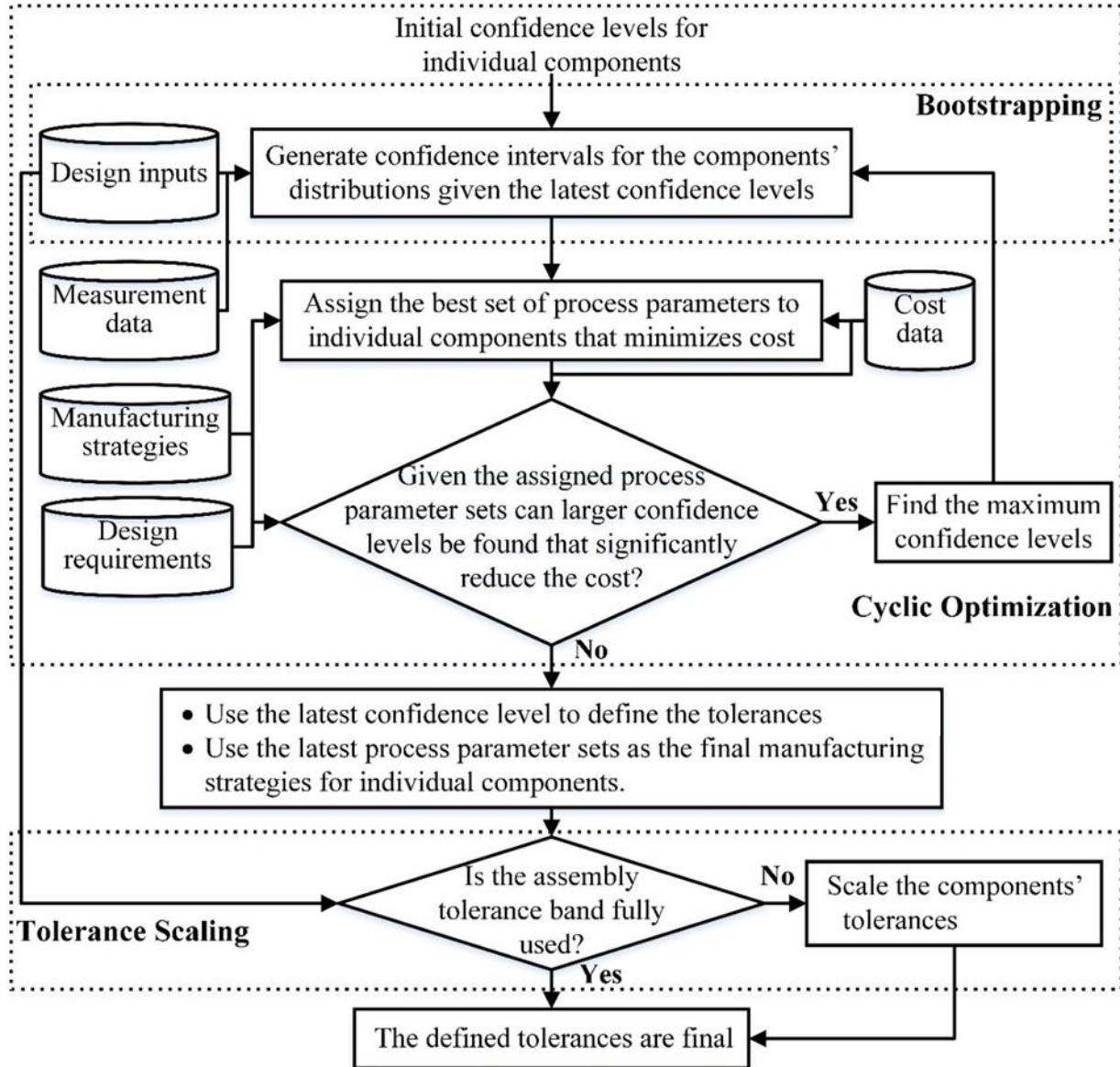
Figure 69. Overall flowchart of the implemented methodology in MATLAB

Figure 70 shows the distribution of the $(1 - p_n)/2$th and $(1 + p_n)/2$th percentile of the components' dimensions for each set of process parameters for a single simulation run based on the initial random vector $\boldsymbol{p}$ (for the given P_A) using the bootstrap technique. Please note that since R is large, P_A is 0.8 and based on Theorem 1, the variability of vector $\boldsymbol{p}$ from one simulation run to another is small, and thus does not affect the provided distributions significantly.
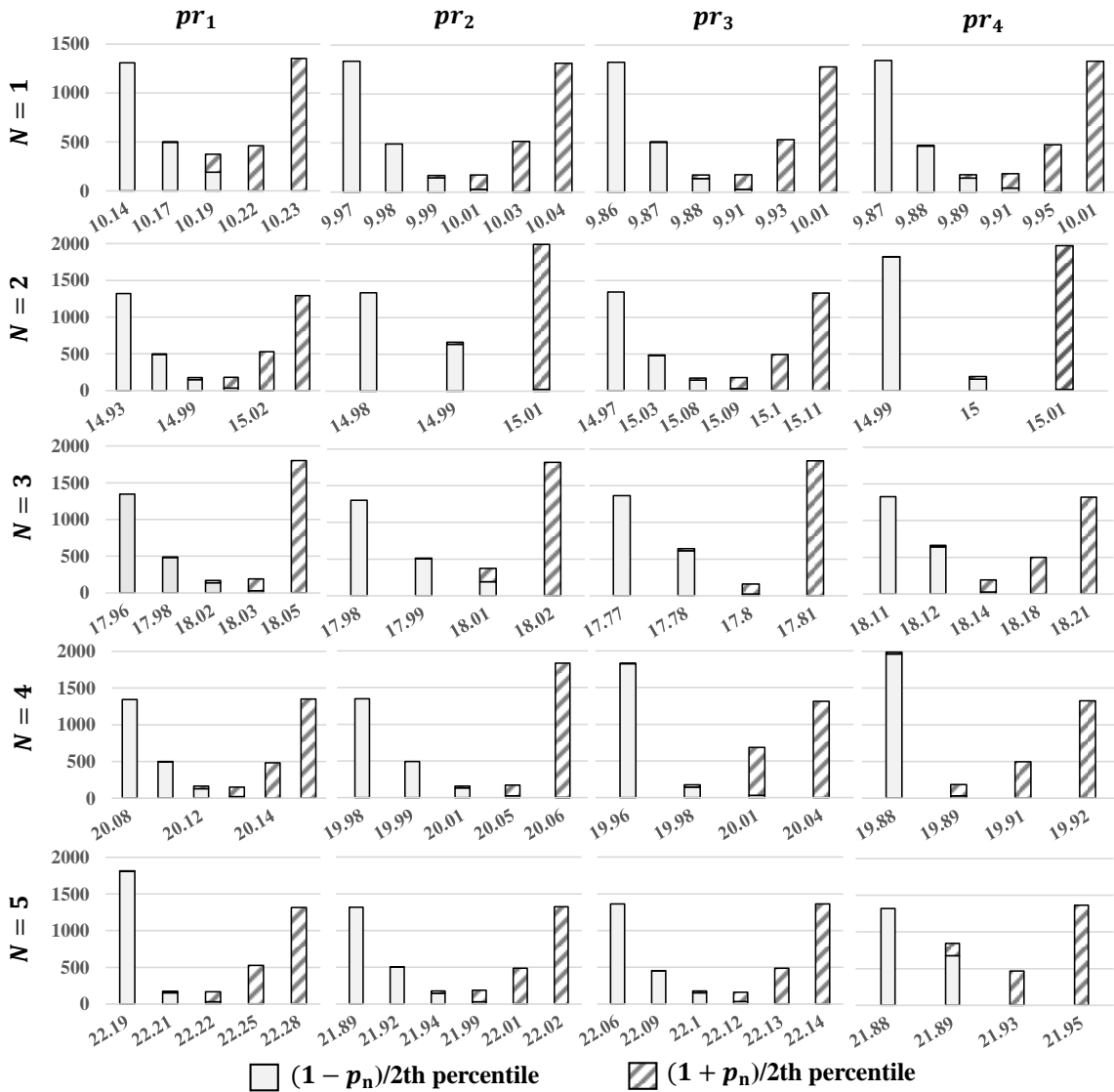
Figure 70. Distribution of the percentiles based on the bootstrap technique

Table XXXII shows the calculated optimum tolerances for components, the selected process parameter sets, and the total cost, based on 20 different runs. The assignment matrix X can be represented using the vector x' with size N which holds the index of the assigned process parameter set to each component. Therefore, the optimal vector x' is selected as (2, 1, 2, 4, 3) with a total cost of 22.49006. As is observed, the allocated tolerances can follow different structures (either bilateral, unilateral, or asymmetric), which thus increases the efficiency of the consumed tolerance bands. Based on the calculated tolerances, the assembly tolerance will fall within the range of [-0.1248, 0.1348] which is still smaller than the initial designed T_A of 0.15. Therefore, the remaining allowances of 0.0252 and 0.0152 are further distributed among the components based on the assumption that all components have a similar weight factor. The updated tolerance values after this tolerance scaling are presented in Table XXXII under the "updated lower and upper tolerance" columns.

Note that the combination of parameters with the total minimum cost of 21.25, $x' = (3, 3, 3, 4, 3)$ or $x' = (3, 3, 2, 4, 3)$ cannot be selected as they do not satisfy the assembly specifications and the required confidence level according to the percentile distributions. In general, without using the proposed method, finding a set of feasible solutions for both the assigned process parameters and tolerance limits is not possible even with exhaustive search approaches as the pdf of data is unknown. In addition, it would be difficult to account for the skewness or asymmetric distribution of dimensions for evaluating the feasibility of random solutions for a given confidence level. To further illustrate this point and the effectiveness of the proposed method, a bootstrap-assisted semi-exhaustive search is used for generating random feasible solutions. Note that to further reduce the search space, the search is implemented based on a feasible randomly generated vector p using Theorem 1. In addition, the bootstrap technique is used for constructing the confidence intervals,

as it would be difficult to account for the skewness or asymmetric distribution of dimensions without this approach. The results of this semi-exhaustive search compared to our proposed method is presented in Table XXXIII. As is observed, the proposed method outperforms the semi-exhaustive search approach with an extremely smaller number of solution points. It is also worthy to note that out of the millions of points searched by the exhaustive search method only around 2.7% of them were found to be feasible, which highlights the difficulty of finding feasible solutions.

Table XXXII. Determined optimum solution

N	Initial lower tolerance	Initial upper tolerance	Updated lower tolerance	Updated upper tolerance	Process parameter set
1	-0.025	0.035	-0.030	0.038	2
2	-0.045	0.035	-0.050	0.038	1
3	-0.015	0.015	-0.020	0.018	2
4	-0.115	-0.085	-0.120	-0.082	4
5	0.075	0.135	0.070	0.138	3

Table XXXIII. Comparison of the proposed method and semi-exhaustive search

	Proposed method	Bootstrap-assisted semi-exhaustive search
Min cost	22.49002	22.4901
Max cost	22.49008	25.7401
Average cost	22.49006 (over 10 points)	23.5358 (over more than 10000000 points)

4.2.9 Sensitivity Analysis

   To further investigate the effect of different input parameters on the decision variables, as well as the manufacturing cost, sensitivity analysis is performed. The analysis is performed by varying a parameter at a time and evaluating its effect on the variability of the decision variables as well as the obtained manufacturing cost. The selected parameters for this analysis include the assembly tolerance (T_A) and confidence level (P_A). The ranges of the values for T_A and P_A parameters are

[0.1, 0.125, 0.15, 0.175, 0.2], and [0.5, 0.6, 0.7, 0.8, 0.9, 0.95, 0.99], respectively. In addition to the 20 number of simulation instances implemented within each simulation run, each simulation run was repeated 10 additional times to derive the average cost for each case and to further investigate the convergence trend of the solutions. The computation time of the studied cases ranged from approximately 1800 to 5000 seconds using a desktop with Intel Xeon E5-2620 2.40 GHz processor and 16 GB RAM.

Table XXXIV. Sensitivity analysis results

	Value	Average cost	Standard deviation	Minimum cost	Maximum cost	Solution	% of solutions
T_A	0.1	22.74005	0.000018	22.74003	22.74008	(2, 2, 2, 4, 3)	100
	0.125	22.74007	0.000012	22.74006	22.74009	(2, 4, 2, 4, 3)	80
						(1, 2, 3, 4, 3)	20
	0.15	22.49006	0.000021	22.49002	22.49008	(2, 1, 2, 4, 3)	100
	0.175	21.74007	0.000015	21.74005	21.74009	(1, 3, 3, 4, 3)	100
	0.2	21.24006	0.000017	21.24002	21.24008	(3, 3, 2, 4, 3)	100
P_A	0.5	22.46522	0.079049	22.24025	22.49026	(2, 1, 2, 4, 3)	70
						(1, 1, 3, 4, 3)	20
						(2, 3, 3, 4, 1)	10
	0.6	22.46513	0.079034	22.24020	22.49019	(2, 1, 2, 4, 3)	80
						(2, 3, 3, 4, 1)	10
						(1, 1, 3, 4, 3)	10
	0.7	22.49009	0.000038	22.49005	22.49015	(2, 1, 2, 4, 3)	100
	0.8	22.49006	0.000021	22.49002	22.49008	(2, 1, 2, 4, 3)	100
	0.9	22.49003	0.000009	22.49001	22.49004	(2, 1, 2, 4, 3)	100
	0.95	22.49001	0.000002	22.49001	22.49002	(2, 1, 2, 4, 3)	100
	0.99	22.49000	0.000001	22.49000	22.49000	(2, 1, 2, 4, 3)	100

Table XXXIV summarizes the results of the sensitivity analysis. In addition, the relative cost as a function of the studied parameters is plotted in Figure 71 and Figure 72. As expected, the relative cost for producing the assembly decreases as the assembly tolerance increases. In addition, relaxing the symmetricity constraint provides better opportunities towards reducing both cost and tolerance simultaneously through tuning the process parameters. Furthermore, it is observed that

the relative cost slightly increases as the assembly confidence level P_A is increased. However, the change in P_A does not significantly affect the final manufacturing cost. Different models were fitted to the obtained data. It appears that the 2nd order polynomial model fits well to the data in Figure 71. However, in Figure 72, the 2nd order polynomial model does not perform as good. Instead, it is observed that the relative cost tends to almost remain unchanged for a range of confidence level values, and then jump to a higher level as the confidence level is increased. This observation suggests that there exists a confidence level threshold after which, the number of nonconforming parts can be reduced with no significant additional cost.
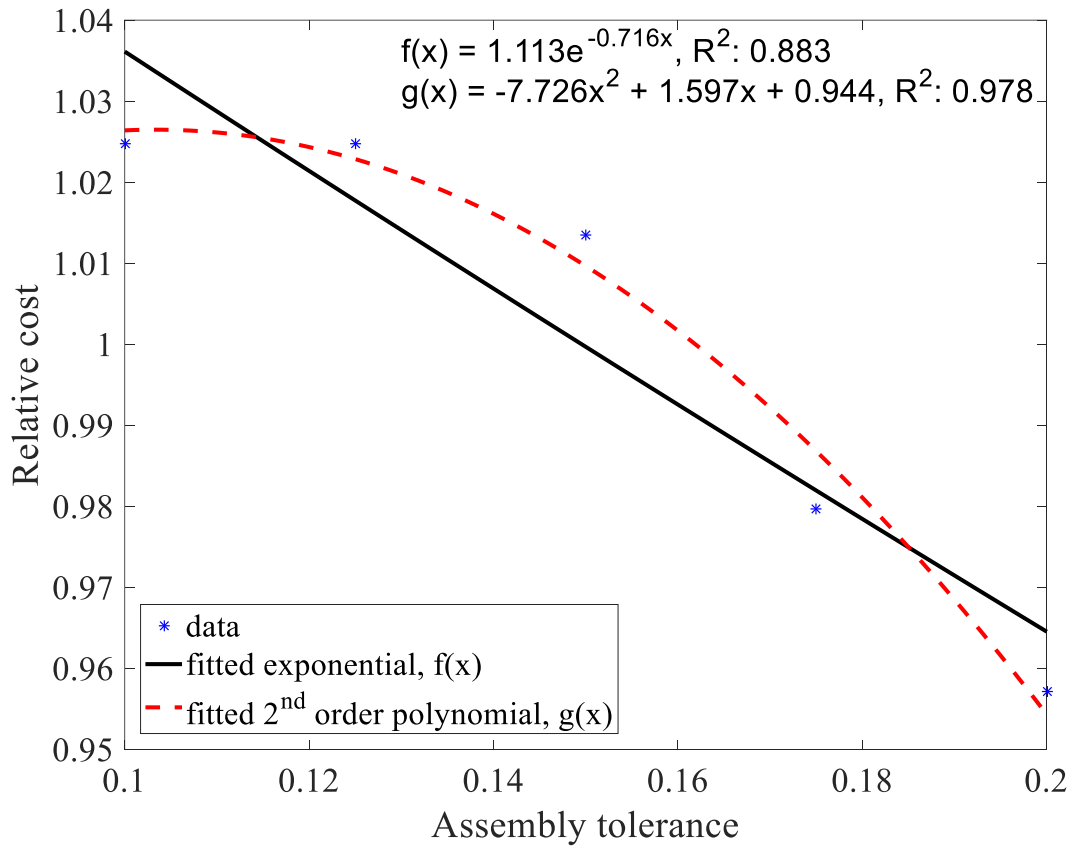
Figure 71. Relative cost of different assembly tolerances
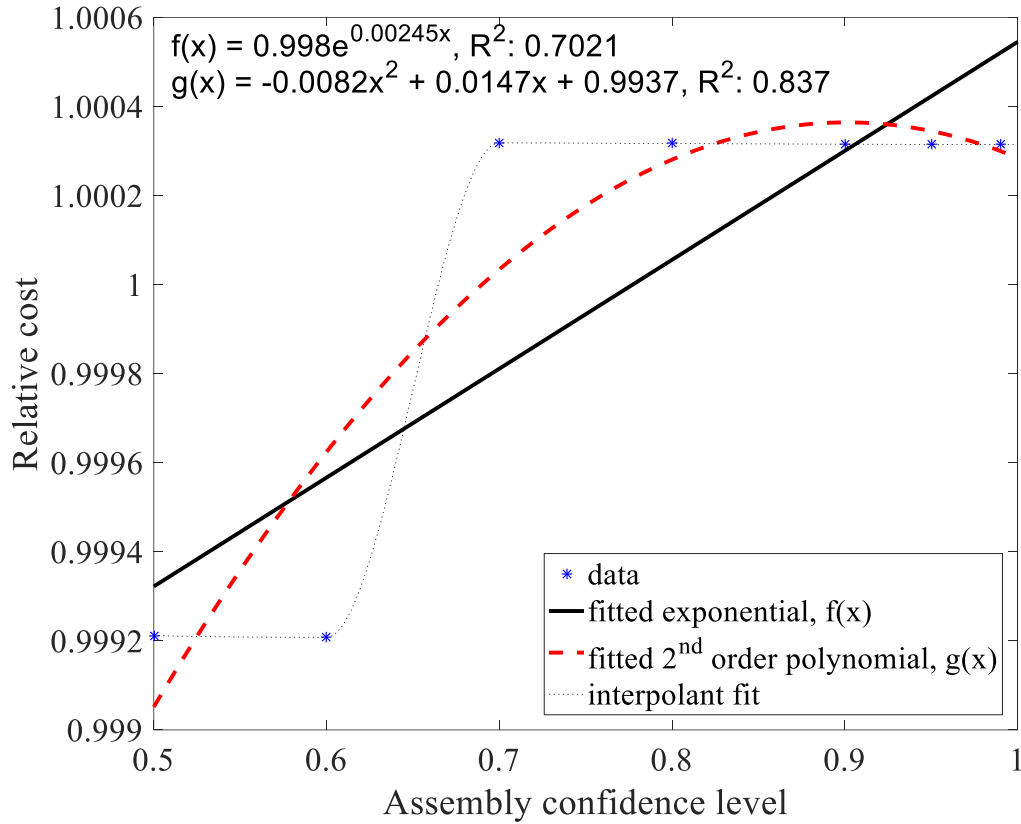
Figure 72. Relative cost of different assembly confidence levels

The width of the tolerance band for components based on different assembly tolerances is studied in Figure 73. It is observed that as the assembly tolerance is increased, increasing the tolerance bandwidth of all components is not necessarily optimum. In other words, depending on the cost of components (function of their geometry, design, and manufacturing parameters) and process capability, sometimes it might be necessary to tighten the tolerance band of some components to further reduce the total manufacturing cost. In addition, the variation of tolerance bandwidth for some components (e.g., components 1 and 2 in our case) is more significant than others. This generally suggests that the selected process for fabricating these components is more stable (has lower process variability) for the studied process parameter sets, while the difference between the cost of different sets is generally significant.

177
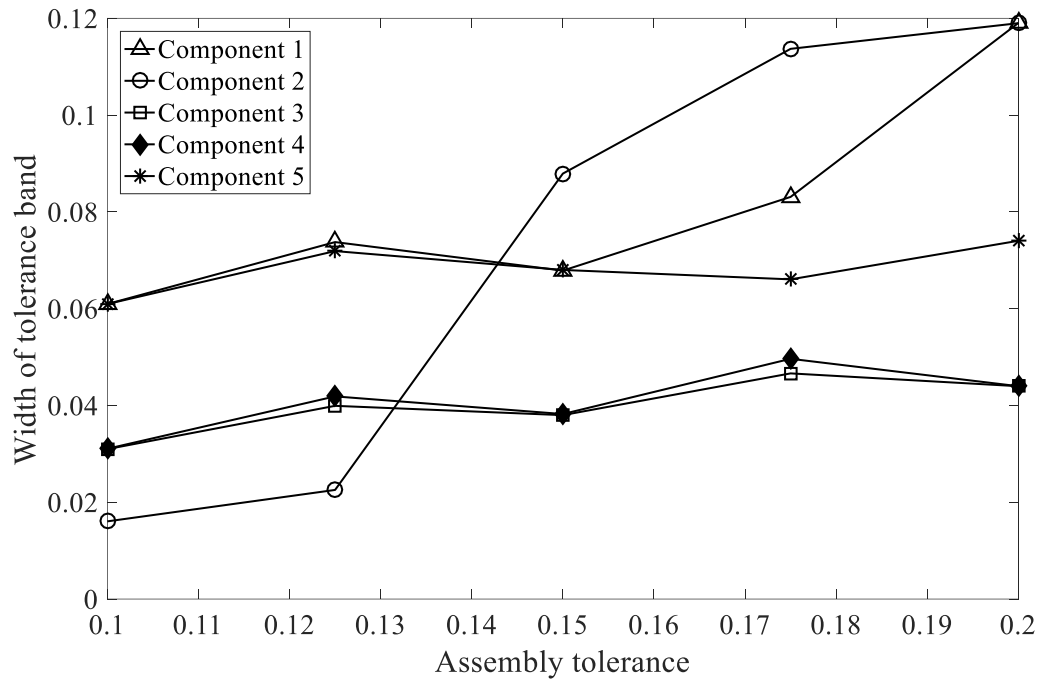
Figure 73. Width of tolerance band for different components

4.2.10 Conclusions

Motivated by the lack of GD&T standards for AM processes and their unique characteristics, in this section, a methodology for joint tolerance design and manufacturing decision making is established to address the complex relationship between design and manufacturing as well as the asymmetric behavior of tolerances. Both assembly specification and confidence level (to reflect the defect rate based on the process capability) are considered as constraints. Dimensional tolerances are formulated based on the optimal confidence level and nominal dimensions. The bootstrap technique is adopted to generate the confidence interval for components' dimensions. The cyclic optimization approach is then used to solve the multivariate optimization problem. Numerical case studies have been performed to evaluate the effectiveness of the proposed methodology.

For the illustrated case study, the proposed methodology managed to reduce the total manufacturing cost compared to the bootstrap–assisted semi-exhaustive search method with almost 10^6 less solution points, while ensuring the assembly requirements. It is expected that as the number and cost of components increases, the methodology will become more effective, and the cost reduction becomes more significant.

4.3 Concluding Remarks

In this chapter, studies towards understanding and addressing the challenges of tolerance design at the product level considering multi-component products with additively manufactured components are performed. First, the effect of assembly design and manufacturing scenario (integrated and overlapped geometries versus individual and non-overlapped geometries) on the assembly clearance and dimensional profile of assembly components are empirically studied in the PolyJet AM process. It was observed that a different dimensional profile behavior exists which affects the tolerance design decisions. As a result, this factor needs to be considered at the tolerance design stage for suggesting feasible and optimal tolerances.

Second, a joint tolerance design and parameter tuning methodology is formulated and established. With respect to the formulation challenges, the bootstrap statistical technique was used to address the challenge of distribution estimation based on a limited number of components. An optimization problem is then formulated to minimize the cost while ensuring the assembly specification and confidence level. The multivariate optimization is then solved using the cyclic optimization approach due to its suitability for the problem's structure. Case studies are performed to validate the methodology and analyze the sensitivity of model outputs by changing the input values. The tolerance design methodology is tailored to be applicable to assemblies with additive manufactured components.

5. SUMMARY AND FUTURE WORK

Motivated by the increasing application of additive and hybrid manufacturing processes for the fabrication of functional products, some of the quality assurance and tolerance design challenges of these emerging products were addressed at two levels of process and product by characterizing the relationship between product design, process characteristics and parameters, product property, and sustainability. At the process level, comprehensive analytical and experimental models for quality characterization and improvement of components from additive and hybrid additive-subtractive manufacturing processes towards higher sustainability were established. Moreover, a robotic hybrid additive-subtractive manufacturing process is developed. At the product level, a decision-making tool for joint tolerance design and manufacturing of multi-component additively manufactured products is established. The established smart process-aware tolerance design methodology and quality assurance models help designers and manufacturers in assigning feasible and optimal tolerances and provide guidelines for design and process improvements.

Possible future research extensions of this work are as follows. The interdependency of dimensional and geometrical errors among overlapped or connected geometries in a single build AM cycle can be further studied towards establishing joint optimal tolerance design and 3D packing algorithms. The quality issues as a result of multi-plane hybrid manufacturing can be further studied. Finally, tolerance design challenges for multi-component products from both additive and hybrid manufacturing processes can be considered.

REFERENCES

[1]   ASTM, "Standard Terminology for Additive Manufacturing Technologies," F2792-12a, vol. i, pp. 11–13, 2012.

[2]   R. Pham, D. and Gault, "A comparison of rapid prototyping technologies," International Journal of Machine tools and Manufacture, vol. 38, no. October, pp. 1257–1287, 1998.

[3]   K. V. Wong and A. Hernandez, "A Review of Additive Manufacturing," ISRN Mechanical Engineering, vol. 2012, pp. 1–10, 2012.

[4]   N. Guo and M. C. Leu, "Additive manufacturing: Technology, applications and research needs," Frontiers of Mechanical Engineering, vol. 8, no. 3. pp. 215–243, 2013.

[5]   A. Boschetto and L. Bottini, "Manufacturability of non-assembly joints fabricated in AlSi10Mg by selective laser melting," Journal of Manufacturing Processes, vol. 37, pp. 425–437, 2019.

[6]   R. Huang et al., "Energy and emissions saving potential of additive manufacturing: the case of lightweight aircraft components," Journal of Cleaner Production, vol. 135, pp. 1559–1570, 2016.

[7]   J. Kwon, N. Kim, and J. Ma, "Environmental sustainability evaluation of additive manufacturing using the NIST test artifact," Journal of Mechanical Science and Technology, pp. 1–10, 2020.

[8]   W. Gao et al., "The status, challenges, and future of additive manufacturing in engineering," Computer-Aided Design, vol. 69, pp. 65–89, 2015.

[9]   Y. Huang, M. C. Leu, J. Mazumder, and A. Donmez, "Additive Manufacturing: Current State, Future Potential, Gaps and Needs, and Recommendations," Journal of Manufacturing Science and Engineering, vol. 137, no. 1, p. 014001, 2015.

[10]   T. J. Horn and O. L. A. Harrysson, "Overview of current additive manufacturing technologies and selected applications," Science Progress, vol. 95, no. 3, pp. 255–282, 2012.

[11]   B. Lyons, "Additive Manufacturing in Aerospace: Examples and Research Outlook," The Bridge, vol. 42, no. 1, pp. 13–19, 2012.

[12]   J. Giannatsis and V. Dedoussis, "Additive fabrication technologies applied to medicine and health care: A review," International Journal of Advanced Manufacturing Technology, vol. 40, no. 1–2, pp. 116–127, 2009.

[13]   P. L. Lewis and R. N. Shah, "3D Printing for Liver Tissue Engineering: Current Approaches and Future Challenges," Current Transplantation Reports, vol. 3, no. 1, pp. 100–108, 2016.

[14]   A. Bhargav, V. Sanjairaj, V. Rosa, L. W. Feng, and J. Fuh YH, "Applications of additive

manufacturing in dentistry: A review," Journal of Biomedical Materials Research Part B: Applied Biomaterials, vol. 106, no. 5, pp. 2058–2064, 2018.

[15] D. Espalin, D. W. Muse, E. MacDonald, and R. B. Wicker, "3D Printing multifunctionality: Structures with electronics," International Journal of Advanced Manufacturing Technology, vol. 72, no. 5–8, pp. 963–978, 2014.

[16] SmarTech, "Additive Manufacturing Market Outlook and Summary of Opportunities," 2020.

[17] 3D Hubs, "The 3D Printing Trends Report," 2019.

[18] C. Weller, R. Kleer, and F. T. Piller, "Economic implications of 3D printing: Market structure models in light of additive manufacturing revisited," International Journal of Production Economics, vol. 164, pp. 43–56, 2015.

[19] D. Bak, "Rapid prototyping or rapid production? 3D printing processes move industry towards the latter," Assembly Automation, vol. 23, no. 4, pp. 340–345, 2003.

[20] G. Krolczyk, P. Raos, and S. Legutko, "Experimental Analysis of Surface Roughness and Surface Texture of Machined and Fused Deposition Modelled Parts," Tehnički Vjesnik-Technical Gazette, vol. 21, no. 1, pp. 217–221, 2014.

[21] J. G. Zhou, D. Herscovici, and C. C. Chen, "Parametric process optimization to improve the accuracy of rapid prototyped stereolithography parts," International Journal of Machine Tools and Manufacture, vol. 40, no. 3, pp. 363–379, 2000.

[22] D. Dai and D. Gu, "Tailoring surface quality through mass and momentum transfer modeling using a volume of fluid method in selective laser melting of TiC/AlSi10Mg powder," International Journal of Machine Tools and Manufacture, vol. 88, pp. 95–107, 2015.

[23] R. Ponche, O. Kerbrat, P. Mognol, and J. Y. Hascoet, "A novel methodology of design for Additive Manufacturing applied to Additive Laser Manufacturing process," Robotics and Computer-Integrated Manufacturing, vol. 30, no. 4, pp. 389–398, 2014.

[24] Wohlers, "Wohlers Report," 2019. [Online]. Available: https://wohlersassociates.com. [Accessed: 29-Apr-2020].

[25] CIRP, "CIRP. The Internal Academy for Production Engineering," 2011. .

[26] Z. Zhu, V. G. Dhokia, A. Nassehi, and S. T. Newman, "A review of hybrid manufacturing processes – state of the art and future perspectives," International Journal of Computer Integrated Manufacturing, vol. 26, no. 7, pp. 596–615, 2013.

[27] V. Le, H. Paris, and G. Mandil, "Using additive and subtractive manufacturing technologies in a new remanufacturing strategy to produce new parts from End-of-Life parts Abstract :," in 22 ème Congrès Français de Mécanique CFM2015, 2015, pp. 1–8.

[28] V. T. Le, H. Paris, and G. Mandil, "Process planning for combined additive and subtractive manufacturing technologies in a remanufacturing context," Journal of Manufacturing Systems, vol. 44, pp. 243–254, 2017.

[29] S. T. Newman, Z. Zhu, V. Dhokia, and A. Shokrani, "Process planning for additive and subtractive manufacturing technologies," CIRP Annals - Manufacturing Technology, vol. 64, no. 1, pp. 467–470, 2015.

[30] M. Behandish, S. Nelaturi, and J. de Kleer, "Automated process planning for hybrid manufacturing," CAD Computer Aided Design, vol. 102, pp. 115–127, 2018.

[31] A. Rossi and M. Lanzetta, "Integration of hybrid additive/subtractive manufacturing planning and scheduling by metaheuristics," Computers & Industrial Engineering, p. 106428, 2020.

[32] Y. Zheng, J. Liu, and R. Ahmad, "A cost-driven process planning method for hybrid additive–subtractive remanufacturing," Journal of Manufacturing Systems, vol. 55, pp. 248–263, 2020.

[33] ASME, "Dimensioning and Tolerancing, ANSI Y14.5M-1982," 1983.

[34] ISO, "Geometrical product specifications (GPS) — Geometrical tolerancing — Tolerances of form, orientation, location and run-out," Iso 1101:2012(E), vol. 3, no. 1, p. 110, 2012.

[35] K. W. Chase and A. R. Parkinson, "A survey of research in the application of tolerance analysis to the design of mechanical assemblies," Research in Engineering Design, vol. 3, no. 1. pp. 23–37, 1991.

[36] A. J. Dunbar et al., "Development of experimental method for in situ distortion and temperature measurements during the laser powder bed fusion additive manufacturing process," Additive Manufacturing, vol. 12, pp. 25–30, 2016.

[37] W. S. Land II, B. Zhang, J. Ziegert, and A. Davies, "In-situ metrology system for laser powder bed fusion additive process," Procedia Manufacturing, vol. 1, pp. 393–403, 2015.

[38] S. Wang, K. Lasn, C. W. Elverum, D. Wan, and A. Echtermeyer, "Novel in-situ residual strain measurements in additive manufacturing specimens by using the Optical Backscatter Reflectometry," Additive Manufacturing, vol. 32, p. 101040, 2020.

[39] X. Zhang et al., "Correlation approach for quality assurance of additive manufactured parts based on optical metrology," Journal of Manufacturing Processes, vol. 53, pp. 310–317, 2020.

[40] D. Dimitrov, W. van Wijck, K. Schreve, and N. de Beer, "Investigating the achievable accuracy of three dimensional printing," Rapid Prototyping Journal, vol. 12, no. 1, pp. 42–52, 2006.

[41] E. S. Gadelmawla, M. M. Koura, T. M. A. Maksoud, I. M. Elewa, and H. H. Soliman,

"Roughness parameters," Journal of Materials Processing Technology, vol. 123, no. 1, pp. 133–145, 2002.

[42] M. Sander, A practical guide to the assessment of surface texture. Mahr Feinprüf, 1991.

[43] E. N. ISO, "4287–Geometrical Product Specifications (GPS)–Surface Texture: Profile Method–Terms, Definitions and Surface Texture Parameters," International Organization for Standardization, Genève, 1997.

[44] Y. S. Hong and T. C. Chang, "A comprehensive review of tolerancing research," International Journal of Production Research, vol. 40, no. 11. pp. 2425–2459, 2002.

[45] K. W. Chase and W. H. Greenwood, "Design issues in mechanical tolerance analysis," Manufacturing Review, vol. 1, no. 1, pp. 50–59, 1988.

[46] G. Ameta, R. Lipman, S. Moylan, and P. Witherell, "Investigating the Role of Geometric Dimensioning and Tolerancing in Additive Manufacturing," Journal of Mechanical Design, vol. 137, no. 11, p. 111401, 2015.

[47] G. Ameta, P. Witherell, S. Moylan, and R. Lipman, "Tolerance Specification and Related Issues for Additively Manufactured Products," in ASME 2015 International Design Engineering Technical Conferences & Computers and Information in Engineering Conference, IDETC/CIE 2015, 2015.

[48] G. Ameta, S. P. Moylan, and P. W. Witherell, "Challenges In Tolerance Transfer for Additive Manufacturing," In Summer Topical Meeting of American Society of Precision Engineering, 2015.

[49] E. Morse et al., "Tolerancing: Managing uncertainty from conceptual design to final product," CIRP Annals, vol. 67, no. 2, pp. 695–717, 2018.

[50] I. Gibson, D. W. Rosen, B. Stucker, and ASTM International, "Additive manufacturing technologies. 2010," Google Scholar, pp. 10–12, 2013.

[51] O. Diegel, S. Singamneni, S. Reay, and A. Withell, "Tools for Sustainable Product Design: Additive Manufacturing," Journal of Sustainable Development, vol. 3, no. 3, 2010.

[52] Y. Chen and C. Zhezheng, "Joint analysis in rapid fabrication of non-assembly mechanisms," Rapid Prototyping Journal, vol. 17, no. 6, pp. 408–417, 2011.

[53] Y. Chen and J. Lu, "Minimise joint clearance in rapid fabrication of non-assembly mechanisms," International Journal of Computer Integrated Manufacturing, vol. 24, no. 8, pp. 726–734, 2011.

[54] C. X. Feng and X. F. Wang, "Surface roughness predictive modeling: neural networks versus regression," IIE Transactions, vol. 35, no. 1, pp. 11–27, 2003.

[55] A. Geddam and S. Kaldor, "Interlinking dimensional tolerances with geometric accuracy

and surface finish in the process design and manufacture of precision machined components," IIE transactions, vol. 30, no. 10, pp. 905–912, 1998.

[56]   Q. Huang, J. Zhang, A. Sabbaghi, and T. Dasgupta, "Optimal offline compensation of shape shrinkage for three-dimensional printing processes," IIE Transactions (Institute of Industrial Engineers), vol. 47, no. 5, pp. 431–441, 2015.

[57]   Y. Jin, S. J. Qin, and Q. Huang, "Out-of-plane geometric error prediction for additive manufacturing," in IEEE International Conference on Automation Science and Engineering, 2015, vol. 2015–Octob, pp. 918–923.

[58]   A. Wang, S. Song, Q. Huang, and F. Tsung, "In-Plane Shape-Deviation Modeling and Compensation for Fused Deposition Modeling Processes," IEEE Transactions on Automation Science and Engineering, vol. 14, no. 2, pp. 968–976, 2017.

[59]   L. Xu, Q. Huang, A. Sabbaghi, and T. Dasgupta, "Shape Deviation Modeling for Dimensional Quality Control in Additive Manufacturing," ASME 2013 International Mechanical Engineering Congress and Exposition, 2013.

[60]   T. Zegard and G. H. Paulino, "Bridging topology optimization and additive manufacturing," Structural and Multidisciplinary Optimization, vol. 53, no. 1, pp. 175–192, 2016.

[61]   A. K. Sood, R. K. Ohdar, and S. S. Mahapatra, "Parametric appraisal of fused deposition modelling process using the grey Taguchi method," Proceedings of the Institution of Mechanical Engineers, Part B: Journal of Engineering Manufacture, vol. 224, no. 1, pp. 135–145, 2010.

[62]   T. Nancharaiah, V. R. d Ranga Raju, and R. Raju, "An experimental investigation on surface quality and dimensional accuracy of FDM components," International Journal on Emerging Technologies, vol. 1, no. 2, pp 106-111, 2010.

[63]   A. K. Sood, R. K. Ohdar, and S. S. Mahapatra, "Improving dimensional accuracy of Fused Deposition Modelling processed part using grey Taguchi method," Materials and Design, vol. 30, no. 10, pp. 4243–4252, 2009.

[64]   L. M. Galantucci, I. Bodi, J. Kacani, and F. Lavecchia, "Analysis of dimensional performance for a 3D open-source printer based on fused deposition modeling technique," in Procedia CIRP, 2015, vol. 28, pp. 82–87.

[65]   A. Noriega, D. Blanco, B. J. Alvarez, and A. Garcia, "Dimensional accuracy improvement of FDM square cross-section parts using artificial neural networks and an optimization algorithm," International Journal of Advanced Manufacturing Technology, vol. 69, no. 9–12, pp. 2301–2313, 2013.

[66]   M. N. Islam, B. Boswell, and A. Pramanik, "An Investigation of Dimensional Accuracy of Parts Produced by Three-Dimensional Printing," Proceedings of the World Congress on Engineering (WCE2013), vol. I, pp. 5–8, 2013.

[67] T. Lieneke et al., "Systematical determination of tolerances for additive manufacturing by measuring linear dimensions," in Solid Freeform Fabrication Symposium – An Additive Manufacturing Conference, 2015, pp. 371–384.

[68] T. Lieneke, V. Denzer, G. A. O. Adam, and D. Zimmer, "Dimensional Tolerances for Additive Manufacturing: Experimental Investigation for Fused Deposition Modeling," in Procedia CIRP, 2016, vol. 43, pp. 286–291.

[69] L. Bochmann et al., "Understanding error generation in fused deposition modeling," Surface Topography: Metrology and Properties, vol. 3, no. 1, pp. 1–9, 2015.

[70] A. Gregorian, B. Elliot, and R. Navarro, "Accuracy improvement in rapid prototyping machine (FDM-1650)," in Solid Freeform Fabrication Proceedings, pp. 77–84, 2001.

[71] A. Boschetto and L. Bottini, "Accuracy prediction in fused deposition modeling," International Journal of Advanced Manufacturing Technology, vol. 73, no. 5–8, pp. 913–928, 2014.

[72] Q. Huang, Y. Wang, M. Lyu, and W. Lin, "Shape Deviation Generator--A Convolution Framework for Learning and Predicting 3-D Printing Shape Accuracy," IEEE Transactions on Automation Science and Engineering, 2020.

[73] B. Vasudevarao, D. P. Natarajan, M. Henderson, and A. Razdan, "Sensitivity of RP surface finish to process parameter variation," in Solid Freeform Fabrication Proceedings, 2000, pp. 251–258.

[74] P. M. Pandey, N. Venkata Reddy, and S. G. Dhande, "Part deposition orientation studies in layered manufacturing," Journal of Materials Processing Technology, vol. 185, no. 1–3, pp. 125–131, 2007.

[75] M. Taufik and P. K. Jain, "Role of build orientation in layered manufacturing: a review," International Journal of Manufacturing Technology and Management, vol. 27, no. 1/2/3, p. 47, 2013.

[76] G. Chryssolouris, J. D. Kechagias, J. L. Kotselis, D. A. Mourtzis, and S. G. Zannis, "Surface roughness modelling of the Helisys laminated object manufacturing (LOM) process," in 8th European Conference on Rapid Prototyping and Manufacturing, Nottingham, 1999, pp. 141–152.

[77] R. Anitha, S. Arunachalam, and P. Radhakrishnan, "Critical parameters influencing the quality of prototypes in fused deposition modelling," in Journal of Materials Processing Technology, 2001, vol. 118, no. 1–3, pp. 385–388.

[78] R. I. Campbell, M. Martorelli, and H. S. Lee, "Surface roughness visualisation for rapid prototyping models," CAD Computer Aided Design, vol. 34, no. 10, pp. 717–725, 2002.

[79] Y. S. Dambatta and A. A. D. Sarhan, "Surface Roughness Analysis, Modelling and Prediction in Fused Deposition Modelling Additive Manufacturing Technology," World

Academy of Science, Engineering and Technology, International Journal of Mechanical, Aerospace, Industrial, Mechatronic and Manufacturing Engineering, vol. 10, no. 8, pp. 1568–1575, 2016.

[80] C. J. Luis Perez, J. Vivancos, and M. A. Sebastián, "Surface roughness analysis in layered forming processes," Precision Engineering, vol. 25, no. 1, pp. 1–12, 2001.

[81] D. Ahn, H. Kim, and S. Lee, "Surface roughness prediction using measured data and interpolation in layered manufacturing," Journal of Materials Processing Technology, vol. 209, no. 2, pp. 664–671, 2009.

[82] A. Boschetto, V. Giordano, and F. Veniali, "Modelling micro geometrical profiles in fused deposition process," in International Journal of Advanced Manufacturing Technology, 2012, vol. 61, no. 9–12, pp. 945–956.

[83] G. Strano, L. Hao, R. M. Everson, and K. E. Evans, "Surface roughness analysis, modelling and prediction in selective laser melting," Journal of Materials Processing Technology, vol. 213, no. 4, pp. 589–597, 2013.

[84] M. Taufik and P. K. Jain, "A Study of Build Edge Profile for Prediction of Surface Roughness in Fused Deposition Modeling," Journal of Manufacturing Science and Engineering, vol. 138, no. 6, 2016.

[85] A. Boschetto and L. Bottini, "Roughness prediction in coupled operations of fused deposition modeling and barrel finishing," Journal of Materials Processing Technology, vol. 219, pp. 181–192, 2015.

[86] D. Thomas et al., "Costs and Cost Effectiveness of Additive Manufacturing," US Department of Commerce, December, 2014.

[87] N. Hopkinson and P. Dicknes, "Analysis of rapid manufacturing—using layer manufacturing processes for production," Proceedings of the Institution of Mechanical Engineers, Part C: Journal of Mechanical Engineering Science, vol. 217, no. 1, pp. 31–39, 2003.

[88] C. Lindemann and U. Jahnke, "Analyzing product lifecycle costs for a better understanding of cost drivers in additive manufacturing," in Solid Freeform Fabrication Proceedings, pp. 177–188, 2012.

[89] P. Mognol, D. Lepicart, N. Perry, P. Mognol, D. Lepicart, and N. Perry, "Rapid Prototyping : energy and environment in the spotlight spotlight," Rapid Prototyping Journal, vol. 12, no. 1, pp. 26–34, 2014.

[90] L. Clemon, A. Sudradjat, M. Jaquez, A. Krishna, M. Rammah, and D. Dornfeld, "Precision and Energy Usage for Additive Manufacturing," In ASME International Mechanical Engineering Congress and Exposition, 2013.

[91] M. Burkhart and J. C. Aurich, "Framework to predict the environmental impact of additive

manufacturing in the life cycle of a commercial vehicle," in Procedia CIRP, 2015, vol. 29, pp. 408–413.

[92]   A. Drizo and J. Pegna, "Environmental impacts of rapid prototyping: an overview of research to date," Rapid prototyping journal, vol. 12, no. 2, pp. 64–71, 2006.

[93]   Y. Luo, M. C. Leu, and Z. Ji, "Assessment of environmental performance of rapid prototyping and rapid tooling processes," Solid Freeform Fabrication Symposium, pp. 783–792, 1999.

[94]   O. Kerbrat, F. Le Bourhis, P. Mognol, and J.-Y. Hascoët, "Environmental Impact Assessment Studies in Additive Manufacturing," in Handbook of {Sustainability} in {Additive} {Manufacturing}, 2016, pp. 31–63.

[95]   G. Strano, L. Hao, K. E. Evans, and R. M. Everson, "Optimisation of quality and energy consumption for additive layer manufacturing processes," in Responsive Manufacturing - Green Manufacturing (ICRM 2010), 5th International Conference on, 2010, pp. 364–369.

[96]   K. Thrimurthulu, P. M. Pandey, N. V. Reddy, and N. Venkata Reddy, "Optimum part deposition orientation in fused deposition modeling," International Journal of Machine Tools and Manufacture, vol. 44, no. 6. pp. 585–594, 2004.

[97]   A. Verma and R. Rai, "Energy Efficient Modeling and Optimization of Additive Manufacturing Processes," Proceedings of the Solid Freeform Fabrication Symposium, no. 1, pp. 231–241, 2013.

[98]   A. M. Phatak and S. S. Pande, "Optimum part orientation in Rapid Prototyping using genetic algorithm," Journal of Manufacturing Systems, vol. 31, no. 4, pp. 395–402, 2012.

[99]   P. Das, R. Chandran, R. Samant, and S. Anand, "Optimum Part Build Orientation in Additive Manufacturing for Minimizing Part Errors and Support Structures," in Procedia Manufacturing, 2015, vol. 1, pp. 343–354.

[100] C. A. Griffiths, J. Howarth, G. D. A. Rowbotham, and A. Rees, "Effect of Build Parameters on Processing Efficiency and Material Performance in Fused Deposition Modelling," in Procedia CIRP, 2016, vol. 49, pp. 28–32.

[101] L. Baich, G. Manogharan, and H. Marie, "Study of infill print design on production cost-time of 3D printed ABS parts," International Journal of Rapid Manufacturing, vol. 5, no. 3/4, p. 308, 2015.

[102] T. Grimm, "Fused Deposition Modeling: A Technology Evaluation," Time-compression technologies, vol. 11, no. 2, pp. 1–6, 2003.

[103] I. Gibson, D. Rosen, and B. (Brent) Stucker, Additive Manufacturing Technologies 3D Printing, Rapid Prototyping, and Direct Digital Manufacturing. 2015.

[104] K. J. De Laurentis and C. Mavroidis, "Rapid fabrication of a non-assembly robotic hand

with embedded components," Assembly Automation, vol. 24, no. 4, pp. 394–405, 2004.

[105] N. B. Crane, J. Tuckerman, and G. N. Nielson, "Self-assembly in additive manufacturing: Opportunities and obstacles," Rapid Prototyping Journal, vol. 17, no. 3, pp. 211–217, 2011.

[106] K. J. De Laurentis, F. F. Kong, and C. Mavroidis, "Procedure for Rapid Fabrication of Non-Assembly Mechanisms with Embedded Components," in Proceedings of the 2002 ASME Design Engineering Technical Conferences and Computers and Information in Engineering Conference, 2002, pp. 1–7.

[107] M. Vaezi, S. Chianrabutra, B. Mellor, and S. Yang, "Multiple material additive manufacturing – Part 1: a review," Virtual and Physical Prototyping, vol. 8, no. 1, pp. 19–50, 2013.

[108] J. D. Hiller and H. Lipson, "STL 2.0: A Proposal for a Universal Multi-Material Additive Manufacturing File Format," Proceedings of the 20th Solid Freeform Fabrication Symposium (SFF), no. 1, pp. 266–278, 2009.

[109] C. Chu, G. Graf, and D. W. Rosen, "Design for additive manufacturing of cellular structures," Computer-Aided Design and Applications, vol. 5, no. 5, pp. 686–696, 2008.

[110] S. Pareek, V. Sharma, and R. Rai, "Design for additive manufacturing of kinematic pairs," in International Solid Freeform Fabrication Symposium, 2014, pp. p732-745.

[111] I. Gibson, D. W. Rosen, and B. Stucker, "Design for Additive Manufacturing," Additive Manufacturing Technologies, pp. 299–332, 2015.

[112] D. W. Rosen, C. C. Seepersad, T. W. Simpson, and C. B. Williams, "Special Issue: Design for Additive Manufacturing: A Paradigm Shift in Design, Fabrication, and Qualification," Journal of Mechanical Design, vol. 137, no. 11, 2015.

[113] I. Campbell, D. Bourell, and I. Gibson, "Additive manufacturing: rapid prototyping comes of age," Rapid Prototyping Journal, vol. 18, no. 4, pp. 255–258, 2012.

[114] J. Calì et al., "3D-printing of non-assembly, articulated models," ACM Transactions on Graphics, vol. 31, no. 6, pp 1-8, 2012.

[115] Z. Zhu, V. G. Dhokia, A. Nassehi, and S. T. Newman, "A review of hybrid manufacturing processes – state of the art and future perspectives," International Journal of Computer Integrated Manufacturing, vol. 26, no. 7, pp. 596–615, 2013.

[116] K. A. Lorenz, J. B. Jones, D. I. Wimpenny, and M. R. Jackson, "A review of hybrid manufacturing," in Solid Freeform Fabrication Conference Proceedings, 2015, vol. 53, pp. 96–108.

[117] J. Y. Jeng and M. C. Lin, "Mold fabrication and modification using hybrid processes of selective laser cladding and milling," Journal of Materials Processing Technology, vol. 110, no. 1, pp. 98–103, 2001.

[118] X. Xinhong, Z. Haiou, W. Guilan, and W. Guoxian, "Hybrid plasma deposition and milling for an aeroengine double helix integral impeller made of superalloy," Robotics and Computer-Integrated Manufacturing, vol. 26, no. 4, pp. 291–295, 2010.

[119] K. P. Karunakaran, S. Suryakumar, V. Pushpa, and S. Akula, "Low cost integration of additive and subtractive processes for hybrid layered manufacturing," Robotics and Computer-Integrated Manufacturing, vol. 26, no. 5, pp. 490–499, 2010.

[120] D.-S. Choi et al., "Development of a direct metal freeform fabrication technique using CO2 laser welding and milling technology," Journal of Materials Processing Technology, vol. 113, no. 1–3, pp. 273–279, 2001.

[121] F. Liou, K. Slattery, M. Kinsella, J. Newkirk, H. Chou, and R. Landers, "Applications of a hybrid manufacturing process for fabrication of metallic structures," Rapid Prototyping Journal, vol. 13, no. 4, pp. 236–244, 2007.

[122] W.-C. Lee, C.-C. Wei, and S.-C. Chuang, "Development of a hybrid rapid prototyping system using low-cost fused deposition modeling and five-axis machining," Journal of Materials Processing Technology, vol. 214, no. 11, pp. 2366–2374, 2014.

[123] J. B. Jones, P. McNutt, R. Tosi, C. Perry, and D. I. Wimpenny, "Remanufacture of turbine blades by laser cladding, machining and in-process scanning in a single machine," 23rd Annual International Solid Freeform Fabrication Symposium, Austin, Texas, USA, pp. 821–827, 2012.

[124] S. Keating and N. Oxman, "Compound fabrication: A multi-functional robotic platform for digital design and fabrication," Robotics and Computer-Integrated Manufacturing, vol. 29, no. 6, pp. 439–448, 2013.

[125] ASTM, "Stardard Terminology for Additive Manufacturing," 2015. .

[126] L. Li, Q. Sun, C. Bellehumeur, and P. Gu, "Composite modeling and analysis for fabrication of FDM prototypes with locally controlled properties," Journal of Manufacturing Processes, vol. 4, no. 2, pp. 129–141, 2002.

[127] D. Popescu, A. Zapciu, C. Amza, F. Baciu, and R. Marinescu, "FDM process parameters influence over the mechanical properties of polymer specimens: A review," Polymer Testing, vol. 69, pp. 157–166, 2018.

[128] G. D. Goh, Y. L. Yap, H. K. J. Tan, S. L. Sing, G. L. Goh, and W. Y. Yeong, "Process–Structure–Properties in Polymer Additive Manufacturing via Material Extrusion: A Review," Critical Reviews in Solid State and Materials Sciences, pp. 1–21, 2019.

[129] S. Bakrani Balani, F. Chabert, V. Nassiet, and A. Cantarel, "Influence of printing parameters on the stability of deposited beads in fused filament fabrication of poly(lactic) acid," Additive Manufacturing, vol. 25, pp. 112–121, 2019.

[130] S. H. Ahn, M. Montero, D. Odell, S. Roundy, and P. K. Wright, "Anisotropic material

properties of fused deposition modeling ABS," Rapid Prototyping Journal, vol. 8, no. 4, pp. 248–257, 2002.

[131] A. K. Sood, R. K. Ohdar, and S. S. Mahapatra, "Parametric appraisal of mechanical property of fused deposition modelling processed parts," Materials and Design, vol. 31, no. 1, pp. 287–295, 2010.

[132] T. W. Kerekes, H. Lim, W. Y. Joe, and G. J. Yun, "Characterization of process–deformation/damage property relationship of fused deposition modeling (FDM) 3D-printed specimens," Additive Manufacturing, vol. 25, pp. 532–544, 2019.

[133] A. C. Abbott, G. P. Tandon, R. L. Bradford, H. Koerner, and J. W. Baur, "Process-structure-property effects on ABS bond strength in fused filament fabrication," Additive Manufacturing, vol. 19, pp. 29–38, 2018.

[134] P. Kulkarni and D. Dutta, "Deposition strategies and resulting part stiffnesses in fused deposition modeling," Journal of Manufacturing Science and Engineering, Transactions of the ASME, pp. 93–103, 1999.

[135] J. F. Rodriguez, J. P. Thomas, and J. E. Renaud, "Characterization of the mesostructure of fused-deposition acrylonitrile-butadiene-styrene materials," Rapid Prototyping Journal, vol. 6, no. 3, pp. 175–186, 2000.

[136] M. H. Too et al., "Investigation of 3D non-random porous structures by fused deposition modelling," International Journal of Advanced Manufacturing Technology, vol. 19, no. 3, pp. 217–223, 2002.

[137] J. F. Rodríguez, J. P. Thomas, and J. E. Renaud, "Mechanical behavior of acrylonitrile butadiene styrene fused deposition materials modeling," Rapid Prototyping Journal, vol. 9, no. 4, pp. 219–230, 2003.

[138] S. J. Kalita, S. Bose, H. L. Hosick, and A. Bandyopadhyay, "Development of controlled porosity polymer-ceramic composite scaffolds via fused deposition modeling," Materials Science and Engineering C, vol. 23, no. 5, pp. 611–620, 2003.

[139] K. C. Ang, K. F. Leong, C. K. Chua, and M. Chandrasekaran, "Investigation of the mechanical properties and porosity relationships in fused deposition modelling-fabricated porous structures," Rapid Prototyping Journal, vol. 12, no. 2, pp. 100–105, 2006.

[140] T. P. T. Phuong, "Development of a combined analytical and experimental approach for the determination of the cohesive strength between material extrusion layers using the true area of contact," Additive Manufacturing, vol. 30, p. 100832, 2019.

[141] Y. S. Ko, D. Herrmann, O. Tolar, W. J. Elspass, and C. Brändli, "Improving the filament weld-strength of fused filament fabrication products through improved interdiffusion," Additive Manufacturing, vol. 29, p. 100815, 2019.

[142] Q. Sun, G. M. Rizvi, C. T. Bellehumeur, and P. Gu, "Effect of processing conditions on the

bonding quality of FDM polymer filaments," Rapid Prototyping Journal, vol. 14, no. 2, pp. 72–80, 2008.

[143] M. Faes, E. Ferraris, and D. Moens, "Influence of Inter-layer Cooling time on the Quasi-static Properties of ABS Components Produced via Fused Deposition Modelling," in Procedia CIRP 42, 2016, pp. 748–753.

[144] C. Bellehumeur, L. Li, Q. Sun, and P. Gu, "Modeling of bond formation between polymer filaments in the fused deposition modeling process," Journal of Manufacturing Processes, vol. 6, no. 2, pp. 170–178, 2004.

[145] O. Pokluda, C. T. Bellehumeur, and J. Vlachopoulos, "Modification of Frenkel's model for sintering," AIChE journal, vol. 43, no. 12, pp. 3253–3256, 1997.

[146] J. Zhang, X. Z. Wang, W. W. Yu, and Y. H. Deng, "Numerical investigation of the influence of process conditions on the temperature variation in fused deposition modeling," Materials and Design, vol. 130, pp. 59–68, 2017.

[147] A. D'Amico and A. M. Peterson, "An adaptable FEA simulation of material extrusion additive manufacturing heat transfer in 3D," Additive Manufacturing, vol. 21, pp. 422–430, 2018.

[148] S. F. Costa, F. M. Duarte, and J. A. Covas, "Estimation of filament temperature and adhesion development in fused deposition techniques," Journal of Materials Processing Technology, vol. 245, pp. 167–179, 2017.

[149] H. Xia, J. Lu, and G. Tryggvason, "A numerical study of the effect of viscoelastic stresses in fused filament fabrication," Computer Methods in Applied Mechanics and Engineering, vol. 346, pp. 242–259, 2019.

[150] R. K. Chen, T. T. Lo, L. Chen, and A. J. Shih, "Nano-CT characterization of structural voids and air bubbles in fused deposition modeling for additive manufacturing," in ASME 2015 International Manufacturing Science and Engineering Conference, 2015.

[151] I. Gajdoš and J. Slota, "Influence of printing conditions on structure in FDM prototypes," Tehnicki Vjesnik, vol. 20, no. 2, pp. 231–236, 2013.

[152] E. Ferraris, J. Zhang, and B. Van Hooreweder, "Thermography based in-process monitoring of Fused Filament Fabrication of polymeric parts," CIRP Annals, 2019.

[153] K. Chase, "Tolerance allocation methods for designers," ADCATS Report, no. 99–6, 1999.

[154] S. Maghsoodloo and M. H. Li, "Optimal asymmetric tolerance design," IIE Transactions (Institute of Industrial Engineers), vol. 32, no. 12, pp. 1127–1137, 2000.

[155] M.-H. Li, "Unbalanced tolerance design and manufacturing setting with asymmetrical linear loss function," The International Journal of Advanced Manufacturing Technology, vol. 20, no. 5, pp. 334–340, 2002.

[156] Q. Jin, S. Liu, and P. Wang, "Optimal tolerance design for products with non-normal distribution based on asymmetric quadratic quality loss," International Journal of Advanced Manufacturing Technology, vol. 78, no. 1–4, pp. 667–675, 2015.

[157] P. Di Stefano, "Tolerance analysis and synthesis using the mean shift model," Proceedings of the Institution of Mechanical Engineers, Part C: Journal of Mechanical Engineering Science, vol. 217, no. 2, pp. 149–160, 2003.

[158] S. Karmakar and J. Maiti, "A review on dimensional tolerance synthesis: paradigm shift from product to process," Assembly Automation, vol. 32, no. 4, pp. 373–388, 2012.

[159] W. H. W. Huang and Z. K. Z. Kong, "Process Capability Sensitivity Analysis for Design Evaluation of Multistage Assembly Processes," IEEE Transactions on Automation Science and Engineering, vol. 7, no. 4, pp. 736–745, 2010.

[160] P. Muthu, V. Dhanalakshmi, and K. Sankaranarayanasamy, "Optimal tolerance design of assembly for minimum quality loss and manufacturing cost using metaheuristic algorithms," International Journal of Advanced Manufacturing Technology, vol. 44, no. 11–12, pp. 1154–1164, 2009.

[161] Y. Chen, Y. Ding, J. Jin, and D. Ceglarek, "Integration of process-oriented tolerancing and maintenance planning in design of multistation manufacturing processes," IEEE Transactions on Automation Science and Engineering, vol. 3, no. 4, pp. 440–453, 2006.

[162] K. Geetha, D. Ravindran, M. Siva Kumar, and M. N. Islam, "Multi-objective optimization for optimum tolerance synthesis with process and machine selection using a genetic algorithm," International Journal of Advanced Manufacturing Technology, vol. 67, no. 9–12, pp. 2439–2457, 2013.

[163] V. Janakiraman and R. Saravanan, "Concurrent optimization of machining process parameters and tolerance allocation," International Journal of Advanced Manufacturing Technology, vol. 51, no. 1–4, pp. 357–369, 2010.

[164] A. Haghighi and L. Li, "Study of the relationship between dimensional performance and manufacturing cost in fused deposition modeling," Rapid Prototyping Journal, vol. 24, no. 2, pp. 395–408, 2018.

[165] L. Li, A. Haghighi, and Y. Yang, "Theoretical Modeling and Prediction of Surface Roughness for Hybrid Additive-Subtractive Manufacturing Processes," IISE Transactions, vol. 51, no. 2, pp. 124–135, 2019.

[166] A. Haghighi and L. Li, "A hybrid physics-based and data-driven approach for characterizing porosity variation and filament bonding in extrusion-based additive manufacturing," Additive Manufacturing, vol. 36, 2020.

[167] C. Ferro, R. Grassi, C. Seclì, and P. Maggiore, "Additive Manufacturing Offers New Opportunities in UAV Research," in Procedia CIRP, 2016, vol. 41, pp. 1004–1010.

[168] M. Baumers, P. Dickens, C. Tuck, and R. Hague, "The cost of additive manufacturing: Machine productivity, economies of scale and technology-push," Technological Forecasting and Social Change, vol. 102, pp. 193–201, 2016.

[169] M. Baumers, C. Tuck, R. Wildman, I. Ashcroft, E. Rosamond, and R. Hague, "Combined build-time, energy consumption and cost estimation for direct metal laser sintering," in From Proceedings of Twenty Third Annual International Solid Freeform Fabrication Symposium—An Additive Manufacturing Conference, 2012, vol. 13.

[170] H. S. Yoon et al., "A comparison of energy consumption in bulk forming, subtractive, and additive processes: Review and case study," International Journal of Precision Engineering and Manufacturing - Green Technology, vol. 1, no. 3, pp. 261–279, 2014.

[171] D. C. Montgomery, Design and Analysis of Experiments, vol. 2. 2013.

[172] NIST, NIST/SEMATECH e-Handbook of Statistical Methods, 2003. .

[173] S. F. Costa, F. M. Duarte, and J. A. Covas, "Thermal conditions affecting heat transfer in FDM/FFE: a contribution towards the numerical modelling of the process.," Virtual and Physical Prototyping, vol. 10, no. 1, pp. 35–46, 2015.

[174] Y. Frenkel, "Viscous Flow Of Crystalline Bodies Under The Action Of Surface Tension," Journal of Physics, vol. 9, p. 385, 1945.

[175] B. B. Shahriar, C. France, N. Valerie, C. Arthur, and G. Christian, "Toward improvement of the properties of parts manufactured by FFF (fused filament fabrication) through understanding the influence of temperature and rheological behaviour on the coalescence phenomenon," in AIP Conference Proceedings, vol. 1896, no. 1, 2017.

[176] J. Escobedo and G. A. Mansoori, "Surface Tension Prediction for Pure Fluids," AIChE Journal, vol. 42, no. 5, pp. 1425–1433, 1996.

[177] M. I. S. Ismail, Y. Okamoto, and A. Okada, "Neural network modeling for prediction of weld bead geometry in laser microwelding," Advances in Optical Technologies, 2013.

[178] D. Eberly, "The area of intersecting ellipses." Technical Report. Geometric Tools, LLC. www. geometrictools. com, 2010.

[179] L. Trhlíková, O. Zmeskal, P. Psencik, and P. Florian, "Study of the thermal properties of filaments for 3D printing," in AIP Conference Proceedings, vol. 1752, no. 1, 2016.

[180] A. Goel, Concepts of Physical Chemistry. Discovery Publishing House, 2006.

[181] D. Garlotta, "A literature review of poly(lactic acid)," Journal of Polymers and the Environment, vol. 9, no. 2, pp. 63–84, 2001.

[182] I. Valentina, A. Haroutioun, L. Fabrice, V. Vincent, and P. Roberto, "Poly (Lactic Acid)-Based Nanobiocomposites with Modulated Degradation Rates," Materials, vol. 11, no. 10,

194

p. 1943, 2018.

[183] A.-I. Botean, "Thermal expansion coefficient determination of polylactic acid using digital image correlation," in E3S Web of Conferences, 2018, vol. 32, p. 1007.

[184] M. Pyda, R. C. Bopp, and B. Wunderlich, "Heat capacity of poly (lactic acid)," The Journal of Chemical Thermodynamics, vol. 36, no. 9, pp. 731–742, 2004.

[185] T. Flaata, G. J. Michna, and T. Letcher, "Thermal conductivity testing apparatus for 3D printed materials," in ASME 2017 Heat Transfer Summer Conference, 2017.

[186] M. Jamshidian, E. A. Tehrany, M. Imran, M. Jacquot, and S. Desobry, "Poly-Lactic Acid: production, applications, nanocomposites, and release studies," Comprehensive reviews in food science and food safety, vol. 9, no. 5, pp. 552–571, 2010.

[187] B. B. Shahriar, C. Arthur, C. France, and N. Valérie, "Influence of parameters controlling the extrusion step in fused filament fabrication (FFF) process applied to polymers using numerical simulation," in AIP Conference Proceedings, 2018, vol. 1960, no. 1, p. 140003.

[188] F. Bähr and E. Westkämper, "Correlations between influencing parameters and quality properties of components produced by fused deposition modeling," Procedia CIRP, vol. 72, no. 1, pp. 1214–1219, 2018.

[189] L. Li, A. Haghighi, and Y. Yang, "A novel 6-axis hybrid additive-subtractive manufacturing process: Design and case studies," Journal of Manufacturing Processes, vol. 33, pp. 150–160, 2018.

[190] L. Wang, N. Cai, H. Y. Feng, and Z. Liu, "Enriched machining feature-based reasoning for generic machining process sequencing," International Journal of Production Research, vol. 44, no. 8, pp. 1479–1501, 2006.

[191] V. T. Le, H. Paris, and G. Mandil, "Extracting features for manufacture of parts from existing components based on combining additive and subtractive technologies," International Journal on Interactive Design and Manufacturing, vol. 12, no. 2, pp. 525–536, 2018.

[192] B. Babic, N. Nesic, and Z. Miljkovic, "A review of automated feature recognition with rule-based pattern recognition," Computers in Industry, vol. 59, no. 4. pp. 321–337, 2008.

[193] W. Ji, L. Wang, A. Haghighi, M. Givehchi, and X. Liu, "A reachability based approach for machining feature sequencing," Journal of Manufacturing Systems, vol. 40, pp. 96–104, 2016.

[194] ABB, 2017, Available: https://global.abb/group/en.

[195] A. Haghighi and L. Li, "Optimal Feature Sequencing in Hybrid Additive-Subtractive Manufacturing Processes,", poster presentation, IISE Annual Conference, 2018.

[196] I. Bin Ishak, J. Fisher, and P. Larochelle, "Robot Arm Platform for Additive Manufacturing Using Multi-Plane Toolpaths," in ASME 2016 International Design Engineering Technical Conferences and Computers and Information in Engineering Conference, American Society of Mechanical Engineers, 2016.

[197] X. Song, Y. Pan, and Y. Chen, "Development of a low-cost parallel kinematic machine for multi-directional additive manufacturing," 24th International SFF Symposium - An Additive Manufacturing Conference, SFF, vol. 137, pp. 297–310, April 2013.

[198] A. Armillotta, "Assessment of surface quality on textured FDM prototypes," Rapid Prototyping Journal, vol. 12, no. 1, pp. 35–41, 2006.

[199] M.-Y. Wang and H.-Y. Chang, "Experimental study of surface roughness in slot end milling AL2014-T6," International Journal of Machine Tools and Manufacture, vol. 44, no. 1, pp. 51–57, 2004.

[200] Y. Yang, A. Haghighi, and L. Li, "Energy Consumption Study for 6-Axis Hybrid Additive-Subtractive Manufacturing Process," in IISE Annual Conference, 2018.

[201] A. Mohammed, B. Schmidt, L. Wang, and L. Gao, "Minimizing energy consumption for robot arm movement," in Procedia CIRP, 2014, vol. 25, no. C, pp. 400–405.

[202] A. Haghighi, Y. Yang, and L. Li, "Dimensional performance of as-built assemblies in polyjet additive manufacturing process," In International Manufacturing Science and Engineering Conference, 2017.

[203] A. Haghighi and L. Li, "Joint Asymmetric Tolerance Design and Manufacturing Decision Making for Additive Manufacturing Processes," IEEE Transactions on Automation Science and Engineering, vol. 16, no. 3, pp. 1259–1270, 2019.

[204] M. Salmi, K. S. Paloheimo, J. Tuomi, J. Wolff, and A. Mäkitie, "Accuracy of medical models made by additive manufacturing (rapid manufacturing)," Journal of Cranio-Maxillofacial Surgery, vol. 41, no. 7, pp. 603–609, 2013.

[205] R. Singh, "Process capability study of polyjet printing for plastic components," Evolutionary Ecology, vol. 25, no. 4, pp. 1011–1015, 2011.

[206] R. K. K and D. Sen, "DFM for non-assembly RP of mechanisms," Proceedings of the 14th IFToMM World Congress, pp. 101–110, 2015.

[207] Stratasys, 2016, Available: https://www.stratasys.com/.

[208] M. Baumers, P. Dickens, C. Tuck, and R. Hague, "The cost of additive manufacturing: Machine productivity, economies of scale and technology-push," Technological Forecasting and Social Change, vol. 102, pp. 193–201, 2016.

[209] G. Costabile, M. Fera, F. Fruggiero, A. Lambiase, and D. Pham, "Cost models of additive manufacturing: A literature review," International Journal of Industrial Engineering

Computations, vol. 8, pp. 263–282, 2017.

[210] H. Piili, A. Happonen, T. Väistö, V. Venkataramanan, J. Partanen, and A. Salminen, "Cost Estimation of Laser Additive Manufacturing of Stainless Steel," in Physics Procedia, 2015, vol. 78, pp. 388–396.

[211] B. Efron and R. J. Tibshirani, An introduction to the bootstrap. CRC press, 1994.

[212] K. Singh and M. Xie, "Bootstrap: a statistical method," Unpublished manuscript, Rutgers University, USA. Retrieved from http://www. stat. rutgers. edu/home/mxie/RCPapers/bootstrap. pdf, 2008.

[213] T. J. DiCiccio and B. Efron, "Bootstrap confidence intervals," Statistical Science, vol. 11, no. 3, pp. 189–228, 1996.

[214] B. Efron, "Better bootstrap confidence intervals," Journal of the American Statistical Association, vol. 82, no. 397, pp. 171–185, 1987.

[215] R. Barlow, "Asymmetric Errors," Phystat2003, no. 2, p. 6, 2003.

[216] R. J. BARLOW, "Asymmetric statistical errors," Statistical Problems In Particle Physics, Astrophysics And Cosmology, pp. 56–59, 2006.

[217] P. Stoica and Y. Selén, "Cyclic minimizers, majorization techniques, and the expectation-maximization algorithm: A refresher," IEEE Signal Processing Magazine, vol. 21, no. 1, pp. 112–114, 2004.

[218] J. C. Bezdek and R. J. Hathaway, "Convergence of alternating optimization.," Neural Parallel Sci. Comput., vol. 11, no. 4, pp. 351–368, 2003.

[219] L. Grippo and M. Sciandrone, "On the convergence of the block nonlinear Gauss-Seidel method under convex constraints," Operations Research Letters, vol. 26, no. 3, pp. 127–136, 2000.

[220] J. C. Bezdek and R. J. Hathaway, "Some notes on alternating optimization," in Fuzzy Systems, AFSS International Conference, 2002, pp. 187–195.

VITA

NAME: Azadeh Haghighi
(pronouns she/her/hers)

EDUCATION: B.S., Industrial Engineering, Sharif University of Technology, Iran, 2011

M.S., Mechanical Engineering (Production Engineering and Management), KTH Royal Institute of Technology, Sweden, 2013

Ph.D., Industrial Engineering and Operations Research, University of Illinois at Chicago, Chicago, Illinois, 2020

HONORS: US DOE IAC Women for Energy Efficiency Mentorship Program Nominee, 2019

Provost's Award for Graduate Research, University of Illinois at Chicago, 2017

Outstanding Paper Award, NAMRI/SME Society of Manufacturing Engineers NAMRC 44, 2016

National Science Foundation (NSF) Student Travel Award, SME NAMRC44, 2016

Student Presentation Award Nominee, SME NAMRC44, 2016

Undergraduate Scholarship, Sharif University of Technology, Iran, 2007-2011

RESEARCH: Research Assistant at Sustainable Manufacturing Systems Research Laboratory, University of Illinois at Chicago, 2016-2020

Research Assistant at Industrial Assessment Center (under US Department of Energy), University of Illinois at Chicago, 2016-2020

Research Assistant at Sustainable Production Systems Division, KTH Royal Institute of Technology, 2014-2016

Research Assistant at Digital Smart Production Division, KTH Royal Institute of Technology, 2013-2014

JOURNAL PUBLICATIONS: Azadeh Haghighi and Lin Li. "A Hybrid Physics-based and Data-driven Approach for Characterizing Porosity Variation and Filament Bonding in Extrusion-based Additive Manufacturing", Additive Manufacturing 36 (2020).

Lin Li, Azadeh Haghighi, and Yiran Yang. "Theoretical Modeling and Prediction of Surface Roughness for Hybrid Additive-Subtractive Manufacturing Processes.", IISE Transactions 51, no. 2 (2019): 124-135.

Azadeh Haghighi and Lin Li. "Joint Asymmetric Tolerance Design and Manufacturing Decision Making for Additive Manufacturing Processes", IEEE Transactions on Automation Science and Engineering 16, no. 3 (2018): 1259-1270.

Lin Li, Azadeh Haghighi, and Yiran Yang. "A Novel 6-axis Hybrid Additive Subtractive Manufacturing Process: Design and Case Studies.", Journal of Manufacturing Processes 33 (2018): 150-160.

Azadeh Haghighi and Lin Li. "Study of the Relationship Between Dimensional Performance and Manufacturing Cost in Fused Deposition Modeling.", Rapid Prototyping Journal 24, no. 2 (2018): 395-408.

Wei Ji, Lihui Wang, Azadeh Haghighi, Mohammad Givehchi, and Xianli Liu. "An Enriched Machining Feature Based Approach to Cutting Tool Selection." International Journal of Computer Integrated Manufacturing 31, no. 1 (2018), 1-10.

Mohammad Givehchi, Azadeh Haghighi, and Lihui Wang. "Cloud-DPP for Distributed Process Planning of Mill-Turn Machining Operations.", Robotics and Computer-Integrated Manufacturing 47 (2017): 76-84.

Lihui Wang, and Azadeh Haghighi. "Combined Strength of Holons, Agents and Function blocks in Cyber-Physical Systems.", Journal of Manufacturing Systems 40 (2016): 25-34.

Wei Ji, Lihui Wang, Azadeh Haghighi, Mohammad Givehchi, and Xianli Liu. "A Reachability Based Approach for Machining Feature Sequencing." Journal of Manufacturing Systems 40 (2016): 96-104.

Mohammad Givehchi, Azadeh Haghighi, and Lihui Wang. "Generic Machining Process Sequencing Through a Revised Enriched Machining Feature Concept." Journal of Manufacturing Systems 37 (2015): 564-575.

CONFERENCE PUBLICATIONS: Azadeh Haghighi, and Lin Li. " Perception of Bonding Degree in Additive Manufacturing via Machine Learning.", IISE Annual Conference and Expo, 2020.

Azadeh Haghighi, and Lin Li. "Optimal Feature Sequencing in Hybrid Additive-Subtractive Manufacturing Processes.", Poster Presentation, IISE Annual Conference and Expo, May 2018.

Yiran Yang, Azadeh Haghighi, and Lin Li. "Energy Consumption Study for 6-Axis Hybrid Additive-Subtractive Manufacturing Process.", In Proceedings of IISE Annual Conference and Expo, May 2018.

Azadeh Haghighi, Yiran Yang, and Lin Li. "Dimensional Performance of As-Built Assemblies in Polyjet Additive Manufacturing Process." In ASME 2017 12th International Manufacturing Science and Engineering Conference, American Society of Mechanical Engineers, 2017.

Lihui Wang, and Azadeh Haghighi. "Combined Strength of Holons, Agents and Function blocks in Cyber-Physical Systems.", SME North American Manufacturing Research Conference (NAMRC), 2016 – (fast tracked to journal paper).

Mohammad Givehchi, Azadeh Haghighi and Lihui Wang. "Latest Advances in Adaptive Process Planning for Machining.", 4th International Conference on Virtual Machining Process Technology, June 2015.

Mohammad Givehchi, Azadeh Haghighi, and Lihui Wang. "Adaptive Distributed Process Planning and Executions for Multi-Tasking Machining Centers with Special Functionalities." In Proceedings of the 25th International Conference on Flexible Automation and Intelligent Manufacturing, vol. 2, pp. 288-295, 2015.

Mohammad Givehchi, Azadeh Haghighi, and Lihui Wang. "Generic Machining Process Sequencing Through a Revised Enriched Machining Feature Concept.", SME North American Manufacturing Research Conference (NAMRC), 2015 – (fast tracked to journal paper).

Azadeh Haghighi, Navid Shariat Zadeh, Gunilla Sivard, Thomas Lundholm, and Yvonne Eriksson. "Digital Learning Factories: Conceptualization, Review and Discussion." In The 6th Swedish Production Symposium, 2014.

SERVICE: Invited Reviewer (2013-present)
- Additive Manufacturing Journal
- IEEE Transactions on Automation Science and Engineering (IEEE T-ASE)
- International Academy for Production Engineering (CIRP)
- North American Manufacturing Research Conference (NAMRC)
- Flexible Automation and Intelligent Manufacturing Conference (FAIM)
- Conference on Automation Science and Engineering (CASE)
- Swedish Production Symposium (SPS)

Organizer
- 4th Conference on Learning Factories KTH Royal Institute of

Technology, Sweden, 2014
- Nobel Prize Nightcap, KTH Royal Institute of Technology, Stockholm, Sweden, 2013
- 1st Conference on Mathematics and Physics, National Organization for Development of Exceptional Talents (NODET), Iran, 2005

Editorial Service:
- Contributed to the editing of the "Handbook of Manufacturing"
  Editors: Yong Huang, Lihui Wang and Steven Y. Liang, 2019 (ISBN 978-981-3271-01-2)
- Editorial board member, Sharif Journal of Industrial Engineering & Management, Iran, 2008-2010

TEACHING: Invited Lecturer
- Time Series Analysis and Forecasting, University of Illinois at Chicago, Fall 2018 and Fall 2019

Teaching/Laboratory Assistant
- University of Illinois at Chicago, 2016-2019
- KTH Royal Institute of Technology, Sweden, 2013
- Sharif University of Technology, Iran, 2010

APPENDIX (COPYRIGHT STATEMENT)

Emerald Publishing Copyright

Haghighi, Azadeh and Lin Li. "Study of the Relationship Between Dimensional Performance and Manufacturing Cost in Fused Deposition Modeling.", Rapid Prototyping Journal 24, no. 2 (2018): 395-408.

Author rights:
https://www.emeraldgrouppublishing.com/services/authors/author-policies/author-rights

Find out how you can reuse your journal articles and/or book chapters.

Reuse	Submitted version under review (SMUR)	Author accepted manuscript (AAM)	Version of record (VoR)
Make photocopies of your article or book chapter for teaching and classroom purposes	Unlimited	Unlimited	Unlimited
Make photocopies of your article or book chapter for conferences, or unlimited to use as handouts	Unlimited	Unlimited	Up to 25 copies. If you require more, please contact us.
Inclusion of your article or book chapter in your dissertation or thesis	Yes	Yes	Yes, this version may be included in the print version of your thesis/dissertation. If an electronic deposit is required, this must be the SMUR or AAM version.

Elsevier Copyright

Haghighi, Azadeh and Lin Li. "A Hybrid Physics-based and Data-driven Approach for Characterizing Porosity Variation and Filament Bonding in Extrusion-based Additive Manufacturing", Additive Manufacturing 36 (2020).

Li, Lin, Azadeh Haghighi, and Yiran Yang. "A Novel 6-axis Hybrid Additive Subtractive Manufacturing Process: Design and Case Studies.", Journal of Manufacturing Processes 33 (2018): 150-160.

Author rights:
https://www.elsevier.com/about/policies/copyright/permissions

Can I include/use my article in my thesis/dissertation?
Yes. Authors can include their articles in full or in part in a thesis or dissertation for non-commercial purposes.

Taylor and Francis Copyright

Li, Lin, Azadeh Haghighi, and Yiran Yang. "Theoretical Modeling and Prediction of Surface Roughness for Hybrid Additive-Subtractive Manufacturing Processes.", IISE Transactions 51, no. 2 (2019): 124-135.
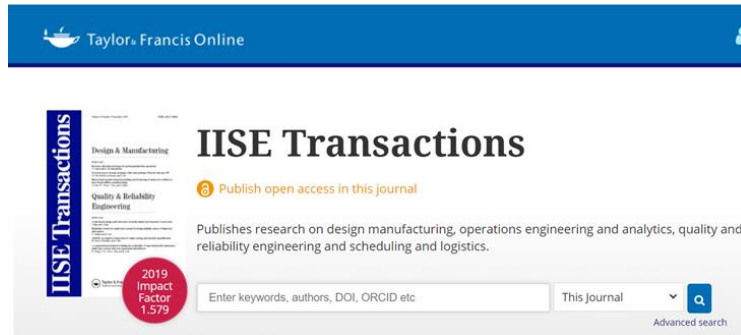
Author rights:

If you would like to reuse content from a Taylor & Francis journal you can quickly and easily get

permission to do so via this website.

RE: uiie21: Theoretical modelling and prediction of surface roughness for hybrid additive–subtractive manufacturing processes
1 message

US Journal Permissions <USJournalPermissions@taylorandfrancis.com>
To: Azadeh Haghighi <ahaghi3@uic.edu>

Dear Azadeh Haghighi,

Thank you for your author reuse request for your dissertation.

You are free to use and post your Accepted Manuscript with full acknowledgment of your article.

Kind regards,

Mary Ann Muller – Permissions Coordinator, US Journals Division

IEEE Copyright

Haghighi, Azadeh and Lin Li. "Joint Asymmetric Tolerance Design and Manufacturing Decision Making for Additive Manufacturing Processes", IEEE Transactions on Automation Science and Engineering 16, no. 3 (2018): 1259-1270.

Author rights:
https://www.ieee.org/content/dam/ieee-org/ieee/web/org/pubs/permissions_faq.pdf

Does IEEE require individuals working on a thesis or dissertation to obtain formal permission for reuse?

The IEEE does not require individuals working on a thesis to obtain a formal reuse license, however, you must follow the requirements listed below:

ASME Copyright

Haghighi, A., Yang, Y., and Li, L. (2017, June). Dimensional performance of as-built assemblies in polyjet additive manufacturing process. In International Manufacturing Science and Engineering Conference (Vol. 50732). American Society of Mechanical Engineers.